



**WIRELESS GRAPHENE-BASED
ELECTROCARDIOGRAM (ECG) SENSOR INCLUDING
MULTIPLE PHYSIOLOGICAL MEASUREMENT
SYSTEM**

**A thesis submitted in partial fulfilment of the requirements for the degree of
Doctor of Philosophy (Ph.D.)**

In

Centre for Electronic Systems Research

Electronic and Computer Engineering

College of Engineering, Design and Physical Sciences

Brunel University London

By

Numan Celik

Supervised by

Professor Wamadeva Balachandran

7 August 2017

ABSTRACT

In this thesis, a novel graphene (GN) based electrocardiogram (ECG) sensor is designed, constructed and tested to validate the concept of coating GN, which is a highly electrically conductive material, on Ag substrates of conventional electrodes. The background theory, design, experiments and results for the proposed GN-based ECG sensor are also presented.

Due to the attractive electrical and physical characteristics of graphene, a new ECG sensor was investigated by coating GN onto itself. The main focus of this project was to examine the effect of GN on ECG monitoring and to compare its performance with conventional methods. A thorough investigation into GN synthesis on Ag substrate was conducted, which was accompanied by extensive simulation and experimentation. A GN-enabled ECG electrode was characterised by Raman spectroscopy, scanning electron microscopy along with electrical resistivity and conductivity measurements. The results obtained from the GN characteristic experimentation on Raman spectroscopy, detected a 2D peak in the GN-coated electrode, which was not observed with the conventional Ag/AgCl electrode. SEM characterisation also revealed that a GN coating smooths the surface of the electrode and hence, improves the skin-to-electrode contact. Furthermore, a comparison regarding the electrical conductivity calculation was made between the proposed GN-coated electrodes and conventional Ag/AgCl ones. The resistance values obtained were 212.4 Ω and 28.3 Ω for bare and GN-coated electrodes, respectively. That indicates that the electrical conductivity of GN-based electrodes is superior and hence, it is concluded that skin-electrode contact impedance can be lowered by their usage. Additional COMSOL simulation was carried out to observe the effect of an electrical field and surface charge density using GN-coated and conventional Ag/AgCl electrodes on a simplified human skin model. The results demonstrated the effectiveness of the addition of electrical field and surface charge capabilities and hence, coating GN on Ag substrates was validated through this simulation.

This novel ECG electrode was tested with various types of electrodes on ten different subjects in order to analyse the obtained ECG signals. The experimental results clearly showed that the proposed GN-based electrode exhibits the best performance in terms of ECG signal quality, detection of critical waves of ECG morphology (P-wave, QRS complex and T-wave), signal-to-noise ratio (SNR) with 27.0 dB and skin-electrode contact impedance (65.82 k Ω at 20 Hz) when compared to those obtained by conventional a Ag/AgCl electrode.

Moreover, this proposed GN-based ECG sensor was integrated with core body temperature (CBT) sensor in an ear-based device, which was designed and printed using 3D technology. Subsequently,

a finger clipped photoplethysmography (PPG) sensor was integrated with the two-sensors in an Arduino based data acquisition system, which was placed on the subject's arm to enable a wearable multiple physiological measurement system. The physiological information of ECG and CBT was obtained from the ear of the subject, whilst the PPG signal was acquired from the finger. Furthermore, this multiple physiological signal was wirelessly transmitted to the smartphone to achieve continuous and real-time monitoring of physiological signals (ECG, CBT and PPG) on a dedicated app developed using the Java programming language. The proposed system has plenty of room for performance improvement and future development will make it adaptable, hence being more convenient for the users to implement other applications than at present.

Declaration

I, Numan Celik, here declare that the work presented in this thesis was carried out by myself at Brunel University London, and no part of this work has been previously submitted to Brunel University London, nor any other academic institution, for admission to a higher degree. Some of the work has appeared in the forms of publications, and those are listed on the List of publications section.

Numan Celik

May 2017.

Dedication

All the devotion to Allah the Almighty for His infinite kindness and mercy throughout my life, and I am deeply grateful to Allah who gave me the ability and confidence to complete my studies.

This thesis is also dedicated to my family, especially my father, who supported me throughout my Masters and Ph.D. in London, and my mother who gave me love, encouragement, and prays of day and night make me able to get such success and honor, my beloved sisters, and brother. A special dedication belongs to my wonderful wife for her great patience and support, especially in the times when I was deeply stressed. I could not conduct such great performance and manage my studies without her sacrificial care for me. Thank you all.

Acknowledgements

I would like to express my sincere gratitude and thanks to my supervisor, Professor Wamadeva Balachandran for his excellent guidance and patience despite his many other academic and personal commitments. His guidance and knowledge have inspired me and helped me a lot throughout my research and the writing up of this thesis. I would like to sincerely thank him for his valuable advices on my research and especially suggesting me to do my PhD on Graphene technology which has still many potential ongoing research and undiscovered applications. Hence, my research has been immensely valuable with several publications in highly ranked journals and conferences. For this I am truly grateful.

All my gratitude also goes to all the members of DocLab research group for their help and coordination. I am truly indebted to Dr. Nadarajah Manivannan for his stimulating and insightful scientific discussions, advices and supports which helped me throughout this research.

I also want to express my appreciation to Dr. Pascal Craw, Dr. Tulasidas Sivanesan, Dr. Sara Chaychian, Prof. Chris Hudson, Dr. Ruth Mackay and Dr. Branavan Manoharanehru for their guidance and invaluable help for completing this study.

Additional thanks go to my friends Dr. Murtadha, Tom, Angel, Tosan, and other friends in the same research group for the fruitful discussions and spending long time together during this project at Brunel University London.

Finally, special thanks to my family, who have always supported and encouraged me and stood by me during all parts of this Ph.D. work.

Contents

ABSTRACT.....	2
Declaration	4
Dedication.....	5
Acknowledgements.....	6
Contents.....	7
List of Figures.....	10
List of Tables	16
List of Abbreviations	17
CHAPTER 1: GENERAL INTRODUCTION	21
1.1. Wireless Body Area Network for Personal Health Monitoring.....	21
1.2. ECG Monitoring System.....	22
1.3. CBT Monitoring System	23
1.4. PPG Monitoring System.....	24
1.5. Aims of this Thesis	25
1.6. Contribution to Knowledge	26
1.7. Thesis Outline.....	26
1.8. List of Publications	28
CHAPTER 2: LITERATURE REVIEW.....	29
2.1 Review of developed different types of electrodes for ECG monitoring.....	29
2.2 Review of body signal acquisition systems using different type of wearable sensors	65
2.3. Summary	79
CHAPTER 3: THEORETICAL BACKGROUND TO MULTIPLE PHYSIOLOGICAL MONITORING SYSTEMS	80
3.1. Analysis of Electrocardiogram (ECG) Measurement	80
3.1.1. The Anatomy of the Heart.....	80
3.1.2. Electrical Activity in the Heart	81
3.1.3. ECG Wave and Lead Positions	83
3.1.4. ECG Measurement and Electrode Properties.....	88
3.1.5. Electrical Model of the Skin-Electrode Interface	89
3.1.6. ECG Signal Processing and Heartbeat Detection	91
3.2. Analysis of the Core Body Temperature (CBT) Measurement	94
3.2.1. Background of Core Body Temperature (CBT) and Thermal Imaging	94
3.2.2. Measurements of Core Body Temperature (CBT)	96
3.2.3. Anatomy of Ear in CBT Measurement.....	97
3.2.4. CBT Measurement using an Infrared Thermopile Sensor.....	98
3.3. Analysis of Photoplethysmography (PPG) Measurement	99

3.3.1. Background to Photoplethysmography (PPG).....	99
3.3.2. Measurements of Photoplethysmography (PPG) Signals.....	101
3.3.3. Heartbeat Detection from PPG Signals	104
3.3.4. Oxygen Saturation (SpO ₂) Detection from PPG Signals.....	106
3.4. Summary	107
CHAPTER 4: THEORETICAL BACKGROUND OF GRAPHENE AND DEVELOPMENT OF THE PROPOSED GRAPHENE BASED ECG ELECTRODE	109
4.1. General Properties of Graphene (GN).....	109
4.2. Graphene Production Methods	111
4.2.1. Micro Mechanical Cleavage Method	111
4.2.2. Epitaxial Method.....	113
4.2.3. Chemical Vapour Deposition (CVD) Method.....	113
4.2.4. Other Graphene (GN) Production Methods	115
4.3. Raman Spectroscopy of Graphene (GN).....	117
4.3.1. Basic Raman Theory	117
4.3.2. The Raman Spectrum of Graphene (GN).....	119
4.3.3. Using Raman Microscopy to Measure the Significant Parameters of Graphene (GN)	120
4.4. Scanning Electron Microscopy (SEM)	124
4.5. Development of Graphene (GN) – An Enabled ECG Electrode Using the CVD Method	125
4.5.1. Details of the CVD Process Implemented in this Work	126
4.5.2. Characterisation of Graphene (GN) - Coated Silver (Ag) Electrode Using Raman Microscopy	127
4.5.3. Scanning Electron Microscopy (SEM) Characterisation.....	129
4.5.4. Electrical Characteristics of a GN-coated Electrode.....	130
4.5.5. Theoretical Comparison of Skin-Electrode Interface and Its Equivalent Circuit Model Using Ag/AgCl and GN-based ECG Electrodes	131
4.6. Summary	133
CHAPTER 5: EXPERIMENTAL SETUP, RESULTS AND DISCUSSION ON GRAPHENE-BASED ECG ELECTRODES.....	134
5.1. COMSOL Simulation of a Graphene-Enabled ECG Electrode	134
5.2. Experimental Setup and Results with Discussion on the ECG Monitoring Using Adhesive Ag/AgCl and Graphene-Coated Electrodes	139
5.3. Performance Evaluation of ECG Signals for Various Electrode Placement Models	144
5.3.1. Measurements and Comparisons of ECG Signals Obtained by Different Types of Electrodes and Different Placements	144
5.3.2. Measurements and Comparisons of Skin-Electrode Contact Impedances	159
5.4. Summary	161

CHAPTER 6: CONCEPT OF INTEGRATED MULTI-FUNCTIONAL WIRELESS BODY MONITORING SYSTEM.....	162
6.1. Design and Experimental Setup of an Integrated Ear-based Device for a Multiple Smart Sensor System.....	162
6.1.1. ECG Sensing Unit.....	163
6.1.2. CBT Sensing Unit.....	164
6.1.3. PPG Sensing Unit.....	166
6.2. Experimental Results of an Integrated Ear-based Device for a Multiple Smart Sensor System.....	167
6.2.1. ECG based Experimental Results.....	169
6.2.2. CBT Based Experimental Results	170
6.2.3. PPG Based Experimental Results.....	172
6.3. Android Based Smartphone Application for Visualising Continuous Health Monitoring	173
6.4. Analysis of the Wireless Transmission of an ECG Mobile Application.....	176
6.5. Summary	178
CHAPTER 7: CONCLUSION and FUTURE WORK	179
7.1. Conclusion.....	179
7.2. Future Works	181
REFERENCES.....	183

List of Figures

Figure 1.1: Typical personal health system with integrated sensor network (wireless body area network) [3]	22
Figure 1.2: The typical 3-lead ECG monitoring system [3].....	23
Figure 1.3: Ear-tympanic device to measure core body temperature [3].....	24
Figure 1.4: A typical reflective PPG sensor for measuring blood oxygen saturation (SpO ₂) and heart rate [3].....	24
Figure 2.1: (a) Image of fabricated electrode; (b) ECG signals from the PDMS-based electrode and from the Ag/AgCl electrode [12].....	30
Figure 2.2: (a) The co-driver's seat featuring capacitive electrodes in the backrest and an additional acceleration sensor in the seat (EMFI-mat); (b) Recorded ECG signals from the backrest from a healthy male volunteer aged 27 sitting on the driver's seat [13].....	31
Figure 2.3: (a) Top view; (b) Exploded view of the proposed dry foam ECG electrode, which was covered by the conductive fabric and then paste on an Au layer; (c) An overview of the whole proposed ECG monitoring system within a wearable medical vest [15]	33
Figure 2.4: (a) Setup of proposed ECG real-time monitoring system; (b) Acquired ECG signals using conventional Ag/AgCl electrode, and proposed non-contact electrode, respectively [18]	34
Figure 2.5: (a) Hairy chest illustrates difficulties for acquiring ECG signals via gel Ag/AgCl electrodes; (b) Non-contact electrodes also show comparable ECG signals to that of Ag/AgCl electrodes without skin preparation. Both signals were obtained before filtering process [19].....	35
Figure 2.6: (a) Cross-sectional scheme of layered non-contact electrode system for ECG monitoring; (b) Acquired ECG signals while the subject was in different positions (standing, long sitting, supine and left lateral). ECG signals were detected during supine and left lateral positions [22]	37
Figure 2.7: (a) Scanning electron microscope image of vertical gold nanowires and a medical plaster that involves of the gold nanowire fabricated electrode; (b) Acquired ECG signals from e-Nanoflex sensor conventional Ag/AgCl electrode and (c) proposed gold nanowire electrode [23].	38
Figure 2.8: (a) Proposed e-Vest system within the plethysmography (PPG) arm band; and (b) the proposed e-Bra system that worn by the subject with the e-Nanoflex sensor module. In addition multichannel signal smartphone display consists of heart rate, and blood pressure [24-25]	39
Figure 2.9: The prototype of the CardioGuard sensor system: (a) The wearing subject: the sensor device is attached at the cleavage of the bra; (b) applied gold-plated wire electrode; (c) the structure of the bra sensor system; (d) the front, back and side views of the proposed sensor system; (e) the hardware components of the system; and (f) an ECG signal recorded by proposed CardioGuard system [27].....	40
Figure 2.10: Measured ECG signals using (a) wet Ag/AgCl electrodes; (b) and (c) capacitive electrodes with different magnifications; and (d) proposed tattoo electrodes; tested electrodes are shown in (e): Ag/AgCl electrodes (left); proposed copper printed capacitive electrodes (middle); and Ag printed electrodes on tattoo paper (right) [28]	41
Figure 2.11: (a) Data sampling module of the proposed system; (b) Using lead V to record ECG signals. ECG signal measurement (c)-(e) ECG signals using wet Ag/AgCl electrode; (f) recorded ECG signals by proposed micro-dome electrode with 80 x 80 arrays; (g) signal from micro-dome electrode with 60 x 60 arrays; (h) signal with 40 x 40 arrays [30].....	42
Figure 2.12: (a) Structure of the composite fabricated electrode composed of a PDMS layer, Ag NW layer, Cu wires and CNT-aPDMS layer. ECG measurements: (b) the measurement area; (c) Comparison the waves of the ECG signals between the propose composite electrode and conventional Ag/AgCl electrode; (d) and (e) shows continuous acquired ECG signals during different postures (sitting, standing, walking) at site 1(d); and at site 2 (e) [32].....	44
Figure 2.13: Motion artifacts and ECG measurements. (a) Experimental set-up to test of motion artifacts for dry, Ag/AgCl and proposed CNT/aPDMS electrodes were attached to the left arm in	

separate tests; (b) Recorded motion artifacts for each dry, Ag/AgCl and proposed CNT/aPDMS electrodes while running at different frequency ranges between 1 and 3 Hz; (c) RMS values; (d) Attachment of the ECG electrode using leads I, II, and III; (e) The attached electrode on the chest; (f) Recorded ECG signals with leads I, II, and III for the dry, Ag/AgCl and proposed CNT/aPDMS electrodes [33].....	45
Figure 2.14: (a) Schematic diagram of the proposed electrode design; (b) Information on the structure of the composite and its interface with the skin and the contact pad of the external (wearable) device; (c) Optical image of the electrode system on the skin; (d) Attaching proposed device on the chest to acquire ECG data; (e) Schematic illustration wireless ECG monitoring system [35].....	46
Figure 2.15: (a) The structure of proposed flexible polypyrrole textile electrodes (FPTE); (b) Distributions of electrodes based on sweatshirt with an ECG monitoring system [37]	48
Figure 2.16: (a) Proposed PEDOT:PSS type of textile electrode; (b) Five sample excerpts of ECG signals obtained with proposed dry and wet electrodes (in blue, lower signals) compared to those obtained with conventional Ag/AgCl electrodes (in red, upper signals) during different activities [38]	49
Figure 2.17: (a) The fabrication procedure of the proposed meshed CB/PDMS electrode; (b) Example of ECG samples from a subject recorded with proposed copper-meshed CB/PDMS electrodes during different conditions and types of water [39]	51
Figure 2.18: (a) Structure of the proposed multilayered dry electrode with expanded view; (b) Recorded ECG signals variation with respect to printed electrode area [40]	52
Figure 2.19: (a) The backside of the neck proposed electrode placements; (b) The subject wearing the necklace-form-1-lead ECG device [42].....	54
Figure 2.20: (a) Image of the Chem-Phys printing stencil; (b) An array of printed Chem-Phys flexible patches; (c) Block diagram of the wireless acquisition system; (d) Image of the Chem-Phys hybrid patch; (e) ECG signals using commercial 3M Red Dot Ag/AgCl electrodes (top), and printed ECG sensor (bottom) [43].....	55
Figure 2.21: (a) Schematic of the proposed sensor patch attached on a person's lower left rib cage. Skin temperature is read via printed thermistor, and ECG signals are acquired via printed gold electrodes. The electrodes and thermistor are integrated into a silicon-based polyimide substrate for data acquisition and signal processing and transmission; (b) System architecture of the proposed hybrid sensor patch with a wireless system on chip; (c) Image of the wearable sensor patch is attached onto the subject's lower left rib cage; (d) Image of the component side of the proposed wearable patch; (e) Image of the sensor side of the proposed wearable hybrid patch. The printed gold ECG electrodes and the thermistor are shown. [36, 44].....	56
Figure 2.22: (a) System overview of the proposed device that measures ECG signals at the wrist and ECG signals are transmitted to a tablet via Bluetooth connection; (b) ECG waveforms using the proposed device within PT algorithm and range detector [45]	57
Figure 2.23: (a) Recorded ECG signals at the stationary state with conventional Ag/AgCl electrodes and proposed CNT polymer electrodes for comparison; (b) structure of the proposed ECG electrode patch composed of a PDMS layer, an aPDMS layer and the proposed CNT polymer electrodes [47].....	58
Figure 2.24: (a) Schematic images of the proposed procedure of conductive dry adhesives (CDA) within ECG application; (b) Digital images of a large-area silicon mold with replicated CDA (~4 in ²); (c) Images of CDA attached on different locations on the body (i: wrist, ii: stomach, iii: ankle); (d) Images of the stretched and banded proposed CDA; (e) Image of an LED application using proposed CDA; (f) Comparison of the ECG signals using CDA and wet Ag/AgCl electrodes under normal conditions (inset in the red box: magnified view of the recorded ECG waveform); (g) Comparison of the ECG signals using CDA and wet Ag/AgCl electrodes under an immersed condition; (h) Series of ECG recordings using CDA under various body postures [50]	60
Figure 2.25: Recorded ECG signals: (a-c) for comparison between proposed PLS type of electrode and wet Ag/AgCl electrode; (d-f) for comparison between proposed PLP electrode and wet	

Ag/AgCl electrode. Saltwater immersed condition: (a, d) without movement; and (b, e) with movement; (c, f) Saltwater wet condition; (g) pencil lead solid-type (PLS) electrode; (h) pencil lead powder-type (PLP) electrode [52]	62
Figure 2.26: (a) Images of a sample of flexible nylon-based proposed textile with rGO coating with area of 35.91 cm ² ; (b) recorded ECG signals after filtering with conventional Ag/AgCl electrode and proposed GN-clad textile electrodes. P-QRS-T waves are shown as one cardiac in the inset [59]	64
Figure 2.27: (a) Integration of sensors at specific locations in the proposed SmartVest; (b) Prototype of the developed wearable data acquisition hardware [65]	66
Figure 2.28: Demonstration of Mobile healthcare monitoring system using portable base station, including ear PPG, finger PPG, and chest ECG sensors [67]	67
Figure 2.29: Prototype of the Heartphones system which is either can be connected to smartphone via serial connection, or to PC via wireless link [73]	69
Figure 2.30: (a) Prototype ear-lead wearable system that includes ECG, PPG, BCG circuits; (b) ECG measured from mastoid area behind the left ear; (c) PPG taken from the mastoid area [74]...	70
Figure 2.31: (a) Optical image of the proposed device on the forearm; (b) Optical image of the proposed device with labels for different parts and modules in the circuit; (c) ECG acquired by using the proposed device mounted on the sternum; (d) a detailed view of P-QRS-T complex acquired from the ECG signal [77]	71
Figure 2.32: (a) Optical image of the proposed device for the wristband use applicable in wearable health applications; (b) Synchronous ECG and PPG data streams, and PB measurement from these bio-signals [80]	73
Figure 2.33: (a) Developed hardware for ECG and PPG acquisition: Chest ECG and Finger PPG; (b) Parameter extraction from synchronized ECG and PPG signals [85].....	75
Figure 3.1: Heart structure and the path of the blood flow [86].....	81
Figure 3.2: Electrical activity in a pacemaker cell (SA node) [87]	82
Figure 3.3: The conduction system of the heart and the path of cardiac excitation [87]	83
Figure 3.4: Major components of a typical electrocardiogram (ECG) waveform [87]	84
Figure 3.5: ECG Genesis while the cardiac cycle is coordinating the activity [87]	85
Figure 3.6: A normal electrocardiogram (ECG), including particular intervals [91].....	85
Figure 3.7: 12-Lead System: (a) Bipolar limb leads; (b) Unipolar limb leads; (c), (d), (e) Chest leads [93]	87
Figure 3.8: Schematic circuit of a typical ECG measurement system with a DRL connection [95]88	
Figure 3.9: Block diagram of an ECG measurement system including DRL plane and capacitively coupled electrodes [96].....	89
Figure 3.10: (a) Electrical model of the interface from the body to the electrode; (b) Electrical coupling of skin-electrode interface for various electrode topologies, including wet-contact gel-based Ag/AgCl, dry contact MEMS and metal plate, thin-film insulated metal plate, and noncontact metal plate coupling through hair or clothing, made of such as cotton [97].....	90
Figure 3.11: The ECG signal spectrum [98]	92
Figure 3.12: Schematic overview of the Pan-Tompkins heartbeat detection method [46].....	93
Figure 3.13: Distribution of temperatures within the body and division of the body into the core and shell during exposure to (a) cold and (b) warm environments [103]	94
Figure 3.14: Obtaining the tympanic temperature by aiming the probe towards the inferior third of the ear canal [112].....	97
Figure 3.15: Principle inner working of an infrared thermopile sensor [113].....	98
Figure 3.16: Variations in blood volume in light attenuation by tissue [118].....	100
Figure 3.17: Light-emitting-diode (LED) and photo detector (PD) placement for transmission mode (left); and reflection mode (right) for PPG signal detection [118].....	101
Figure 3.18: (a) The structure of the proposed six-channel PPG measurement and analysis system; (b) an example of recorded PPG signals from the right and left earlobes, right and left index fingers, and the right and left toes of a healthy subject [127]	102

Figure 3.19: Definition of the PPG timing measures, including PPT, PPT _f , PPT _p , AMP [9]	103
Figure 3.20: PPG pulse wave analysis with its characteristics during a deep gasp inspiratory occurrence [9].....	104
Figure 3.21: Signal processing steps for PPG peak and HR detection [68].....	105
Figure 3.22: (a) Original PPG signal obtained from an LED-LED sensor before filtering; (b) filtered AC component of a PPG signal using low-pass Butterworth filter; (c) Fast Fourier Transform (FFT) spectrum of the AC component of the PPG signal; (d) HR detection in the FFT spectrum of the AC component [131]	106
Figure 3.23: PPG signal with AC and DC components [132]	107
Figure 4.1: Graphene as a “building material” of fullerene, graphite, single wall nanotubes (SWNTs), multi wall nanotubes (MWNTs) [137].....	110
Figure 4.2: (a) Attaching a piece of graphite to sticky-tape; (b) Using the sticky tape to thin out the graphite; (c) Placing the thin graphite on a silicon wafer, with a surface layer of silicon dioxide; (d) Removing most of the layers of graphite leaving behind a single layer, two-layer or multilayer graphene (GN); (e) AFM image of low magnification; and (f) a higher magnification optical micrograph just after micromechanical cleavage.....	112
Figure 4.3: Epitaxial synthesis of GN on a SiC wafer [147].....	113
Figure 4.4: CVD method of GN on copper foil [153].....	114
Figure 4.5: (a) Carbon atoms are deposited on the surface of metal (Cu, Si, or Ni); (b) At high temperature this forms GN; (c) A layer of polymer is deposited on top of the GN; (d) The polymer is removed and the GN with it; (e) The polymer is placed on a suitable substrate; (f) The polymer is dissolved away leaving the GN behind.....	115
Figure 4.6: Methods for GN synthesis. There are various methods to be chosen depending on the specific application; each one differs from the others in terms of quality and price [159].....	116
Figure 4.7: Raman spectra of graphite, metallic and semiconducting carbon nanotubes as well as low and high sp ³ amorphous carbons [162].....	118
Figure 4.8: Schematic image of Raman instrumentation for obtaining the Raman spectra of a sample.....	119
Figure 4.9: (a) Comparison of the Raman spectra of GN and graphite measured at 514.5 nm; (b) comparison of the 2D peaks in GN and graphite [162].....	120
Figure 4.10: (a) The 2D band exhibits a sharp peak of single layer GN; (b) the 2D band of bi-layer GN; (c) The 2D band of three layer GN; (d) 4 layer; (e) the 2D band of multiple layer GN (nearly graphite); GN mapping of these different layers of GN is shown on the right side of the figure [165]	121
Figure 4.11: Raman spectrum of a single layer CVD-grown graphene sample transferred onto SiO ₂ [166].....	122
Figure 4.12: (a) (i) Zigzag edge of GN structure and (ii) armchair edge of GN structure; (b) Raman spectra of graphite and graphene edges [169].....	123
Figure 4.13: The Raman spectra of single layer GN on different substrates via the mechanical cleavage method [169].....	124
Figure 4.14: Output signals in SEM [170].....	124
Figure 4.15: (a) Schematic of emitted secondary electrons (SE) blocked by graphene (GN); (b) typical SEM image of CVD grown GN on copper foil. The areas 1,2,3, and 4 with increasing darkness can be attributed to single layer, bilayer, three layer and four layer GN samples, respectively [171].....	125
Figure 4.16: Schematic diagram showing the CVD coating process for synthesising a GN-coated Ag electrode.....	127
Figure 4.17: Raman analysis of graphene (GN) and a bare Ag/AgCl electrode. (a) Raman spectrum of GN-grown on Cu is shown after chemical vapour deposition (CVD); and (b) Raman spectrum of a GN-coated Ag electrode and a conventional dry Ag/AgCl electrode, which is shown for comparison	128

Figure 4.18: Scanning electron micrographs (SEMs) showing: (a) and (b) typical SEM images of a dry electrode before coating; (c) and (d) a graphene-coated dry ECG electrode	130
Figure 4.19: Schematic of two-point probe configuration for the resistance measurement of samples [170].....	130
Figure 4.20: The simplified equivalent circuit for the electrodes system in bio-impedance measurements	131
Figure 5.1: (a) The layers of the human skin [174]; (b) simplified skin model with two electrodes constructed in COMSOL software. Upper layer of both electrodes is filled by Cu, and bottom layer of the electrodes is applied by Ag and GN, respectively	136
Figure 5.2: Comparison of the electric field effect and surface charge density of the electrodes using GN-based (a); and conventional Ag/AgCl based electrodes (b)	137
Figure 5.3: Mesh construction of the skin model in COMSOL	137
Figure 5.4: The relationship between the inter-distance of the electrodes and the electrical field	138
Figure 5.5: The relationship between the width of the electrodes and the electrical field magnitude	138
Figure 5.6: (a) Braun patient monitoring system [176]; and (b) the schematic of electrode placement with a 3-lead configuration ECG system.....	139
Figure 5.7: Ambu-type bigger size of electrode: (a) Before coating; and (b) after GN coating; (c) Covidien-type smaller size of electrode before coating; (d) after GN is coated on top of the Ag layer of the electrode; and (e) dry Ag/AgCl electrode (even smaller in size than 1 British pound coin)	140
Figure 5.8: (a) ECG Measurement setup including 3-lead wire-connections; (b) a typical image of ECG measurement using chest-lead (3-lead) configuration	141
Figure 5.9: ECG recording with (a) a conventional Ag/AgCl electrode; (b) a GN-coated Covidien (smaller size); and (c) a GN-coated Ambu type (bigger size) of electrode	144
Figure 5.10: (a) ECG data acquisition system with Arduino; (b) block diagram of the ECG measurement system including a wireless communication module	145
Figure 5.11: Scenario 1 (S1): (a) Electrode placement with E1 type electrodes on the chest; (b) obtained ECG signals while the subject was in a sitting position	147
Figure 5.12: Scenario 2 (S2): (a) Electrode placement with E1 type electrodes near-the-ear; (b) obtained ECG signals while the subject was in a sitting position	148
Figure 5.13: Scenario 3 (S3): (a) Electrode placement with E2 type electrodes on the chest; (b) obtained ECG signals while the subject was in a sitting position	148
Figure 5.14: Scenario 4 (S4): (a) Electrode placement with E2 type electrodes on the ear; (b) obtained ECG signals while the subject was in a sitting position	149
Figure 5.15: Scenario 5 (S5): (a) Electrode placement with E3 type electrodes on the chest; (b) obtained ECG signals while the subject was in a sitting position	149
Figure 5.16: Scenario 6 (S6): (a) Electrode placement with E3 type electrodes on the ear; (b) obtained ECG signals while the subject was in a sitting position	150
Figure 5.17: Scenario 7 (S7): (a) Electrode placement with E4 type electrodes on the chest; (b) obtained ECG signals while the subject was in a sitting position	151
Figure 5.18: Scenario 8 (S8): (a) Electrode placement with E4 type electrodes on the ear; (b) obtained ECG signals while the subject was in a sitting position	151
Figure 5.19: Scenario 9 (S9): (a) Electrode placement with E5 type electrodes on the chest; (b) obtained ECG signals while the subject was in a sitting position	152
Figure 5.20: Scenario 10 (S10): (a) Electrode placement with E5 type electrodes on the ear; (b) obtained ECG signals while the subject was in a sitting position	153
Figure 5.21: Scenario 11 (S11): (a) Electrode placement with E3 type electrodes on the ear and the reference electrode being placed on the left arm; (b) obtained ECG signals while the subject was in a sitting position.....	153
Figure 5.22: Chest-based ECG Signals from an Ag/AgCl electrode and from a GN-based electrode using the Ambu (larger size) and Covidien (smaller size) types of electrodes (a) – (d).....	156

Figure 5.23: Ear-lead based ECG Signals from an Ag/AgCl electrode and from a GN-based electrode using the Ambu (larger size) and Covidien (smaller size) types of electrodes (a) – (d) .	157
Figure 5.24: Comparison of ECG signals recorded using different electrodes. (a) ECG signals recorded by the Ag/AgCl electrode in Da He et al.'s report using an ear-lead position (only R peaks are visible); (b) ECG signals recorded by a GN-based electrode using an ear-lead position (all P-QRS-T morphology is identified).....	158
Figure 5.25: Comparison of the frequency response of filtered ECG signals from Ag/AgCl and GN-based electrodes up to 75 Hz: (a) Power spectral density (PSD) of ECG recordings (from Figure 8a) for an Ag/AgCl electrode; (b) PSD of ECG recordings (from Figure 8c) for a GN-based electrode.....	159
Figure 5.26: The skin-electrode contact impedance of the Ambu (bigger) and Covidien (smaller) types of a conventional Ag/AgCl electrode (shown as ImpedanceAmbu and ImpedanceCovidien) and Graphene-coated electrodes (shown as ImpedanceGNAmbu and ImpedanceGNCovidien)....	160
Figure 6.1: System block diagram which including ECG and CBT sensors in an earbud form as well as and PPG sensor attached to the finger.....	163
Figure 6.2: (a) ECG acquisition system using an e-Health and Arduino microcontroller platform along with a Bluetooth module for communicating with a smartphone. The ECG monitoring process was carried out by a Lithium Battery which has a capacity of 500mAh; (b) the behind-the-ear proposal with the combination of earbud application.	164
Figure 6.3: (a) The proposed earbud device, which consists of a thermopile infrared sensor, for CBT measurements; (b) MLX 90614 infrared thermometer was used for CBT monitoring experiments.....	165
Figure 6.4: (a) The connection of MLX90614 to an MCU with 3.3V power supply; (b) initial experimental setup of CBT measurement using Arduino UNO on a bread board.....	166
Figure 6.5: (a) Haemoglobin absorption spectra [189]; and (b) the tested Amperor PPG monitoring sensor, which shows SpO ₂ and the heart rate (HR).....	167
Figure 6.6: (a) The prototype of an ear-based multifunctional wireless monitoring system; (b) a data acquisition hardware unit that consists of ECG, CBT sensor connections, Bluetooth module (HC-05 type [182]) for wireless communication and a lithium-ion battery for powering the sensory system.....	168
Figure 6.7: Typical setup of the use of the proposed integrated wireless multiple sensors; a CBT sensor was inserted into the proposed earbud device; and GN-coated ECG electrodes were placed on the behind-the-ear and upper neck areas; and a PPG sensor was clipped onto the finger.....	169
Figure 6.8: (a) Visualisation of the obtained ECG signals on an oscilloscope; and (b) ECG visualisation using Matlab software via the proposed ear-based multisensory system.....	170
Figure 6.9: Continuous CBT measurements for 100 seconds: (a) Raw CBT data taken from the ear; (b) CBT data just after exercise – five mins running; (c) CBT data after walking outside in cold weather; and (d) final temperature data after sitting for five mins wearing a thick jacket.....	171
Figure 6.10: (a) Measuring HR and SpO ₂ using an Amperor Bluetooth PPG sensor; (b) a PPG measurement on a subject during exercise using the same device.....	172
Figure 6.11: Software flow diagram of the proposed ECG continuous monitoring system for smartphone application.....	173
Figure 6.12: Monitoring of ECG signals on a smartphone by (a) Ag/AgCl electrodes; and (b) GN-coated electrodes; (c) HR calculation is shown; (d) a health condition match process: an obtained ECG sequence is compared to the stored values of health issues such as Tachycardia.....	174
Figure 6.13: Smartphone applications for CBT and PPG signals: (a) CBT measurement shows the body temperature in this case as Celcius (31.18 °C) and Fahrenheit (88.1 °F); (b) PPG application on a smartphone using a commercially available Amperor Bluetooth PPG sensor produced by Contec [181].....	175
Figure 6.14: A view of the Bluetooth module while pairing it with a smartphone.....	177

List of Tables

Table 2.1: Mean of Amplitude reduction (%) between dry and wet conditions (N = 10 subjects)...	50
Table 2.2: Comparison of Printed Electrode Area.....	53
Table 2.3: Parameters Used for Systolic and Diastolic BP Extraction [85].....	74
Table 2.4: A summary of the recent wearable monitoring systems presented in the literature review	76
Table 3.1: Summary of ECG Waves, Intervals and Duration [92].....	86
Table 3.2: Descriptions of the parameters given in Figure 3.10a.....	91
Table 3.3: CBT variations corresponding to an individual's health status [102]	95
Table 3.4: Human body temperature range [102].....	95
Table 4.1: Comparison of the relevant electronic, physical and thermal properties of GN with other related carbonic and metallic materials (Si, Cu, single wall carbon nanotube – SWCNT) [141] ...	111
Table 4.2: A brief summary of GN production techniques [141]	117
Table 4.3: Estimated values for electrode circuit model components (R_d , C_d , and R_s).....	132
Table 5.1: Electrical conductivity and relative permittivity values of each layer in COMSOL modelling	135
Table 5.2: The properties of electrodes used for the experiments in ECG monitoring	140
Table 5.3: Obtained ECG signals from 10 volunteers using conventional Ag/AgCl, GN-coated Ambu and GN-coated Covidien types of electrodes.....	141
Table 5.4: Calculated SNRs and the response times of the ECG signals obtained with different electrodes and placements	154
Table 6.1: A summary of the wireless technologies for wearable wireless health monitoring systems	176

List of Abbreviations

AC	Alternating Current
ADC	Analog Digital Converter
AF	Atrial Fibrillation
AFE	Analog-Front-End
AFM	Atomic Force Microscopy
Ag NW	Silver Nanowires
AgCl	Silver Chloride
AI	Augmentation Index
AMP	Foot-to-Peak Amplitude
APTES	Aminopropyl Triethoxysilane
ASD	Autism Spectrum Disorders
ATP	Adenosine Triphosphate
AV	Atrioventricular Node
BP	Blood Pressure
BPM	Beat per Minute
BR	Baud Rate
BSC	Ballistocardiogram
CB	Carbon Black
CBT	Core Body Temperature
CCD	Charge Coupled Detector
CCE	Capacitively Coupled Electrodes
CDA	Conductive Dry Adhesives
CNT	Carbon Nanotube
CNT-aPDMS	Carbon Nanotubes Adhesive Polydimethylsiloxane
CPOD	Crew Physiologic Observation Device
Cu	Copper
CVD	Chemical Vapour Deposition
DC	Direct Current
DI	Deionised
DRL	Driven Right Leg
ECG	Electrocardiography
EEG	Electroencephalogram

EMFI	Electromechanical Film
EMG	Electromyography
EOG	Electrooculography
EU	European Union
FEG	Field Emission Electron Gun
FEM	Finite Element Modelling
FFT	Fast Fourier Transform
FPT	Flexible Polypyrrole Textiles
FWHM	Full Width at Half Maximum
GDP	Gross Domestic Product
GN	Graphene
GND	Ground
GO	Graphene Oxide
GPS	Global Positioning System
GSR	Galvanic Skin Response
HF/HNO ₃	Hydrofluoric Nitric Acid
HR	Heart Rate
HRV	Heart Rate Variability
IIR	Infinite Impulse Response
IR	Infrared
ISM	Industrial Scientific and Medical
KOH	Potassium Hydroxide
LA	Left Arm
LED	Light Emitting Diode
LL	Left Leg
MAE	Mean Absolute Errors
MCU	Microcontroller Unit
MEMS	Micro-Electromechanical Systems
MIT-BIH	Massachusetts Institute of Technology Beth Israel Hospital
MNA	Microneedles Array
MWCNT	Multi-Walled Carbon Nanotube
NA	Not Applicable
OLED	Organic Light Emitting Diode
PAT	Pulse Arrival Time

PC	Personal Computer
PCB	Printed Circuit Board
PCG	Phonocardiogram
PD	Photo Detector
PDMS	Polydimethylsiloxane
PEDOT:PSS	poly-3,4-ethylenedioxythiophene poly(styrene sulfonate)
PEP	Pre-Ejection Period
PET	Polyethylene Terephthalate
P-FCB	Planar-Fashionable Circuit Board
PI	Polyimide
PLP	Pencil Lead Powder
PLS	Pencil Lead Solid
PMIC	Power Management Integrated Circuit
PMMA	Poly(methyl methacrylate)
PPG	Photoplethysmography
PPI	Peak-Peak Interval
PSD	Power Spectral Density
PSOC	Programmable System on Chip
PT	Pan Tompkins
PTT	Pulse Transmit Time
RA	Right Arm
RF	Radio Frequency
RFID	Radio-Frequency Identification
RGO	Reduced Graphene Oxide
RMS	Root Mean Square
SA	Sinoatrial Node
SD	Storage Device
SE	Secondary Electrons
SEM	Scanning Electron Microscopy
SLG	Single Layer Graphene
SMS	Short Message Service
SNR	Signal-to-Noise Ratio
SpO ₂	Blood Oxygenation
SPV	Skin Potential Variation

SWCNT	Single Wall Carbon Nanotube
TSV	Through-Silicon Via
UART	Universal Asynchronous Receiver/Transmitter
USB	Universal Serial Bus
UV	Ultra Violet
WBAN	Wireless Body Area Network
WHMS	Wearable Health Monitoring Systems
WLAN	Wireless Local Area Network
WMSSS	Wireless Multiple Smart Sensor System
WPAN	Wireless Personal Area Network

CHAPTER 1: INTRODUCTION

1.1. Wireless Body Area Network for Personal Health Monitoring

The rapid growth of wireless technologies brings with it new innovative ideas that enable continuous real-time remote patient monitoring in healthcare services using compact wireless body sensors. The services and technologies provide relatively uncontroversial, well-communicated and monitoring devices, developed to give more affordable solutions. Specifically for mobile healthcare, such as daily activity monitoring, personal healthcare and monitoring systems as well as body sensor systems that can alert clinicians via patients' mobile phones. The new trend in remote patient monitoring is moving towards the use of personal mobile devices compatible with multiple biomedical sensors using wireless communication, such as Bluetooth and Zigbee [1].

Recent mobile health (m-health) technology is enabling the monitoring of people's daily activity on their smartphones. In addition, these mobile-based portable embedded devices will be able to provide platforms to monitor their critical physiological data continuously and remotely. In order to accomplish this, advancing technology in sensors, low-power integrated systems, and wireless communication will need to be brought together to enable the design of low-cost, miniature, and smart physiological sensor nodes [2]. An assessment report was prepared for the European Union (EU) regarding the effectiveness of m-health in biomedical applications and the diagnosis of diseases in 2013. According to this report, m-health applications could save €99 billion in healthcare costs in the EU and add €93 billion to the EU GDP in 2017, if its adoption were embraced [3].

The integrated wearable monitoring systems, which aim to bring together compact body sensors, including such as electrocardiography (ECG), blood pressure, photoplethysmography (PPG), core body temperature (CBT), heart rate, pulse oximetry, and electroencephalogram (EEG). The wearable monitoring systems also aim to form the concept of a wireless body area or personal area network (WBAN or WPAN) using the intelligent nodes of body sensors, and displays the physiological vital signs on a monitoring device. One of the benefits that WBAN systems brings is the ability to integrate multiple smart sensors, wireless connectivity and a small battery into a wearable patch unit that sends the physiological data to a mobile device. Figure 1.1 illustrates the general concept of a typical WBAN, where the general tasks of the electronics designer are compactness, integration of body sensors and wireless communication in a specified telemedicine system, which can alert a clinician when life-threatening changes occur, or provide feedback to the patient to help maintain an optimal health status using Cloud health services.

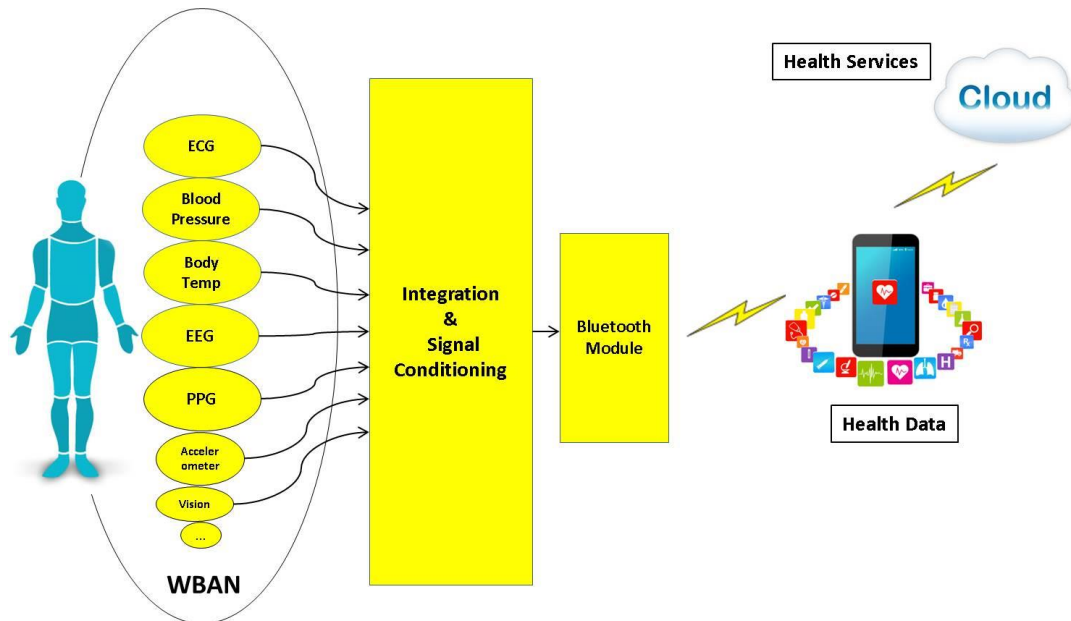


Figure 1.1: Typical personal health system with integrated sensor network (wireless body area network) [3]

1.2. ECG Monitoring System

Cardiovascular diseases are the leading cause of death worldwide, killing more than 15 million people every year [4]. Continuous and real-time monitoring of heart activities with well-established medical test electrocardiography (ECG) is increasingly playing an important role in the early diagnosis and treatment of cardiovascular diseases. The ECG waveform that reflects electrical activity of the heart is widely used for early detection and management of heart problems. Using the concept of wearable wireless monitoring, any critical change in the heart or health status of an individual can be identified by the patient his/herself or transmitted to a clinician for early diagnosis and further analysis regarding his/her status. Figure 1.2 shows an ECG monitoring system using the conventional method of three Ag/AgCl electrodes (wet adhesive electrodes) that are affixed to the chest and waist. The other methods of ECG monitoring systems and types of electrodes will be explained in depth in the next chapter.



Figure 1.2: The typical 3-lead ECG monitoring system [3]

1.3. CBT Monitoring System

Core body temperature (CBT) is a significant parameter for long-term measurements of the human body's efficiency in maintaining its conducting temperature within a stable range, generally between 36 °C and 37 °C. Continuously measuring the CBT for extended periods of time is useful for studying human thermoregulation in ambulatory settings and during exercise. In particular, in sports medicine, an accurate measurement of CBT throughout exercise can be beneficial for maintaining the body's operating temperature and preventing heat injury problems, such as hypothermia, hyperthermia, and heat stroke. Specifically, decreasing body temperature can lead to hypothermia, whereas rising core body temperature is a sign of impending heat illness, starting with heat stress (beyond 37 °C), advancing to hyperthermia, and heat exhaustion (beyond 39 °C), and then, to heat stroke (beyond 40 °C) [5]. Heat illnesses, in combination with such as climate change, overdressing or overacting may lead to a deterioration in physical performance and a rising risk of heat stroke consequences [6]. Consequently, early detection of a critical temperature (beyond 37 °C), especially after prolonged exercise, is a crucial way of preventing heat injuries. CBT is monitored continuously in recent technology using wearable wireless communication with body sensors. In the literature chapter, recent studies on such matters will be reviewed in detail. Figure 1.3 illustrates one such method of CBT that is measured by an ear thermometer.



Figure 1.3: Ear-tympanic device to measure core body temperature [3]

1.4. PPG Monitoring System

Common diseases, such as pneumonia and diarrhea are taking the lives of millions of young people every year [7], mostly due to the onset and growth of an inflammatory disease of the body, termed sepsis. This inhibits the lungs transporting oxygen molecules to the haemoglobin in the blood, which is a vital operation for the functioning of the cells throughout the body. A short term disorder in producing or transfer enough oxygen to the blood will damage the cellular function and this will affect badly the function of the cellular movement or the tissues, often leading to death [8]. Consequently, the early detection of decreased oxygen levels in the blood is essential for identifying anybody requiring diagnosis to see whether he/she has this specific disease. The common method of measuring arterial oxygen level in the blood is pulse oximetry, which refers to using optical sensing technology. Photoplethysmography (PPG) is a technique for measuring the change in light absorption by the skin by an optical method involving pulse waves to ascertain the rate of blood flow [9]. That is, by using PPG technology, the output of the photo-detector will show whether the signals are moving in accordance with every heartbeat and thus, the heart rate or pulse rate will also be provided from those signals. Figure 1.4 shows a typical reflective PPG sensor, which measures both blood oxygen saturation (SpO_2) and the heart rate.



Figure 1.4: A typical reflective PPG sensor for measuring blood oxygen saturation (SpO_2) and heart rate [3]

1.5. Aims of this Thesis

The main aim of this project is to investigate the effect of different types of electrodes for ECG monitoring and to develop an ECG sensor with a view to providing a consistent method for producing high quality, electrically conductive graphene (GN) films that can be integrated onto ECG electrodes, thereby improving ECG results. It has been shown the the growth of GN on an Ag/AgCl electrode provides better electrical properties than that of the traditional adhesive Ag/AgCl electrode. Another aim of this work is to integrate multiple body sensors including an electrocardiogram (ECG), core body temperature (CBT), and photoplethysmography (PPG) into a miniaturised device. This device wirelessly transmits physiological data to a smartphone to visualise them on. A smartphone application is written in Java to display these ECG, CBT, heart rate and SpO₂ data wirelessly. A wide of variety wearable body sensors have already been implemented for continuously and wirelessly monitoring healthcare data. In order to design an optimised smart sensor system, several available wearable monitoring systems have been reviewed (see literature review presented in Chapter 2). Another objective of this research is to implement a smart body sensor system in an innovative ear bud designed to collect ECG and CBT data from the ear. This means that two physiological data can be collected with an unobtrusive method using ear bud technology within the proposed design.

In summary, the main objectives of this research are:

- To develop a novel graphene (GN) based ECG electrode with improved electrical properties and able to provide more information about the heart;
- To investigate the electrical characteristics of GN-based ECG electrodes;
- To integrate GN-based ECG electrodes with other body sensors (CBT and PPG) to perform a multiple smart sensor system in healthcare applications;
- To send these physiological data wirelessly to a smartphone that displays continuously collected data including ECG, CBT, heart rate and SpO₂ in a written application;
- To design a novel method to sense ECG and CBT data within an ear bud system that sends the integrated data to the hardware acquisition system;
- To obtain ECG and CBT measurements from the ear with the designed ear bud device;
- To show demonstrate the superiority of the experimental results for ECG monitoring when comparing the traditional adhesive Ag/AgCl and the newly developed GN-based ECG electrodes.

1.6. Contribution to Knowledge

This work makes the following novel contributions to the study domain:

- A novel ECG electrode is developed through grown graphene (GN) substrates. GN based electrodes are proposed, implemented and tested for ECG monitoring, for the locations of chest, and both in-the-ear and behind-the-ear;
- A novel ear-bud design is proposed for integrating ECG and CBT sensors together through at hardware acquisition unit. The proposed ear-bud device was designed, fabricated and tested using 3D printing technology;
- For the first time, ECG, CBT and PPG sensors are brought together and the acquired physiological data (ECG, CBT, heart rate and SpO₂) are transmitted wirelessly to the smartphone to be displayed on an application.

A new GN-based ECG electrode is designed and developed within a novel ear-bud system combining CBT and PPG sensors together to show physiological data on the smartphone.

1.7. Thesis Outline

This thesis is organised into the following chapters.

Chapter 2 gives a literature review of the wearable monitoring systems in healthcare applications and describes the different types of electrodes and materials used for ECG monitoring. This chapter begins with an explanation of the proposed development of electrodes that use different types of materials for ECG monitoring systems. Subsequently, a comprehensive review is provided on wearable healthcare systems using different type of body sensors. Mostly the developments within ECG, CBT and PPG sensors are observed and presented. At the end of this chapter, one paragraph explains shortcomings regarding the applications of mobile wearable healthcare applications within traditional methods and puts forward suggestions for future trends and possible research directions to improve the efficiency of such healthcare applications.

Chapter 3 explains the theoretical backgrounds to ECG, CBT, and PPG monitoring systems, respectively. In the subsection on the foremost, ECG waves and lead positions are described. In addition, the electrical model of ECG measurement and skin-electrode interface are proposed for defining an ECG acquisition system mathematically. Then, heartbeat detection is presented using R-R waves from the functions of ECG signal processing. Likewise, descriptions of CBT and PPG monitoring systems are explained within the proposed methodology used in this work and demonstrated in Chapter 6 to obtain core body temperature, heart rate and SpO₂.

Chapter 4 focuses on graphene (GN) technology and the methods regarding how GN is produced for biosensing applications. After giving some examples using GN in an electronic device, the details of the fabrication process are presented regarding GN growth implementation on an Ag/AgCl electrode substrate. Furthermore, the Raman microscopy of graphene is described to show the significant parameters of GN-grown electrode using a confocal Raman spectrometer. Subsequently, scanning electron microscopy (SEM) images of GN-coated electrode are taken after several experimental studies. Finally, the electrical properties of the proposed GN-coated electrodes have been analysed.

Chapter 5 is dedicated to the preliminary simulations and results of GN-enabled electrodes for ECG monitoring. Then, a simulation is presented to show the efficiency of GN, which has attractive electrical properties for ECG monitoring using COMSOL. Following this, experimental analysis is performed using adhesive Ag/AgCl electrodes and GN-coated electrodes on 10 people to ascertain the effect of GN for ECG monitoring. Comparisons for ECG results are also conducted using the electrodes in different locations (chest, ear, and waist) on the body to show where they provide the best efficiency for ECG monitoring.

Chapter 6 presents the design and experiments pertaining to the multiple smart sensor system. Firstly, the design for the ear-lead is presented and how the CBT sensor is included in it. The experimental results of each ECG, CBT and PPG monitoring system are, shown respectively, not only for the PC-based software, but also, for mobile application.

Finally, Chapter 7 concludes the work with a summary of the contributions and proposed ideas for future work.

1.8. List of Publications

Book Chapter:

- **Celik, N.**, Manivannan, and Balachandran, W., **2017**. Wearable Graphene Based Electrophysiological Biosensing System for Real-Time Health Monitoring. *Graphene Bioelectronics for Advanced Nanomaterials*, (accepted in revision for publishing) Elsevier, pp. 1-25.

Journal Articles:

- **Celik, N.**, Manivannan, N., Strudwick, A. and Balachandran, W., **2016**. Graphene-enabled electrodes for electrocardiogram monitoring. *Nanomaterials*, 6(9), pp.156-168.
- **Celik, N.**, Balachandran, W. and Manivannan, N., **2015**. Graphene-based biosensors: methods, analysis and future perspectives. *IET Circuits, Devices & Systems*, 9(6), pp.434-445.
- **Celik, N.**, Manivannan, N. and Balachandran, W., **2016**. Evaluation of a Behind-the-Ear ECG Device for Smartphone based Integrated Multiple Smart Sensor System in Health Applications. *International Journal of Advanced Computer Science and Applications (IJACSA)*, 7(7).

Conference Papers:

- **N. Celik**, W. Balachandran, N. Manivannan, “Graphene-based electrode for an Electrocardiogram (ECG) recording system with a Tele-Health Application”, *IEEE SENSORS 2017* (submitted), Glasgow, UK, 30 October – 1 November 2017.
- **N. Celik**, W. Balachandran, N. Manivannan, “Ear-lead multiple smart bio sensor system in m-health”, In *Proceedings of the 10th EAI International Conference on Body Area Networks* (pp. 39-43). ICST (Institute for Computer Sciences, Social-Informatics and Telecommunications Engineering), Sydney, 30 September – 2 October 2015.
- **N. Celik**, W. Balachandran, N. Manivannan, “Wireless multi-parameter ear-lead smart sensor system with fingerprint identity management in m-health”, *37th Annual International Conference of the IEEE Engineering in Medicine and Biology Society*. Milan, Italy. 25 - 29 August 2015. IEEE Engineering in Medicine and Biology Society (EMBS).

CHAPTER 2: LITERATURE REVIEW

This chapter presents a review of the literature on different types of development of electrodes for ECG acquisition, and also this chapter reviews wearable wireless smart sensor systems for telemedicine or healthcare systems. In Section 2.1, alternatives to conventional wet electrode types are reviewed in depth for cardiac monitoring using different types of materials. In Section 2.2, a review of multiple smart sensor systems is provided for personalized healthcare monitoring and management, in particular ECG, CBT, and PPG monitoring.

2.1 Review of developed different types of electrodes for ECG monitoring

The electrode is the main component affecting the quality of measured ECG signals. In terms of developing ECG electrodes, various applications proposed by a number of researchers using different types of materials. Traditionally, clinical ECG recorders commonly use the adhesive Ag/AgCl electrodes, which require conductive gels and skin preparation to lower the skin-electrode contact impedance. Nevertheless, various kinds of electrode developments, such as metal electrodes, textile electrodes, carbon nanotube based electrodes, dry electrodes which can measure bio-potentials without applying any conductive gels or skin preparation, have been proposed for miniaturized ECG acquisition systems. Puurtinen et al [10] proposed dry textile electrodes to show how the electrode size and preparation of the electrode (dry electrode - wet Ag/AgCl electrode – textile electrode) affect the measurement noise, and the skin-electrode contact impedance. Dry textile electrodes moistened with water, and then textile electrodes covered by hydrogel were studied with five different sizes. The experimental results demonstrated that noise level increases as the electrode size decreases. The noise level was high in dry textile electrodes (75 dB), comparing to wet electrodes (Ag/AgCl), which had quite low noise (55 dB) similar to that of textile electrodes covered by hydrogel (51 dB). Gruetzmann et al [11] presented the development, fabrication and characterization of two novel dry electrodes for ECG monitoring. Four different types of electrodes (wet Ag/AgCl electrodes – dry Ag/AgCl electrodes – skin adaptive electrode – capacitive electrode) were prepared for the experimental work. Furthermore, a passive filter algorithm was integrated into the new electrodes to suppress fluctuation of the ECG signal caused by motions due to breathing or body movements. Compared to wet Ag/AgCl electrodes, the novel dry electrodes (adaptive and capacitive) indicated a higher contact impedance but acceptable ECG signals.

Another flexible dry electrode was developed for the long term monitoring of ECG by Baek et al [12] by using elastomer polydimethylsiloxane (PDMS), which is known to be inexpensive, biocompatible and amenable to micro-molding. A mixture metallic layer (Au and Ti layers) was

patterned on a thin PDMS substrate and they produced a PDMS-based surface electrode for the long-term measurement of ECG signals. The group fabricated a forearm-wearable electrode by connecting the Velcro to the PDMS electrode which is shown in Figure 2.1a. The skin-electrode contact impedances were measured of proposed electrode and wet Ag/AgCl electrode. Regarding the experimental results, although the contact impedance of PDMS-based electrode was higher than Ag/AgCl electrodes, measured ECG signals of PDMS electrodes showed comparatively good fidelity, which is shown in Figure 2.1b. Furthermore, proposed PDMS electrodes exhibited that has no negative influence on the skin, even applying after one week of continuous wear.

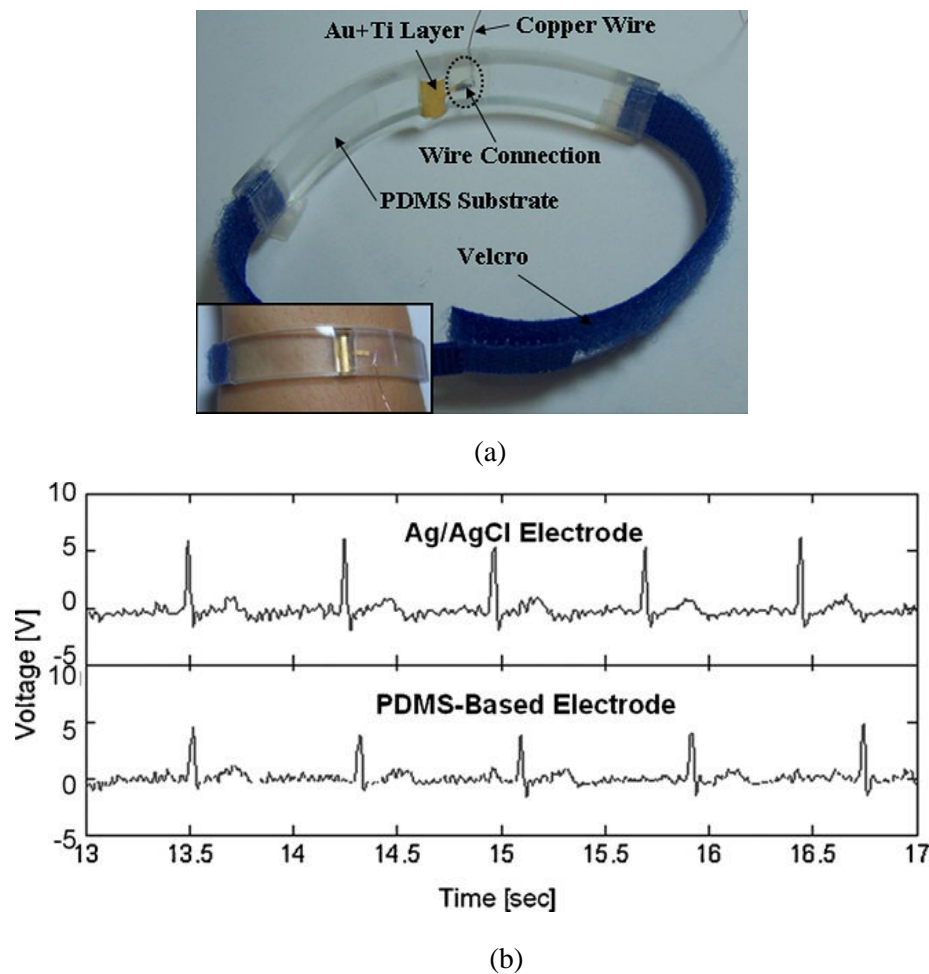


Figure 2.1: (a) Image of fabricated electrode; (b) ECG signals from the PDMS-based electrode and from the Ag/AgCl electrode [12]

Leonhardt and Aleksandrowicz [13] have studied a sensing technique suitable for non-contact ECG monitoring inside a car, when the engine was running, and car was stationary and moving. As a non-contact measurement is desirable for long-term ECG acquisition, capacitive ECG electrodes were implemented for an automotive application. Figure 2.2a shows the co-driver's seat featuring two capacitive electrodes in the backrest, and an additional acceleration sensor in the seat. In addition, a driven-right-leg circuit was used to reduce common mode effects by negative feedback

with an additional reference electrode. Figure 2.2b indicates the results of ECG signals during different scenarios: engine switched off, engine running idle, and car in driving mode. During all trials, driver was wearing normal cotton shirts with a thickness of 0.3 mm. According to the results, the P-wave of all cases were detected, however, the resulting body movements on the seat caused fluctuations on the ECG signal, as can be seen in (b).

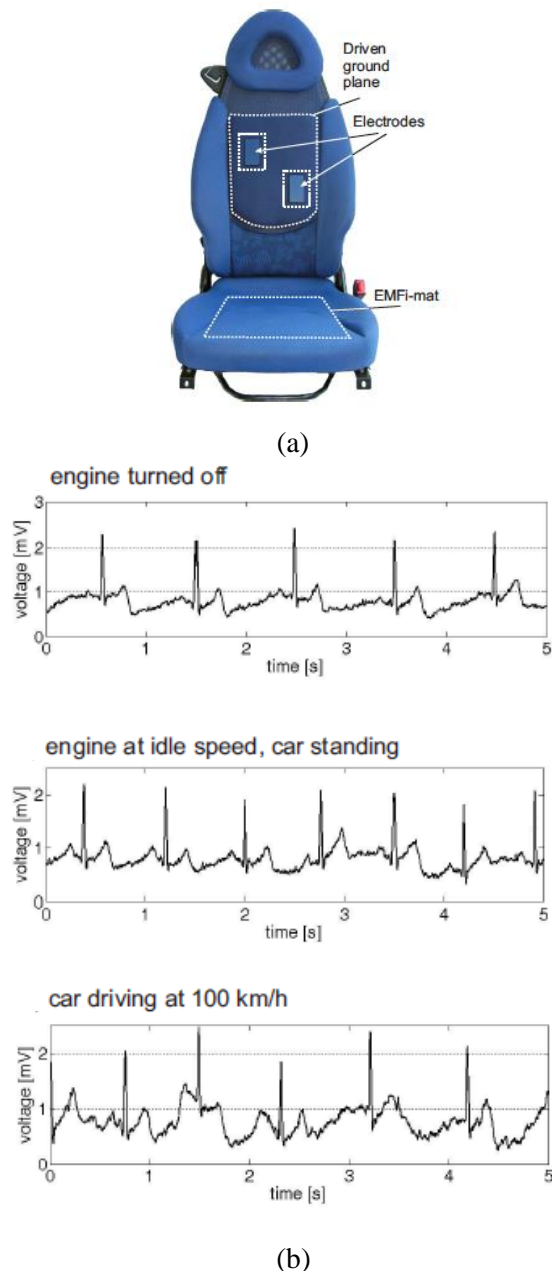


Figure 2.2: (a) The co-driver's seat featuring capacitive electrodes in the backrest and an additional acceleration sensor in the seat (EMFI-mat); (b) Recorded ECG signals from the backrest from a healthy male volunteer aged 27 sitting on the driver's seat [13]

Yoo et al [4] proposed a wearable ECG monitoring system with planar-fashionable circuit board (P-FCB) based shirt. Dry electrodes were fabricated and used for long-term monitoring of proposed ECG system to avoid use of wet electrodes due to toxicological concerns of electrolyte gels. The results revealed that the monitoring system was capturing the ECG signal successfully when both wet Ag/AgCl and P-FCB dry electrodes attached to the chest. The P-FCB electrode indicated a little more distortion, since this type of dry electrode had larger contact impedance than that of the wet Ag/AgCl electrode. However, the captured ECG waveform with the P-FCB dry electrode showed good information that included all signs of ECG waveform (P, QRS and T). Fuhrhop et al [14] implemented a textile integrated capacitively coupled electrodes (CCE) based ECG monitoring system for a long-term application. This system comprises of a convenient textile, active capacitive electrodes, and low power acquisition unit with a Bluetooth module. Two capacitive electrodes have been developed and placed on the textile and one reference electrode was used for driving right leg circuit method to reduce power line interference. ECG measurements were taken in both sitting and walking positions. Even though the capacitively coupled electrodes exhibited sufficient ECG signals for sitting position, a distorted signal was observed during walking that needs to be improved. Wang et al [15] developed a wearable mobile ECG monitoring system using a novel dry foam electrode. The proposed wearable mobile ECG monitoring system of this group consists of a wearable ECG acquisition device, a mobile phone with Global Positioning System (GPS), and a healthcare server. The wearable ECG acquisition device in this system contains three proposed dry foam electrodes. Researchers designed these dry foam electrodes to monitor ECG signals for long-term application and comfortably used in daily life for the patients. This wearable ECG device, which is small in size (4 cm x 2.5 cm x 0.6 cm), wireless and low power consumption (long-term ECG monitoring over 33 hours), has been tested for patients suffer from atrial fibrillation (AF) in China Medical University Hospital, Taiwan. For 25 AF patients, the sensitivity and positive predictive value of the proposed system were 94.56 % and 99.22 % respectively. Figure 2.3 shows top view (a) and exploded view (b) of the proposed dry foam ECG electrode and gives an overview of the whole wearable ECG acquisition system (c). Regarding the performance of this proposed electrode, the impedance variation was investigated under different frequency ranges and the impedance of proposed dry electrodes was similar to that of the conventional wet electrode. The impedance variation of the proposed dry foam electrode was observed in the range from 14 to 24 k Ω , and is in the acceptable range for a typical ECG measurement.

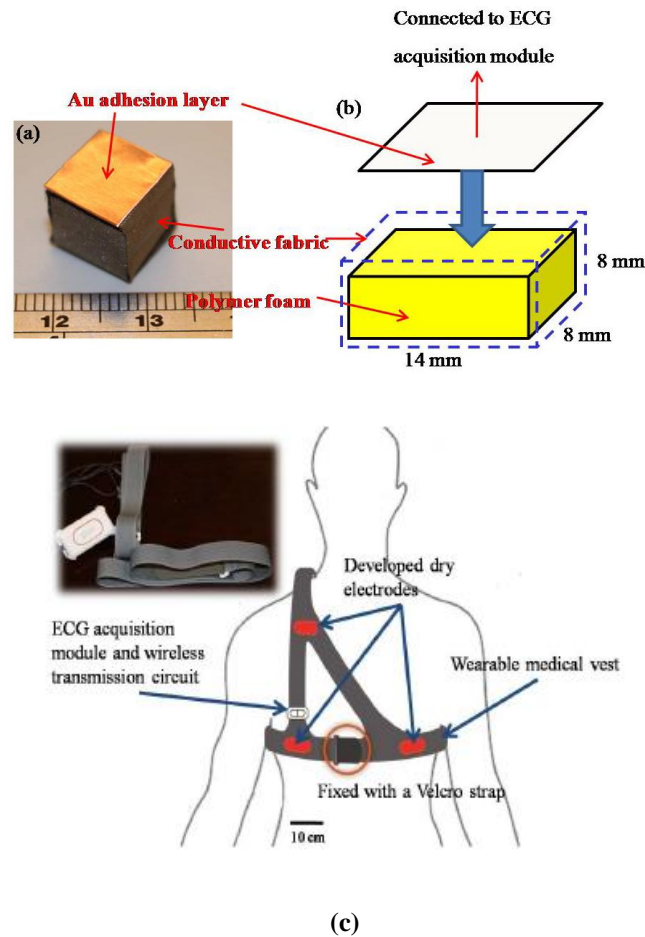


Figure 2.3: (a) Top view; (b) Exploded view of the proposed dry foam ECG electrode, which was covered by the conductive fabric and then paste on an Au layer; (c) An overview of the whole proposed ECG monitoring system within a wearable medical vest [15]

Gandhi et al [16] presented a theory and characterization of several different types of electrodes that contained dry and non-contact electrodes, including PCB solder finish, latex, cotton, silver cloth and soldermask. The noise spectra of the electrodes were measured on a subject to analyse the effects of biological or chemical noise that is triggered by skin-electrode contact impedance. In order to do that, two electrodes are mounted on the forearm to record the baseline noise for different types of dry and non-contact electrodes while a third electrode was used to ground the instrumentation. ECG measurements were also studied to see the performances of each type of electrode and compared to the signal from a wet Ag/AgCl electrode. Results demonstrated that the type of electrode which was made using lead-free PCP solder finish, can function as a general purpose, low-noise dry electrode. Latex and soldermask types can work as insulated electrodes. Rashkovska [17] et al developed a telemedicine application that provides a comfortable option for monitoring of the heart activity on the mobile phone using wireless bipolar body electrode in real-time. For displaying wirelessly recorded ECG data on a smartphone, wireless bipolar body electrodes were used. In order to transmit the ECG data wirelessly, a wireless transmission protocol

called SimpliciTI was used for converting the packets to an appropriate Bluetooth protocol. Additionally, they also showed that the standard 12-lead ECG can be reconstructed and displayed using these type wireless electrodes.

Fong and Chung [18] proposed a healthcare monitoring system based on mobile phones and non-contact electrodes. A subject wearing a cotton shirt sits on a chair with conductive non-contact electrodes are attached on the seat, which has also other electronic equipment including battery supply, transmitter and Bluetooth module. ECG signals are acquired from the subject through the cotton shirt and filtered by an electronic circuit module. After retrieving ECG signal from the sensory module, users can see the ECG signal on their mobile phones via Bluetooth module. Figure 2.4 shows the setup of ECG real-time monitoring system (a) and also the comparisons of ECG signals obtained using adhesive Ag/AgCl and proposed non-contact electrode system (b). Additionally, a web page performance was developed to test latency monitoring and provide an efficient health tracking system by clinicians or doctors.

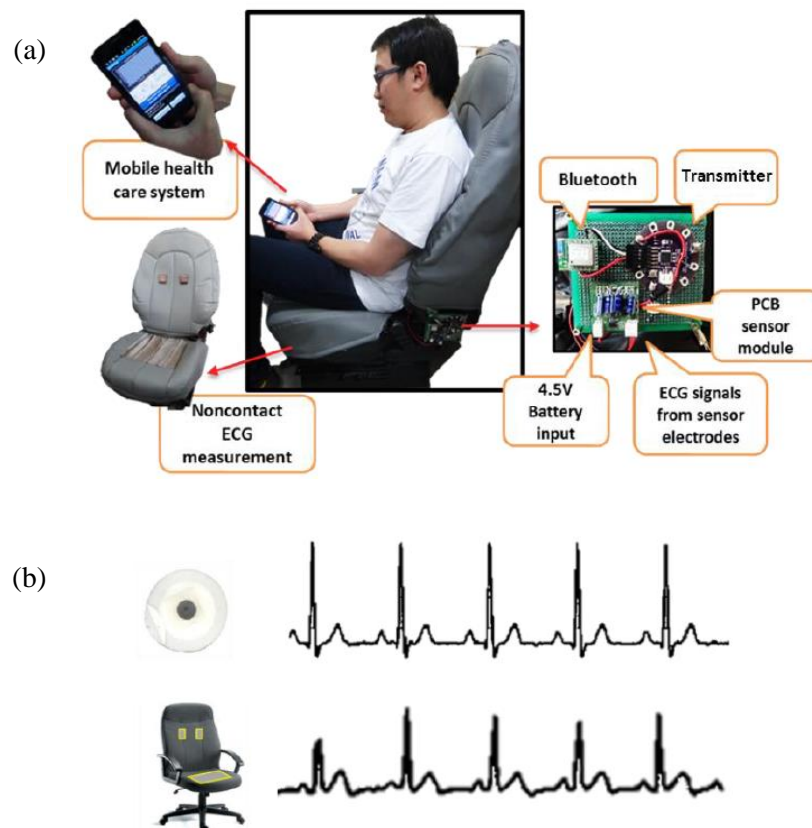


Figure 2.4: (a) Setup of proposed ECG real-time monitoring system; (b) Acquired ECG signals using conventional Ag/AgCl electrode, and proposed non-contact electrode, respectively [18]

Yang et al [19] examined the performance of a contactless capacitive electrode for ECG measurement. Recordings and comparison is made regarding ECG measurement using both explored non-contact electrodes and conventional pre-gelled electrodes on a hairy chest, with the same bio-sensing circuits. As can be seen in Figure 2.5, the experimental results indicated that wet electrodes have difficulties during ECG measurements from a hairy chest. Using proposed non-contact electrodes, ECG signal can be acquired from a hairy chest as well as improving long term monitoring of ECG without use of gel or skin preparation.

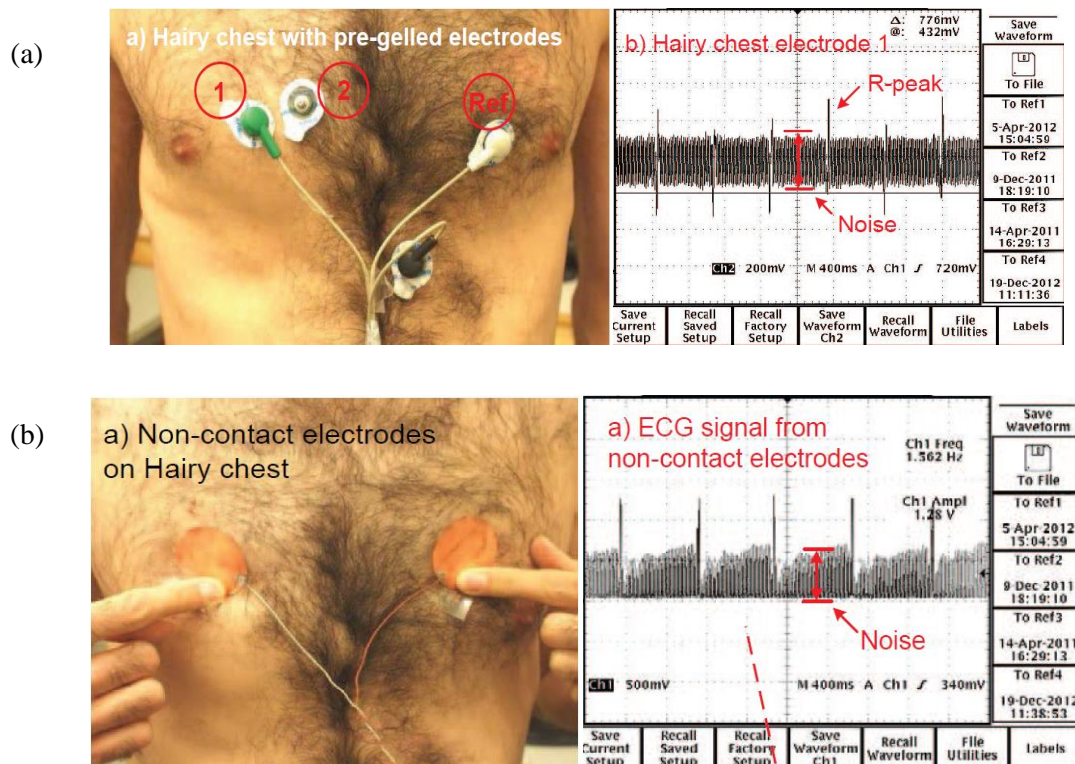


Figure 2.5: (a) Hairy chest illustrates difficulties for acquiring ECG signals via gel Ag/AgCl electrodes; (b) Non-contact electrodes also show comparable ECG signals to that of Ag/AgCl electrodes without skin preparation. Both signals were obtained before filtering process [19]

Likewise, another long-term monitoring of ECG is done for ubiquitous healthcare systems using dry textile electrodes by Oh et al [20]. They investigated the performance of proposed five different dry electrodes (two of five are different electrospun conductive nanofiber web electrodes; and the rest three are metal plated fabrics). The researchers have evaluated contact impedance, step response, noise signal performance indices for the proposed five dry electrodes, and also compared the results to those of traditional wet Ag/AgCl electrodes. Regarding the results, explored nanofiber web electrodes revealed the performance closely to that of Ag/AgCl electrode than other proposed metal plated fabric electrodes. Another observation from the experiments is that ECG waveforms from nanofiber web electrodes were better than for metal plated fabrics including lower noise

power spectral densities. Lin et al [21] developed novel non-contact electrodes for mobile ECG system based on ubiquitous computing. Proposed contactless electrodes can measure bio-potentials through clothing, allowing the electrode can be integrated on a patient's normal clothing to record ECG data in daily life. Here, the proposed non-contact electrodes were utilized within a wearable wireless ECG acquisition module, which sends the ECG data through mobile phone to monitor real-time continuously. The group has also tested the implemented non-contact electrodes for monitoring the heart rate of six patients (between 40 and 70 ages) with heart arrhythmia under motion and action. Despite of the movements of the non-contact electrodes under motion and action resulted with noise, the key points of an ECG waveform was detected. Besides, using the QRS detection algorithm, heart rate can be calculated easily from the R waves. Furthermore, the experimental results revealed that both of the sensitivity and accuracy values for detecting arrhythmia seem efficient using the proposed non-contact electrodes.

Ito et al [22] examined the non-contact sensing of ECG signals of a human body on the bed in different positions. Six pieces conductive fabrics were used for the experiments. Three of them were used for ECG amplifying feature to have high impedance, and the rest three of them were used for reading capacitance meters. Capacitances for upper and lower bodies were separately measured. The non-contact electrodes were tested on a male subject who is instructed to sit down on a bed, lie on the bed in a supine position, and lie on lateral position to see the differences in the ECG signal. Results showed that ECG signal was detected in the periods when the subject was in supine or lateral position as can be seen in Figure 2.6. In addition, QRS complexes, P-waves, and T-waves were confirmed, although some distortions have been observed.

Varadan et al [23] developed a wearable wireless textile based nano-biosensor system for cardiac health monitoring, called as e-Nanoflex platform. This implementation was made of nano-biosensor with Bluetooth module for communication with smartphone to display bio-potentials simultaneously. As can be investigated in Figure 2.7a, the pair of nano-biosensor electrode pads, which was made of gold nanowire on flexible Titanium foil, was mounted on a wound dressing plaster to facilitate easy implementation for the patients. Lead I ECG signal obtained from the sensor in the frequency content between 0.2 and 70 Hz. The sampling rate was fixed at 200 Hz to conduct Nyquist sampling theorem. A comparison was also made using commercial Ag/AgCl electrodes and gold nanowire electrodes regarding three lead ECG signals as shown in Figure 2.7b and 2.7c. The signals from the both two type of electrodes were observed nearly similar. The ECG data from the e-Nanoflex sensor system can also be sent to a remote server via 3G network within the current GPS location and time. In case of emergency, a message with recorded information can also be sent to emergency team to monitor remotely.

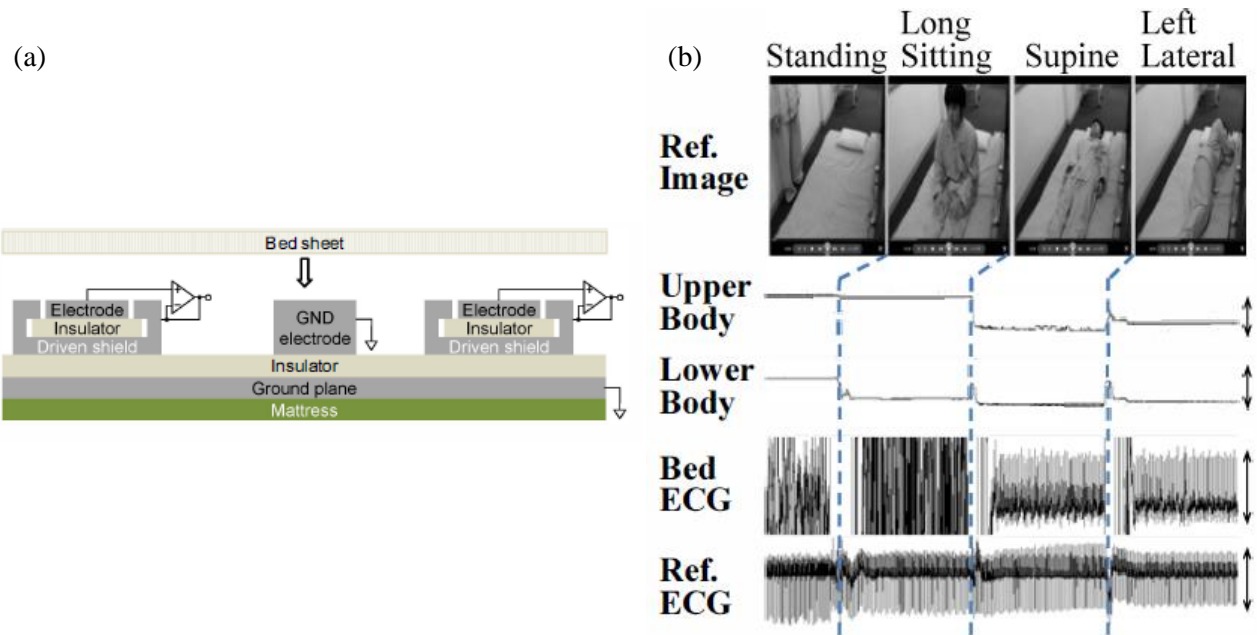


Figure 2.6: (a) Cross-sectional scheme of layered non-contact electrode system for ECG monitoring; (b) Acquired ECG signals while the subject was in different positions (standing, long sitting, supine and left lateral). ECG signals were detected during supine and left lateral positions [22]

Co-authors of this group also implemented two textile platforms that monitors ECG, PPG, blood pressure using e-Nanoflex sensory system from a t-shirt and a bra, and display multi body potentials on the smartphone wirelessly, called e-vest, and e-bra respectively [24,25]. The e-vest platform is development of a multi-parameter wearable wireless textile-based nano-biosensor that records ECG and blood pressure. As can be seen in Figure 2.8a, e-vest textile platform was structured by three textile electrodes and connected to a sensor electronics module (SEM). A photoplethysmography (PPG) technique was used in forming armband that has infrared LEDs and photodiodes which were connected to the SEM through conductive traces. SEM of e-vest application consists of an amplifier, filter circuits, a microcontroller, and a ZigBee wireless radio to transmit multi-parameter signals to the mobile phone. Besides, Figure 2.8b illustrates e-bra system that incorporated in the inner garment for women using e-Nanoflex wireless sensor platform. The aim of this work was to wirelessly acquire ECG signals from subjects using e-bra system and perform heart rate variability analysis on a PC. They also successfully monitored ECG waveforms, heart rate and blood pressure values on a smartphone using R-R interval calculations from ECG.

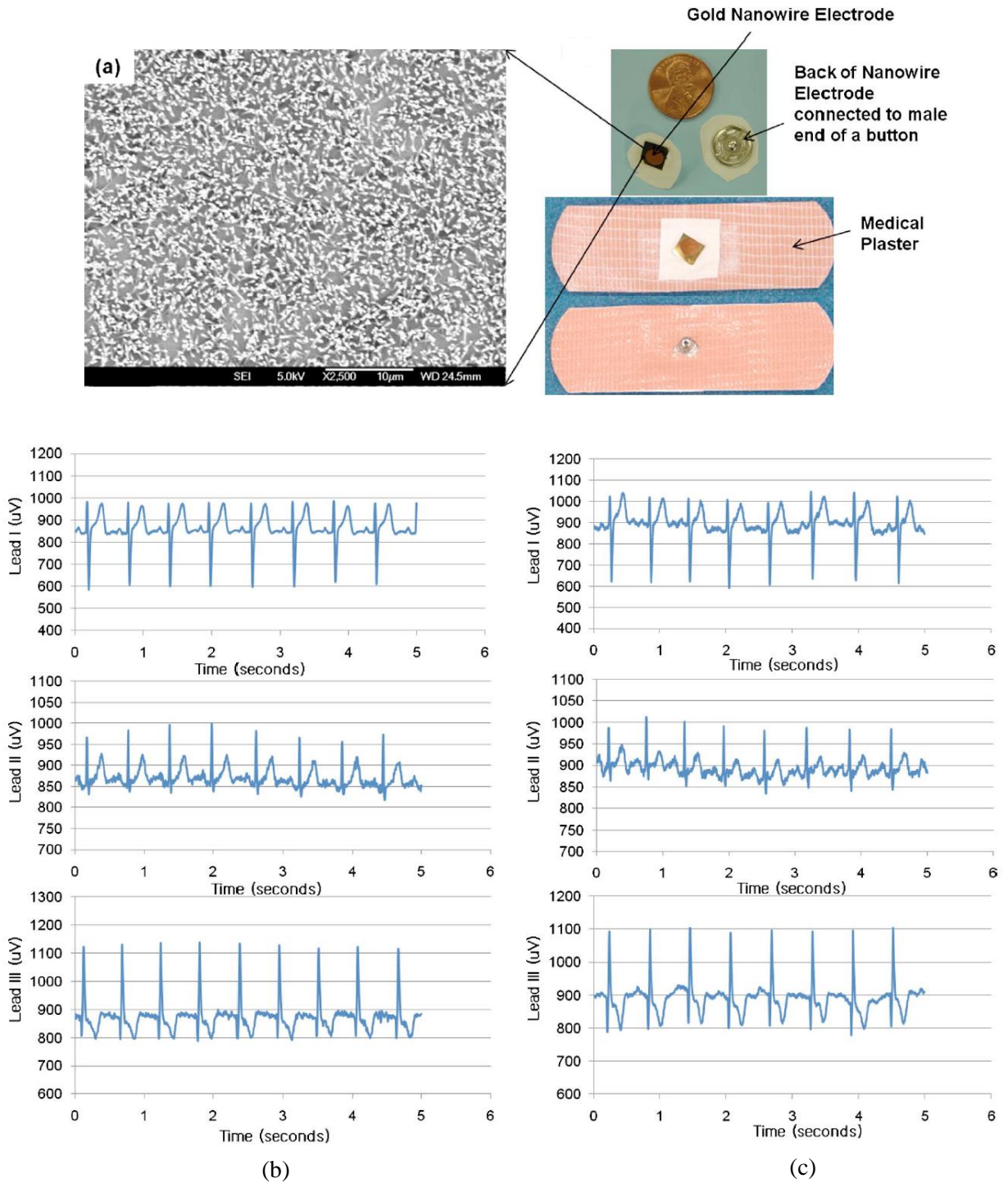


Figure 2.7: (a) Scanning electron microscope image of vertical gold nanowires and a medical plaster that involves of the gold nanowire fabricated electrode; (b) Acquired ECG signals from e-Nanoflex sensor conventional Ag/AgCl electrode and (c) proposed gold nanowire electrode [23]

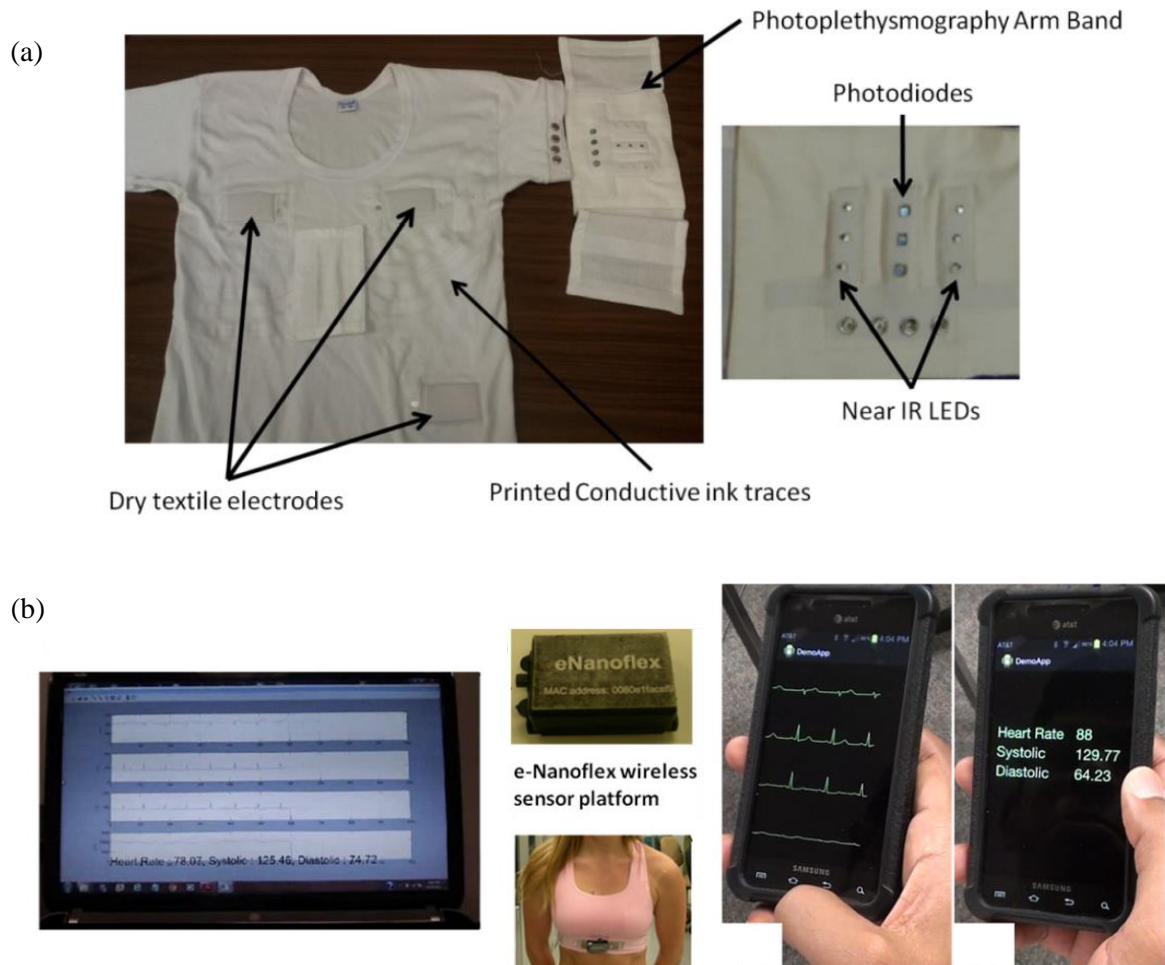


Figure 2.8: (a) Proposed e-Vest system within the plethysmography (PPG) arm band; and (b) the proposed e-Bra system that worn by the subject with the e-Nanoflex sensor module. In addition multichannel signal smartphone display consists of heart rate, and blood pressure [24-25]

Hsu et al [26] proposed barbed microtip-based electrode arrays for monitoring ECG and EEG signals by using silicon wet etching. In order to form a standard pyramidal microtip array, KOH anisotropic wet etching was performed and HF/HNO₃ was used to synthesize barbs on the microtips. Additionally, a through-silicon via (TSV) method was proposed to improve the electrical conductivity between the tip array and the electrode lead during the wet etching process. The impedances of the skin-electrode interface were compared using wet Ag/AgCl electrode and proposed barbed type dry electrodes. Furthermore, EEG and ECG recordings were demonstrated using both Ag/AgCl and barbed type dry electrodes. The experimental results indicated that the contact impedance of the barbed dry electrode was lower than was that of the wet Ag/AgCl electrode that also needs skin preparation. Regarding ECG recordings, both proposed barbed dry electrodes and conventional wet electrodes demonstrated similar waveforms. Kwon et al [27] developed a brassiere-based reliable ECG monitoring system, called CardioGuard, in supporting daily mobile healthcare (m-health) applications for women. The system comprises of two key

components: (1) a brassiere-based wearable sensor and (2) smartphone middleware for a daily ECG-based healthcare application. Figure 2.9 shows the prototype of the bra sensor and the sensor device. Gold-plated wire electrodes were used to acquire ECG signal in this application and the sensor device was placed at the cleavage so that the free space was utilized by structure and shape of the brassiere. They have observed the motion artifacts caused by daily activities (such as walking, riding or car driving) to see the robustness of the proposed system. Moreover, 2.9f shows the ECG signal using proposed CardioGuard system. Regarding the results of the system, QRS peaks were detected during 12 daily activities with different degrees of movement, such as resting, eating, desk working, lying supine, car driving, riding a bicycle or a bus, and with 10 participants. The average QRS peak detection ratio is 89.53% over all activities.

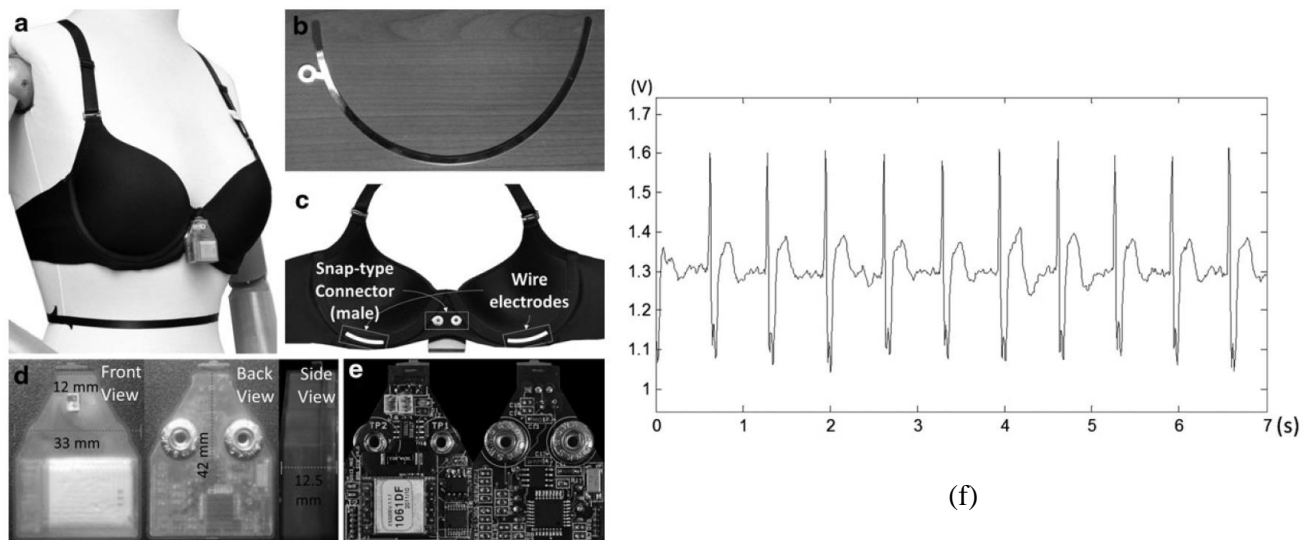


Figure 2.9: The prototype of the CardioGuard sensor system: (a) The wearing subject: the sensor device is attached at the cleavage of the bra; (b) applied gold-plated wire electrode; (c) the structure of the bra sensor system; (d) the front, back and side views of the proposed sensor system; (e) the hardware components of the system; and (f) an ECG signal recorded by proposed CardioGuard system [27]

Batchelor and Casson [28] examined the performance of proposed inkjet printed electrodes for ECG monitoring in personalized healthcare. They manufactured two types of electrodes: (a) inkjet printed capacitive and (b) tattoo-style inkjet printed ECG electrodes (printed metal electrode on a very thin, around 10 μm , layer of plastic) for long term biosignal monitoring. Regarding the performance comparison, three types of electrodes were tested on the subject to see recorded ECG signals as can be seen in Figure 2.10. This was followed by a test in which the subject walked around to investigate motion artifacts in the acquired traces. All recordings used a 10 bit resolution, 1024 Hz sampling rate, downsampled to 256 Hz and a 0.3 Hz high pass filter. Regarding signal-to-

noise ratio (SNR) variations, the conventional Ag/AgCl electrodes have the highest SNRs by 19.9 dB mean value. On the other hand, the SNR of the tattoo electrodes was marginally below that of the Ag/AgCl electrodes by 19.3 dB, and capacitive electrodes had 12.7 dB of SNR value. Regarding skin-contact impedance measurements, Ag/AgCl electrodes had impedance of 96 k Ω at 30 Hz and then falling down to 67 k Ω after two hours of use. In contrast, both the capacitive and tattoo electrodes had impedances above 200 k Ω .

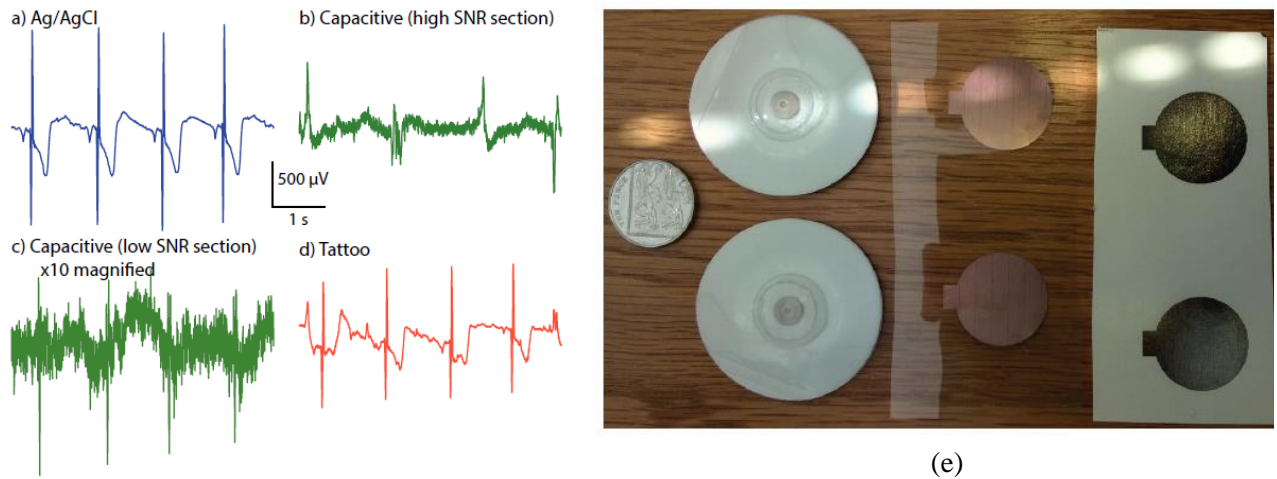


Figure 2.10: Measured ECG signals using (a) wet Ag/AgCl electrodes; (b) and (c) capacitive electrodes with different magnifications; and (d) proposed tattoo electrodes; tested electrodes are shown in (e): Ag/AgCl electrodes (left); proposed copper printed capacitive electrodes (middle); and Ag printed electrodes on tattoo paper (right) [28]

Chlahawi et al [29] proposed a flexible dry electrode based on multi-walled carbon nanotube (MWCNT)/polydimethylsiloxane (PDMS) composite for ECG monitoring. Dry electrodes were generated by screen printing Ag ink on flexible polyethylene terephthalate (PET) substrate, and then MWCNT/PDMS composite was coated onto the surface of the electrode. In order to see the performance of the proposed electrode, three same types of electrodes were fabricated in different sizes with radius of 8 mm, 12 mm, and 16 mm. The results were also compared to that of conventional Ag/AgCl electrode. Experimental studies showed that the proposed dry ECG electrode with the largest area (16 mm) exhibited better performance than conventional Ag/AgCl electrodes regarding signal intensity and correlation. Another flexible dry electrode with micro domes was proposed by Meng et al [30] based on PDMS for ECG monitoring system. The fabrication method of the proposed dry electrode was comprised of melting photoresist, double-PDMS-molding, Nickel (Ni) plating and encapsulation between two PDMS substrates. Similarly with the previous work, the researchers have developed three dry electrodes with different sizes to consider the performance of the proposed dry electrode. Experimental results revealed that the fabricated dry electrodes

provided a comparable ECG signal to that of conventional wet Ag/AgCl electrode without the need for skin preparation and use of gel. Moreover, skin-electrode contact impedance of the proposed dry electrode was decreased as the size of the electrode was increasing. Although the impedance of the proposed dry electrode with 80x80 arrays was larger than that of wet Ag/AgCl electrode at the beginning, the impedance of the wet Ag/AgCl electrode was increasing from around 15 k Ω to more than 100 k Ω after 6 hours. Nevertheless, the impedance of the fabricated dry electrode was stable at around 15 k Ω even after 6 hours. Figure 2.11a indicates the sampling module ECG monitoring system, and Figure 2.11b ECG signals recording using lead V. Figure 2.11(c-h) shows the ECG signal measurements using different size of fabricated dry electrodes and Ag/AgCl electrodes.

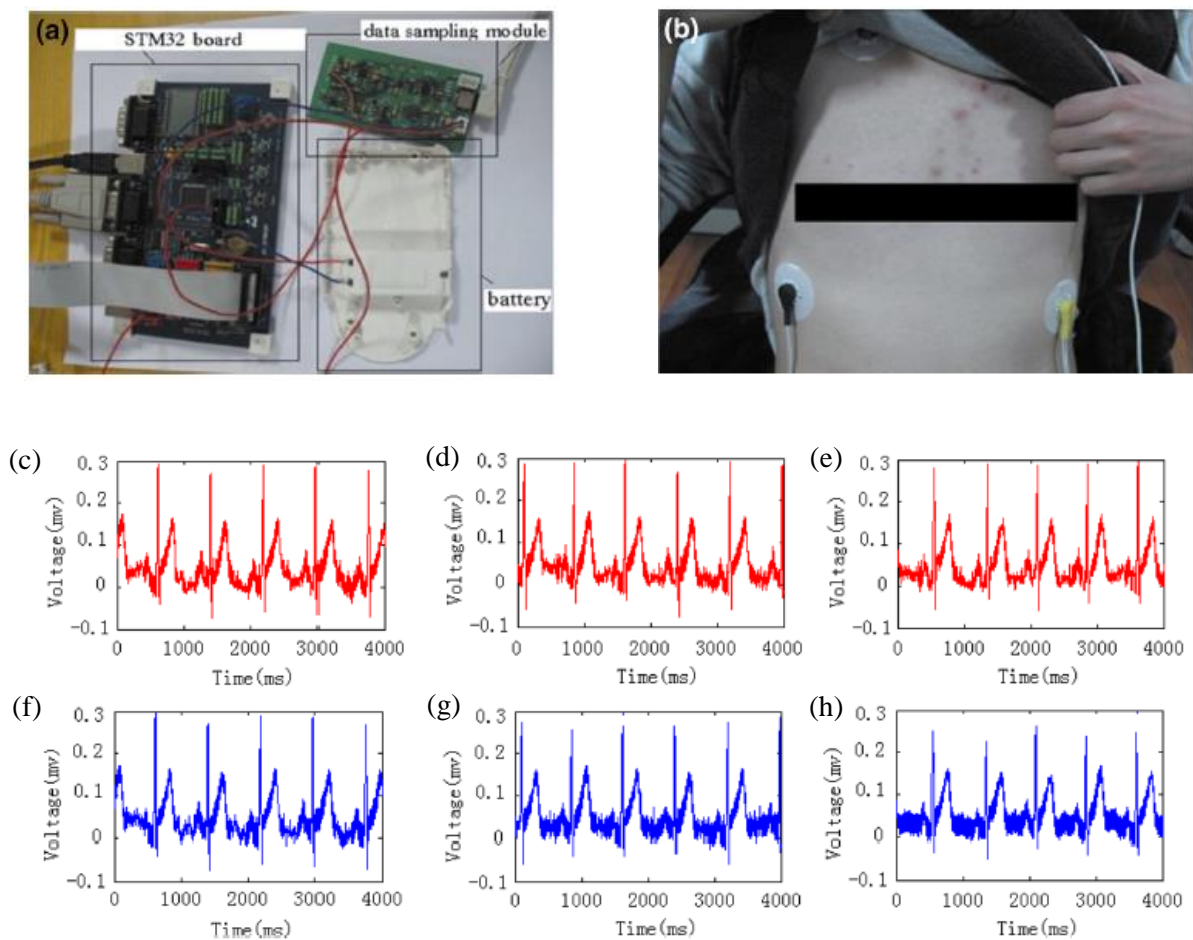


Figure 2.11: (a) Data sampling module of the proposed system; (b) Using lead V to record ECG signals. ECG signal measurement (c)-(e) ECG signals using wet Ag/AgCl electrode; (f) recorded ECG signals by proposed micro-dome electrode with 80 x 80 arrays; (g) signal from micro-dome electrode with 60 x 60 arrays; (h) signal with 40 x 40 arrays [30]

Additionally, same research group [31] developed another dry electrode by depositing metal film on (3-aminopropyl) triethoxysilane (APTES)-anchored PDMS substrate for ECG recording system. They have used APTES solution before depositing metal film to overcome the adhesion problem

that gave poor connection between metal and PDMS substrate. Furthermore, the performance of the proposed dry electrode was carried out by skin-electrode contact impedance and SNR of the ECG signals and compared it to those of Ag/AgCl electrodes. The impedance variations illustrated that the proposed dry electrode had higher contact impedance (580 k Ω at 50 Hz) than conventional Ag/AgCl electrodes (390 k Ω at 50 Hz). Regarding ECG waveform experiments, obtained ECG signal using the proposed dry electrodes with micro domes was similar to that obtained using conventional Ag/AgCl electrodes. Clear observations of QRS-complex and T-wave cardiac points can be seen. Moreover, experimental results have revealed that SNR of conventional Ag/AgCl electrodes was higher than the fabricated dry electrodes with micro domes, 23.35 dB and 21.82 respectively.

Recently, there have several research activities on ECG monitoring using different types and materials-enabled electrodes. Following studies have been proposed in the last year (2016) to observe essential findings of ECG signal using different approaches to ECG monitoring systems. Liu et al [32] developed silver nanowire and PDMS based composite electrodes for long-term ECG monitoring. The fabricated electrode patch comprised of three composite electrodes and an adhesive PDMS layer is combined with a wireless acquisition system to obtain ECG signals. The composite electrodes consisted of a PDMS layer, silver nanowires (Ag NW) layer, carbon nanotubes adhesive PDMS (CNT-aPDMS) layer and integrated with Cu wires to enable the external circuitry, as can be seen in Figure 2.12a. After the fabrication process of the electrodes, three electrodes were integrated into an ECG patch within ECG acquisition system, which enabled wireless transmission through radio-frequency (RF) module, via connected Cu wires. Experimental results showed that the contact impedance of the proposed composite electrode was higher than that of the conventional Ag/AgCl electrode because of the low conductivity of the CNT-aPDMS layer, the monitored impedance values were 1.55 M Ω and 651 k Ω respectively at 10 Hz. Moreover, ECG waveform of the fabricated electrode was observed and compared with that of the Ag/AgCl electrode. Figure 2.12b shows the results at different sites for the proposed and conventional Ag/AgCl electrodes. As can be seen in the figure, each wave of the ECG signal (P wave, QRS-complex, T waves) can be observed. Furthermore, ECG signals of each electrode type were indicated in the Figure 2.12b during different postures (sitting, standing, and walking). Even though the ECG signals were stable during sitting and standing postures, the signal was affected by walking posture as considerable amount of noise have been observed.

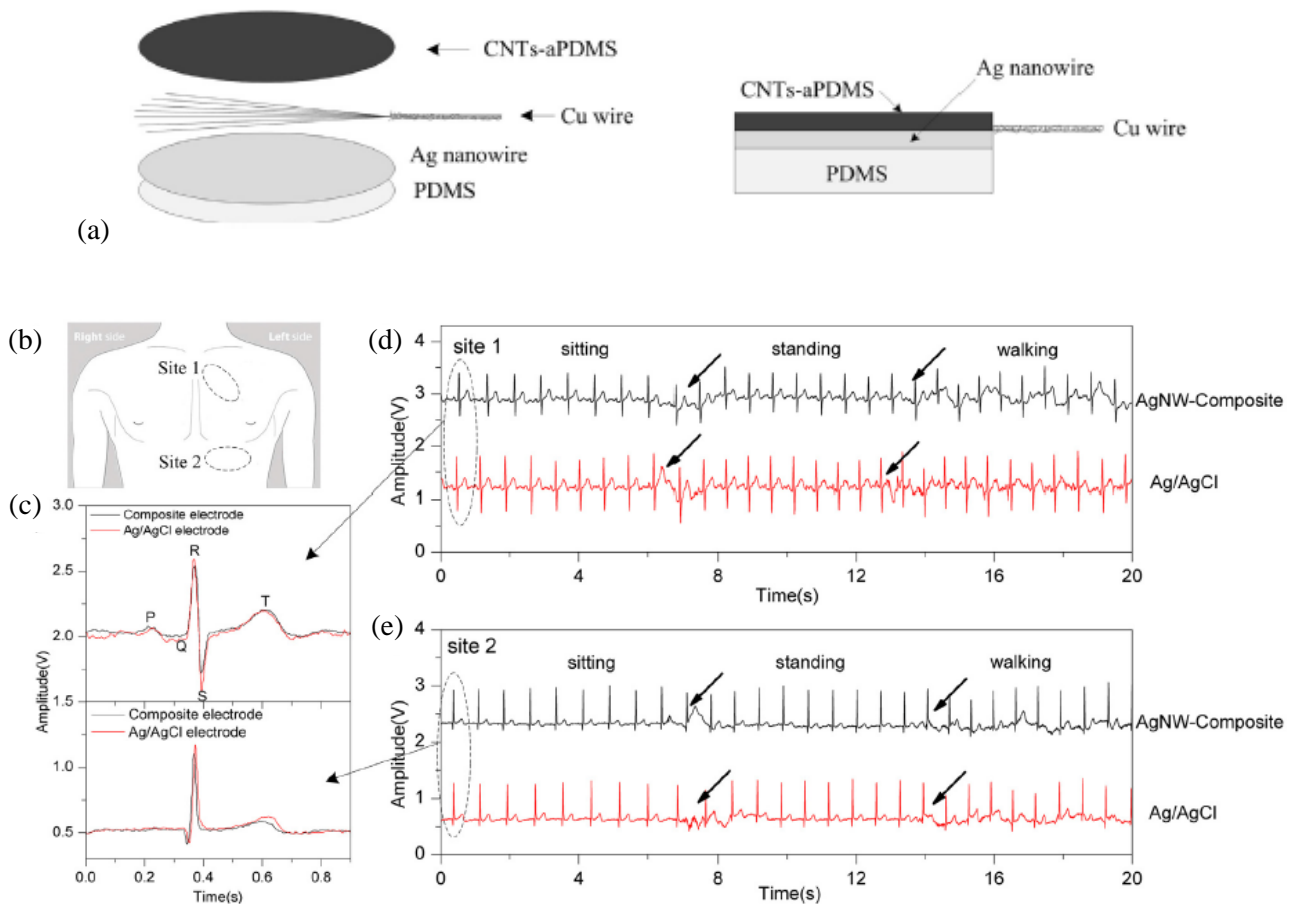


Figure 2.12: (a) Structure of the composite fabricated electrode composed of a PDMS layer, Ag NW layer, Cu wires and CNT-aPDMS layer. ECG measurements: (b) the measurement area; (c) Comparison the waves of the ECG signals between the propose composite electrode and conventional Ag/AgCl electrode; (d) and (e) shows continuous acquired ECG signals during different postures (sitting, standing, walking) at site 1(d); and at site 2 (e) [32]

Similarly to the previous work, Lee et al [33] fabricated a self-adhesive ECG patch using CNT electronics for long-term ECG monitoring system. The self-adhesive patch consisted of a PDMS layer, an Au/Ti/Polyimide metal layer, a PDMS frame layer, and a CNT/aPDMS interfacial layer for signal acquisition. To evaluate the results, the comparison has been made between dry, Ag/AgCl and CNT/aPDMS electrodes with the same locations at the right arm (RA), left arm (LA), and left leg (LL) positions of the ECG patch. Figure 2.13 also shows the comparison results for motion artifacts and ECG measurements using three types of electrodes (dry, Ag/AgCl and CNT/aPDMS). Regarding the motions with different frequencies, the root-mean-square (RMS) value of the motion artifacts was substantially lower than that of dry electrodes for all motion frequencies, and the value was slightly smaller than that of Ag/AgCl electrodes at 3 Hz, as can be seen in Figure 2.13c. Figure 2.13f also indicates that the waveforms of CNT/aPDMS are comparable to those of conventional Ag/AgCl electrode, while there are significantly noisy and shows artifacts in the signals of the dry

electrode. Furthermore, skin-to-electrode contact impedance was 241 k Ω at 40 Hz for the CNT/aPDMS electrode as compared to 74.2 k Ω for the conventional Ag/AgCl electrode.

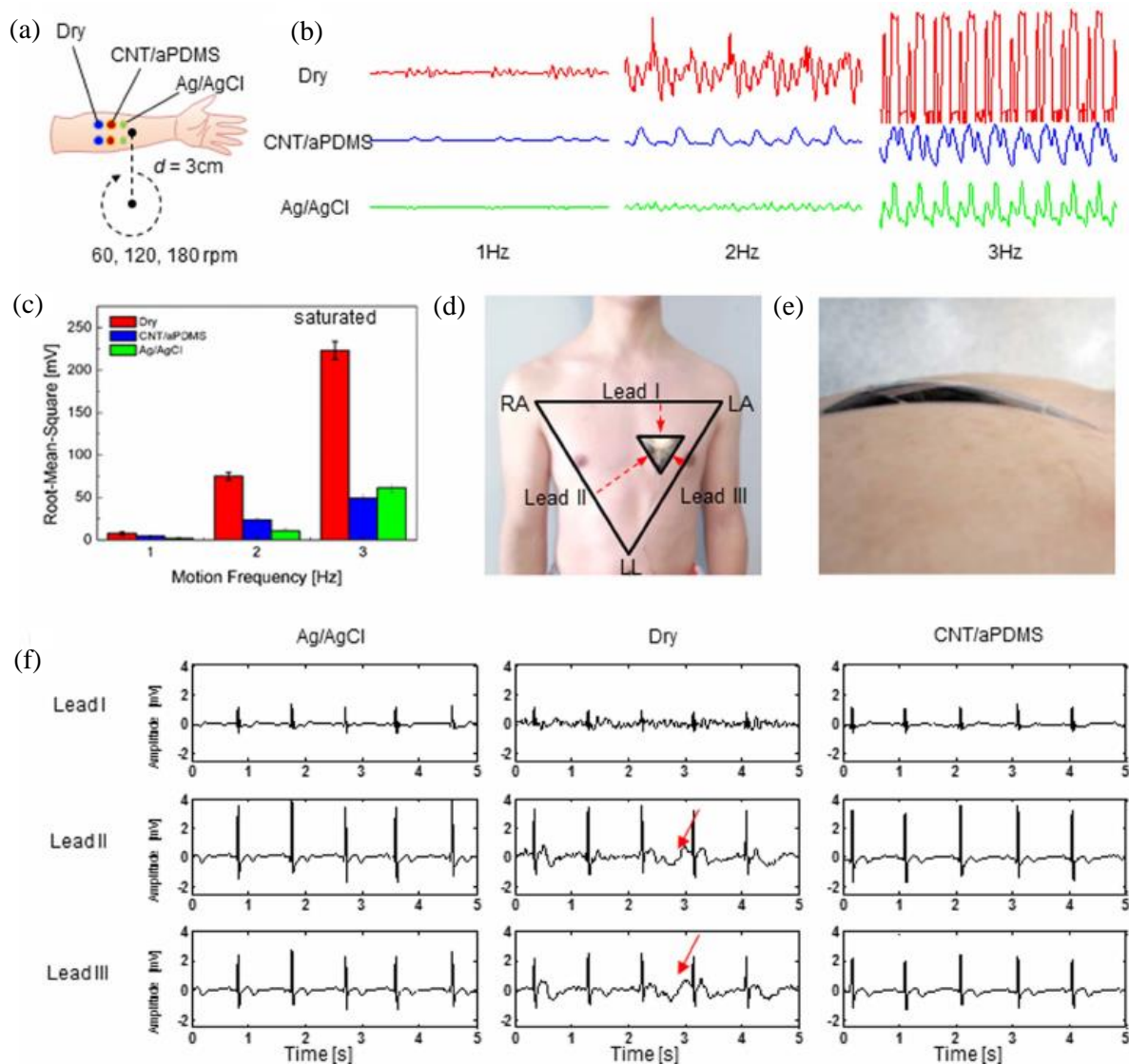


Figure 2.13: Motion artifacts and ECG measurements. (a) Experimental set-up to test of motion artifacts for dry, Ag/AgCl and proposed CNT/aPDMS electrodes were attached to the left arm in separate tests; (b) Recorded motion artifacts for each dry, Ag/AgCl and proposed CNT/aPDMS electrodes while running at different frequency ranges between 1 and 3 Hz; (c) RMS values; (d) Attachment of the ECG electrode using leads I, II, and III; (e) The attached electrode on the chest; (f) Recorded ECG signals with leads I, II, and III for the dry, Ag/AgCl and proposed CNT/aPDMS electrodes [33]

Pei et al [34] developed a dry electrode based on conventional microneedles array (MNA) to remove the interference of skin-potential variation (SPV). Based on this technique, Parylene membrane layer is coated to the root of the microneedles for insulating the electrode from the corneum layer. Thus, skin-potential variation will not affect ECG recording while the subject was moving around. They compared the impedance measurements of the commercial wet electrode,

conventional MNA-based electrode and proposed SPV-based dry electrode. According to the results, the skin-electrode contact impedance of the proposed dry electrode was similar (around 120 k Ω) to that of commercial wet electrode (115 k Ω) and higher than that of conventional MNA-based electrode (66 k Ω) at 10 Hz. Likewise, the skin-to-noise ratio (SNR) of ECG signals measured by proposed SPV-based dry electrode, conventional MNA-based electrode and commercial wet electrode were 36.9 dB, 43.2 dB, and 44.5 dB respectively. Recently, Jang et al [35] fabricated a ferromagnetic, folded electrode composite for wireless electrophysiological acquisition systems. As can be seen in Figure 2.14, ferromagnetic, folded composite structure lays on a permanent magnet (NdFeB) layer. The transparent adhesive layer is coupled with ferromagnetic layer to provide adherent interfaces to the skin that maintains robust conformal contact. On the other hand, the magnet conducts a permanent electrical bond to the acquisition system. As in Figure 2.14c, the electrodes rest between the electrical lead-out (or magnet layer), and the skin. Furthermore, Figure 2.14d presents the proposed magnetic folded soft composite electrodes with wireless operation (Bluetooth module). Each electrode placed onto a permanent magnet (NdFeB) with a force that contributed an electrical contact from the skin and a mechanical bond. The group have developed several electrode types for recording ECG, EMG, EOG, and EEG using this proposed electrode composite. Figure 2.14e also shows recorded ECG acquired with capacitive and direct contact electrodes from the chest indicated that P, QRS, and T waves were collected with a quality of measurement that is comparable to that of hydrogel electrode.

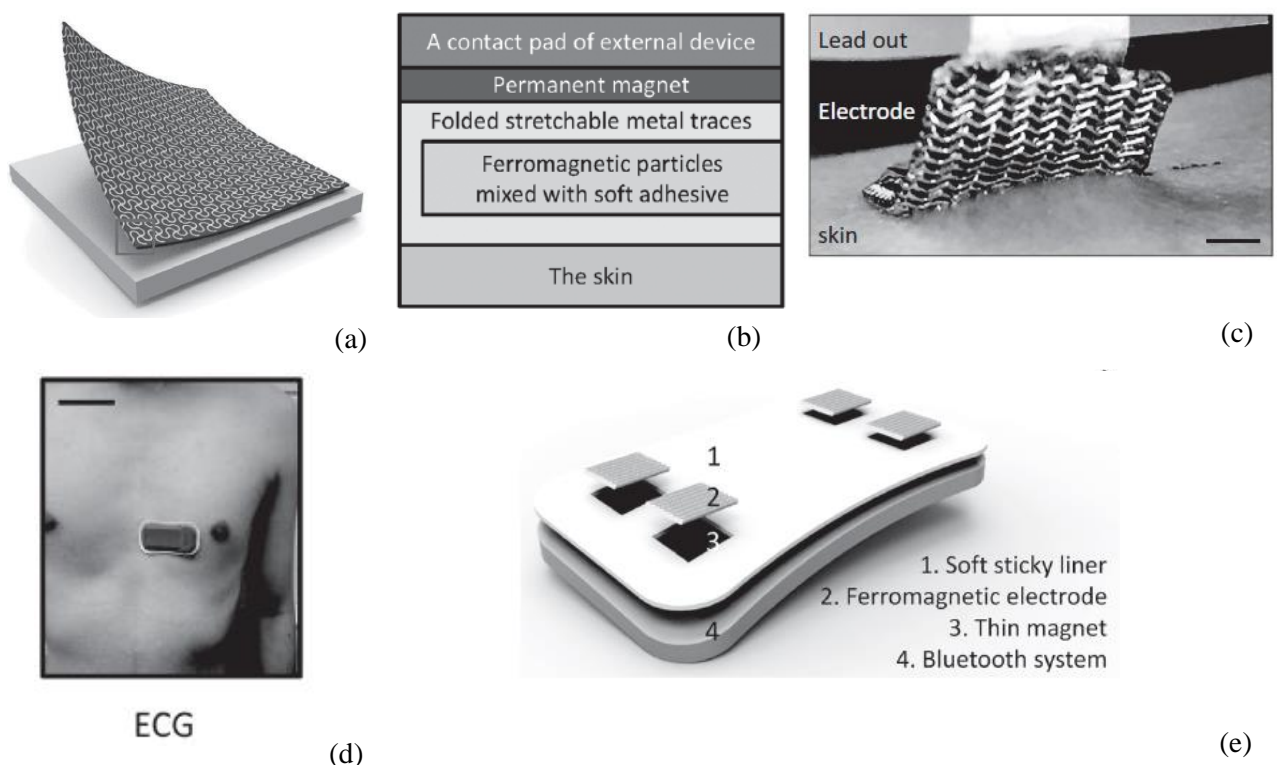


Figure 2.14: (a) Schematic diagram of the proposed electrode design; (b) Information on the structure of

the composite and its interface with the skin and the contact pad of the external (wearable) device; **(c)** Optical image of the electrode system on the skin; **(d)** Attaching proposed device on the chest to acquire ECG data; **(e)** Schematic illustration wireless ECG monitoring system [35]

Poliks et al [36] investigated hybrid flexible electronics that integrate conventional printed circuits and thinned silicon chips in order to produce a wearable ECG and skin temperature sensor. The wearable monitor is consisted of a flexible polyimide substrate with printed ECG electrodes, thermistor, and a connecting traces printed on one surface using ECG conducting gel electrodes printed with gold ink, and the electronic components placed on the other surface. ECG signals were transmitted to a mobile phone wirelessly via Bluetooth after signal conditioning process to be monitored in real-time. The wearable device is in 2x2 inches in size and worn on the chest. The group has analysed the ECG recordings using proposed gel based printed electrodes by performing signal-to-noise ratio, peak detection, and heart rate variability. The experimental results demonstrated that the recorded ECG signals were comparable to those of archived and certified ECG signals at MIT-BIH database. Dai et al [37] developed a wearable ECG acquisition system using three proposed textile electrodes and a specialized circuit system. The proposed system used various digital filter methods to eliminate the baseline wander, thus reduce skin contact noise and also the system presented several methods to reduce the power consumption of the system. Furthermore, presented ECG system designed new type of electrodes using flexible polypyrrole textiles (FPTs) to increase the system performance by eliminating the need of electrolyte gel. Due to decreased electrochemical impedance between the skin and electrode [38], thus improved conductivity, the FPT electrodes were used, and the 5 x 4 cm fabric electrodes were integrated into the garment for ECG acquisition system. Figure 2.15a shows the structure of proposed FPT electrodes and Figure 2.15b illustrates wearable ECG unit on a sweatshirt. Regarding the performance of the system, a series of continuous impedance measurements were carried out for 8 hours to analyze the variation of contact impedance and also to compare them to those of wet Ag/AgCl electrodes. Results demonstrated that while the skin-electrode contact impedance of wet Ag/AgCl electrodes was increasing, the contact impedance of proposed FPT electrodes was decreasing which will be efficient for long-term ECG monitoring. Experimental results also revealed that the presented ECG acquisition system has lower power dissipation of 29.74 mW in full round of ECG acquired system when compared with two commercial ECG acquisition systems (Heal Force and BodiMetrics).

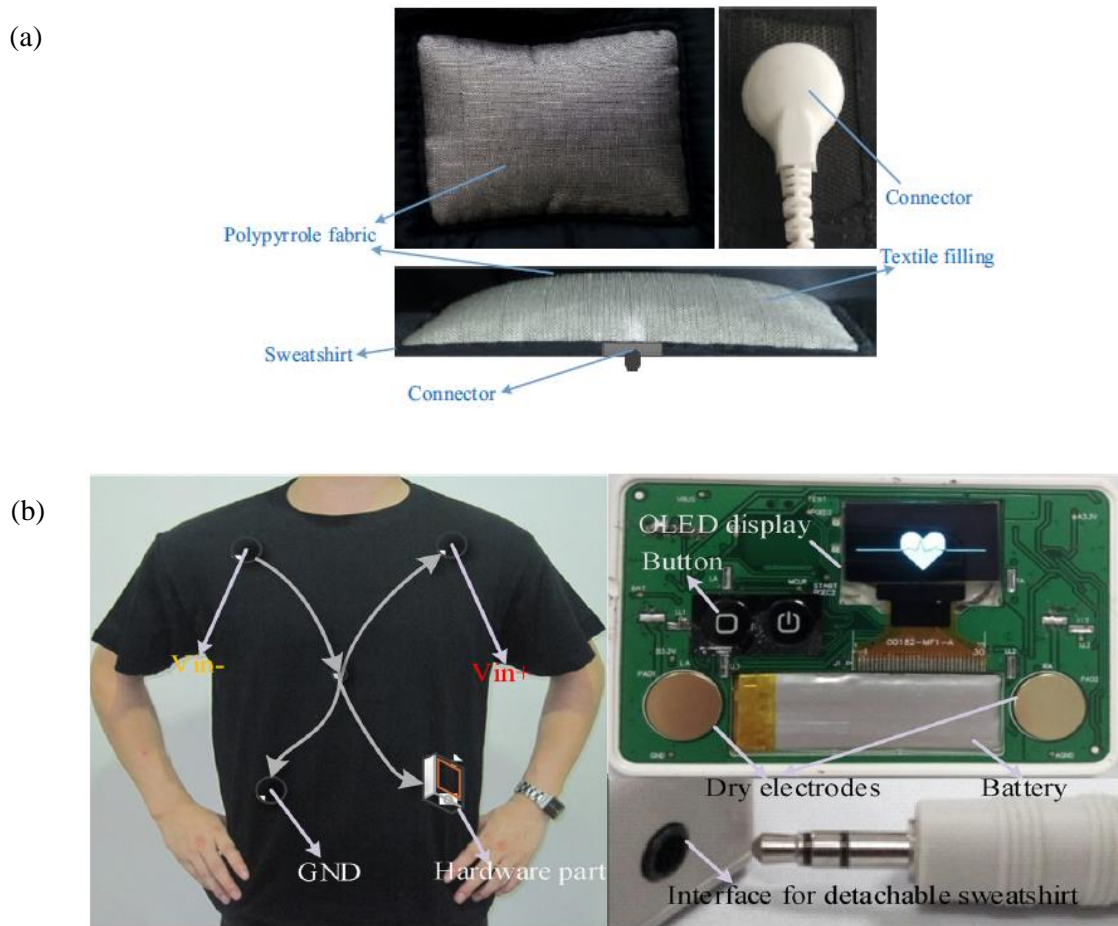


Figure 2.15: (a) The structure of proposed flexible polypyrrole textile electrodes (FPTe); (b) Distributions of electrodes based on sweatshirt with an ECG monitoring system [37]

Another textile-electrode for ECG recordings was designed by Pani et al [38] based on woven fabrics applied with conducting polymers, poly-3,4-ethylenedioxythiophene doped with poly(styrene sulfonate) (PEDOT:PSS). Due to excellent characteristics of this conducting polymers group such as low band gap and high electrochemical stability, this research group has fabricated new type of electrode based on fabric soaking in PEDOT:PSS using a second dopant, squeezing and annealing. The proposed electrodes were tested for both skin-electrode contact impedance and the quality of ECG signals recorded at rest and during physical activity. The experimental results showed that the electrodes are good enough in both wet and dry conditions. However, dry type of electrodes had higher noise artifacts in particular during physical activity exercise. Wet type of proposed electrodes indicated that better contact impedance than dry ones, and they were comparable to that of traditional Ag/AgCl electrodes. Figure 2.16a illustrates the proposed PEDOT:PSS type textile electrode, and Figure 2.16b shows recorded ECG signals from a single subject during rest and different activities with dry and wet type of proposed electrodes and compared to those acquired with gelled Ag/AgCl electrodes. The results revealed that the gelled Ag/AgCl electrodes indicated better stability than dry textile electrodes, but worse than the wet

ones. Performance of wet textile and gelled Ag/AgCl electrodes were generally similar, however, dry textile electrodes exhibited higher sensitivity to high frequency noise.

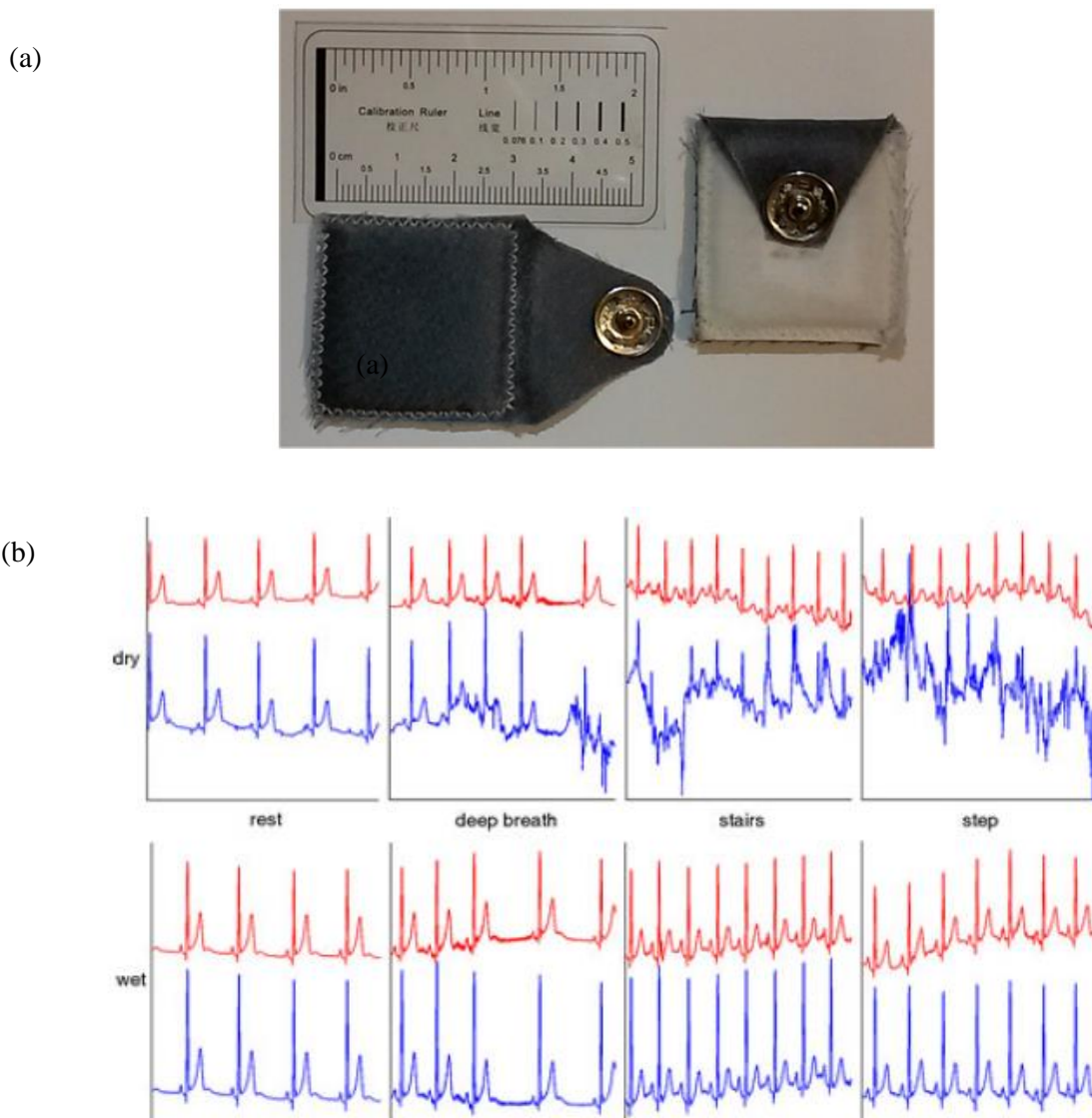


Figure 2.16: (a) Proposed PEDOT:PSS type of textile electrode; (b) Five sample excerpts of ECG signals obtained with proposed dry and wet electrodes (in blue, lower signals) compared to those obtained with conventional Ag/AgCl electrodes (in red, upper signals) during different activities [38]

Noh et al [39] developed two type of conductive carbon black (CB), and PDMS bio-potential electrodes, with and without an integrated flexible copper mesh to compare with commercially available electrodes (Polar textile, Ag-coated textile, and carbon rubber). The proposed electrodes were tested in three types of water: fresh water, chlorinated water, and salt water to see the qualities of recorded ECG signals. The developed hydrophobic CB/PDMS electrodes were fabricated based on filling conductive CB/PDMS composites on 3D printed cavity molds, and then a copper mesh was affixed on the CB/PDMS mix to allow signal acquisition via the monitoring device. A diagram of the proposed meshed CB/PDMS is shown in Figure 2.17a. Experimental results exhibited that

the proposed CB/PDMS electrode with integrated copper mesh indicated a high quality of ECG signal without any amplitude degradation in all types of water tested for 10 subjects. Regarding the electrode-skin contact impedance magnitudes, all 5 types of electrodes had comparable performance in the frequency range between 4 Hz and 1 kHz. The impedance characteristics of proposed CB/PDMS with and without copper meshed electrodes did not change throughout the frequency range (from 600 k Ω to 80 K Ω), however, other 3 types of electrodes had much lower impedances in wet conditions when compared to dry condition. According to the ECG amplitude studies of this work, Table 2.1 draws the signal amplitude reduction values of each electrode type between dry and wet conditions. Among all 5 electrodes types, the meshed CB/PDMS electrode was the most successful in preserving the ECG signal amplitudes in all types of water. Figure 2.17b shows the ECG recordings for all experimental conditions (dry, immersed, wet conditions) with the proposed meshed CB/PDMS electrode in fresh, chlorinated, and salt water. Regarding the results, all ECG waveforms (P waves, QRS complex, and T waves) were detected in all conditions and water types. Only, the meshed CB/PDMS electrode showed the best performance in chlorinated water for all conditions as can be seen in the Figure 2.17b. Furthermore, both mesh and non-meshed CB/PDMS electrodes also were evaluated for long-term test under water for 6 hours period of continuous use and exhibited that electrodes maintained ECG signal quality without a significant degradation.

Table 2.1: Mean of Amplitude reduction (%) between dry and wet conditions (N = 10 subjects)

Electrodes	Fresh water	Chlorine water	Salt water
Polar textile	+27.20	-16.13	-37.91
Silver-coated textile	+13.41	-16.04	-51.98
Carbon rubber	+8.10	-2.67	-22.99
CB/PDMS	+12.87	-2.46	-14.17
Meshed CB/PDMS	+31.77	+0.48	+3.60

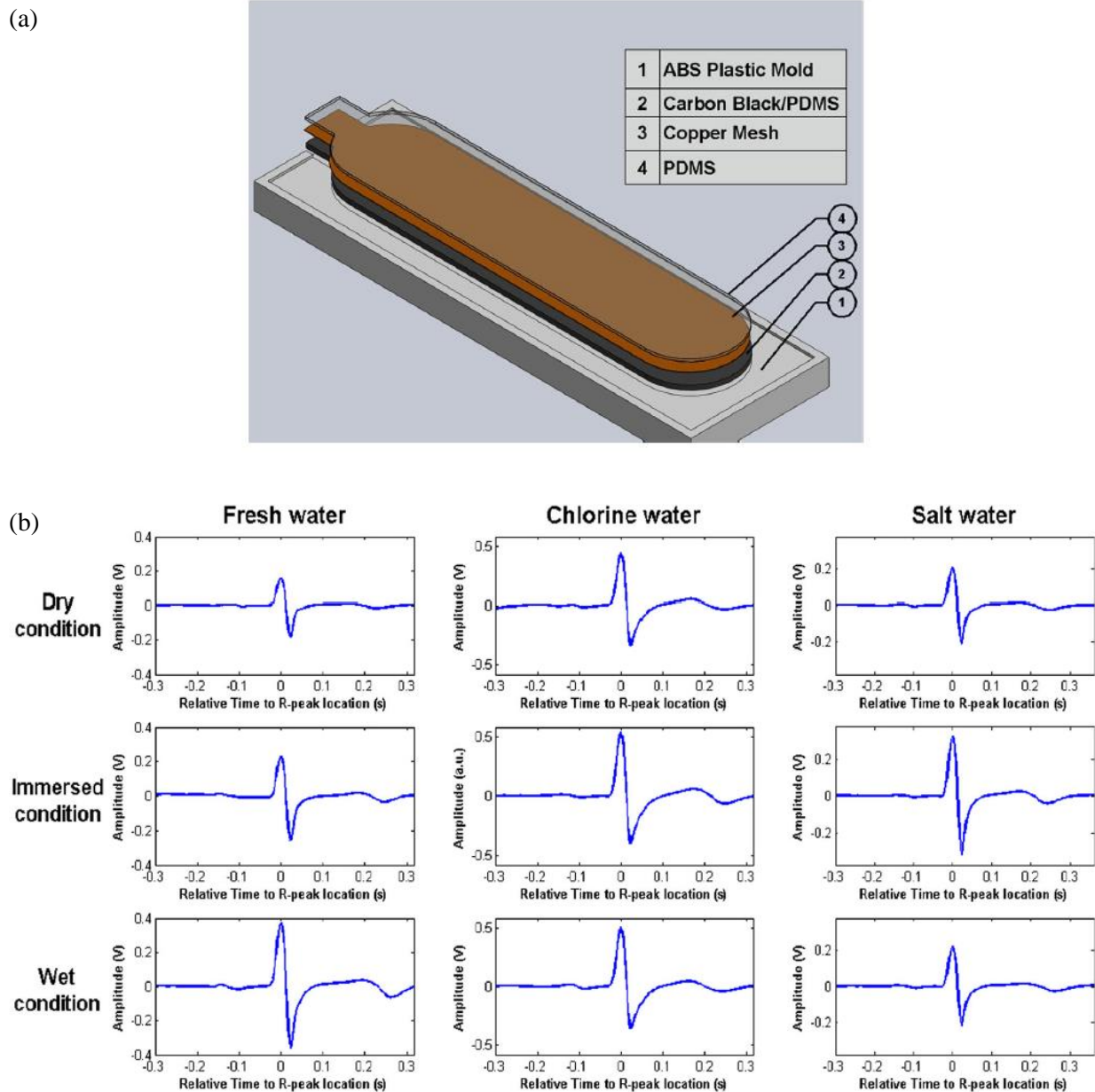


Figure 2.17: (a) The fabrication procedure of the proposed meshed CB/PDMS electrode; (b) Example of ECG samples from a subject recorded with proposed copper-meshed CB/PDMS electrodes during different conditions and types of water [39]

Another fabric based wearable dry electrode was developed by Yokus and Jur [40] for ECG recording measurements. The proposed multilayered dry electrodes were fabricated by screen-printing of Ag/AgCl conductive inks on non-woven fabrics, which is examined as a sensing platform (see Figure 2.18a). Impedance measurements were carried out on the printed dry electrodes with 10, 20, 30 mm diameters and 3M red dot wet Ag/AgCl electrodes were used as a reference measurement in the frequency range between 0.1 Hz and 1 kHz. The printed dry electrodes with 10, 20, 30 mm diameters had higher impedance values than wet electrodes (10 M Ω , 8 M Ω , 1 M Ω , and 100 K Ω respectively at 1 Hz) due to the absence of conductive medium at the

interface. The results from the experiments revealed that the larger electrode area, and stable skin contact, exhibited in higher ECG amplitudes, as can be seen in Figure 2.18b. A comparison of the printed dry electrodes was provided in Table 2.2, SNR of acquired signals were observed to be proportional to the printed area.

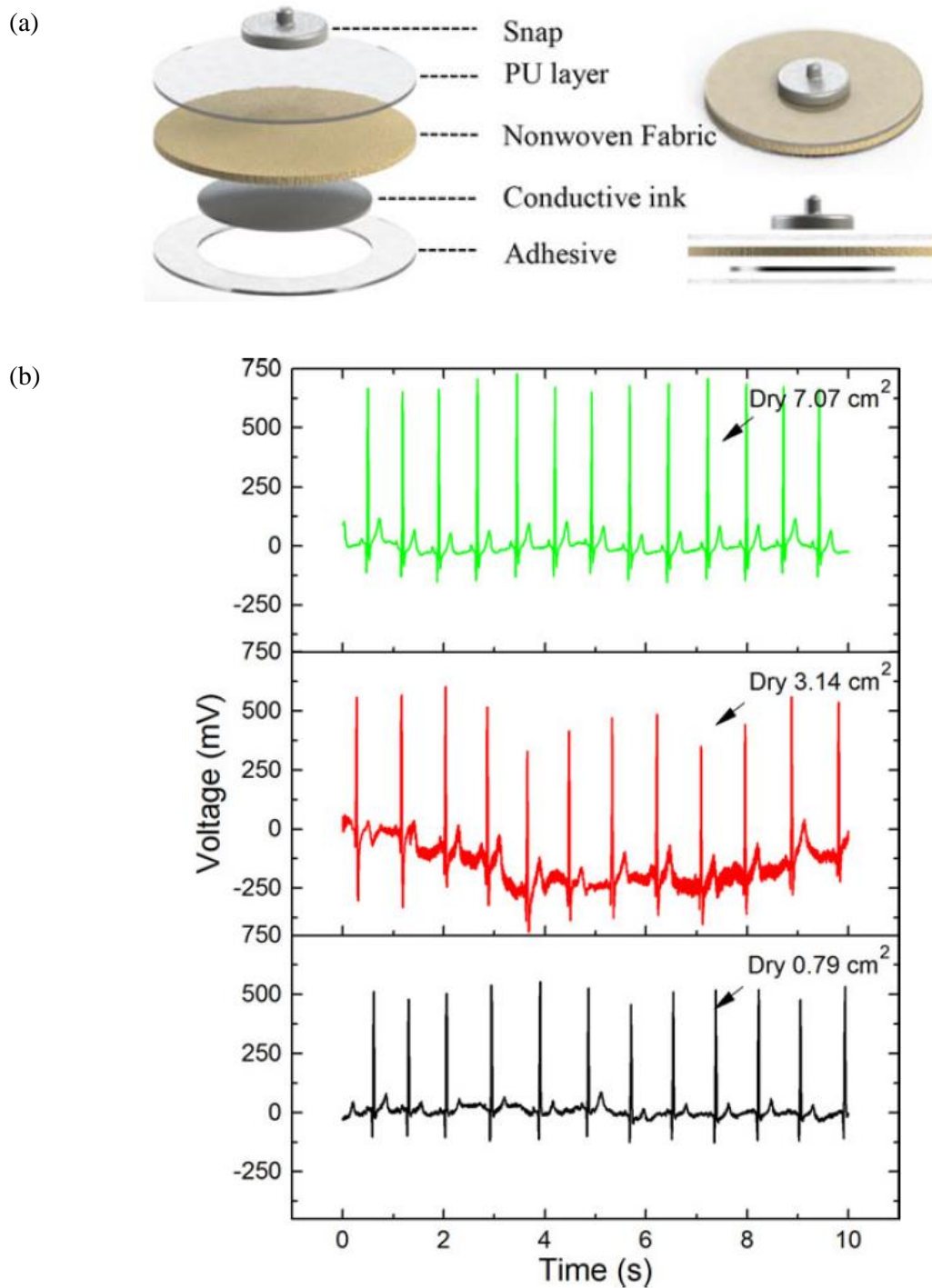


Figure 2.18: (a) Structure of the proposed multilayered dry electrode with expanded view; (b) Recorded ECG signals variation with respect to printed electrode area [40]

Table 2.2: Comparison of Printed Electrode Area

Electrode diameter (mm)	R wave peak amplitude (mV)	Signal power ((mV)²)	Noise power ((mV)²)	SNR (dB)
10 mm	460.47 (± 22.5)	4719.80	23.01	23.11
20 mm	591.86 (± 34.9)	8655.90	202.56	16.30
30 mm	630 (± 28.4)	9473.50	12.71	28.72

O'Mahony et al [41] also proposed polymeric dry ECG electrode that used microneedle structures to make a direct contact between the electrode and the body. Regarding the fabrication process, two moulds were attached to provide 500 μm length of microneedle structure on the front side of a polymeric wafer, and electrical components and detachable arrays were on the back side. Afterwards, the wafers were metal-coated and integrated with a self-adhesive pad to configure ECG electrodes to be able to measure the electrical signs of cardiac heart in mV-amplitude. Based on the skin-electrode contact impedance, pairs of wet Ag/AgCl electrodes and the proposed dry microneedle electrodes were attached to the subject's forearm and impedance measurement performed between 1 and 950 Hz frequency range. At the end of the evaluation, the impedance of the pre-gelled Ag/AgCl electrodes were between 30% and 33% lower than that of the proposed microneedle electrodes for all measured frequencies. The acquired ECG signals were comparable to those recorded using pre-gelled Ag/AgCl electrodes and all the waveforms (P wave, QRS complex and T wave) were clearly visible. Another observation from the experiments is that in contrast to conventional wet electrodes, SNR of ECG waveforms recorded using proposed microneedle dry electrodes was dependent on the skin-electrode contact force. Apart from fabric electrode fabrication, Aulia et al [42] designed a wearable ECG device that was studied in the regard of the electrode positions to fulfill the clinical placement. Moreover, a new way of electrode placement is developed in terms of a fitness lifestyle for continuous real-time healthcare monitoring in a form of a necklace. The proposed biomedical device has a single lead ECG analog front-end that is connected to the microcontroller unit (MCU), and it also composes of Bluetooth technology for wireless communication with an Android mobile phone to display ECG data on. ECG signal was acquired from the electrode placement at the backside of the neck shows Lead I waveform and heart rate can be calculated from recorded R peaks. Figure 2.19 shows the electrode placements on the backside of the neck, and proposed 3D-printed, necklace-form ECG device.



Figure 2.19: (a) The backside of the neck proposed electrode placements; (b) The subject wearing the necklace-form-1-lead ECG device [42]

Hybrid multi-sensory systems also offer flexible and wearable electronics for biopotential recordings in simultaneous healthcare monitoring. Imani et al [43] presented a wearable (skin-worn) hybrid sensing system that provides real-time monitoring of a biochemical (lactate) and an electrophysiological signal (ECG). The proposed hybrid wearable, Chem-Phys patch, composed of three-electrode (3×2.5 mm) for monitoring lactate and two ECG electrodes (1.5×1.5 cm²) for monitoring of ECG and heart rate. The fabrication of Chem-Phys patch was carried out by screen-printing technology on a thin (50 μ m thickness), human-skin-morphology-like polyester sheet to offer minimum noise signal. The fabrication of hybrid sensor system is shown in Figure 2.20a and 2.20b, as screen-printing process is done by a polyester sheet, and also Figure 2.20c indicates the block diagram of chemical-electrophysiological acquisition system including wireless transmission. A comparison was made using printed ECG electrodes and commercial wet Ag/AgCl electrodes to validate the proposed electrodes for ECG monitoring. The results showed that, as illustrated in Figure 2.20e, recorded ECG signals had similar morphologies when the same analog circuitry was used. Figure 2.20d also indicates the proposed Chem-Phys patch that fuses the monitoring of ECG with on-body chemical sensing into a printable wearable platform.

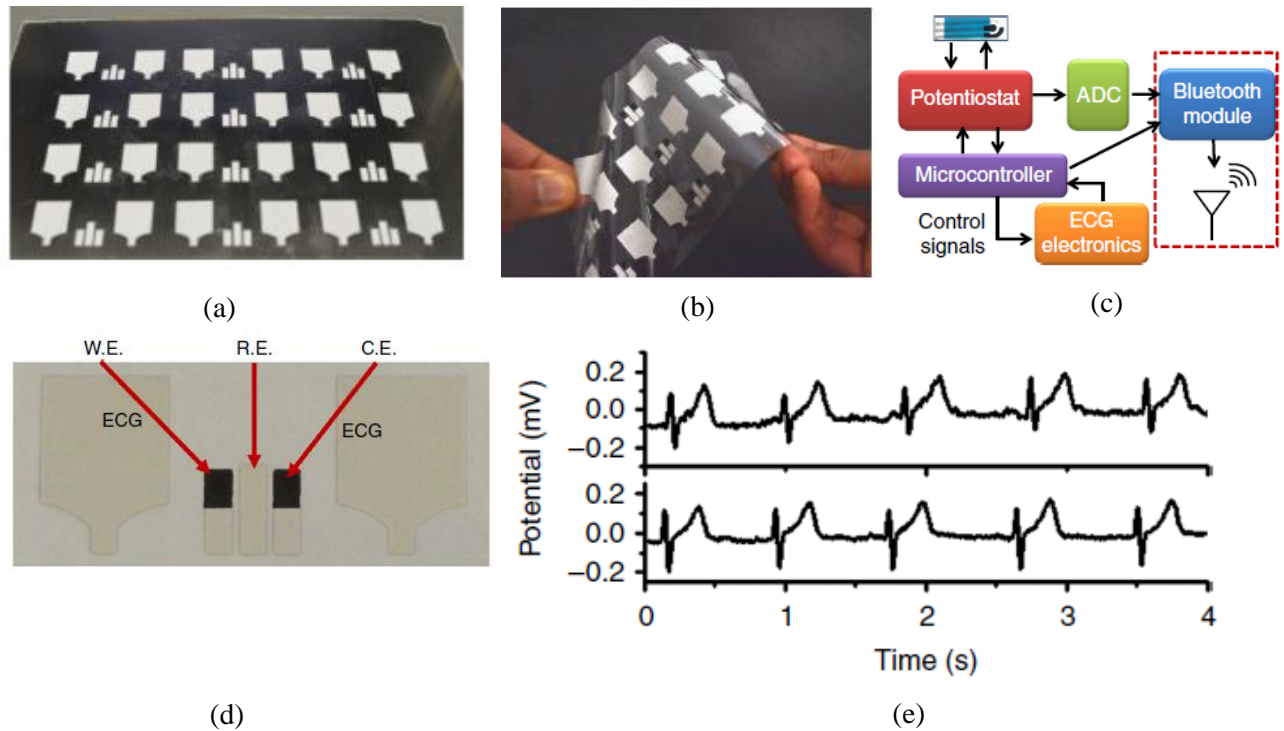


Figure 2.20: (a) Image of the Chem-Phys printing stencil; (b) An array of printed Chem-Phys flexible patches; (c) Block diagram of the wireless acquisition system; (d) Image of the Chem-Phys hybrid patch; (e) ECG signals using commercial 3M Red Dot Ag/AgCl electrodes (top), and printed ECG sensor (bottom) [43]

Another hybrid wearable sensor system is done by Khan et al [44] for measuring ECG and skin temperature. The proposed wearable hybrid patch system is shown in Figure 2.21, in detail, where ECG and temperature sensors are integrated into a sensing platform. The sensor patch was carried out by a pair of printed gold electrodes for ECG monitoring, and a printed nickel oxide thermistor for skin temperature monitoring (see Figure 2.21a). The hybrid wearable platform is assembled on a Kapton polyimide (PI) substrate that hosted the silicon-based integrated circuits (analog front-end, wireless components-Bluetooth system). The hybrid patch is proposed and designed on a 5.08 cm x 5.08 cm, 50 μm thick flexible Kapton PI substrate (Figure 2.21b) for the need of the space between ECG electrodes to allow acquiring ECG data. The complete system was powered by a coin cell battery of 220 mAh capacity (8 hours battery lifetime), and was weighted by 6.1 g. Figure 2.21c-e illustrates wearable hybrid sensor patch mounted on a subject, and also printed sensor patch including electronic components. Experimental studies revealed that, recorded ECG signals provided peak-to-peak 0.6 mV using two gold printed electrodes compared to conventional Ag/AgCl electrodes which provided peak-to-peak 0.8 mV when placed on the chest.

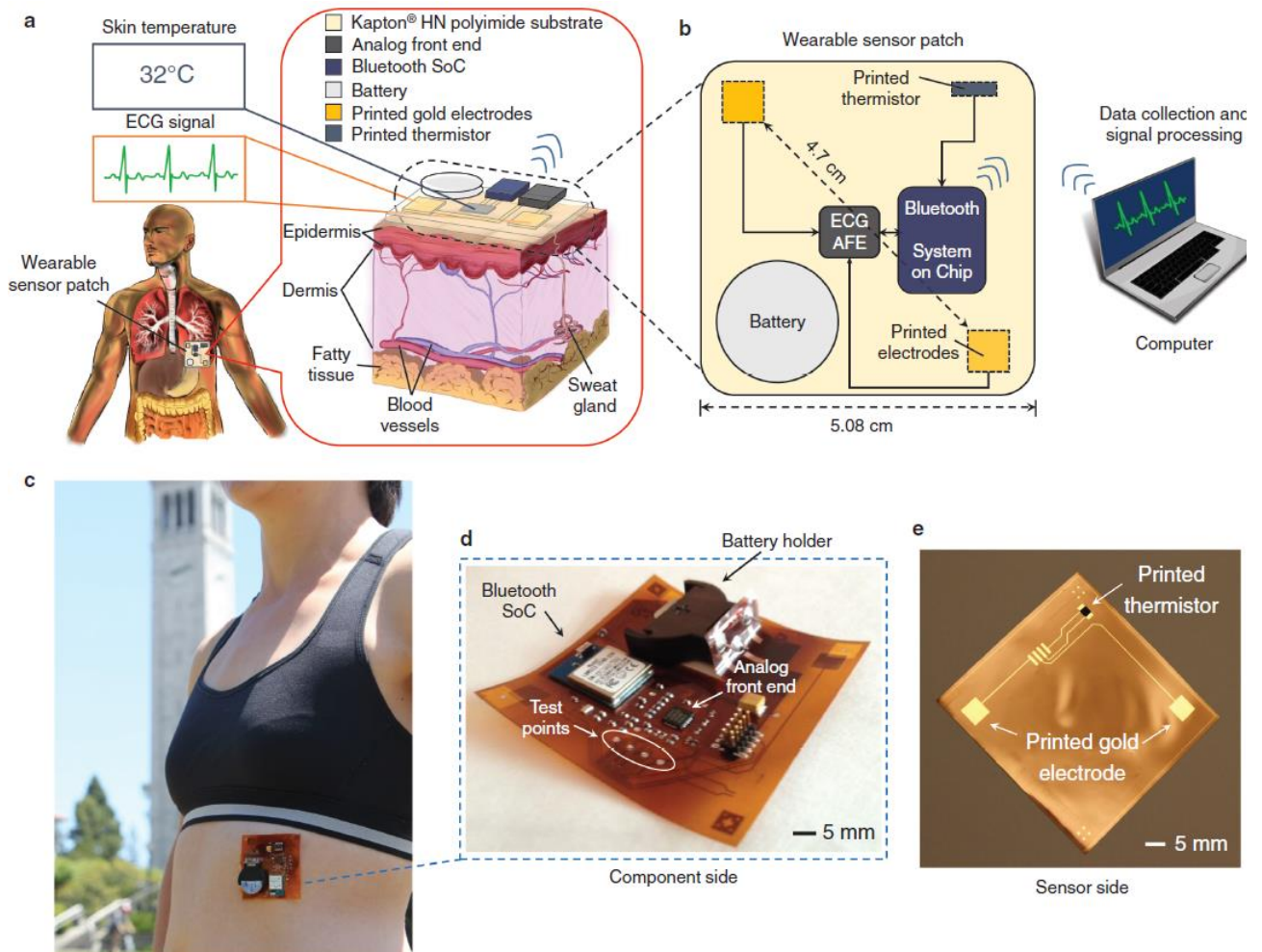


Figure 2.21: (a) Schematic of the proposed sensor patch attached on a person's lower left rib cage. Skin temperature is read via printed thermistor, and ECG signals are acquired via printed gold electrodes. The electrodes and thermistor are integrated into a silicon-based polyimide substrate for data acquisition and signal processing and transmission; (b) System architecture of the proposed hybrid sensor patch with a wireless system on chip; (c) Image of the wearable sensor patch is attached onto the subject's lower left rib cage; (d) Image of the component side of the proposed wearable patch; (e) Image of the sensor side of the proposed wearable hybrid patch. The printed gold ECG electrodes and the thermistor are shown. [36, 44]

Another application for measuring ECG of children with autism spectrum disorders (ASD) in the living environment is done by Takahashi et al [45] using textile electrodes within a wearable ECG monitoring device. The proposed device is developed in a clothe, and the ECG measurements were done through the wrists. During the tests, the ECG signals of three children with ASD were captured, and R-R intervals were obtained with high reliability (90% of the duration of tasks). Due to having difficulties for measuring a perfect ECG signal (including all morphologies), the group has focused on the R-R intervals from ECG signal regarding the mental stress by adopting a bipolar lead from three electrodes at two different places on the body. Figure 2.22a illustrates the system overview of the proposed device on the clothe, and also Figure 2.22b shows ECG waveforms

including captured R-R intervals using the Pan-Tompkins (PT) algorithm [46]. Regarding the experimental studies, three children with ASD wore the cloth with the proposed integrated device for the whole session (~60 min) under different therapeutic tasks (motor imitation, card selection, vocal imitation, exercise, manipulation, reading, playing). The results showed that the tasks of card selection and reading revealed measurements rates of over 90% for the all participants.

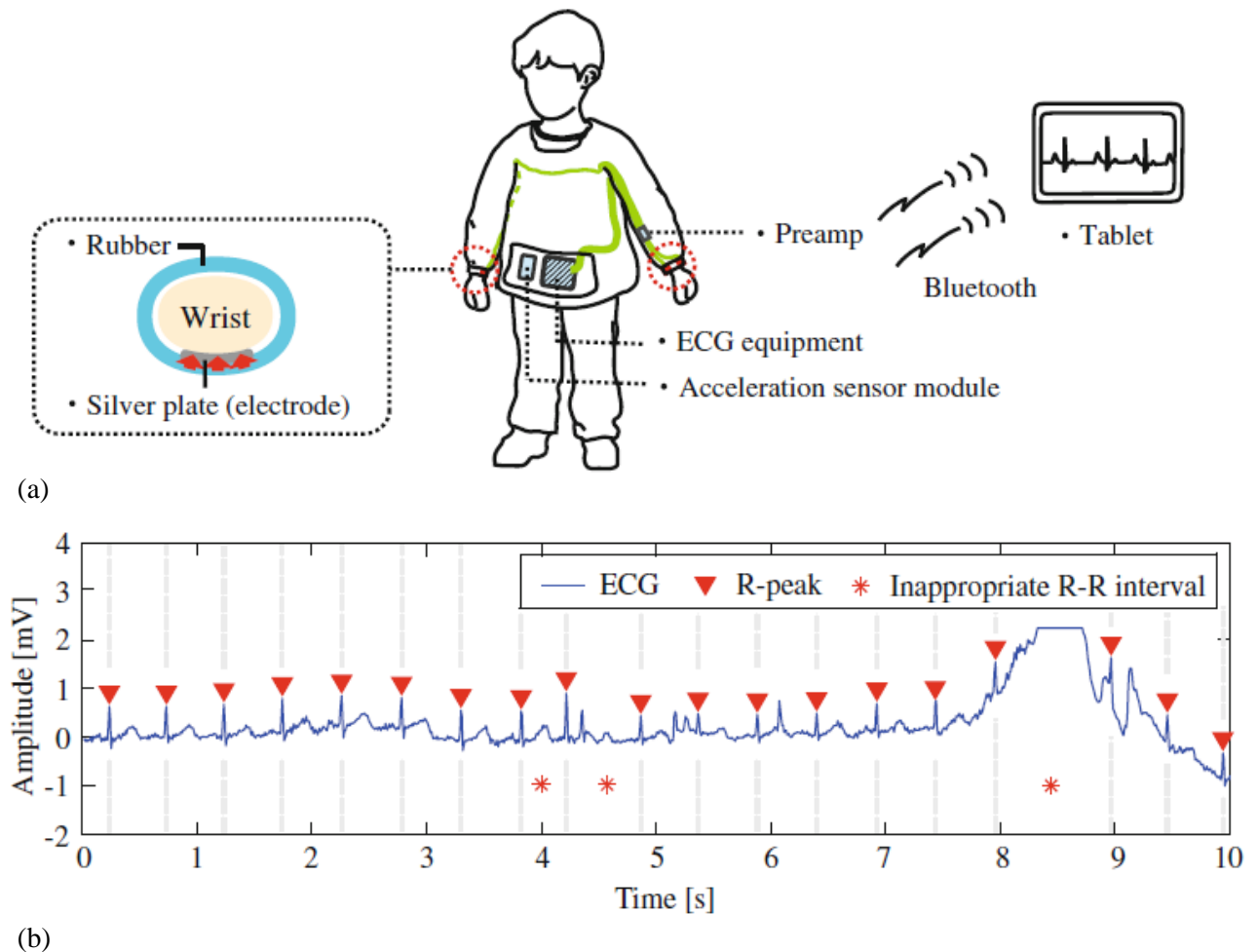


Figure 2.22: (a) System overview of the proposed device that measures ECG signals at the wrist and ECG signals are transmitted to a tablet via Bluetooth connection; (b) ECG waveforms using the proposed device within PT algorithm and range detector [45]

Liu et al [47] demonstrated the concept of carbon nanotube (CNT) based self-adhesive polymer electrodes integrated with a wireless long-term ECG monitoring system. The fabrication process of the proposed polymer electrodes was based on loading high proportion of CNTs in PDMS, which was filled onto the holes of the electrode, as a layer of adhesive PDMS. Additionally, silver nanoparticles (Ag NPs) was used to increase the electrical conductivity of the electrodes and flexibility of the polymer. Figure 2.23b indicates the schematic of fabrication process of proposed CNT-based PDMS electrode within different layers. Wireless transmission was done through a radio frequency (RF) module to monitor ECG signals remotely in a mobile phone. Experimental

results exhibited that the skin-electrode contact impedance of developed adhesive CNT based polymer electrode was higher than that of the wet conventional Ag/AgCl electrodes due to the lack of the gel. The impedance values varied from 6.7 M Ω to 89 k Ω and 1.1 M Ω to 11 k Ω for the proposed CNT-based and Ag/AgCl electrodes, respectively, in the frequency range between 5 Hz and 1 kHz. For ECG measurements, the developed CNT-based three-electrode patch was attached onto the chest for five subjects during the tests. Figure 2.23a shows the comparison of ECG signals obtained by wet Ag/AgCl electrodes and proposed CNT-based polymer PDMS electrodes. Despite having similar ECG signals from both type of electrodes, the signal amplitude with the proposed CNT-based electrode was lower than that of the wet Ag/AgCl electrodes. The average amplitude of R-wave was 0.89 V and 0.98 V for the CNT-based PDMS and wet Ag/AgCl electrodes, respectively. Furthermore, this research group has also examined the long-term recording of the proposed polymer electrodes by detaching and re-attaching electrode patch after each day for 11 days. After 5 days, there was no significant variations on the obtained ECG signals, however, the signal has started to float during walking in the 6th day (6th attachment) due to decreasing of adhesion force, thus the electrode-skin contact was poor and motion artifacts became evident.

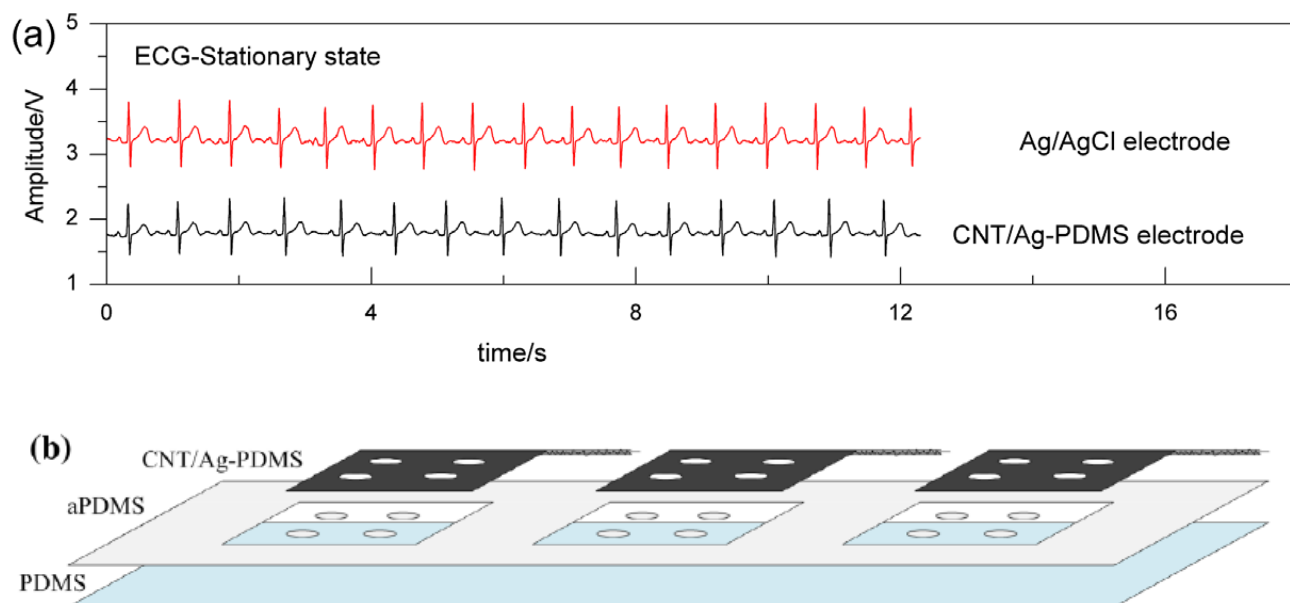


Figure 2.23: (a) Recorded ECG signals at the stationary state with conventional Ag/AgCl electrodes and proposed CNT polymer electrodes for comparison; (b) structure of the proposed ECG electrode patch composed of a PDMS layer, an aPDMS layer and the proposed CNT polymer electrodes [47]

Regarding recent methods of capacitive coupling ECG signals, Mathias et al [48] designed a non-contact ECG electrode through micro-electromechanical systems (MEMS) process. The developed ECG electrode is designed as 3 layers: a reference copper plate; an insulating material; and a sensing plate. The electrode lead wires were coaxially formed to block wires from coupling to

ground or other electronic components. The proposed ECG electrode has an area of 2.324 cm^2 , and could obtain the signal at about $500 \text{ }\mu\text{m}$ distance from the subject's chest. Le et al [49] presented a mobile ECG monitoring device using two active dry electrodes. Normally, three-electrodes are used for acquiring good ECG signals, however, here two-electrode setup is designed and a digital notch filter was embedded into the circuit to reduce the power-line noise due to absence of third electrode. Furthermore, high impedance effect was reduced by a unity gain amplifier, which also reduced the interference from the environment. Regarding the experimental work, the proposed device was tested with 30 people to show heart rate values by comparing results with commercially available Omron HEM-7111 device. The results from the two devices showed nearly similar heart rate values, by making the correlation factor of 0.9914. Moreover, the group has investigated the quality of ECG signals of proposed ECG device using active dry electrodes in comparison with passive dry electrodes. The studies showed that acquired ECG signals by passive dry electrodes were less reliable than that of the active dry electrodes. Acquired R peaks using passive electrodes were around $0.555 \pm 0.034 \text{ mV}$, on the other hand the R peaks of active dry electrodes were more stable at around $0.558 \pm 0.034 \text{ mV}$.

In a recent work, Kim et al [50] developed a concept of conductive dry adhesives (CDA) that is based on gecko-inspired Si architectures and nanocomposites. Unlike the current dry adhesives, the group has studied here in CDA by combining carbon nanofillers and PDMS in a conductive elastomer. Two different forms of carbon nanomaterials, composing of a 1-dimensional (1D) CNT, and a 2-dimensional (2D) graphene (GN) nanopowder, were mixed into an elastomeric matrix for increasing electrical percolation. Figure 2.24a-e shows the concept, fabrication and functionality of the proposed conductive dry adhesives (CDA). The polymer PDMS layer embedding 1D-2D carbon nanocomposites with a low loading rate ($\sim 1 \text{ wt } \%$) is distributed on the Si surface and filled into high-aspect-ratio holes (Figure 2.24a). The proposed CDA pad can also be wrapped on various surfaces and different places on the human body due to its flexibility and stretchability (Figure 2.24c-d). Furthermore, an LED experiment is done through the CDA pad as an electrical linkage with a weight of around 1kg (Figure 2.24e). Regarding the electrical characteristics of the proposed device, the CDA pad has achieved $\sim 1 \text{ S/m}$ electrical conductivity which is enough to obtain biopotentials from a human skin [51] at low carbon nanofiller content ($\sim 1.0 \text{ wt } \%$). Regarding the experimental work, Figure 2.24f demonstrates the comparison of the ECG signals using the proposed CDA pad, and wet Ag/AgCl electrodes with 3M adhesives under normal conditions. Both type of electrodes achieved to indicate all morphologies of an ECG signal (P waves, QRS complex, and T waves). Figure 2.24g shows that the CDA pad was active underwater and biopotentials were still being acquired from the body with decreased amplitudes in an underwater environment,

however, conventional wet type of electrodes were detached from the body and biosignals were lost within 5 secs. In addition to this, proposed conductive dry adhesive based electrodes were tested in a series of movement conditions (wrist curl, squat, and writing), and the results revealed that ECG signals were still monitored during the tests including all available waveforms (see Figure 2.24h).

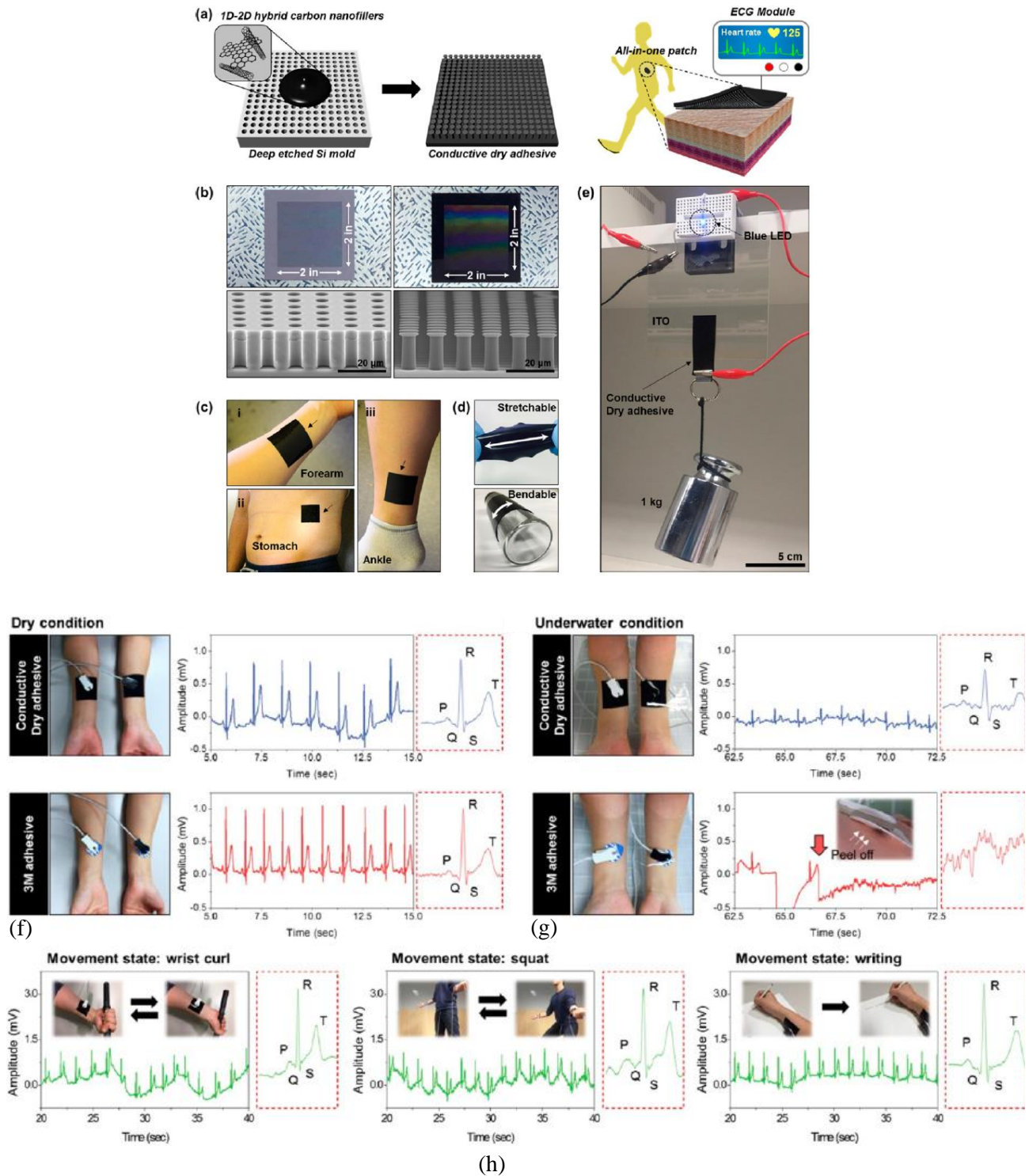


Figure 2.24: (a) Schematic images of the proposed procedure of conductive dry adhesives (CDA) within ECG application; (b) Digital images of a large-area silicon mold with replicated CDA (~ 4 in²); (c) Images of CDA attached on different locations on the body (i: wrist, ii: stomach, iii: ankle); (d) Images of the

stretched and banded proposed CDA; **(e)** Image of an LED application using proposed CDA; **(f)** Comparison of the ECG signals using CDA and wet Ag/AgCl electrodes under normal conditions (inset in the red box: magnified view of the recorded ECG waveform); **(g)** Comparison of the ECG signals using CDA and wet Ag/AgCl electrodes under an immersed condition; **(h)** Series of ECG recordings using CDA under various body postures [50]

As we can see here, carbon-related materials have been used in several times for manufacturing ECG related electrodes. Another example to this, Thap et al [52] proposed novel ECG electrodes that were capable of acquiring signals under fresh-water, and salt-water conditions using Graphite, which is an allotrope of carbon and is also used in bio-mechanical manufacturing as an electron moderator [53]. Two-type of electrodes were developed based on graphite pencil leads: (a) pencil lead solid (PLS) type, and (b) pencil lead powder (PLP) type electrodes. Fabrication of PLS type of electrode was done by using 4B pencil leads which were cut into pieces and then these cutting leads were flattened to form a rectangle shape and so that a circular graphite based pencil lead was carried out after several chemical functions. On the other hand, PLP type of electrodes were synthesized through similar method by using graphite based 4B pencil leads as raw materials. After that, the pencil leads were peeled and grinded into a powder solution. After mixing with chemical bonds, the powder-pencil solution was poured into a cylindrical tube until to make it a flat and smooth surface. Figure 2.25g-h shows the both proposed type of electrodes which were fabricated with a diameter of 10 mm, and a thickness of 1mm which is the same size as the commercially available wet Ag/AgCl electrode for this study to compare all 3-type of electrodes. Experimental work was done by investigating the performances of the proposed PLS and PLP electrodes and comparing them with that of wet Ag/AgCl electrode in seven different conditions: dry, fresh-water immersion with/without movement, post fresh-water wet condition, salt-water immersion with/without movement, and post salt-water wet condition. Experimental results revealed that all ECG recordings were clearly visible (including PQRST waves), with all type of electrodes, under both dry and post fresh-water wet conditions. It was also observed that the proposed PLS and PLP electrodes exhibited better ECG signal quality than conventional Ag/AgCl electrode under the fresh-water and salt-water immersion with/without movement, and post salt-water wet conditions. Figure 2.25a-f illustrates the recorded ECG signals using all three-type of electrodes under different conditions. Furthermore, the skin-electrode contact impedance measurement was done for all PLP, PLS and conventional Ag/AgCl electrodes. Impedance characterization showed that the impedance of proposed graphite-PLP electrodes was lower than that of proposed graphite-PLS electrodes and conventional Ag/AgCl electrodes. The skin-electrode contact impedance was 49.47 k Ω , 51.37 k Ω , and 86.12 k Ω for graphite-PLP, and PLS, and conventional Ag/AgCl electrodes, respectively, at 40 Hz.

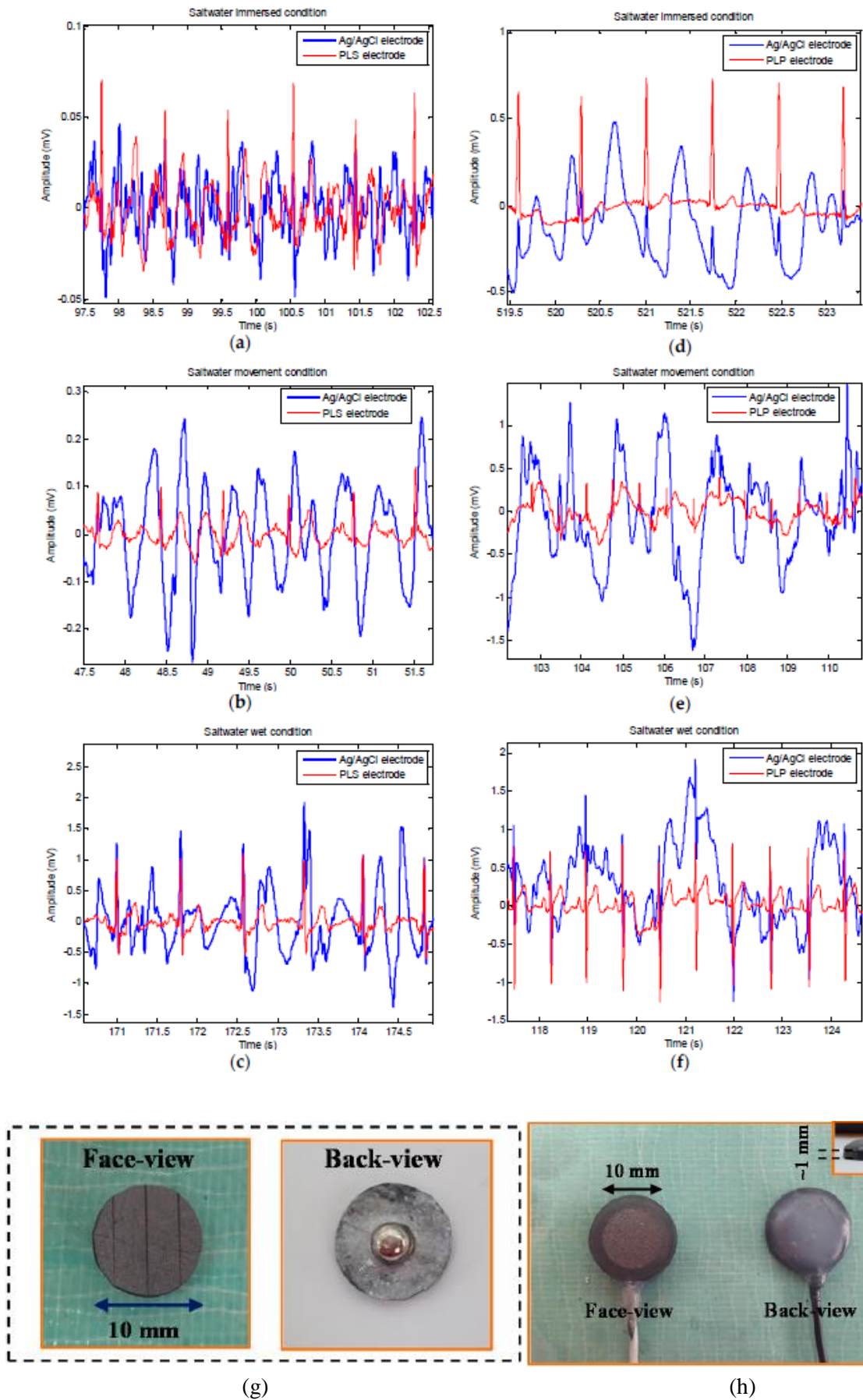


Figure 2.25: Recorded ECG signals: (a-c) for comparison between proposed PLS type of electrode and wet Ag/AgCl electrode; (d-f) for comparison between proposed PLP electrode and wet Ag/AgCl

electrode. Saltwater immersed condition: **(a, d)** without movement; and **(b, e)** with movement; **(c, f)** Saltwater wet condition; **(g)** pencil lead solid-type (PLS) electrode; **(h)** pencil lead powder-type (PLP) electrode [52]

Among graphite and carbon-related nanomaterials, graphene (GN), which was recently invented by Geim and Novoselov [54], has received heightened attention for its exceptional physical, mechanical, electrical, chemical, and optical properties that lead to the wide range of applications from electronics to biomedicine [55, 58]. Recently, Yapici et al [59] developed conductive graphene (GN) textile electrodes using dip-dry-reduce process for biosignal acquisition in cardiac monitoring. The proposed electrode was fabricated by dipping nylon fabric in a graphene oxide (GO) solution, and the GO was chemically reduced into reduced graphene oxide (rGO) followed by a thermal treatment to allow dry process by coating with conductive GN layers around the fabric (see Figure 2.26a). The proposed GN-clad conductive textile electrode exhibited an electrical conductivity of 450 S/m, and it remained to form five cycles of washing. Regarding experimental results of this work, performance of the proposed GN-based textile electrodes were compared to the conventional Ag/AgCl electrodes in terms of ECG signal quality and skin-to-electrode contact impedance. Figure 2.26b shows recorded ECG signals using both proposed GN-clad textile and conventional Ag/AgCl electrodes with a cross correlation of 97% between the signals. Moreover, the proposed textile electrode-skin impedance ranged from 87.5 k Ω to 11.6 k Ω for frequencies swept from 10 Hz to 1 kHz, which was larger than that of the conventional Ag/AgCl electrode (varied between 50.9 k Ω and 2.2 k Ω at the same frequency range). Recently, the same group [191] developed a fully-wearable medical garment for mobile monitoring of cardiac biopotentials from the wrists and the neck using GN-functionalized textile electrodes. Comparison of the ECG recordings obtained from the wearable prototype against conventional wet electrodes indicated better conformity and spectral coherence among the two signals. Ameri et al. [192] demonstrated a GN-based epidermal sensor system with total thickness below 500 nm. The proposed system is fabricated by the cost-effective method on tattoo paper and can be laminated on human skin. Without any tape or adhesive, the proposed GN-based epidermal sensor system has been successfully applied to measure ECG, EEG, and EMG with comparable SNR to that of obtained by Ag/AgCl electrodes. In a recent work, Lou et al. [193] produced a flexible GN-based dry ECG electrode and a portable wireless measurement system. The experimental results in this work exhibited that the proposed GN-based dry electrode was able to acquire the typical waves and features of ECG signals with a high SNR in different states of motion. In addition, a week-long continuous measurement test showed no degradation in the ECG signal quality over time, in which it is useful for long-term ECG monitoring.

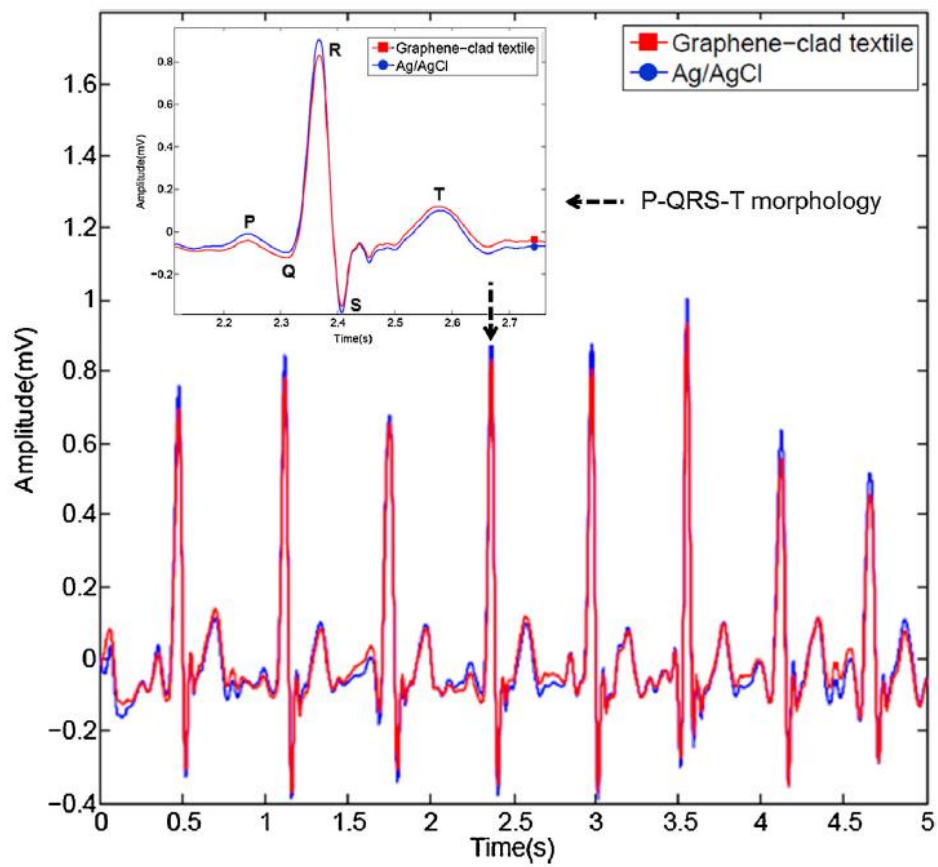
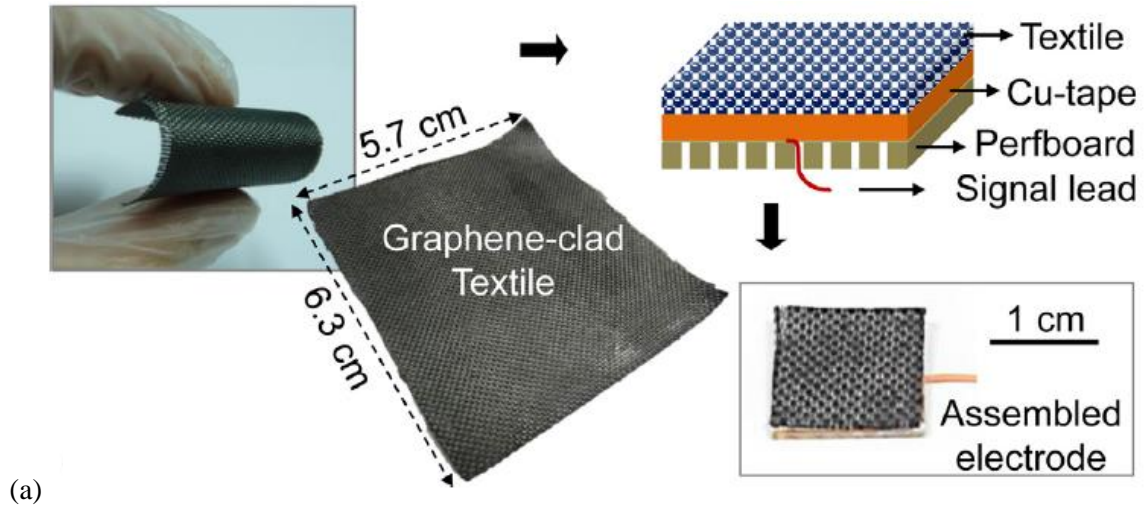


Figure 2.26: (a) Images of a sample of flexible nylon-based proposed textile with rGO coating with area of 35.91 cm^2 ; (b) recorded ECG signals after filtering with conventional Ag/AgCl electrode and proposed GN-clad textile electrodes. P-QRS-T waves are shown as one cardiac in the inset [59]

2.2 Review of body signal acquisition systems using different type of wearable sensors

In this section, various wearable health monitoring systems will be reviewed using different types of body-worn sensors. The combined information obtained from body sensors, such as ECG, EEG, CBT, PPG, can be transferred to a healthcare server in the case of emergency or can be stored and investigated as a part of preventive health issues. In this regard, Mundt et al [60] developed a wearable multi-parameter ambulatory physiologic monitoring system, called 'LifeGuard', for space and terrestrial applications. The proposed system provides the capability to measure two ECG leads, respiration rate via impedance plethysmography, heart rate, oxygen saturation (SpO₂), body temperature, blood pressure, and body movement. Commercially available sensors are used to record these physiological signals and are communicated via wired connections with the crew physiologic observation device (CPOD) data logger. The obtained physiological information can be continuously recorded for 9 hours on a memory card or transmitted to a base station using Bluetooth connection. Experimental works demonstrated that biosignals (SpO₂ and heart rate) were measured in real-time satellite data streaming while CPOD was connected to the serial port of a tablet PC. Paradiso et al [61] proposed a wearable healthcare system by integrating fabric sensors, conducting and piezoresistive materials on vest-like garment to measure and monitor ECG, electromyogram (EMG), abdominal respiration rate, skin and core temperature, and body position and movements. The proposed system, called 'WEALTHY', is targeted for clinical patients such as elderly people and individuals with chronic diseases. The developed miniaturized system is integrated into shirt-garment and used to transmit the biosignals wirelessly to PCs, PDAs and mobile phones. The proposed algorithm is capable of generating alert messages to deliver appropriate health information to the doctors and patients.

In another project, Shnayder et al [62] developed a platform, called 'CodeBlue', to address issues of reliable communication between medical sensors and multiple receivers achieved by health professionals at Harvard University. The researchers have developed several medical sensors for multiple-patient-monitoring systems based on the ZigBee-compliant MicaZ [63] and Telos [64] motes, including pulse oximeter, three lead ECG, and motion activity sensor. A software algorithm also has been implemented to enable requests for specific biological data from a specified network node. Additionally, CodeBlue incorporated a decentralized RF-based localization system to be able to accurately locate patients, doctors or other caregivers for remotely medical purposes. Likewise, Pandian et al [65] presented a wearable physiological monitoring system which, is a washable shirt, called SmartVest, that consists of a vest and a variety of sensors integrated into the garment's fabric to continuously monitor physiological signals, such as ECG, PPG, heart rate, blood pressure (BP), body temperature and galvanic skin response (GSR). The proposed wearable system was

implemented using microcontroller and wireless communication within global positioning system (GPS) modules. The collected biosignals are sampled at 250 samples/s, digitized at 12-bit resolution and transmitted wireless to a remote monitoring server along with the geo-location of the subject. Figure 2.27 shows schematic of the proposed wearable multi-parameter remote monitoring system including proposed device. SmartVest is designed by high-pass, low-pass, and notch filters to enable recording ECG signals without the use of gel and free of baseline noise and also motion artifacts. BP is extracted using a detection algorithm that individually calibrates based on the subject's ECG.

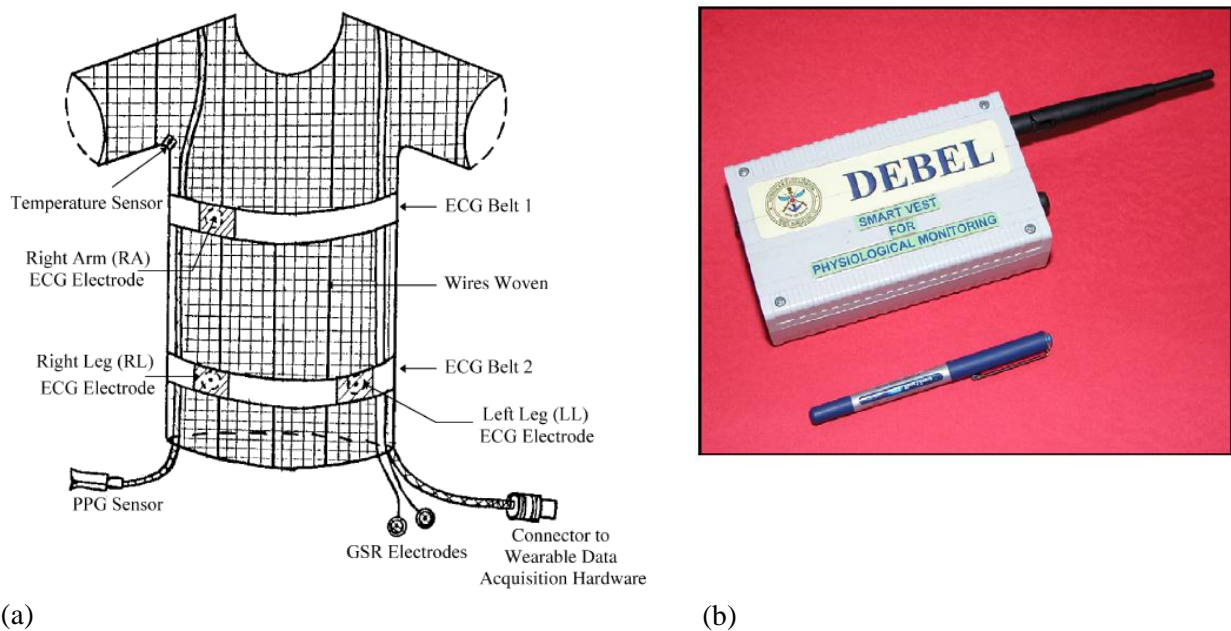


Figure 2.27: (a) Integration of sensors at specific locations in the proposed SmartVest; (b) Prototype of the developed wearable data acquisition hardware [65]

As an example of mobile wearable monitoring system, Kwon et al [66] developed a smartphone-integrated ECG recording platform, called ‘Sinabro’, which monitors the user’s ECG opportunistically during daily smartphone use. Based on this opportunistic ECG sensing theory, the ECG sensor is designed in the form of a phone case that can be integrated with a smartphone for unobtrusive sensing. The multiple electrodes are placed mostly at the corners, front, and back of the smartphone, which could allow maximal opportunities for ECG measurement when a user touches the phone with two body limbs during daily use, such as two hands when sending a text message or an ear and a hand when making a phone call. Sinabro is a collaborative system that includes the phone-case sensor and the smartphone middleware. The sensor reliably measures ECG data and transfers it to the middleware. The middleware delivers diverse ECG-derived contexts to multiple apps with Sinabro APIs. A similar mobile-based healthcare monitoring platform is carried out by Yap et al [67] using multiple body-worn sensors. As can be seen in Figure 2.28, the ECG sensor is

attached to user's chest area to record ECG signal, on the other hand, the ear pulse oximeter sensor is clipped to user's ear lobe, and finger pulse oximeter is clipped to user's thumb to obtain PPG signal. Due to the integration of K mote technology for ear and finger pulse oximeter sensors, both of the PPG signals are sampled and transmitted to portable base station via Zigbee transmission. After that, collected and processed ECG, ear PPG, and finger PPG signals are sent to user's mobile device in real-time and simultaneously to display on an application. Furthermore, smartphone uploads the physiological signals to a server via Bluetooth connection. In the server side, a healthcare-monitoring algorithm is developed to display vital signals graphically for analyzing them to prevent any further serious medical issues.

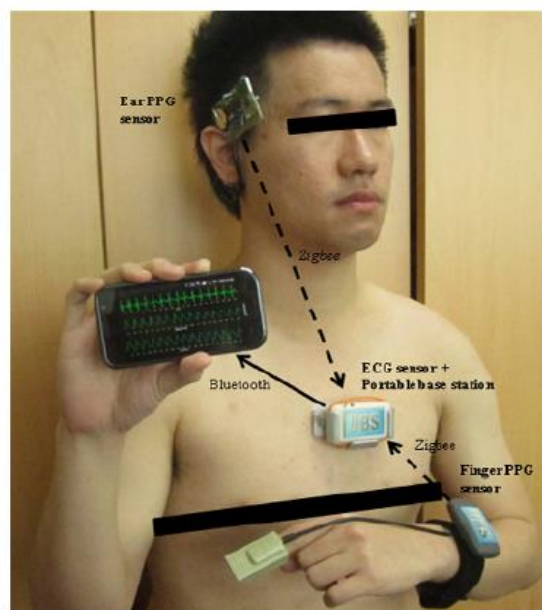


Figure 2.28: Demonstration of Mobile healthcare monitoring system using portable base station, including ear PPG, finger PPG, and chest ECG sensors [67]

Lin et al [68] studied a wearable PPG sensor module for a driver's physiological monitoring system based on a Programmable System on Chip (PSoC). A couple of sensors are used for this work: (a) an optical sensor within magnetic rings for PPG measurement; and (b) a three-axis accelerometer (G-sensor) is used to detect head status. The sensor module is placed on the earlobe, and signal acquisition and analog circuits are designed in PSoC. Furthermore, a heart rate (HR) detection method is implemented derived from the Peak-Peak interval of PPG waveforms. The PPG data along with HR and head status are then transmitted to the smartphone for displaying health data via Bluetooth. According to their work, when the abnormal HR is detected, the smartphone will trigger the sound and vibration unit to alert the driver. This project is expected to reduce the traffic accidents due to the drivers' physiological movements or health problems. Sanches et al [69] proposed a headset Bluetooth device for continuously monitoring core body temperature (CBT) at

the ear in the characterization and diagnosis of sleep disorders. An electronic temperature sensor (LM334) is fixed into the microphone of commercially available auricular Bluetooth device that continuously transmits the measured CBT at the inner ear to a paired mobile phone. Afterwards, the stored temperature data can be transferred periodically to a medical server for further analysis by email or SMS service. The proposed device is tested on a subject for 24 hours and results revealed that the ability of the system to record even small temperature changes along the circadian cycle. Another outcome from the tests also is that the maximum current consumption of the electronic thermometer was about 3 mA, which allowed reading around 500 samples in total test. Song et al [70] also developed a body monitoring system, which is a combination of measuring CBT, EEG and ECG, based on a smartphone via Bluetooth. They used infrared thermopile sensor [71] for monitoring CBT and the collected health data are stored in an SD card which is inserted in the Android based smartphone.

New studies have illustrated that ear-worn devices will bring high attention into the wearable technology due to ability of unobtrusive and comfortable design. Furthermore, as proven by hearing aids and headsets, the ear is a location for anchoring the devices. This could advance to device attachment without the need of adhesives [72]. Poh et al [73] proposed an ear-worn PPG monitoring system, called 'HeartPhones', that involves a reflective photo sensor which is integrated into each earbud on a pair of regular earphones. To obtain PPG measurements, a PPG peak detection algorithm is developed, thus the data can be monitored in 90 ms segments and can be extracted from the threshold values to avoid false peak detections. After sending raw PPG waveforms, average HR is also derived from algorithm and sent to the mobile device via serial communication for visualization and further processing. Alternatively, the measured PPG data can be transmitted wirelessly using a pair of wireless 2.4 GHz radio transceiver module. Figure 2.29 shows the proposed Heartphones system including wireless receiver unit. The proposed PPG sensor earphones have been tested on 31 healthy subjects, and obtained HR measurements. Furthermore, participants have been asked to attach adhesive Ag/AgCl electrode to their chests to record ECG signals as reference HR measurements. Experimental results exhibited that the recorded HR measurements using the proposed Heartphones system have agreed with 95 percent to those obtained via ECG adhesive electrodes.

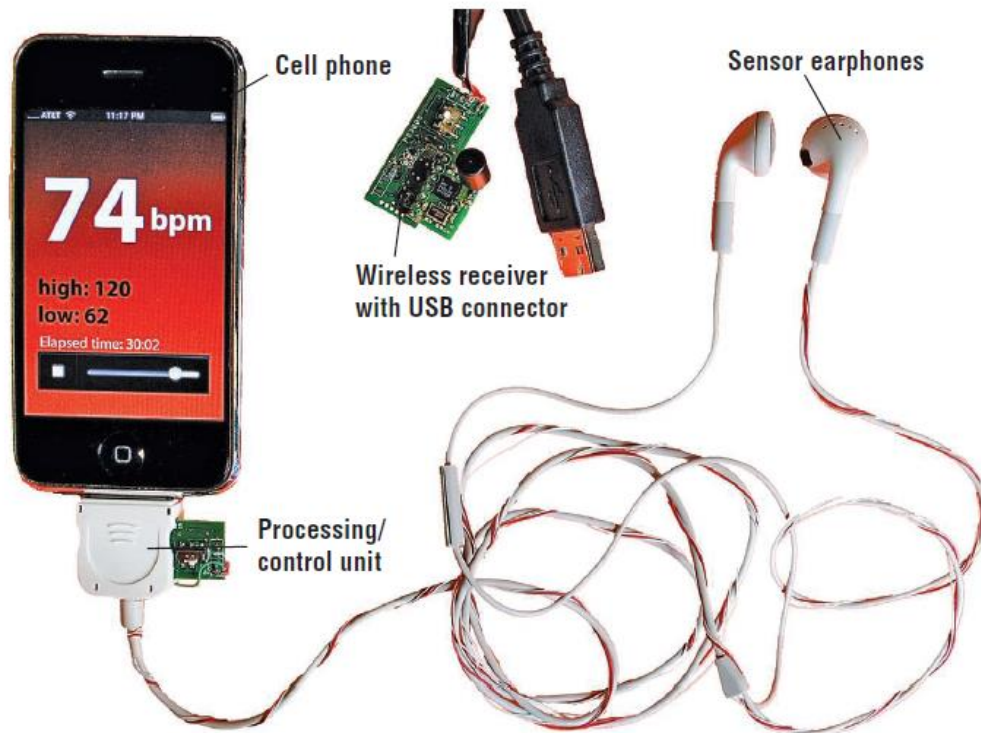


Figure 2.29: Prototype of the Heartphones system which is either can be connected to smartphone via serial connection, or to PC via wireless link [73]

Similarly, Da He et al [74] developed a compact multi-parameter monitoring device that measures ECG, ballistocardiogram (BCG), which is a measure of the body's reaction force to the blood expelled by the heart [75], and PPG at the ear. Furthermore, a heart rate (HR) algorithm is developed using all measured three signals and the proposed monitoring device has been tested on 13 healthy subjects in a clinic to verify recorded data. Experimental studies showed that periodic head movements, as a type of BCG, have been identified and also HR can be extracted using cross correlation with all measured BCG, ECG, and PPG signals. Figure 2.30 indicates the proposed ear-worn wearable device along with measured ECG and PPG signals from behind the left ear. It can clearly be seen in Figure 2.30b that the obtained ECG signal only shows R peaks and other critical waves such as P-wave, QRS complex, and T-wave are not visible due to lack of DRL electrode in ECG measurement setup. However, the proposed design is consisted of multiple physiological sensors that practically achieved to acquire ECG, BSC, and PPG from the ear within a design perspective of hearing aid.

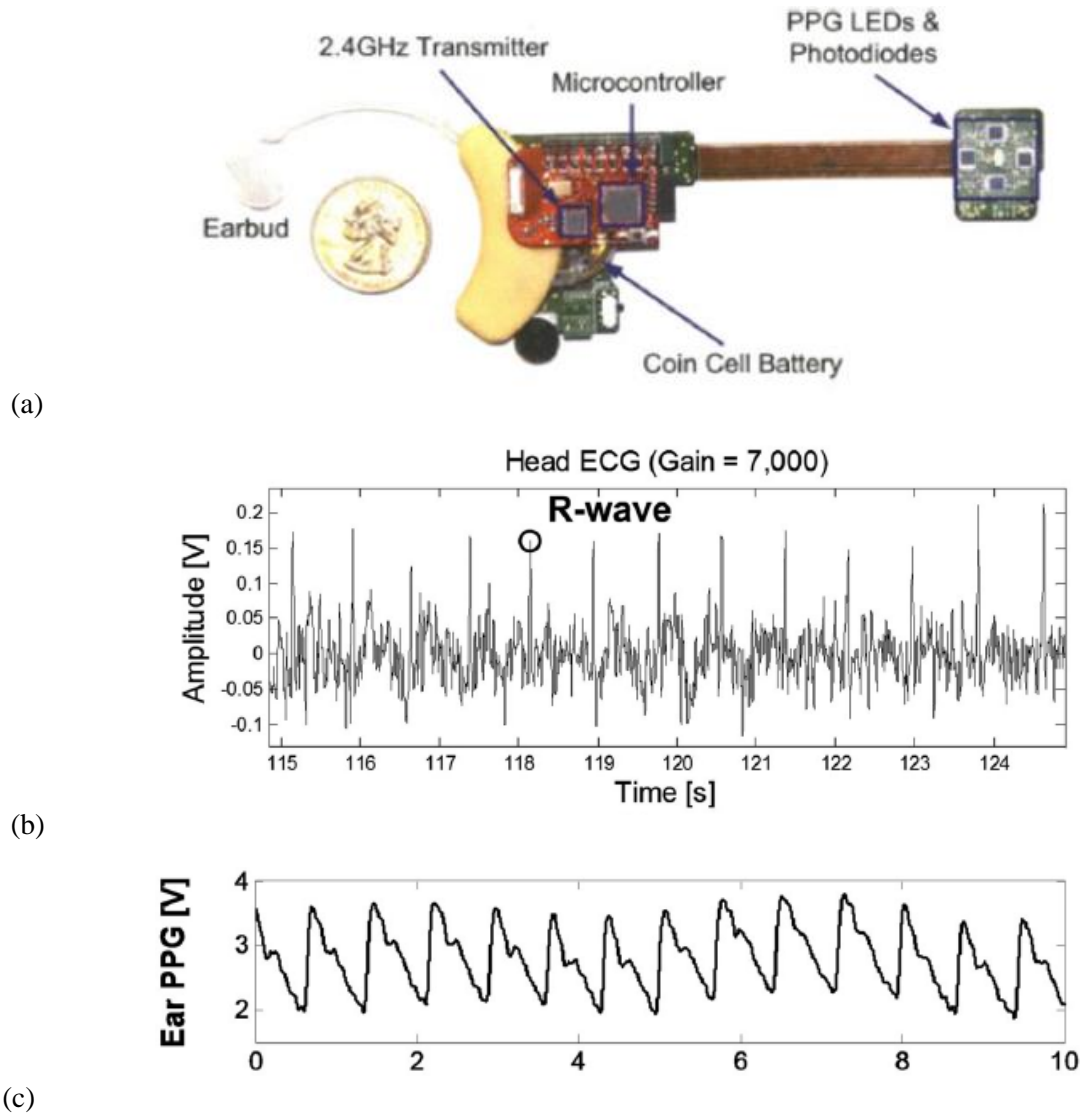


Figure 2.30: (a) Prototype ear-lead wearable system that includes ECG, PPG, BCG circuits; (b) ECG measured from mastoid area behind the left ear; (c) PPG taken from the mastoid area [74]

Lochner et al [76] presented all-organic optoelectronic pulse oximetry probe composed of solution-based OLEDs and a printed organic photodiodes. The proposed organic optoelectronic devices were implemented using flexible plastic substrates that enable a conformal way for fitting to human body. In the developed pulse oximeter, an OLED emits in the red spectrum with 626 nm peak wavelength, and other OLED emits in the green spectrum with 532 nm peak wavelength. The organic optoelectronic pulse oximeter is integrated with the traditional electronics at 1 kHz and monitored HR and SpO_2 are calibrated and compared to those recorded by commercially available pulse oximeter. Experimental results revealed that low error rate (1%) is observed for pulse rate, and 2% error rate is observed for SpO_2 when comparing the organic optoelectronic sensor with the commercial one. The calculated HR is derived from PPG signals from organic optoelectronic sensor probes are around 65-70 beats per minute (BPM). Xu et al [77] developed a thin, conformable band aid form the device softly attached onto the skin to monitor physiological signals, including ECG,

EMG, and EEG. The proposed multi-sensory device ($\sim 1.7 \times 1.8 \text{ cm}^2$) was consisted of electrodes, electronic circuits, and radios for wireless communication in a soft microfluidic assembly. Figure 2.31 a-b shows the proposed sensor system attached onto the skin, Figure 2.31 c-d shows the obtained ECG signal, respectively, using the proposed flexible sensory system. The total power consumption of the proposed system is $\sim 35 \text{ mW}$. Results clarified that recorded ECG signals included visible all waveforms, P waves, QRS complex, and T waves. Due to ECG signal being periodic, the HR also can be obtained from the R-R intervals of the ECG signal.

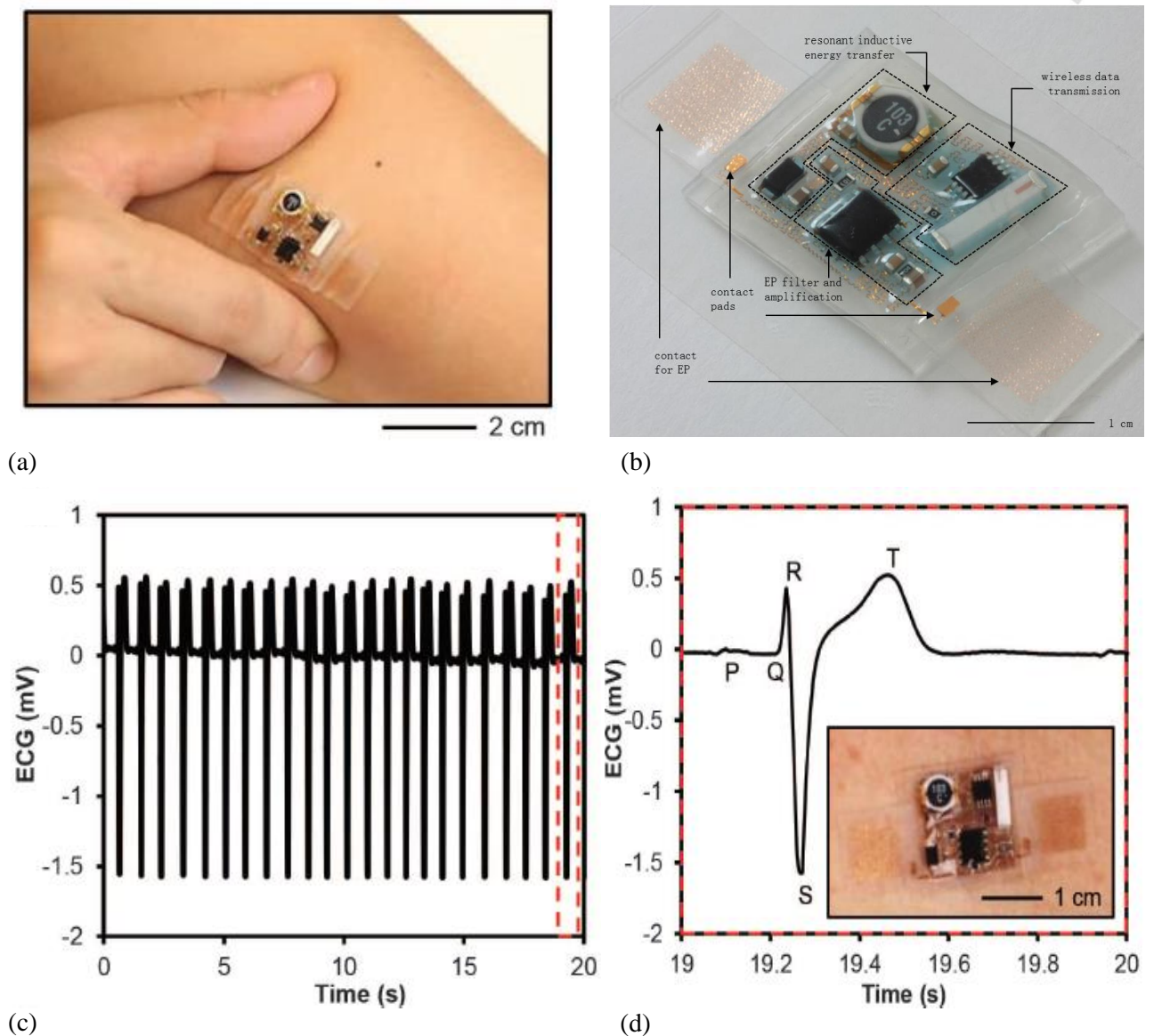
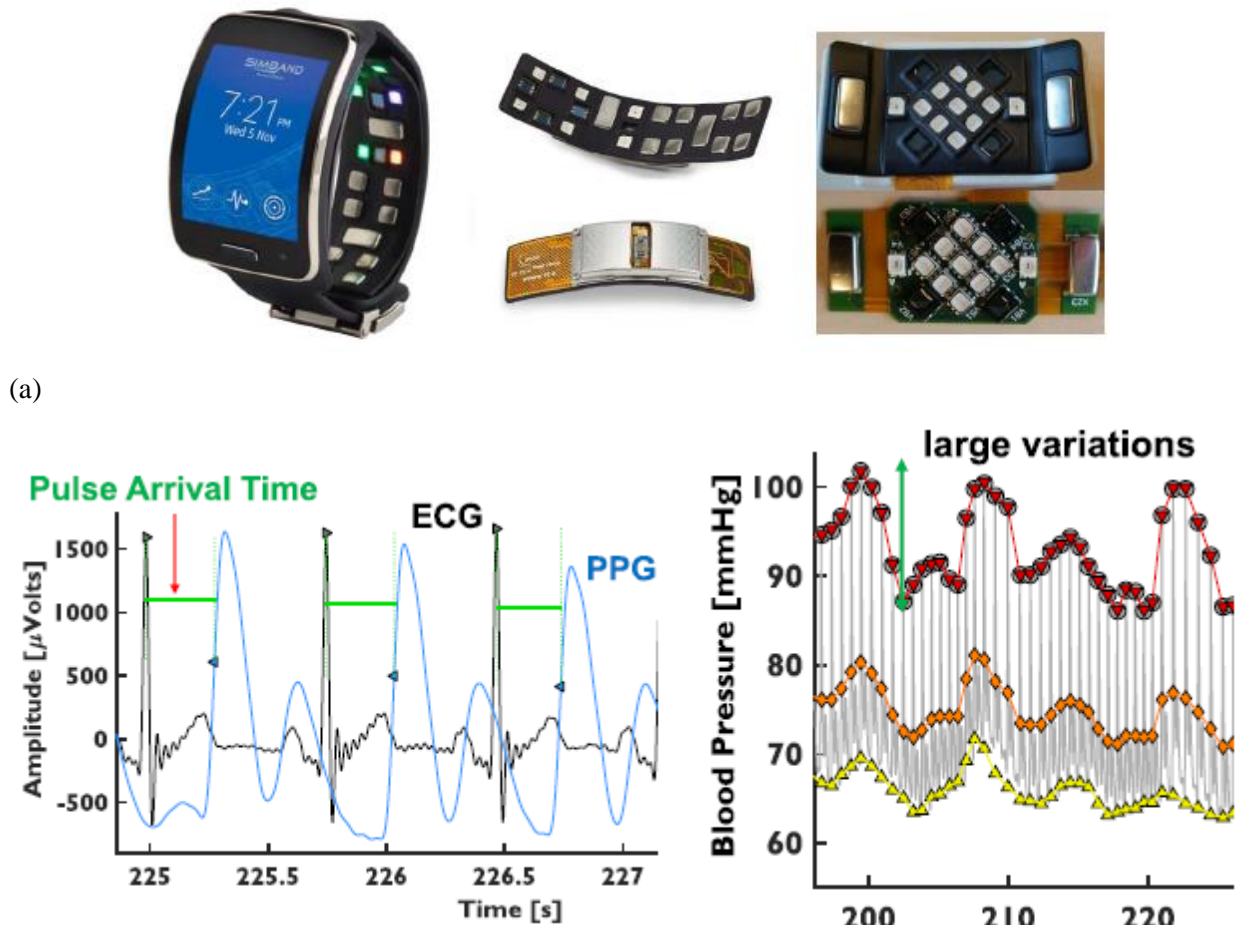


Figure 2.31: (a) Optical image of the proposed device on the forearm; (b) Optical image of the proposed device with labels for different parts and modules in the circuit; (c) ECG acquired by using the proposed device mounted on the sternum; (d) a detailed view of P-QRS-T complex acquired from the ECG signal [77]

Kakria et al [78] demonstrated a real-time monitoring system that consists of a wearable sensor, mobile device, and a web interface to carry out recording of HR, BP, and body temperature. The commercially available wearable sensors have been used to acquire these physiological signals, which are then transmitted to an Android based mobile device wirelessly using Bluetooth. Afterwards, the gathered multiple health data on the smartphone is transferred to a web interface via WiFi or 3G system. Furthermore, the proposed remote wearable system generates the emergency alerts to the doctor or health assistant in case of abnormalities such as arrhythmia, hypotension, fever, and hypothermia. The proposed system has been tested on 40 cardiac patients in order to evaluate the practical implementation. The results exhibited that the proposed real-time monitoring system is validated and was sending alerts if recorded HR was higher than threshold value for tachycardia patients ($\sim \text{HR} > 100 \text{ BPM}$). However, false alarms have also been observed due to the battery issues of sensors during the tests in the proposed system. Another multi-parameter physiological acquisition module is developed by Kim and Ko [79] for low power wearable systems. They have presented a low noise reconfigurable analog-front-end (AFE) system which can be used in ECG, bioimpedance, EMG, EEG, and PPG sensory systems. The power consumption of the AFE in one readout channel is less than $52 \mu\text{W}$. Regarding experiments, a lead I ECG signals were acquired along with blood glucose levels to validate the proposed system. The results showed that the proposed multimodal reconfigurable system for several biosignal monitoring applications can reduce the required number of electronic chips.

Recently, Konijnenburg et al [80] developed a multi-parameter biosignal acquisition system with five dedicated channels: (a) ECG, (b) bioimpedance, (c) galvanic skin response, (d) 2 x PPG. The proposed system also includes a power management integrated circuit (PMIC), which is used for optimizing the power efficiency for multiple readout streams. The whole system is powered by a Li-ion rechargeable battery at 3.7 V. Figure 2.32a illustrates the proposed multiple sensory system in a wristband. When all five channels are enabled, the total power consumption is $1073 \mu\text{W}$ for data collection and management in the system. Figure 2.32b shows recordings of both ECG and PPG data streams simultaneously, and they pointed that blood pressure (BP) can be derived from these two signal modalities using the pulse arrival time (PAT) [81]. PAT is defined as the interval time between the successive R-peaks of the ECG signal, and variable point on the rising part of the PPG signal. The figure 2.32b also shows large variations of BP due to asynchronized multiple data measurements.



(b)

Figure 2.32: (a) Optical image of the proposed device for the wristband use applicable in wearable health applications; (b) Synchronous ECG and PPG data streams, and BP measurement from these bio-signals [80]

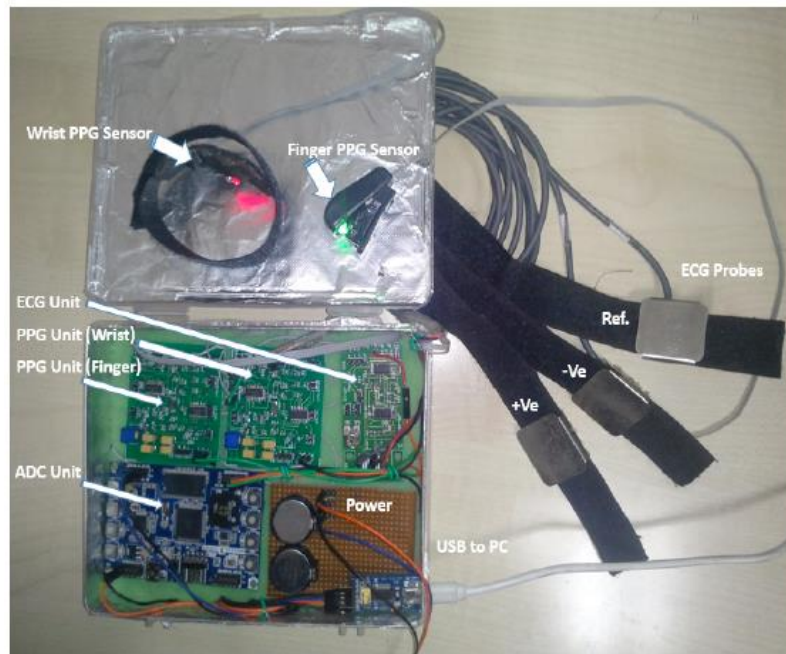
Prawiro et al [82] proposed a wearable monitoring system that integrates HR measurement with the proposed step counter algorithm during physical activities. The developed wearable system comprises of a wireless wearable device, a mobile device and a remote server. Furthermore, a smartphone application has been developed for the display of data related to HR, step count, exercise intensity, speed, distance, and calories burned, included with ECG waveforms and step cycle. Two-electrode circuits are used for ECG measurements, and a 3-axis accelerometer is used for the measurement of step signals. Data transmission is carried out by Bluetooth low energy between the wearable device and smartphone. Moreover, the collected information of HR, step count and GPS location are transferred to a remote server via 3G mobile network to locate the subject and monitor the activity status of the user by clinical staff of remote health care centre. In order to observe the performance of ECG peak detection, MIT-BIH ST Change Database [83] was used as open source input ECG data. Experimental results showed that the accuracy of ECG peak detection was around 99.7%.

New technologies revealed that vital biopotentials (especially BP and HR) can be derived by investigating only recorded ECG, and PPG signals [84]. Jain et al [85] demonstrated a portable multi-parameter signal acquisition system that monitors, stores and transmits ECG, PPG, SpO₂, and Phonocardiogram (PCG), which is the graphic representation of sound generated by the heart, for a tele-monitoring application. The proposed device also provides BP, HR, QRS width, pulse transmit time (PTT), pre-ejection period (PEP) derived from acquired four biomedical signals mentioned above (ECG, PPG, SpO₂, PCG). The research group has used ECG and finger PPG sensors to exhibit BP and HR extraction in the proposed wearable device. Figure 2.33a shows the proposed hardware unit for ECG and PPG acquisition. ECG sensors are attached on both the wrists and right leg using commercial bands, and PPG sensors is clipped on the right hand index finger of the subject. ECG and PPG signals are recorded simultaneously for 10 seconds followed by signal processing and plotting the graph on a PC. BP is extracted from both recorded signals; however, HR is derived only from ECG signal. Figure 2.33b shows the detected peak values for both ECG and PPG signals and Table 2.3 gives the extracted parameters from this figure. Regarding the evaluation of BP and HR, commercially available OMRON digital BP monitor is used for comparing the performance of the proposed device. Experimental results showed that mean absolute errors (MAE) were around 3.80 mmHg and 3.52 mmHg for systolic and diastolic BP respectively when respected to OMRON device. Likewise, the recorded MAE was 2.26 BPM for HR measurements when respected to commercial OMRON device.

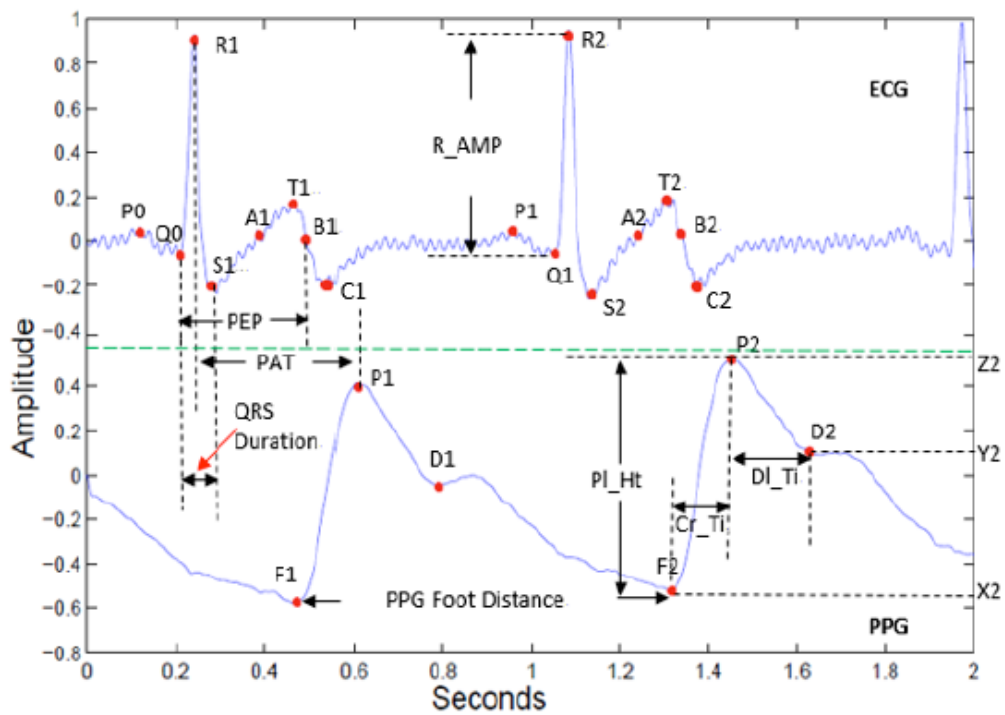
Table 2.3: Parameters Used for Systolic and Diastolic BP Extraction [85]

Parameter source	Parameter	Short Description
Both ECG and PPG	Pulse Transit Time	Pulse Arrival Time – Pulse Ejection Period
ECG	Pulse Ejection Period	Duration between Q-peak and Point B
	R-Peak Amplitude	Amplitude of R-peak
	QRS Duration	Duration between Q and S peak
PPG	PPG Foot Distance	Duration between two consecutive foots
	PPG Pulse Height	Amplitude of peak in PPG signal
	Crest Time	Duration between Foot and Peak
	Delta Time	Duration between Peak and Dicrotic notch

	Augmentation Index (AI)	$(Y_n - X_n) / (Z_n - X_n)$
	Reflection Index	1-AI



(a)



(b)

Figure 2.33: (a) Developed hardware for ECG and PPG acquisition: Chest ECG and Finger PPG; (b) Parameter extraction from synchronized ECG and PPG signals [85]

Although reviewed research studies can be classified according to several characteristics (wireless communication technology, purpose and hardware equipment), the reviewed articles so far (only second section of this chapter) are grouped according to their measured signals characteristics listed in Table 2.4.

Table 2.4: A summary of the recent wearable monitoring systems presented in the literature review

Measured Signals	Purpose	Hardware	Wireless Comm. Technology	Ref.	Critics
ECG, HR, SpO ₂ , Skin temperature, BP, and activity	Medical monitoring in space and terrestrial (extreme) environments	Custom microcontroller-based devices and commercial biosensors	Bluetooth	[60]	Real-time Demonstrations are carried out only in serial port of connection (not in wireless)
ECG, EMG, body temperature, and activity	Rehabilitation, elderly patients, and chronic disease monitoring	Textile/electronic sensors on jacket	Bluetooth	[61]	Vitals are obtained with an integrated device. In an activity motion artefact happens and SNR is decreasing
ECG, SpO ₂ , and activity	Real-time physiological monitoring using wearable sensors	Sensor nodes with custom processing boards	ZigBee	[62]	Accuracy is not good enough for activity purposes
ECG, BP, PPG, galvanic skin response (GSR), and body	General remote health monitoring	Vest woven with sensors and microcontroller	2.4-GHz radio/ISM RF link	[65]	Wireless transmission range of medical data to remote station needs to

temperature					be improved
ECG, HR	Unobtrusive smartphone-integrated ECG monitoring	Dry electrodes attached on the outer frame of the smartphone case	Bluetooth	[66]	Lack of continuous monitoring of ECG signals
ECG, PPG	Mobile healthcare monitoring	Sensor nodes with custom microcontroller boards	ZigBee, Bluetooth	[67]	The system needs to be upgraded to get reliable data
PPG, HR, activity, location	Remote physiological monitoring for drivers	Ear-lobe worn sensor module on programmable system on chip	Bluetooth, 3G mobile network	[68]	More Real-time demonstrations need to be done for accuracy
Core body temperature (CBT)	Continuous CBT monitoring for sleep disorders diagnosis	Temperature sensor is coupled to the microphone of a commercial Bluetooth device	Bluetooth	[69]	The proposed CBT sensor needs to be compared to other sensors to validate itself
ECG, EEG, body temperature	Real-time body monitoring system on mobile devices	Multiple commercial sensors on a single chip microcontroller	Bluetooth	[70]	System needs to be tested on several subjects to be classified
PPG, HR	Non-invasive Cardiovascular monitoring using earphones and mobile devices	Reflective photosensors embedded earphones and a microcontroller	2.4-GHz radio/ISM RF link	[73]	The wireless communication needs to be updated to send higher data rate
ECG, BCG,	Ear-worn multiple	A customized	2.4-GHz	[74]	Obtained ECG

PPG, HR	physiological monitoring	earbud design integrated with microcontroller	wireless transceiver		signal is not satisfactory, it needs to be improved
PPG, HR, SpO ₂	Enabling medical professionals to better monitor patients' care	Organic optoelectronic oximeter sensor is interfaced with electronics on finger	NA/(UART)	[76]	Wireless communication channel needs to be added to the system
ECG, EMG, EEG, EOG	Soft and tiny circuits for multiple physiological monitoring	Customized tiny device (1.7x1.8 cm ²) includes microcontroller and sensors	2.4-GHz radio/ISM RF link	[77]	System needs to be tested on more subjects to compare accuracy
HR, BP, body temperature	General remote health monitoring, cardiac patients	Commercial wearable sensors	Bluetooth	[78]	Battery issues need to be solved to reduce false alarms
ECG, EMG, Body temperature, PPG, BP	To advance healthcare services with proposed reconfigurable sensing channel	Reconfigurable analog front-end, multiple readout channels, and fully programmable microcontroller	NA	[79]	Wireless communication channel needs to be added to the system to provide a better integration
ECG, bio-impedance, GSR, PPG, SpO ₂ , BP, HR	Efficient power management for multiple physiological monitoring	Power management integrated circuit optimized for low power sensor readout. (64 LED	NA/(UART)	[80]	Wireless communication channel needs to be added to the system to provide a better

	systems	Drivers)			integration
ECG, HR, step count, exercise intensity, speed, distance, calorie burn	Advancing general healthcare mobile monitoring systems	Accelerometer and ECG circuits integrated with microcontroller	Bluetooth	[82]	The system needs to be tested on real patients to observe SNR
ECG, PCG, PPG, SpO ₂	Multi-signal acquisition system for preventive cardiology, early diagnosis from BP	Finger PPG and ECG sensors on the wrist are integrated with the microcontroller	NA/(UART)	[85]	Wireless communication channel needs to be added to the system to provide a better integration

2.3. Summary

First of all, this chapter extensively reviewed the recent studies of ECG monitoring applications using different types of electrodes. Various methods such as gel, dry, and textile electrode types, were examined for ECG recording and the obtained results in terms of signal quality and skin-electrode impedance values have been compared with the traditional method of ECG monitoring which is the type of adhesive Ag/AgCl electrode. Furthermore, ECG acquisition systems have been reported using different types of materials such as Ag, Au, CNT, graphite and graphene with various flexible substrates such as PDMS. The recent technologies with different materials have improved the design and reduced the test requirements such as eliminating the need of gel, and skin preparation. However, the signal quality of the demonstrated results in the recent studies was not good as much as the conventional Ag/AgCl electrodes. Due to high electrical conductivity values of Graphene, as it is investigated in this research, it can improve the signal quality of acquired ECG signals by lowering the skin-electrode contact impedance. Subsequently, a critical review of multiple smart sensor systems was provided for personalized healthcare monitoring and management, in particular ECG, CBT, and PPG monitoring systems.

CHAPTER 3: THEORETICAL BACKGROUND TO MULTIPLE PHYSIOLOGICAL MONITORING SYSTEMS

In this chapter, the theoretical background of electrocardiogram (ECG), core body temperature (CBT) and photoplethysmography (PPG) measurements will be given, respectively. It comprises three sections, with the first focusing on the electrical activity of the heart, ECG physiology, including lead positions and the electrical model of ECG measurement. CBT measurement analysis is covered in the second section by considering the mathematical functions and calculations on how CBT is measured from the ear. Finally, the analytical background of PPG is provided including the algorithm of taken measurements for calculating the heartbeat and SpO₂ data from the finger.

3.1. Analysis of Electrocardiogram (ECG) Measurement

Since the development and evaluation of the proposed smart sensor system throughout the thesis is focused on the ECG, this section also gives a brief background of the anatomy of the heart and physiology to understand better how the concept of ECG works. Moreover, ECG waves and lead positions, the electrical model of ECG measurement and skin-electrode interface are explained in the following subsections. The importance of ECG electrode interfaces and how they interact with electrolyte gel and skin are also discussed in this chapter. Finally, signal processing research of ECG data is briefly covered together with a method of heartbeat detection.

3.1.1. *The Anatomy of the Heart*

The heart is a muscular tissue, the size of a fist size, consisting of four chambers: left and right atria, and left and right ventricles. It functions as the distributor of molecules, hormones, and body temperature to the billions of cells by pumping the blood throughout the body. As can be seen in Figure 3.1, each atrium is placed above a ventricle, with the right one being filled with blood via the superior and inferior vena cava. Then, the blood moves passively into the right ventricle under simple pressure, which is pumped into the pulmonary artery by contraction of the right ventricle and into the nearby pulmonary circulation of the lung. In the lung, the blood is exposed to air in the alveoli, releasing CO₂ and binding with O₂. In return, the pulmonary veins receive this oxygenated blood and return it to the left atrium via the pulmonary veins. In the same way, the blood passes down passively through the left ventricle. Here, the left ventricle pumps oxygenated blood into the aorta to complete systematic circulation for the body. After delivering blood within molecules with high levels of O₂ molecules and hormones to the cells, CO₂, metabolic waste products, and metabolites are transmitted back to the right atrium via the vena cava. Another interesting point is

that the heart muscle is different from skeleton muscles. First of all, cardiac muscle cells are triggered by its own autorhythmic cells and thus, activated without any required action. Moreover, cardiac muscle fibres are bonded to one another by intercalated disks, which include gap junctions. These gap junctional proteins allow for very low resistance conduction from cell to cell in the cardiac muscle. Simultaneous contraction is essential, if a coordinated force is to be established to pump blood out of the heart on each beat. Moreover, the heart is the first organ to function in a human embryo and continues to work throughout its life. In order to maintain this continual muscle effort, heart cells are fueled with very rich mitochondria, which provide the ATP required for contraction [86]. Figure 3.1 illustrates the basic structure of the heart and the path of the blood flow through it.

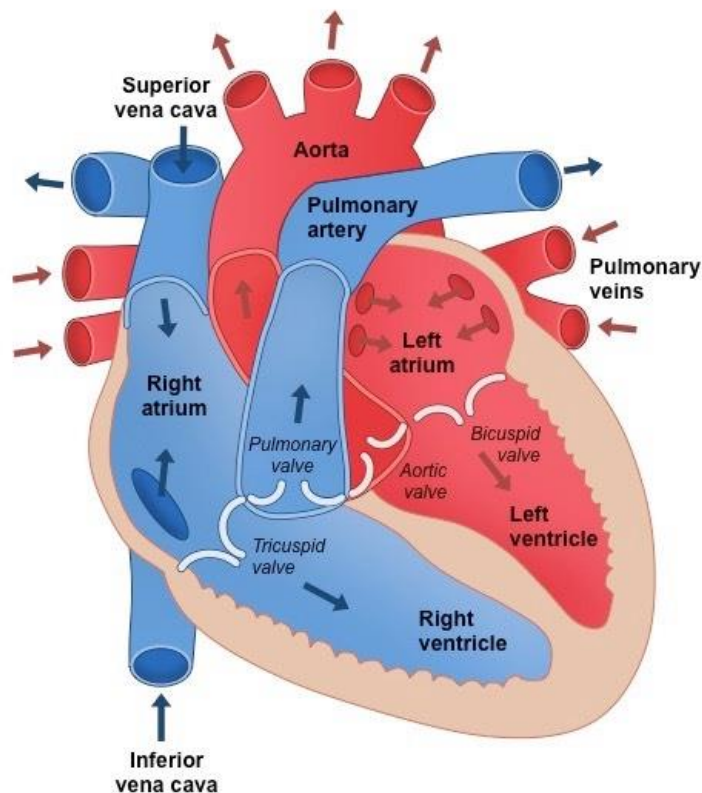


Figure 3.1: Heart structure and the path of the blood flow [86]

3.1.2. Electrical Activity in the Heart

All cardiac muscle contraction is stimulated by the operation of an electrical signal; an action potential that is continuously provided by the heart itself. The cellular mechanism in a cardiac muscle tissue begins the cardiac action potential by triggering a sinoatrial node (SA node). The reason for the commencement of the action potential is activity of the ion channels in the cardiac cell membrane. That is, the cell membrane has ion channels that arrange the diffusion of ions along their electrochemical gradient. There are three types of voltage-gated ion channels to initiate

pacemaker action potential (triggering SA node). The first is a the Na^+ channel, which opens at approximately -60 mV. As Na^+ ions enter the cells of the SA node, the membranes are depolarised and gradually the membrane potential reaches the voltage capacity of a Ca^{2+} channel, which opens at around -50 mV. As Ca^{2+} ions enter the cells, the membrane depolarises further, unless the voltage range of the channel reaches 0 mV, in which case the last K^+ channels open. In the SA node, only the calcium channels play a role in the final depolarisation of the action potential. The depolarisation process stops at 0 mV and by opening the K^+ channels, K^+ ions leave the cells and repolarisation starts. This is the difference between the SA node and any other process, whereby K^+ ions repolarise the cell and the membrane potential returns back to -60 mV to begin the next action potential (see Figure 3.2). Another interesting point of this mechanism is that there is no resting membrane potential in the SA node [87].

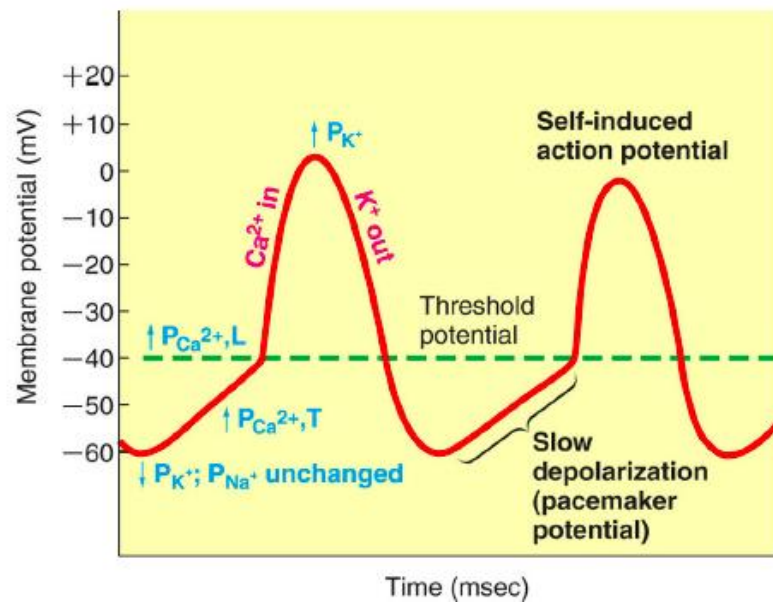


Figure 3.2: Electrical activity in a pacemaker cell (SA node) [87]

Regarding the conducting system of the heart, five major structures can be described within its network. Figure 3.3 shows these main structures in terms of their locations in the heart. The sinoatrial node (SA node) is located in the right atrium wall and contains pacemaker cells from which action potentials are formed at regular intervals by the changing ions in these cells. As a result, the electrical impulse arises in this node for heart contraction (the sinus rhythm), and hence, is often referred as “natural pacemaker of the heart” [88]. Subsequently, this SA nodal electrical impulse propagates in several directions: to the left atrium (Bachman’s bundle) [89], and to the intermodal pathways, which lead into the atrioventricular node (AV node). This is located in the medial wall of the right atrium, near its junction with the right ventricle. The pacemaker cells in the AV node have very low conduction values, thus the speed of depolarisation in the AV node is very

slow and this causes a delay from when action potentials form in an AV node cell for 0.1 sec. From the AV node, the action potential is transferred to a structure called the atrioventricular bundle (AV bundle) or Bundle of His, which conducts the impulse through the interventricular septum. Soon after, the interventricular septum is bifurcated into two separated branches, called the AV bundle branches. Once the signal has travelled down to the apex of the heart, the action potential is conducted up both the left and right walls of the ventricle through branched tracts of pacemaker cells, referred to as the Purkinje fibres, which run up the electrical signal to the ventricular walls. Finally, the action potential moves between the ventricular cells, until and both right and left ventricular are depolarised. These electrical changes occurring throughout the cardiac cycle can be monitored and recorded using the electrocardiogram technique, which is explained in depth in the next section [86].

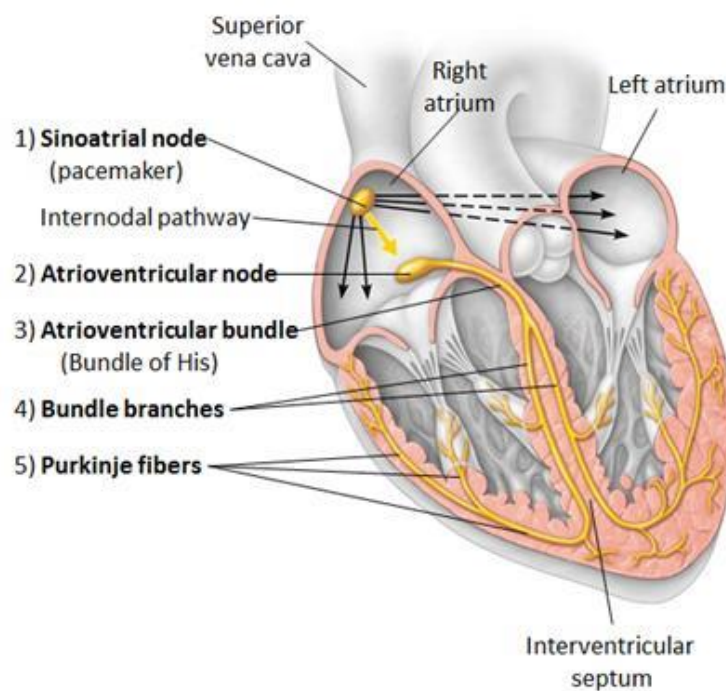


Figure 3.3: The conduction system of the heart and the path of cardiac excitation [87]

3.1.3. ECG Wave and Lead Positions

Electrocardiogram (ECG) analysis is referred as a non-invasive measurement of the sum of all electrical activity in the heart [90]. An ECG does not give the action potential, but rather, the total electrical changes throughout the cardiac cycle provided while the action potentials travel in the heart from the SA node to the AV node, bundles, and Purkinje fibres via the interventricular septum for the depolarisation and repolarisation process. Figure 3.4 illustrates a typical ECG signal in terms of its basic components.

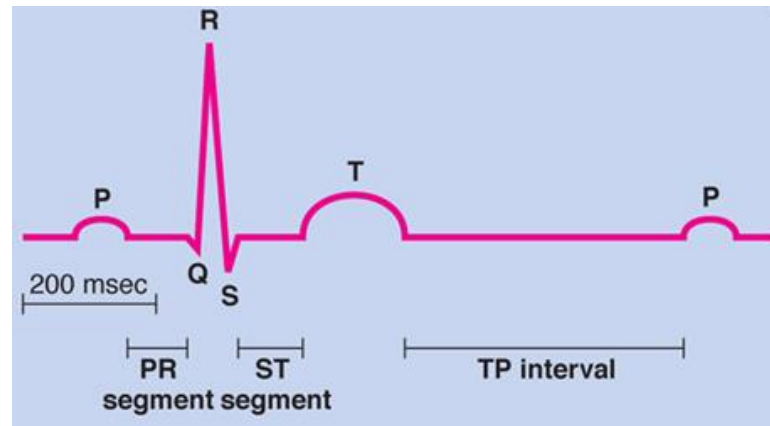


Figure 3.4: Major components of a typical electrocardiogram (ECG) waveform [87]

According to the picture, there are three main wave parts in a basic ECG diagram and several baseline segments. The P wave represents atrial depolarisation, which initiates at the SA node. The PR segment demonstrates AV nodal delay, which is the time taken for the cardiac impulse to be distributed from the atrium to the AV node and bundle system. The QRS complex (wave) pertains to the ventricular depolarisation with simultaneous atrium repolarisation. The T wave corresponding to the ventricular repolarisation and the TP interval, represents the time of ventricular relaxing as well as preparing for the next depolarisation.

Figure 3.5 shows the events in the heart in depth during cardiac conduction. Before setting an action potential, there is still a small electrical signal in the SA node and then the impulse is generated in this node (a-P wave). Once it is depolarised and atrium contraction has happened (b-P wave), the electrical signal slowly reaches the AV node and travels down through the AV bundle branches (c-beginning of QRS complex). After this, the signal expands to the ventricular wall via the Purkinje fibres for ventricle depolarisation (d-QRS complex). Finally, during the T wave, the ventricle repolarises and the heart makes itself ready for the next depolarization, which will be initiated from the SA node. The baseline segments in an ECG signal reflect when there is no ongoing depolarisation or repolarisation process during the cardiac cycle.

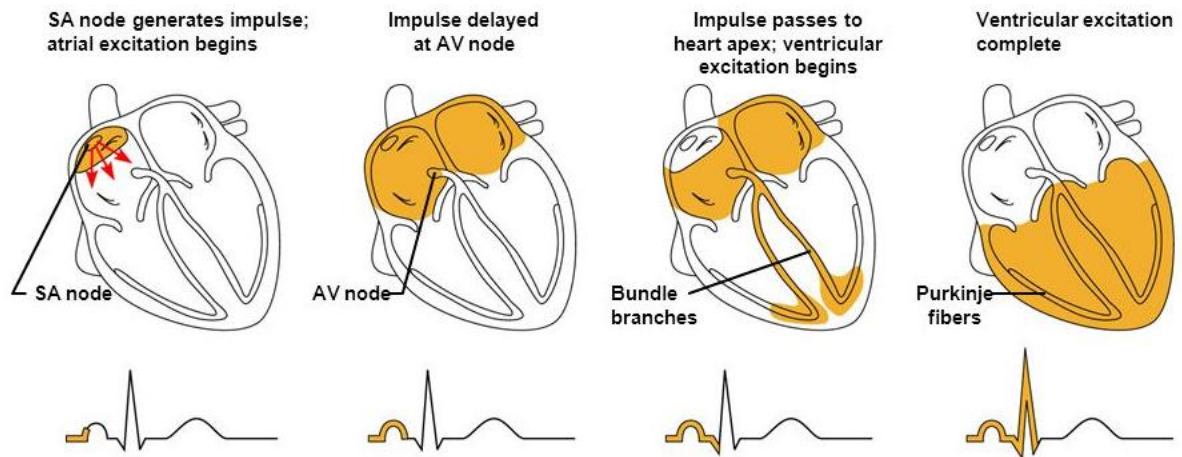


Figure 3.5: ECG Genesis while the cardiac cycle is coordinating the activity [87]

A number of intervals can be measured and analysed from an ECG recording, with a normal signal giving very important information regarding the heart status during a cardiac cycle. The time between the beginning of a particular point in a cycle and the beginning of another particular point in the next cycle is the interval between the commencing of the electrical response of those points in the heart. For example, Figure 3.6 demonstrates a normal ECG for two beats of the heart.

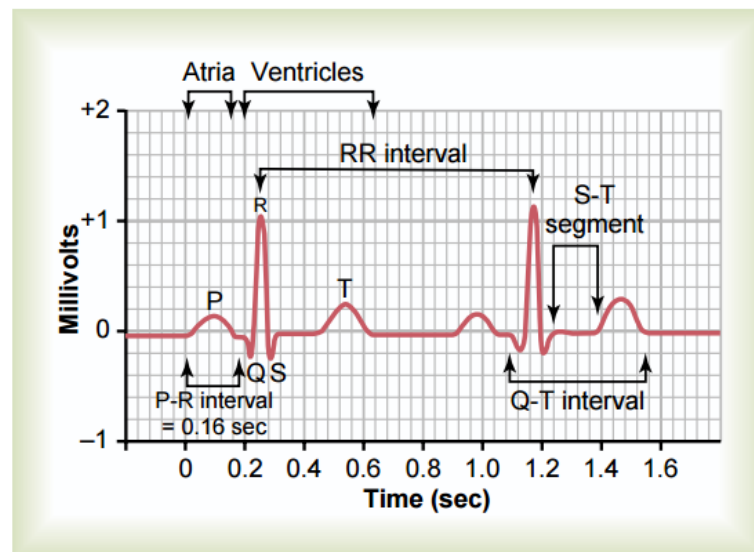


Figure 3.6: A normal electrocardiogram (ECG), including particular intervals [91]

Regarding the diagram, the P-R interval, which means the duration between the beginning point of a P wave and the peak of an R wave, illustrates the depolarisation of the atrium. In addition, this interval gives the information of how long an electrical impulse will pass through the ventricle from the atrium, including AV delay. Generally, the P-R interval takes between 0.14 and 0.16 seconds. During the Q-T interval, which refers to the duration between the Q point and the starting point of a T wave, the ventricles become in a depolarised state. The Q-T interval reveals the amount of time

that blood is being pumped out of the heart and into the arteries, which ordinarily lasts about 0.35 seconds. The most known interval is the R-R (beat-to-beat) interval, which indicates the time between two consecutive QRS complexes in an ECG recording. Looking at this interval, the heart rate can be measured by a simple calculation, as explained later in this chapter. Lastly, the S-T segment, which endures from the S point until the beginning of the T wave, is a crucial interval for diagnosing heart-related problems, such as a heart attack or depression in individuals with coronary problems.

In general, ECG recording provide essential information for assessing cardiac anomalies [92]. For instance, long Q-T or S-T intervals might help in diagnosing serious health problems, such as hypothermia, or ischemia. A typical ECG lasts between 720 and 780 milliseconds. Table 3.1 shows a summary of ECG waves and intervals including durations.

Table 3.1: Summary of ECG Waves, Intervals and Duration [92]

ECG Component	Definitions	Duration (s)
P Wave	Atrial depolarisation	0.08-0.10
QRS Complex	Ventricular depolarisation	0.06-0.10
T Wave	Ventricular repolarisation	~ 0.20 (usually not measured)
P-R Interval	Atrial depolarisation including AV delay	0.12-0.20
S-T Interval	Isoelectric period of depolarised ventricles	0.07-0.08
Q-T Interval	Length of depolarisation	0.20-0.40

A conventional ECG signal comprises tracing from 12 viewpoints for recording cardiac electrical activity [93]. Each point is obtained by recording the electrical potential between a pair of electrodes (positive and negative electrode), called a ‘lead’. Twelve viewpoints correspond to 12 leads, which can be separated into two parts: six limb leads (bipolar and unipolar leads, as can be seen in Figures 3.7a and 3.7b); and six chest leads. The ECG is normally recorded using three electrodes, one on each arm, and another one placed on the left leg (Einthoven’s triangle) [94]. Furthermore, recordings are commonly made using six chest electrodes (unipolar precordial leads). According to Einthoven’s theorem, the three limb electrodes can be connected across a voltmeter and an ECG signal can be recorded in three different combinations, called three bipolar limb leads,

which are denoted as I, II, and III [94]. In recording limb lead I, the negative electrode is connected to the right arm and the positive terminal to the left. For lead II, the negative terminal of the ECG is connected to the right arm and positive electrode will be placed on the left leg. Finally, in lead III, the negative electrode will be on the left arm and the positive will be connected to the left leg. Consequently, when the negative side is measured negatively with respect to the positive side, then the ECG will be recorded positively. According to Einthoven's law, bipolar limb leads are calculated as:

$$\text{lead I} = V_{LA} (\text{Voltage of Left Arm}) - V_{RA} (\text{Voltage of Right Arm}) \quad (3.1)$$

$$\text{lead II} = V_{LF} (\text{Voltage of Left Leg}) - V_{RA} (\text{Voltage of Right Arm}) \quad (3.2)$$

$$\text{lead III} = V_{LF} (\text{Voltage of Left Leg}) - V_{LA} (\text{Voltage of Left Arm}) \quad (3.3)$$

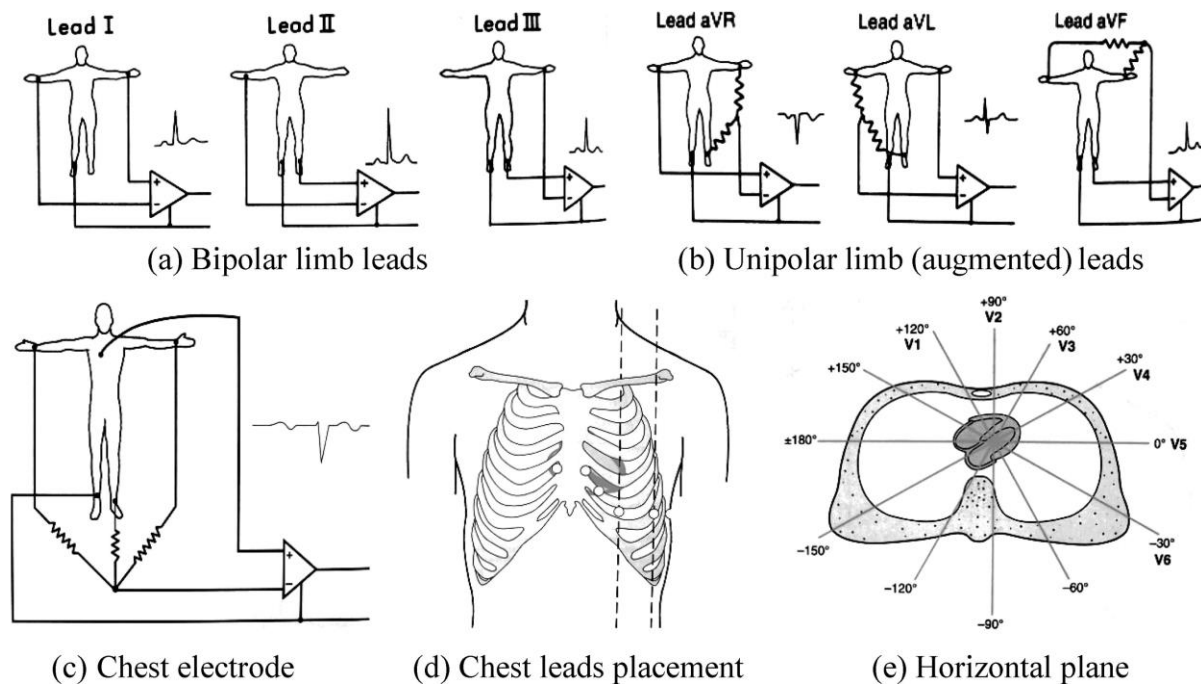


Figure 3.7: 12-Lead System: (a) Bipolar limb leads; (b) Unipolar limb leads; (c), (d), (e) Chest leads [93]

Figure 3.7b illustrates unipolar limb leads (aVR, aVL, and aVF), which measure the exact electrical potential at the place of the positive electrode (placed on the right arm, left arm, and left leg, respectively). The signals are augmented, because the results are too small to be used, thus they are also called augmented leads. In Figures 3.7c, 3.7d, and 3.7e the chest lead placement and horizontal plane are shown. There are six chest leads (V1, V2, V3, V4, V5, and V6) in order to record the electrical signal of the heart using chest-type electrodes. By combining all the described leads together, a conventional 12-lead system is formed as the basis of a modern clinical ECG measurement system.

3.1.4. ECG Measurement and Electrode Properties

In order to obtain a reliable ECG, the electrodes are commonly used to carry out the measurement chain. As mentioned and reviewed earlier, there are different types of electrodes made using several techniques, including gel, dry, non-contact, capacitive, textile, nanomaterial-based electrodes for ECG monitoring systems. If they are used incorrectly, there will be unwanted distortion of order of magnitude larger than the ECG itself. Figure 3.8 introduces the typical measurement system for ECG recording consisting of two or more metal-lead (generally Ag/AgCl electrodes) electrodes attached to the skin and connected to a differential amplifier.

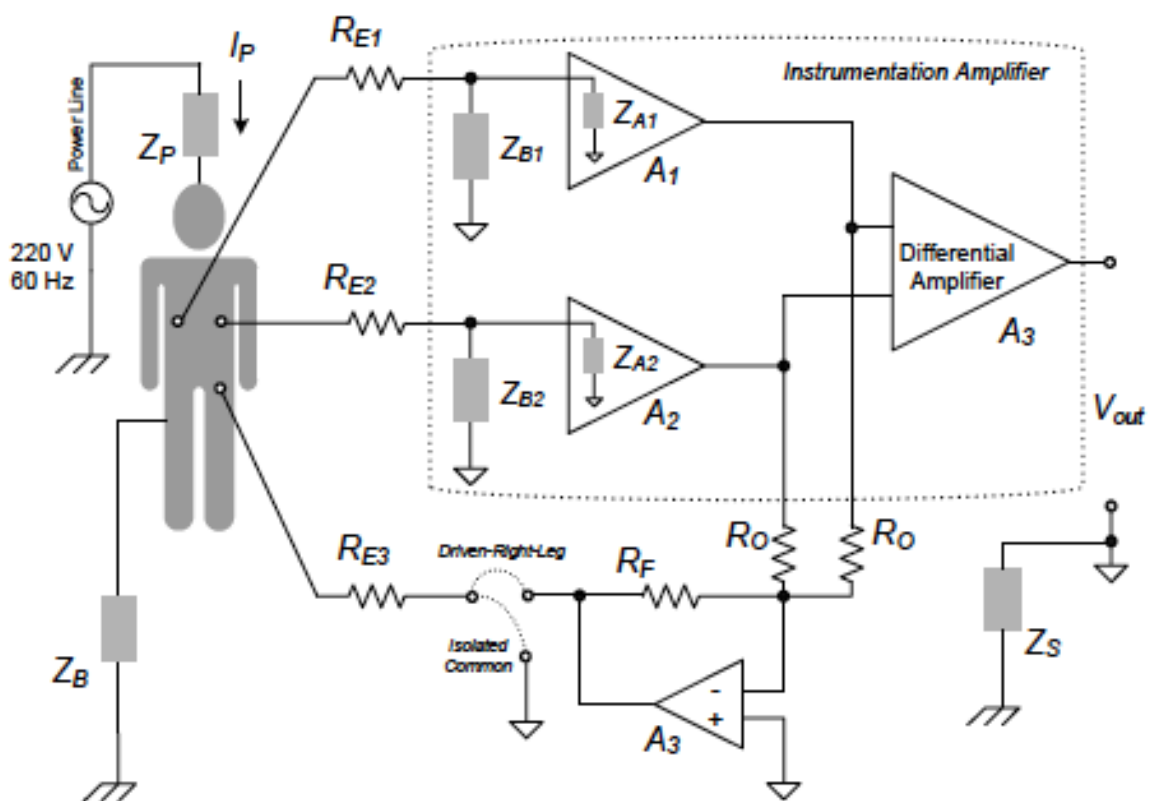


Figure 3.8: Schematic circuit of a typical ECG measurement system with a DRL connection [95]

The goal of the right leg drive circuit is to reduce interference from the amplifier. When an ECG signal is amplified by an instrumentation amplifier, it is possible to create a DC common mode interference. The drive right leg (DRL) connection inverts and amplifies the common mode signal back into the right leg of the person as shown in the figure. As a consequence, the 60-Hz common mode bias from AC power is avoided, thus leading to a better ECG signal. In order to get a clearer ECG signal at the output of the instrumentation amplifier, this is filtered to reduce the noise and then the denoised signal is sent to an operational amplifier that conditions the signal to better levels for the microcontroller for further signal processing algorithms of the ECG signal. After filtering and converting signals to the appropriate levels, the obtained ECG signal is transmitted to a

monitoring device, as shown in Figure 3.9. In the proposed system [96] shown in the figure, there is an insulation layer between the electrodes and body so that there will be a high input impedance of the measurement system due to the capacitively coupled electrodes and the interacting extra impedance of capacitance. The equivalent circuits of typical ECG measurement systems and their impedance calculations for the various types of electrodes are discussed in the next subsection.

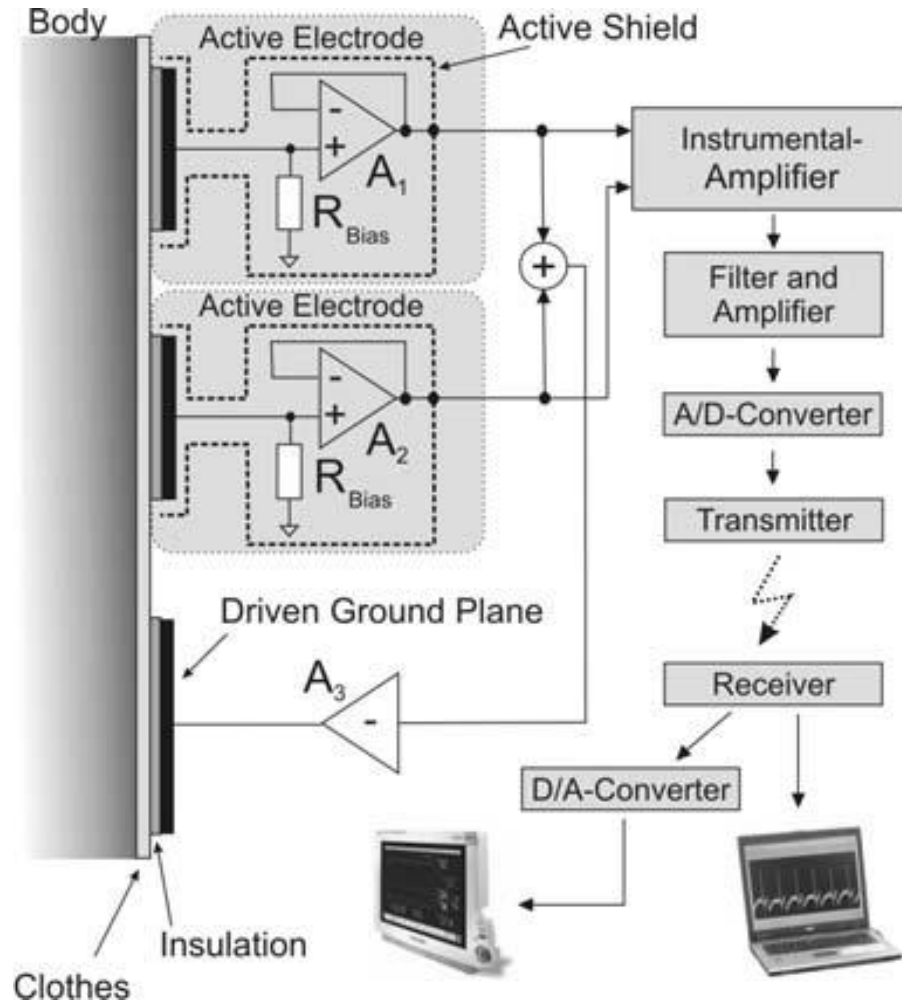


Figure 3.9: Block diagram of an ECG measurement system including DRL plane and capacitively coupled electrodes [96]

3.1.5. Electrical Model of the Skin-Electrode Interface

The term of “electrode” comes from the study of electrochemical cells, where electrical transport is conducted via oxidation and reduction (redox) reactions taking role between the metallic layer and electrolyte gel [97]. In accordance with several studies, the wet type of conventional Ag/AgCl electrodes are fitted to this description due to their metallic layer being bathed in an electrolyte gel that shields the electrical composition through the outer and inner layers of the body surface. It is worth noting that the impedance, Z , includes elements (resistance or capacitance) sourced from body tissue (epidermis, dermis, stratum corneum), the skin-electrolyte interface, the electrolyte, the

electrolyte-electrode interface and the electrode leads. Accordingly, the wet type conventional electrode is well-characterised by double layer capacitance and parallel series resistors for coupling electrical signal through the skin. In contrast, dry and non-contact types of electrodes are more complex due to additional input impedances that cause difficulties for skin-electrode coupling. Figure 3.10a shows an equivalent electrical circuit of a model from the body to the electrode, and Figure 3.10b illustrates the electrical coupling of skin-electrode interfaces for various electrode topologies.

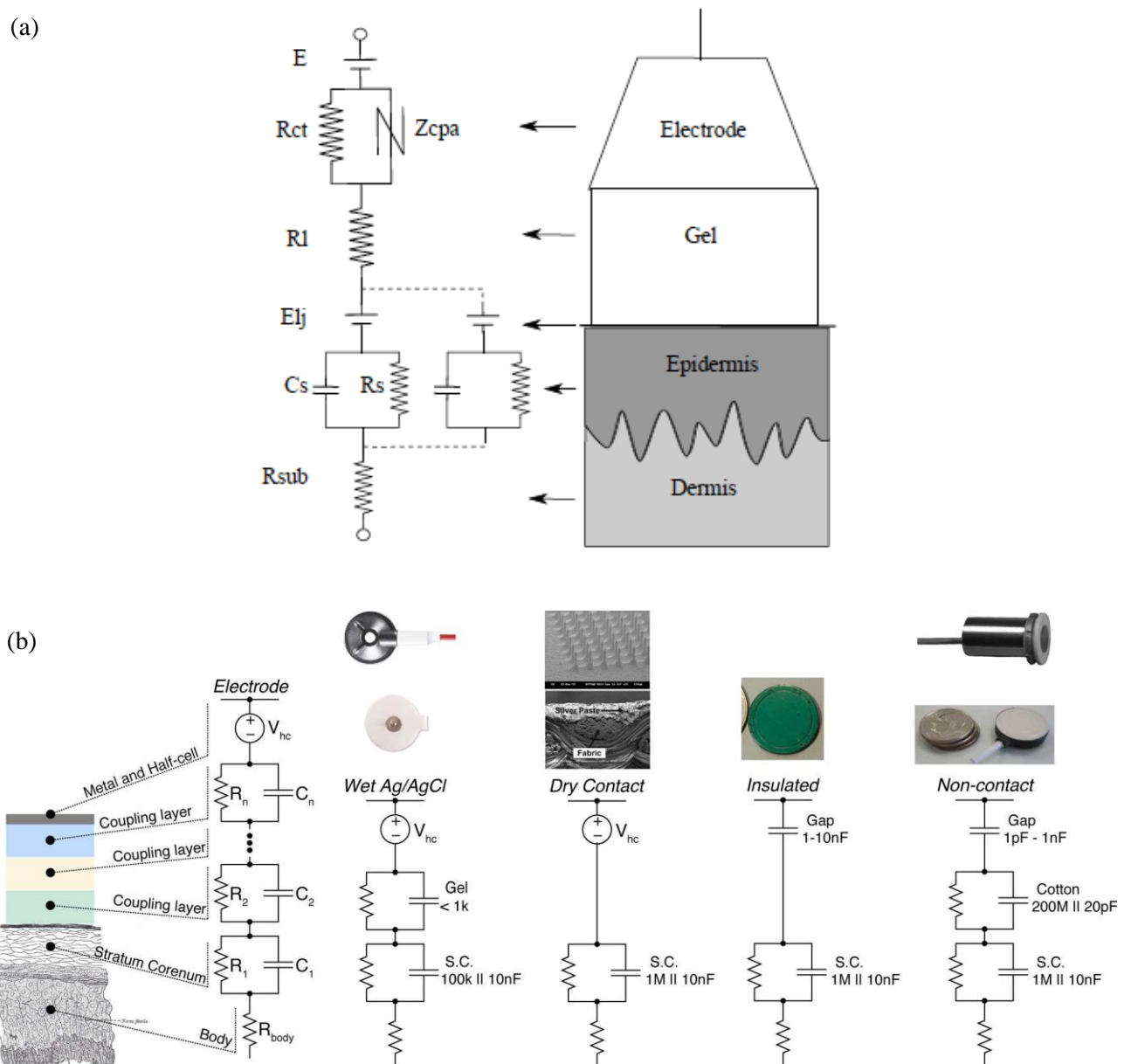


Figure 3.10: (a) Electrical model of the interface from the body to the electrode; (b) Electrical coupling of skin-electrode interface for various electrode topologies, including wet-contact gel-based Ag/AgCl, dry contact MEMS and metal plate, thin-film insulated metal plate, and noncontact metal plate coupling through hair or clothing, made of such as cotton [97]

It is important to realise that low resistance (impedance) is essential for good electrode performance, thus effecting ECG signals in a better way. To this end, the wet type conventional Ag/AgCl electrodes are used in clinical applications today as they provide better ECG signals than other types of electrodes due to lower skin-electrode impedance values. Table 3.2 gives the descriptions of parameters depicted in Figure 3.10a.

Table 3.2: Descriptions of the parameters given in Figure 3.10a

Parameter	Description
R_{sub}	Internal body resistance, approximately constant ($\sim 100\Omega$)
R_s	Resistance of skin, which depends on skin preparations, electrode gel and time after application
C_s	Capacitance of skin, which depends on skin preparation, electrolyte concentration and contact area
E_{lj}	Liquid junction potential due to the concentration gradient of ions between body fluids and the electrolyte
R_l	Resistance of the electrolyte
R_{ct}	Charge transfer resistance of the oxidation/reduction at the electrode/electrolyte interface
Z_{cpa}	Constant phase angle impedance due to the double layer between electrolyte and electrode
E	Half cell potential of the reaction at the electrode and electrolyte interface

3.1.6. ECG Signal Processing and Heartbeat Detection

ECG signals have been controlled for signal processing to enhance the signal quality by filtering techniques. Another benefit from signal processing that it facilitates detection and quantification of signal properties. For instance, an ECG waveform is indicated in Figure 3.6 with the parameters of ECG morphology when interpreting its diagnostic information. Cardiac pathologies are extracted using these parameters (P wave, QRS complex and T waves) and cardiac diseases are monitored as changes from normal values of these parameters. For example, as mentioned earlier, a small change in the S-T segment, which starts at the S point and lasts until the beginning of the T wave, can be a vital deviation for diagnosing heart-related problems, such as a heart attack or depression in individuals with a coronary problem. Similarly, R peaks play a key role in detecting heartbeats

using their peak points and the R-R interval time series is the first information to evaluate heart rate variability (HRV).

Normally, ECG information is investigated under the frequency content of 100 Hz with a significant frequency range of 10 Hz for the QRS complex, as can be seen in Figure 3.11. Signal processing within ECG applications is carried out generally in three steps: (a) pre-processing; (b) heartbeat detection; and (c) post-processing. Firstly, the influence of some disturbances, such as power line interference or motion artifacts, needs to be reduced in the pre-processing stage using an infinite impulse response (IIR) notch filter or Butterworth digital filter (band-pass filter). After this, R waves, which are the mostly used to represent the occurrence of a heartbeat, are formed thus facilitating heartbeat detection. Lastly, in the post-processing stage, the acquired and filtered ECG signals are compared and classified according to the total segmentation of the different waves associated with analysis of the heart rate time series.

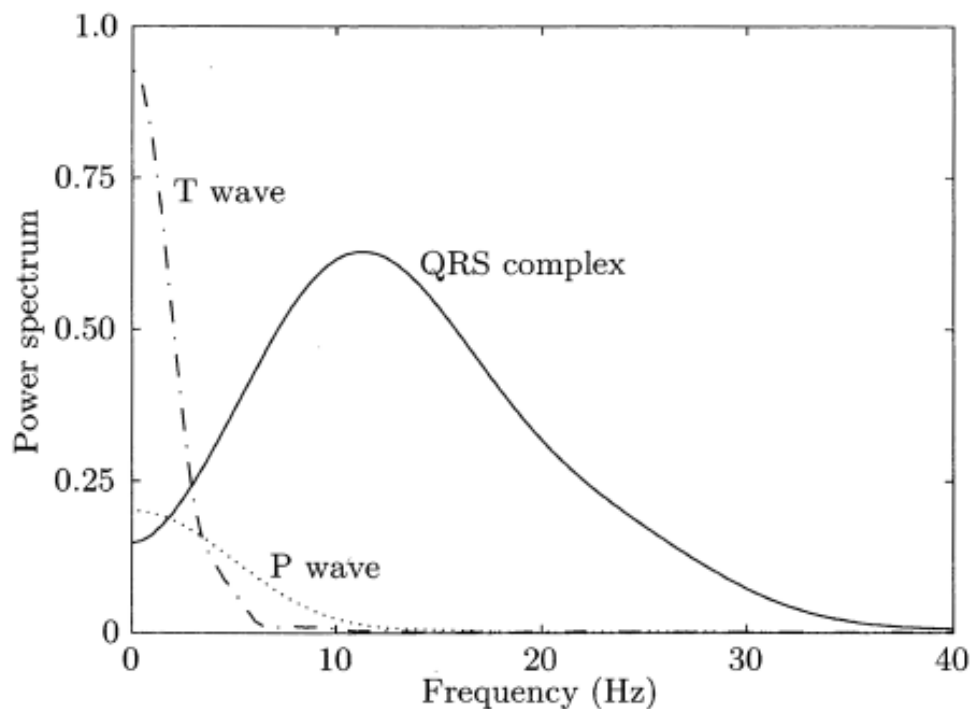


Figure 3.11: The ECG signal spectrum [98]

Regarding heartbeat detection, several algorithms are applied to identify heartbeats correctly. The most common method is to determine the peaks of R waves and to calculate the time series between these peak points. Friesen et al [99] compared nine different types of non-adaptive QRS detectors with noisy ECG signals and the best result was shown for algorithms using the first derivative only. A widely used method for heartbeat detection is known as the Pan-Tompkins method, which was mentioned earlier [46]. As can be seen in Figure 3.12, the proposed method involves the steps of

pre-filtering, differentiating, squaring, moving average integration and finally, decision rule after thresholding.

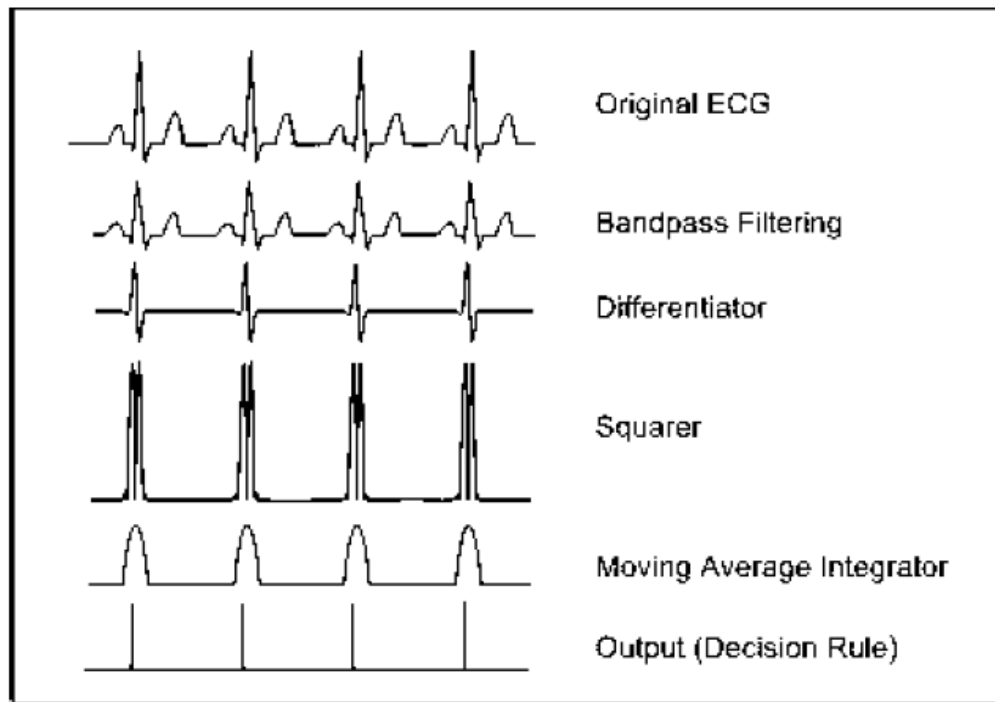


Figure 3.12: Schematic overview of the Pan-Tompkins heartbeat detection method [46]

To sum up the heart rate calculation, a typical ECG signal of a person heartbeat can be sectioned into three parts, as shown in Figure 3.6 [91]: the P wave, which illustrates the beginning and completion of the atrial depolarisation of the heart; the QRS complex, which conducts the ventricular depolarisation; and lastly, the T wave which manages the ventricular repolarisation. The R-peak in the ECG signal is the most important parameter for calculating heart rate and is easy to distinguish from noisy components and other parameters due to its large amplitude. Lee et al. [100] developed a variable threshold method to detect the R-peak further, the formula for which is given below.

$$V_{TH} = [x(n) - x(n-1)] * 70\% \quad (3.4)$$

Here, the R-peak can be differentiated from the baseline, which corresponds to 70% of recorded ECG peak signal detection. In addition, the formula for determining HR from R-R intervals provided by Lee et al. [100] is given below. In clinical environments, heart rate is generally measured as beats per minute (BPM).

$$\text{Heart Rate (HR) in BPM} = 60,000 / \text{RR Interval (ms)} \quad (3.5)$$

3.2. Analysis of the Core Body Temperature (CBT) Measurement

The measurement of core body temperature (CBT) is essential for diagnosing and preventing serious climatic injuries, such as hypothermia, hyperthermia, and heat stroke, especially during exercise, sport activities and infectious diseases. Here, a brief background of core body temperature measurement is given and this is followed by analysis of the non-invasive measurements of CBT. The anatomy of the ear is described and the process of measuring CBT using an infrared thermopile sensor, which is applied for this purpose throughout this section.

3.2.1. Background of Core Body Temperature (CBT) and Thermal Imaging

Core body temperature (CBT) measurement is one of the oldest methods for diagnosing diseases and a significant indicator of health in both personal life monitoring and medical care [101]. Human CBT can vary from day to day, but these variations have small margins, being generally no more than 1.0°C . CBT is kept in the normal range (between 36.1°C and 37.2°C) by the thermoregulatory centre in the hypothalamus [102]. The aim of monitoring CBT is to capture any signs of systemic infection in the presence of fever or to discover whether it is too high above normal temperature, i.e. there is hyperthermia or very low, in the case of hypothermia. It is invariably clinically important to observe the trend in a patient's temperature on a daily basis. Figure 3.13 shows the thermal imaging of a human body as the temperature of the internal body varies through its surface.

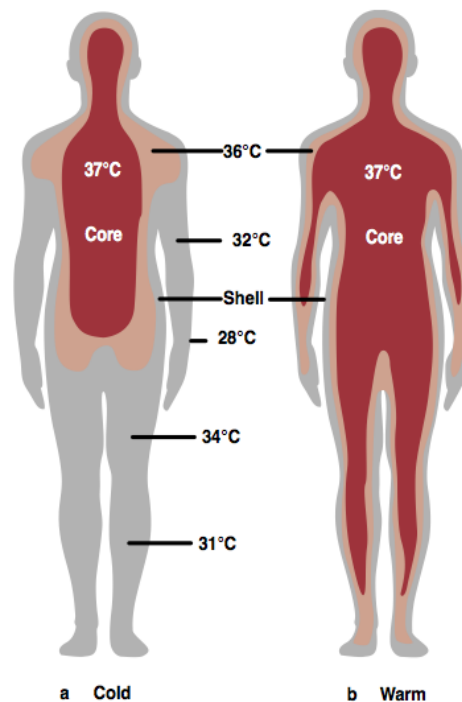


Figure 3.13: Distribution of temperatures within the body and division of the body into the core and shell during exposure to (a) cold and (b) warm environments [103]

There can be different factors can affecting the human thermoregulation system. When assessing the core temperature of the body, it is worth noting that the CBT should be in the optimum range, which is between 36.1°C and 37.2°C for adults, but it can vary depending on gender, age and the site of measurement [101]. Table 3.3 gives some CBT values corresponding to related diseases or body system infection, whilst Table 3.4 shows the human body temperature range according to ageing status.

Table 3.3: CBT variations corresponding to an individual's health status [102]

Temperature	Health status
44°C	Near death
43°C	Normally death or brain/cardiorespiratory collapse
41-42°C	Fainting, confusion, very fast heart rate (HR), low/high blood pressure
38-40°C	Severe sweating, dehydration, weakness, vomiting, headache, fast HR
37°C	Normal temperature
36°C	Mild shivering and normal status
34-35°C	Numbness and bluish/greyness of the skin. Heart irritability. Confusion and loss of movement of fingers
29-33°C	Severe confusion, sleepiness, slow heartbeat, shallow breathing, unresponsive to stimuli
24-28°C	Breathing may stop. Close to death.

Table 3.4: Human body temperature range [102]

Body Temperature Range	Hypothermia (low temperature)	Normal range	Hyperthermia (high temperature)
Baby (0-2 years)	36°C	36°C-37°C	37°C-38°C
Child (3-12 years)	36°C	36°C-36.77°C	38°C

Adult (13-40 years)	36.1°C	36.1°C-37.2°C	37.5°C
Elder (above 40)	35°C	35.77°C-36.94°C	37.44°C-37.94°C

3.2.2. Measurements of Core Body Temperature (CBT)

CBT measurements can be carried out using invasive and non-invasive methods. Regarding the former, temperature readings can be taken from the following locations.

- (a) Rectal: This location is commonly used for measuring CBT with accurate readings and generally, recorded temperatures from here are higher than from the other areas. The rectum site is mostly used in scientific research for heat exhaustion and stroke occurrences, particularly for babies. Moreover, this method has a long response time compared to other methods for CBT measurement [104].
- (b) Oesophagus: This site is preferred for recording CBT due to its deep body location close to the left ventricle, the aorta and to the blood flow to the hypothalamus [105]. Furthermore, this method is chosen for its quick response readings. Nevertheless, it is difficult to insert a thermistor to read CBT via this method.
- (c) Pulmonary Artery: The readings for this method are acquired through a catheter. This measurement is the most accurate method, because the artery brings blood directly from the core body surroundings [106].

However, invasive methods are undesirable for measuring CBT due to the difficulties of inserting medical devices into specific locations of the body. Hence, non-invasive methods are generally preferred for recording it owing to their rapid response and the easy to use equipment. The non-invasive measurements for CBT monitoring are as follows.

- (a) Oral: This method is the most popular method, especially during clinical experiments. Whilst this measurement has the advantages of easy accessibility and giving very quick response times, it can be problematic for babies and small children because of the required behaviour.
- (b) Axilla: It can take longer to read CBT than oral measurement and researchers have found that measuring it here is less accurate than in the rectum or at the tympanic membrane [107].
- (c) Tympanic Membrane: This type of measurement is ideal, because the tympanic membrane and thermoregulation centre in the hypothalamus are fed by the same arterial blood supply flowing from the carotid artery and thus, it is considered that it reflects the core

temperature [108]. This method of measurement and analysis of the tympanic membrane is explained in detail in the next subsection.

3.2.3. Anatomy of Ear in CBT Measurement

Tympanic membrane measurement for CBT, which can be defined infrared ear thermometry, became a popular alternative with several advantages compared to that of traditional measurements [109]. First of all, infrared ear thermometry measurements provide rapid response and secondly, they are easy to use and convenient both for patients and health clinicians. Moreover, the risk of exposure to infectious diseases is reduced for clinical staff throughout the CBT measurement [110]. On the other hand, the accuracy of tympanic membrane measurement for CBT is still of concern, when comparing the results to those of rectal temperature measurement for which studies have revealed contradictory results [111].

The tympanic membrane site takes the blood from the internal carotid artery, which also supplies blood to the hypothalamus in the brain for the thermoregulation centre and the ear thermometer has been developed for this specific area to measure CBT. Furthermore, the ear canal is accessible for reading CBT from the tympanic membrane, as can be seen in Figure 3.14. When the temperature of the tympanic membrane is 37.3°C , it stands at between 34.5°C and 36.6°C in the ear canal (see Figure 3.24).

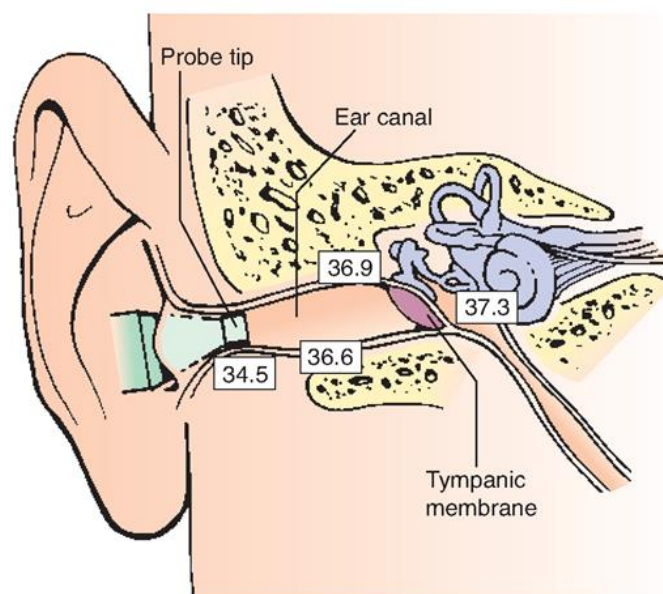


Figure 3.14: Obtaining the tympanic temperature by aiming the probe towards the inferior third of the ear canal [112]

3.2.4. CBT Measurement using an Infrared Thermopile Sensor

The most popular non-invasive method for measuring CBT is from the ear canal. Using infrared waves, it is possible to do so with a rapid response by just attaching the probe inside the ear canal. There are two locations in the ear where CBT can be measured, namely the ear canal and tympanic membrane, which gets blood from a branch of aorta that also supplies it to the hypothalamus in the brain for the thermoregulation centre [104]. Hence, the tympanic membrane is very important location in the body for measuring CBT.

When an infrared thermopile sensor within a probe is placed in the ear canal, the waveguide takes infrared radiation from part of the ear canal, or tympanic membrane depends on the viewing angle and distance from the target object. Figure 3.15 shows a drawing of how a thermopile sensor transmits the infrared radiation to an object in principle. The targeted objects emit infrared radiation proportionally, depending on the viewing angle, for reading current temperature. Subsequently, the absorbed infrared radiation by the thermopile sensor leads to a temperature difference compared to the original temperature of the sensor. This difference in temperature is proportional to the amount of infrared radiation absorbed and thus, the temperature of the tympanic membrane can be retrieved from this difference [113].

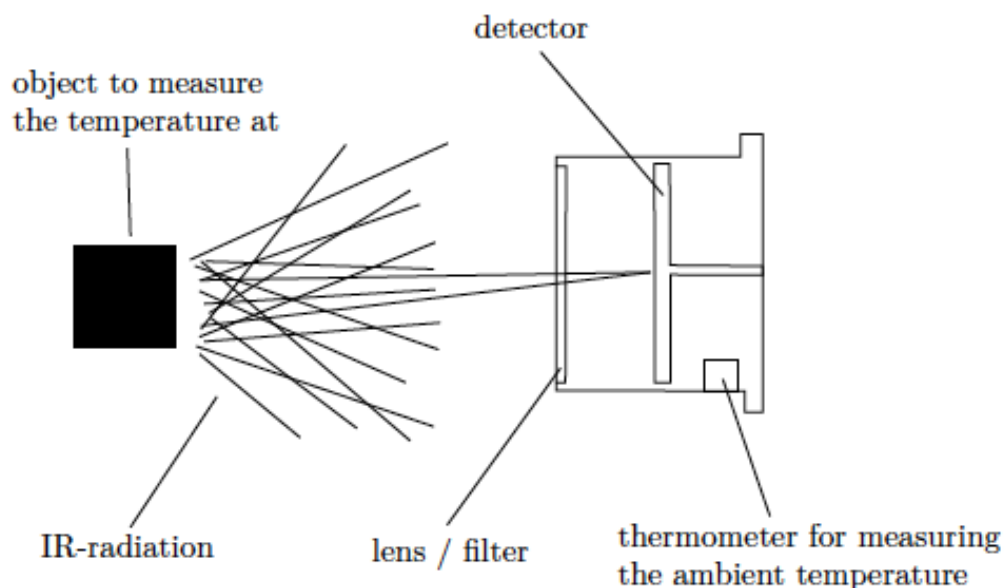


Figure 3.15: Principle inner working of an infrared thermopile sensor [113]

In theory, the thermopile sensor radiates electromagnetic waves into the surroundings including IR radiation [114]. According to Peng et al., the correlation between the radiation energy density and temperature of a targeted object is in accordance with Planck's law when using a tympanic

membrane thermometer [114]. Since the radiated energy is related to an object's temperature, the following equation (3.6) is deployed to obtain E (radiant exitance):

$$E = \delta\epsilon(T^4 - T_0^4) \quad (3.6)$$

In the equation (3.6), E corresponds to the radiant exitance, W.m^{-3} ; δ is the Stefan-Boltzmann constant, $5.67 \times 10^{-8} \text{ W.m}^{-2}.\text{K}^{-4}$; ϵ is object radiation rate; T is the temperature of an object, K; and T_0 corresponds to the ambient temperature around the object, K. In the proposed system, a Melexis MLX90614 infrared thermopile sensor [115] is employed to measure CBT from the ear. This type of tympanic membrane thermometer has high accuracy, particularly for a human body temperature monitoring system and the principle of this thermopile sensor will be explained in depth in a later chapter (Chapter 6) through experimental studies and subsequent discussion.

3.3. Analysis of Photoplethysmography (PPG) Measurement

This section describes what photoplethysmography (PPG) is and how it can be measured as well as from which sites of the body. It is also explained how heart rate (HR) and oxygen saturation (SpO_2) can be determined from PPG waves. Furthermore, a basic correlation is illustrated between PPG and ECG waves.

3.3.1. Background to Photoplethysmography (PPG)

PPG is a non-invasive optical measurement technique for the detection of cardiovascular pulse waves produced around the human body [116]. The principle of PPG sensors is optical detection of blood volume changes in the appropriate sites or tissues of the body by deploying light intensity technologies. Blood flow differs during cardiac cycle activities. For example, blood volume can be higher in the arteries during the systolic phase of the cardiac cycle than during the diastolic phase. The aim of PPG sensors is to detect changes in the blood flow volume during these cardiac cycle events. After analysing the changes in the blood flow, PPG can provide information about vital body signs, such as heart rate (HR), arterial blood oxygen saturation (SpO_2), blood pressure and cardiac output, thus making important for wearable sensing technology [117].

The basic principle of the PPG method is that it requires a couple of opto-electronic components: a light source (e.g. infrared LED) to illuminate the tissue (e.g. finger); and a photo detector (PD) to measure the variations in light intensity related to the changes in the blood volume. These variations at the PD are amplified, filtered and finally recorded as a voltage signal, which is called a PPG signal. There are two components in a PPG signal. Figure 3.16 illustrates an example of a PPG waveform, including direct current (DC), and alternating current (AC) components. The DC

component of the PPG signal corresponds to the detected reflected optical signal from the tissue, depending on the nature of the tissue and also the average blood volume of both venous and arterial blood. It is worth noting that the DC component of the PPG signal changes slowly with respiration and thus, it is a relatively constant voltage according to the AC component of the PPG signal. On the other hand, the AC component of the PPG waveform indicates the changes in the blood volume during cardiac cycle events (e.g. the systolic and diastolic phases). The pulsatile component of a PPG signal, the AC component, has its fundamental frequency typically around 1 Hz depending on HR. It is the most significant part of the PPG signal, because it gives the information on HR and other cardiac outputs, whilst also being superimposed onto the DC component [118].

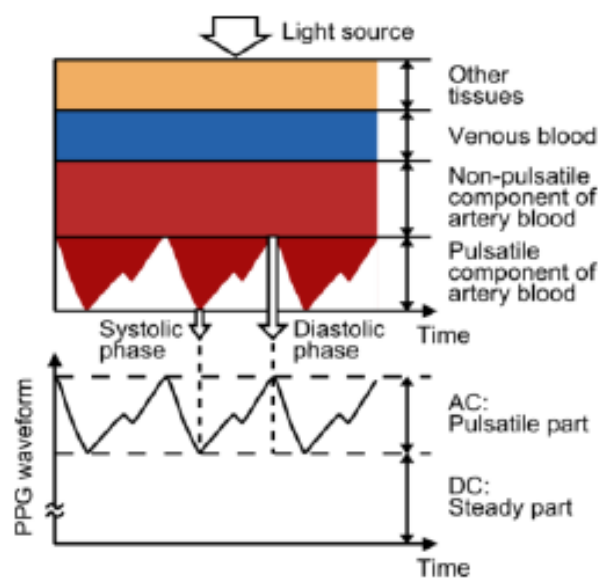


Figure 3.16: Variations in blood volume in light attenuation by tissue [118]

A PPG signal is operated by a red and near infrared (IR) wavelength from a light source. Anderson et al. studied the optical characteristics of light for human skin [119]. According to their analysis, the dominant absorption peak is observed within the blue region of the spectrum, followed by the green-yellow region (between 500 and 600 nm wavelengths), which corresponds to red blood cells. Consequently, this shows that PPG signals can be observed using IR wavelengths as light sources, such as IR LEDs (at around 600 - 800 nm near-IR wavelengths). There are two main modes of PPG signal detection: (a) transmission mode, where the tissue sample (e.g. fingertip or ear lobe) is placed between the light source and PD, so that the light is transmitted through the medium and is detected by the PD; (b) reflection mode, where the IR LED and PD are placed side-by-side, so that the PD detects the reflected light from the tissue or blood vessels. Figure 3.17 shows both types of modes for detecting PPG signals.

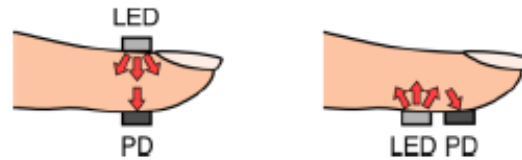
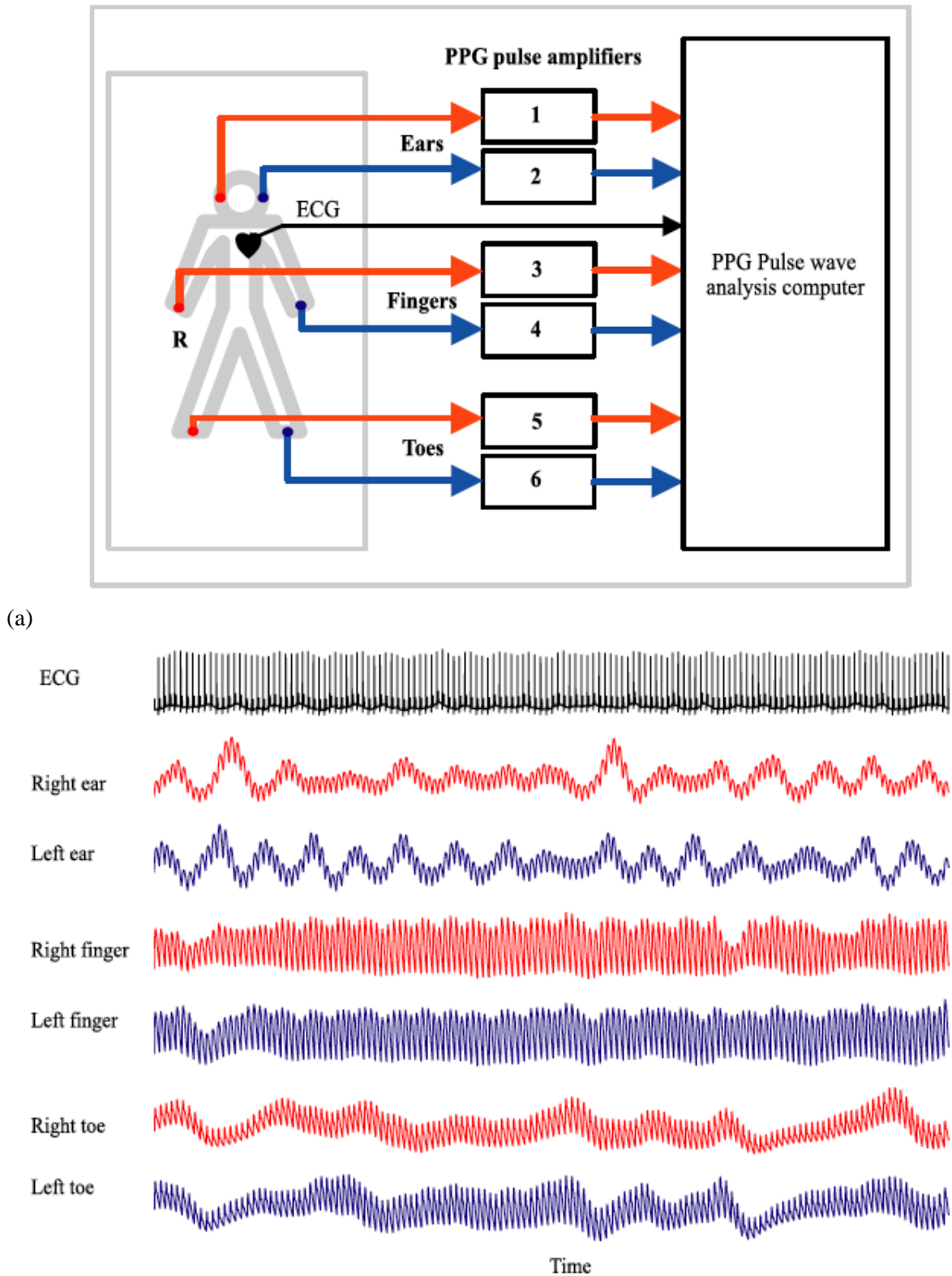


Figure 3.17: Light-emitting-diode (LED) and photo detector (PD) placement for transmission mode (left); and reflection mode (right) for PPG signal detection [118]

3.3.2. Measurements of Photoplethysmography (PPG) Signals

In order to measure good PPG signals, it is important to choose suitable sites on the body. Several studies have elicited that PPG measurements can be made at different locations on the body, including the finger [120], wrist [121], earlobe [122], toes [123]. Commercially, PPG sensors are also available to get signals mostly from the ear, finger, and forehead [124]. According to Tur et al., the earlobe offers a higher perfusion value when compared to those with other measurement sites, when a PPG signal transmitted [125]. Furthermore, earlobe PPG sensors have become popular as fabricating the sensor is easier than for other locations. However, it is not desirable to apply PPG sensors onto the earlobe for long-term monitoring of HR. Whilst there is the potential to design a wearable PPG sensor using the earlobe, it not a user-friendly monitoring method.

The most ideal and common commercially available PPG sensor is based on finger measurements. One of the key elements for obtaining a clear PPG signal pertains to the method of probe attachment to tissue. The finger is quite a suitable site as it has tissue that enables effective probe-tissue interface pressure, such that a good PPG signal can be obtained [126]. In order to characterise PPG signals associated with the measurement sites, multi-body site measurements have been proposed by Allen et al. [127]. Figure 3.18 shows the proposed method of multi-bilateral site PPG measurement and also gives the results from their experiments. As can be seen from the figure, Allen and his colleagues wanted to track PPG records for both right and left body sites to see the differences for healthy and patient subjects. According to their results, there is a similarity in the pulse characteristics between the left and right body sides, but, it is clear from Figure 3.18b that there are differences on the signals' amplitudes at the sites where the body measurements are taken. In particular, finger sites give higher amplitudes than those of ears and toes. The same authors also investigated the PPG measurements for patient subjects and it is seen that the PPG signals are varied on toes sites for vascular patient due to have diseases on the affected leg, thus the amplitude of the PPG pulse is reduced [127].



(b)
Figure 3.18: (a) The structure of the proposed six-channel PPG measurement and analysis system; (b) an example of recorded PPG signals from the right and left earlobes, right and left index fingers, and the right and left toes of a healthy subject [127]

PPG pulse analysis is quite important for clinical aspects and applications including clinical physiological monitoring (SpO_2 , heart rate (HR), blood pressure) as for determining several disease assessments (arterial disease, vascular assessment, ageing health problems, venous assessment) by considering its wave characteristics analysis. Pulse wave analysis was studied many years ago to assess several diseases by Hertzman and Dillon in 1940 [9]. They estimated a crest time measurement from the rising point from the pulse and correlated this to HR. Some years after this investigation, Murray and Foster [128] extracted diagnostic information from the PPG pulse and Figure 3.19 provides a description of the PPG pulse timing measurements, including beat-to-beat PPG rise time, PTT and the main artifacts of PTT information. As can be seen from the figure, the key elements are:

- (a) (PTT_f): beat-to-beat pulse transmit time to the foot of the pulse;
- (b) (PTT_p): pulse transmit time to the peak of the pulse;
- (c) (AMP): foot-to-peak amplitude.

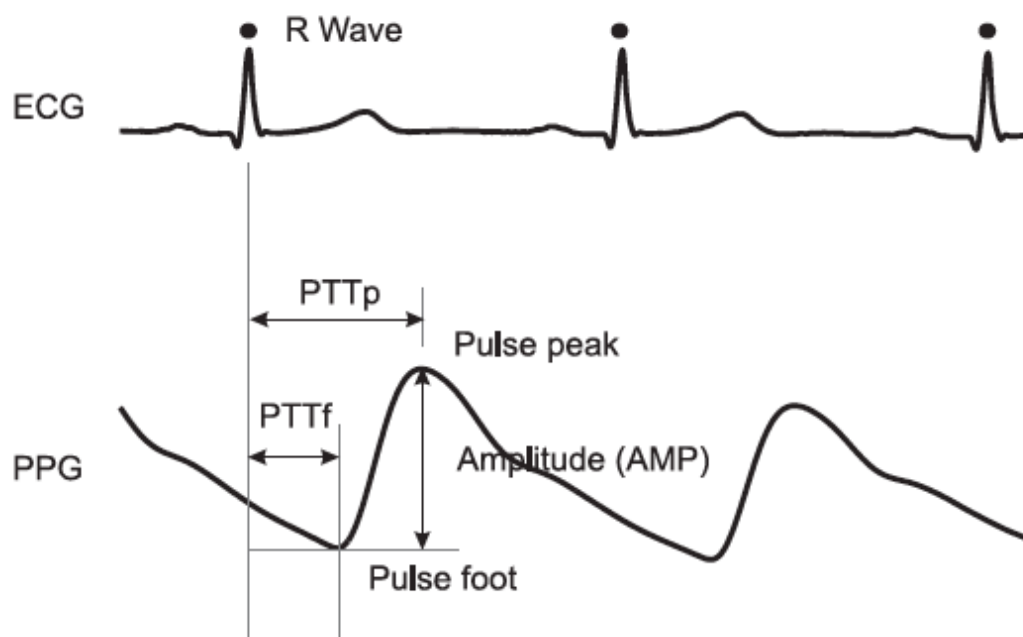


Figure 3.19: Definition of the PPG timing measures, including PPT, PPT_f, PPT_p, AMP [9]

These key landmarks are used to assess various health diseases and the inter-relationship between these characteristics was considered by Allen et al. [129]. According to this study, during the gasping period of a subject, the inter-relations between PTT, and AMP can be analysed for skin temperature variations. Figure 3.20 shows the variations of skin temperature on the finger of the patient against gasping occurrences. Gasp-induced degradations in PTT and AMP can occur along with the respiratory-related changes during the gasping period, or just after or before recovery from the gasp. It can from the figure, that the finger skin temperature (T_f) decreases just after gasp-

induced reductions in PTT and AMP, thus indicating that there is a clear relationship between these characteristics.

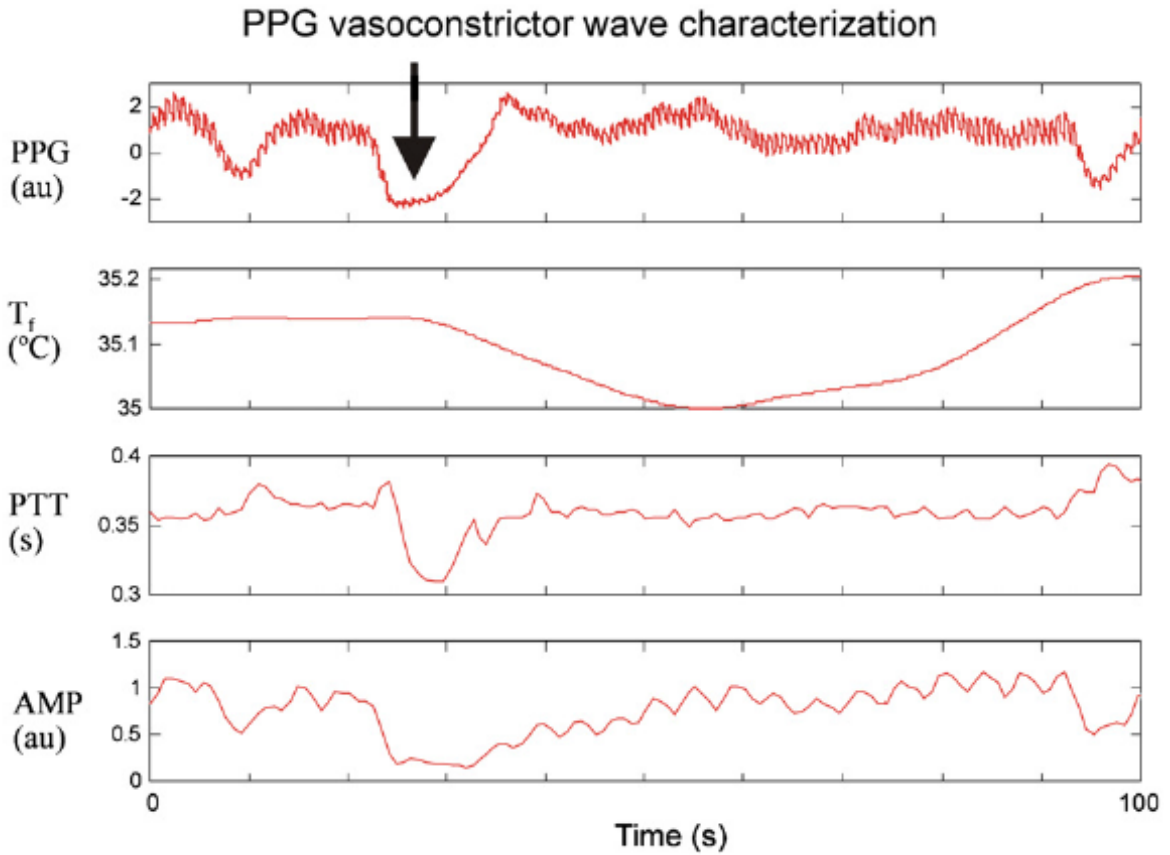


Figure 3.20: PPG pulse wave analysis with its characteristics during a deep gas inspiratory occurrence [9]

3.3.3. Heartbeat Detection from PPG Signals

PPG waveform is a very important for estimating HR and SpO₂ using various clinical applications. Pulse oximetry is one of the efficient tools for detecting and diagnosing cardiac arrhythmias, especially through finger-clip applications [130].

HR can be ascertained from the AC component of the PPG waveform by two different methods. The first involves identifying the peaks of each heartbeat and determining the time interval between the identified peak values of each heartbeat, referred to as the Peak-Peak Interval (PPI). The equations for detecting HR from a PPI calculation are as follows:

$$PPI_n = \frac{P_n - P_{n-1}}{S} \quad (3.7)$$

$$HR_n = \frac{60}{PPI_n} \quad (3.8)$$

As can be seen in equation (3.7), the n^{th} peak-peak interval time (PPI) is defined as PPI_n by the n^{th} peak value (P_n), and $n-1^{\text{th}}$ peak value (P_{n-1}), and sampling rate of the system (S). After this, HR can be calculated by equation (3.8) in beats per minute (BPM).

In order to derive HR, the peak values of the indexes (P_n) and PPI variables need to be identified from the PPG waveform, which involves using several signal processing functions. Figure 3.21 sets out the process of signal conditioning for detection of PPG peak detection and heartbeat.

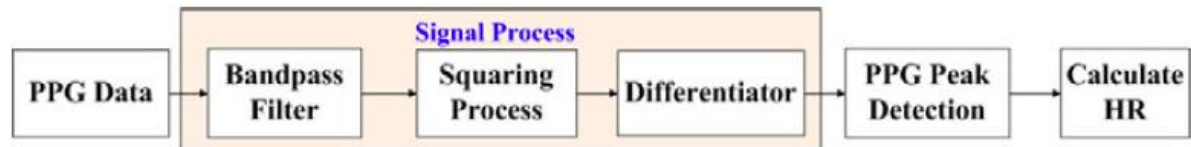


Figure 3.21: Signal processing steps for PPG peak and HR detection [68]

The second method for the detection of HR from the PPG waveform is based on the identification of the frequency response of cardiac outputs. Since the frequency of the power spectrum correlates with HR, energy variations can be identified in the frequency domain by transforming the signals via a Fourier transform. Regarding this method, Stojanovic and Karadaglic have developed an LED-LED based PPG sensor and analysed the acquired PPG signal in frequency domain to obtain HR [131]. Figure 3.22a-c shows, respectively, the original PPG signal obtained by the IR LED-IR LED combination, the filtered AC component of the PPG signal obtained by a third-order low-pass Butterworth filter and the Fourier spectrum of the AC component of the PPG signal along with the frequencies corresponding to HR (dominant). The x-axis of the Fourier spectrum is scaled in beats per minute (BPM), as can be seen in Figure 3.22d, thus HR can be identified in the graph as the dominant index in the frequency domain.

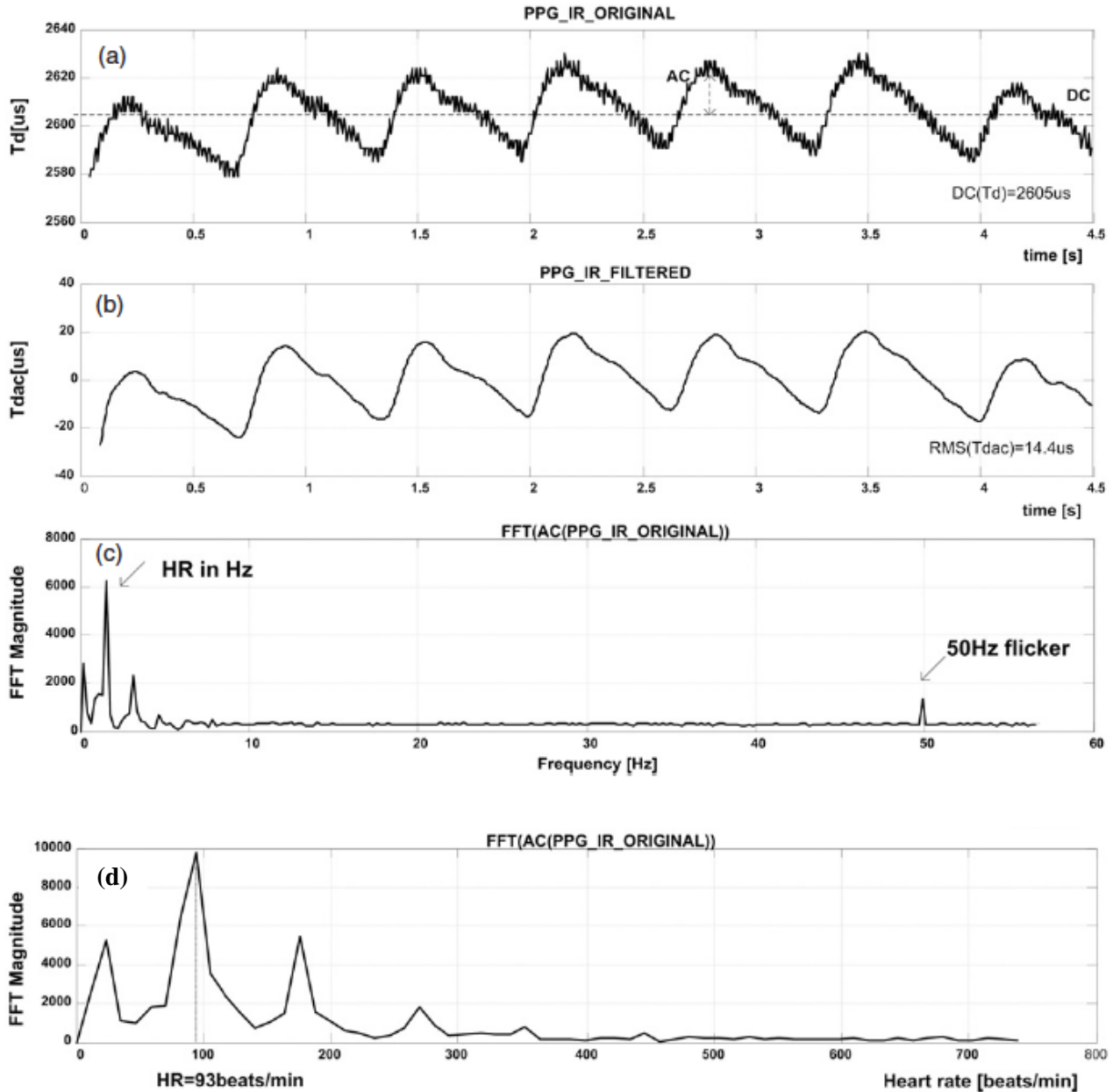


Figure 3.22: (a) Original PPG signal obtained from an LED-LED sensor before filtering; (b) filtered AC component of a PPG signal using low-pass Butterworth filter; (c) Fast Fourier Transform (FFT) spectrum of the AC component of the PPG signal; (d) HR detection in the FFT spectrum of the AC component [131]

3.3.4. Oxygen Saturation (SpO_2) Detection from PPG Signals

One of the most useful parameters from the PPG waveform is blood oxygen saturation (SpO_2). According to Rusch et al. [132], SpO_2 measurements were made by comparing red and infrared (IR) diode signals using the equations (3.9) and (3.10). Furthermore, the AC and DC components of the pulse signal are needed in order to calculate the SpO_2 information. As mentioned earlier, an

obtained PPG signal involves both AC and DC components of the red and IR LED signals, an example of which is given in Figure 3.23, showing the AC and DC components of the PPG signal.

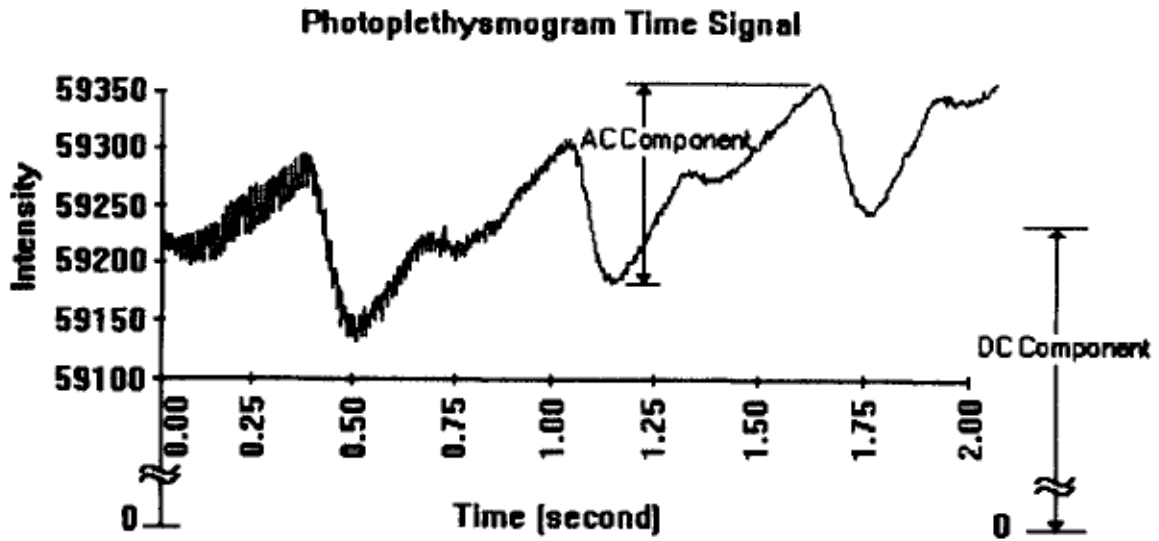


Figure 3.23: PPG signal with AC and DC components [132]

The first stage for expressing SpO_2 is to calculate the R -value by identifying the red and IR signals. The R -value is referred to as the normalised ratio of the red signal to IR transmitted light density. The oximeter ratio R -value is determined by measuring the AC component of the signal and dividing by DC component of the signal, as given by the following equation:

$$R = \frac{AC_{red}/DC_{red}}{AC_{IR}/DC_{IR}} \quad (3.9)$$

When the calculated R -value is plotted against measured arterial oxygen saturation (SaO_2), there will be a linear approximation between them and then SpO_2 can be determined from the following equation [132]:

$$SpO_2 = 110 - 25R \quad (3.10)$$

3.4. Summary

The theoretical backgrounds of electrocardiogram (ECG), core body temperature (CBT) and photoplethysmography (PPG) measurements have been presented in this chapter along with the mathematical expressions of HR, CBT, SpO_2 measurements. Firstly, ECG physiology has been explained in this chapter including ECG waves and lead positions, the electrical model of ECG measurement, and the skin-electrode interface. It was also elucidated how heart beat detection is derived from an ECG signal. Secondly, CBT measurement was explained through the deployment mathematical functions and calculations, in particular, how this can be achieved from the ear canal.

Lastly, the analytical background of a PPG signal was investigated including the algorithm for obtaining measurements to calculate HR and SpO₂ from the finger. In addition, a comparison of the PPG signals obtained from the ear and toe has been made in this chapter.

CHAPTER 4: THEORETICAL BACKGROUND OF GRAPHENE AND DEVELOPMENT OF THE PROPOSED GRAPHENE BASED ECG ELECTRODE

In this chapter, to begin with, graphene (GN) theory explained in terms of its electrical, mechanical, and thermal characteristics and subsequently, the production methods of GN will be explored categorically. Furthermore, the proposed GN-coated ECG electrode is demonstrated step-by-step using the chemical vapour deposition (CVD) method. Moreover, after covering the theory underpinning Raman spectroscopy, its relation with GN is explained. Scanning electron microscopy (SEM) analysis of GN-coated electrodes is presented. At the end of this chapter, a theoretical background is considered in regard the effect of GN on skin-electrode interface.

4.1. General Properties of Graphene (GN)

It has been clearly elicited that nanomaterials improve the physiochemical characteristics of bulk materials, such as conductivity, strength and reactivity, due to their high volume surface ratio, high tensile strength and high electron mobility attributes [133]. Among other nanomaterials, graphene (GN) has received worldwide attention owing to its extraordinary physical, electronic, thermal, optical, chemical, and mechanical properties [134, 135]. GN is composed of a two-dimensional (2D) single-atom-thick layer of sp^2 -bonded carbon atoms arranged in a honeycomb lattice [136]. Due to the unique structure, it is examined as main carbon allotropy to carry out other related carbon nanomaterials, such as carbon nanotubes (CNT), graphite, and fullerenes, as can be seen in Figure 4.1. Geim and Novoselov [135] discovered GN, the thinnest known material with a thickness of 0.35 nm, in 2004 and received the Nobel Prize in Physics for inventing this extraordinary material by a simple mechanical exfoliation. They were studying graphite flakes at the beginning, and after applying several thinner process into the graphite, the monolayer and bilayer of GN were produced.

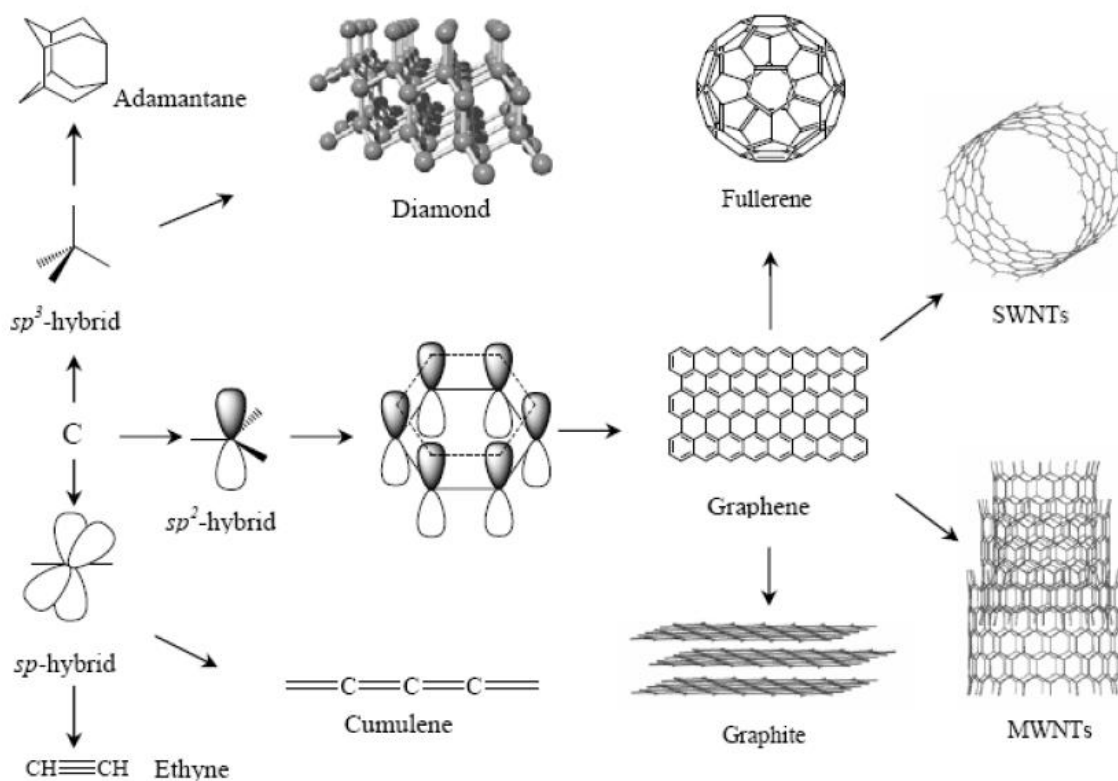


Figure 4.1: Graphene as a “building material” of fullerene, graphite, single wall nanotubes (SWNTs), multi wall nanotubes (MWNTs) [137]

Since then, GN and its related derivatives have attracted the interest of various scientific fields, such as nanoelectronics [138], energy applications (e.g. supercapacitor, solar panels) [139, 140], biosensing applications [141], gas sensing applications [142], transparent flexible electronics [143] due to their physiochemical and electric-electronic properties. A summary of the key properties of GN can be classified as follows:

- It has the highest tensile strength of any material (is the strongest material) – Young’s modulus of 1 TPa is approximately 200 times stronger than steel;
- It is the thinnest material ever tested, only 0.34 nm thick – a single atomic layer of carbon;
- It is entirely transparent - ~97.7%;
- Even though it is the thinnest material in the world, it absorbs a very high amount of light per layer - ~2.3%;
- It is the lightest continuous film (per unit area) – 0.38 mg/m²;
- It has the highest surface to volume ratio of any material – 2,630 m²/g (for this reason, GN is an eminently suitable material for bio-sensing applications);
- It is the best conductor of electricity – it has resistivity of 10⁻⁸ Ωm (better values than any other metal, such as Au or Cu);

- It has the fastest moving electrons of any material $\cong 10^6$ m/s (quite close to speed of light and thus, these are referred to as relativistic particles);
- It has the highest electron mobility of any material – more than $200,000 \text{ cm}^2\text{V}^{-1}\text{s}^{-1}$;
- It is the best conductor of heat – thermal conductivity of $5,300 \text{ Wm}^{-1}\text{K}^{-1}$;
- It is one of the most elastic and flexible materials, because of its thin and strong characteristics.

Furthermore, Table 4.1 compares the key properties of GN with its related carbon materials and good conductive metals.

Table 4.1: Comparison of the relevant electronic, physical and thermal properties of GN with other related carbonic and metallic materials (Si, Cu, single wall carbon nanotube – SWCNT) [141]

Key Parameters	Si	Cu	SWCNT	GN
DC max current density, A/cm^2	-	10^7	$>10^9$	$>10^8$
Melting point, K	1,687	1,357	3,800	3,800
Electron mobility, $\text{cm}^2/\text{V s}$	1,400	-	$>10,000$	$>10,000$
Thermal conductivity, ($\times 10^3 \text{ W/m K}$)	0.15	0.385	1.75-5.8	3-5
Mean free path (nm) at room temperature	30	40	$>10^3$	1×10^3

4.2. Graphene Production Methods

4.2.1. Micro Mechanical Cleavage Method

A number of different algorithms to synthesise GN sheets have been demonstrated since it was first obtained in 2004. Geim and Novoselov [135] followed the route in which a typical Scotch tape was used to extract thin layers of graphite from highly ordered pyrolytic graphite and then transferred these layers onto a silicon (Si) substrate several times. This method is called ‘mechanical exfoliation or micro-mechanical cleavage’, which is one of the procedures for synthesising GN sheets. When the cleaving process is repeated enough times, the remainder produced on the Scotch tape is then transferred to the Si substrate with either a 100 or 300 nm silicon oxide (SiO) layer. These two layer thicknesses can be differentiated from other thicknesses of multi-layer graphene or

bulk graphite via the difference in light absorption. This method of production is the best quality GN synthesis so far, in terms of structural integrity and it is also relatively cheaper than other production methods [144]. Figure 4.2a-d shows the production of GN using the micro-mechanical cleavage technique with ‘scotch tape’, and Figure 4.2e-f shows atomic force microscopy (AFM) images of GN layers on SiO substrate.

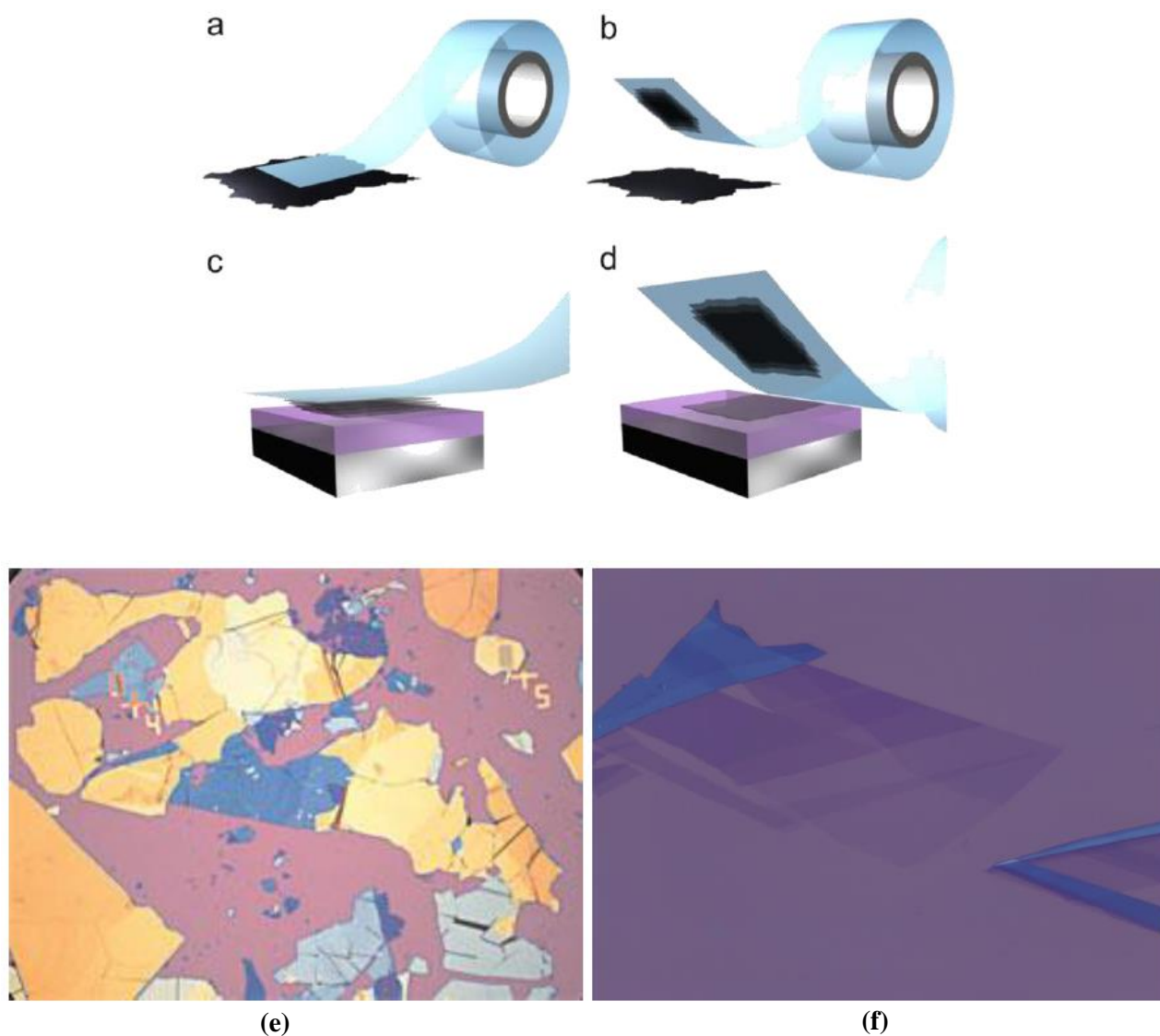


Figure 4.2: (a) Attaching a piece of graphite to sticky-tape; (b) Using the sticky tape to thin out the graphite; (c) Placing the thin graphite on a silicon wafer, with a surface layer of silicon dioxide; (d) Removing most of the layers of graphite leaving behind a single layer, two-layer or multilayer graphene (GN); (e) AFM image of low magnification; and (f) a higher magnification optical micrograph just after micromechanical cleavage

As can be seen in the Figure 4.2, different colours refer to different layers of GN in the AFM images. While a lighter purple means a monolayer GN, a darker layer of purple can be a bilayer, and a one-step darker area can refer to a tri-layer or multiple layer of GN.

4.2.2. Epitaxial Method

Around the same time of the discovery of GN layers from the thin graphite via the micro-mechanical cleavage method, in 2004, researchers at the Georgia Institute of Technology presented an ultra-thin large-scale graphite deposit on a silicon carbide (SiC) wafer [145], providing another method for production of high-quality mono or multiple layer of GN. . This method is referred as ‘epitaxial growth’ and GN is produced by converting this ultra-thin graphite deposited SiC via sublimation of Si atoms at a very high temperature (generally at $\sim 1300^{\circ}\text{C}$) [146]. Figure 4.3 illustrates the process of GN grown by Si sublimation from the SiC surface.

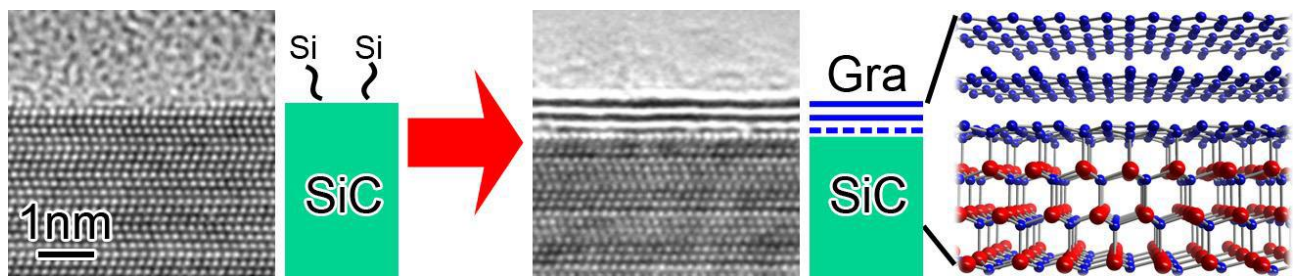


Figure 4.3: Epitaxial synthesis of GN on a SiC wafer [147]

Benefiting from the relatively large yield and fine quality, GN from the epitaxial growth methodology can be good potential for large-scale integration of nano-electronic devices [148]. Nevertheless, it has been noticed that because temperatures up to around 1300°C are required, an ultra-high level of vacuum is needed for this methodology.

4.2.3. Chemical Vapour Deposition (CVD) Method

The chemical vapour deposition (CVD) method can also be applied to the GN grown by epitaxial methodology due to the similar technology needed for high temperature synthesis, but not only on Si substrates, for it can also be employed with Ni and Cu substrates. Among all other strategies for producing GN, CVD on metal substrates has become the most promising approach that has excellent advantages, including the best quality for large-scale applications (with areas larger than 1cm^2), allowing transfer of GN to other metallic substrates (including Au, Ag, SiO_2), which makes it appropriate for different kinds of applications and delivers inexpensive production methods [149]. The first GN grown by the CVD method was applied in 2008 and 2009, using Ni and Cu substrates [150, 151], which was followed by many research applications and publications in transition metal

substrates [152]. CVD operation for GN growth on metallic substrates can be performed in a vacuum with atmospheric pressure (Ar, H₂, CH₄ gasses) and at high temperatures of around 1000°C. One of the most innovative processes for producing single layer GN using CVD is GN growth on copper (Cu). Figure 4.4 shows a schematic of an experimental setup of the CVD operation, which is a commonly used method in order to produce high quality single layer GN by Cu. This method consists of a tube furnace for high temperature heating (at around 1000°C), a quartz vacuum chamber, a vacuum and pressure control system for the growth condition adjustment and several mass flow controllers to provide enough carbon source (CH₄) and reactant gases (Ar or H₂) with the necessary flow rate [153].

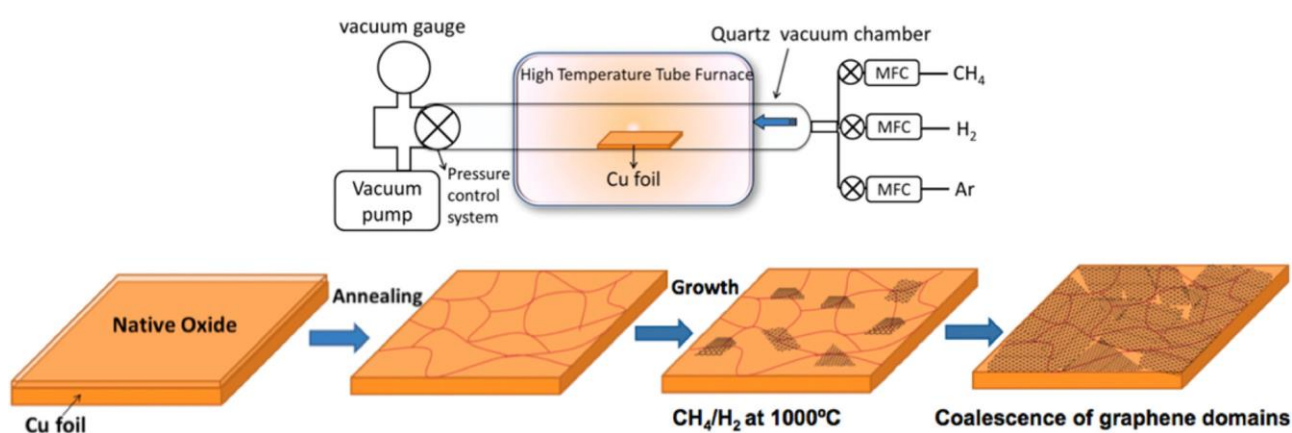


Figure 4.4: CVD method of GN on copper foil [153]

Another advantage of using CVD for GN growth is to enable GN to be grown on transition metals, such as Ag, Au and glass. This method of transferring GN onto another metallic substrate is done through the Cu substrate and subsequently, through chemically etching processes the GN membrane will be free for transferring onto the targeted metallic substrate. Figure 4.5 demonstrates the process of transferring GN from a Cu, Ni, or Si substrate to another targeted metallic substrate. According to this process, first of all, carbon atoms are deposited on the surface of a metal. This carbon-coated metal is heated to a very high temperature (1,000°C), and a gas of C mixed in the metal, thus GN is formed onto the metal (CVD). As in the scotch-tape method, a thin layer of polymer (PMMA or PDMS) is then deposited on top of the GN to start the transferring process. After this, the thin polymer layer is removed with GN from the metallic substrate (mostly Cu or Ni). This polymer-GN layer is then placed on a suitable substrate, which is targeted for device fabrication. Finally, the polymer layer is dissolved away with acetone, leaving GN behind on the arbitrary metallic substrate.

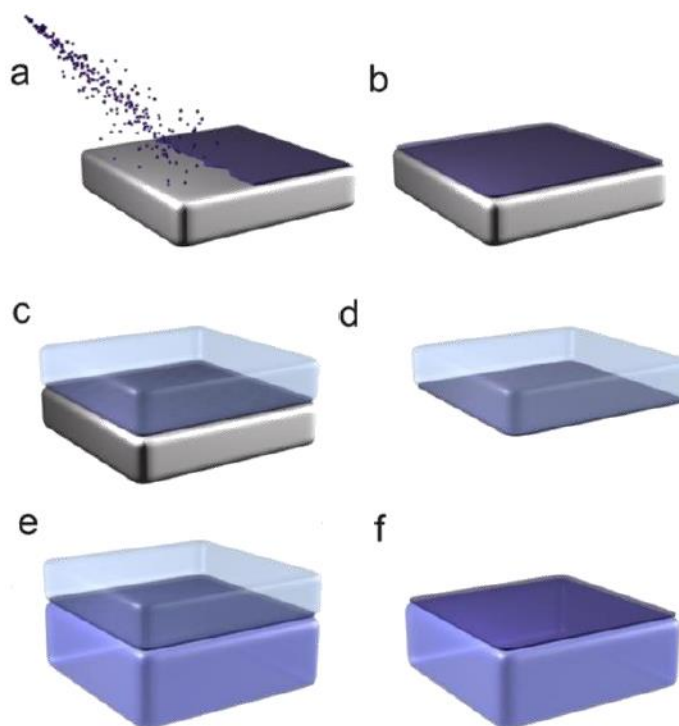


Figure 4.5: (a) Carbon atoms are deposited on the surface of metal (Cu, Si, or Ni); (b) At high temperature this forms GN; (c) A layer of polymer is deposited on top of the GN; (d) The polymer is removed and the GN with it; (e) The polymer is placed on a suitable substrate; (f) The polymer is dissolved away leaving the GN behind

4.2.4. Other Graphene (GN) Production Methods

Up to this point, the main production methods for GN have been explained and several other methods are briefly mentioned here. Another synthesis of GN is liquid-phase exfoliation that involves solution-based exfoliation of GN oxide (GNO) via a dispersion technique [154], which can then be used for producing composite materials [155]. In liquid-phase exfoliation, GNO is mostly formed from graphite by ultrasonic bath sonication with chemically functionalised GN [156]. In terms of applications in particular electrochemical biosensors, GN synthesised by solution suspension of GNO followed by chemical reduction, usually referred to as the reduced GN oxide (RGO) process, and is used most extensively. However, the GN produced by the RGO process offers smaller sizes, more structural defects, and more functional groups than that produced by other synthesis techniques [157]. Overall, the RGO is a better fit for large-scale applications of small GN sheets, while the CVD technique is more efficient for large-scale applications of high quality GN. Accordingly, the application for which GN is being produced should first be ascertained before the most appropriate GN synthesis can be selected, as can also be seen in Figure

4.6. Another alternative method for GN production is through the unzipping of carbon nanotubes (CNTs) via transition metal nanoparticles to form GN nanoribbons [158].

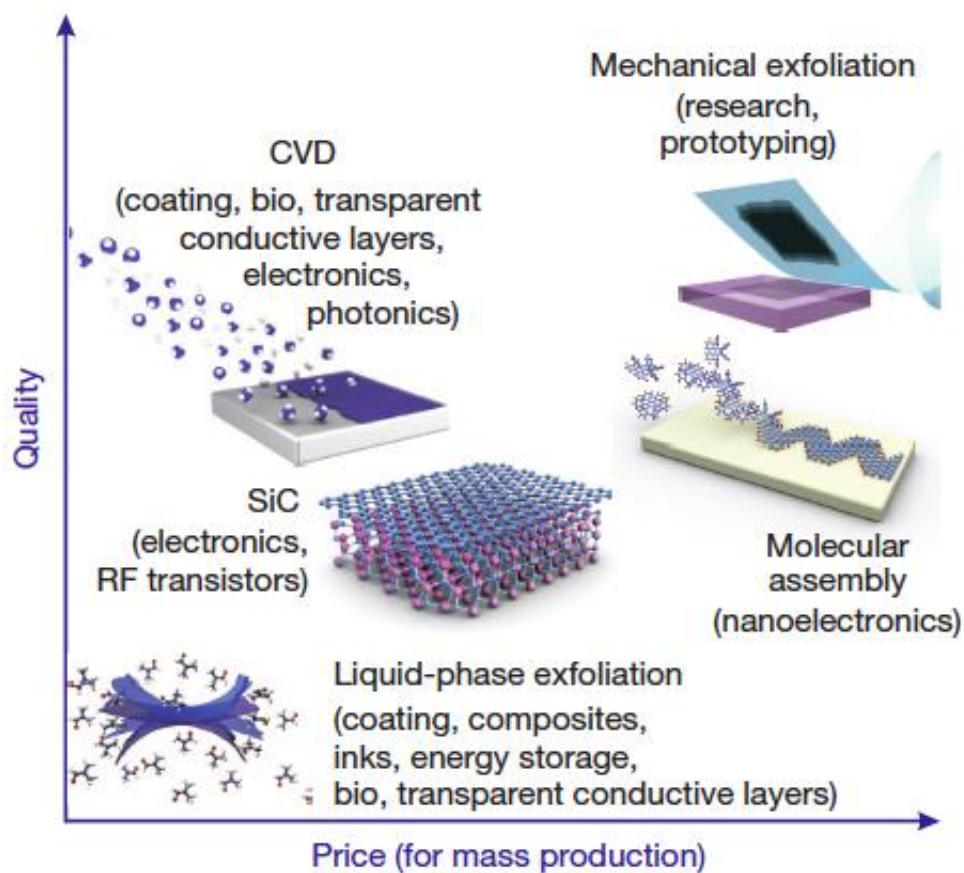


Figure 4.6: Methods for GN synthesis. There are various methods to be chosen depending on the specific application; each one differs from the others in terms of quality and price [159]

There have been many production methods for GN suggested and for an overview, the current GN synthesis techniques are listed in Table 4.2.

Table 4.2: A brief summary of GN production techniques [141]

Synthesis method	Brief description
Mechanical exfoliation	<ul style="list-style-type: none"> • Atomic layer of GN can be seen on ~300 nm SiO₂ substrates • Pristine GN with the highest quality of electrical properties • The size and thickness are uncontrollable, thus limited practical applications
Liquid-based exfoliation	<ul style="list-style-type: none"> • Graphite powders are initially oxidized by chemical modification to be dispersed in solution • Large-scale production for bulk applications, i.e. supercapacitors, composite materials • Serious structural defects
Epitaxial growth	<ul style="list-style-type: none"> • A conversion of SiC substrate to GN via sublimation of Si atoms on the surface • Performed at a very high temperature (~1300°C) • Accessibility is limited due to high-end equipment
CVD growth GN	<ul style="list-style-type: none"> • Most promising, inexpensive and feasible method for single-layer GN synthesis • Uses transition metal (Ni, Cu, Si) substrates • Can be scaled up for large area GN production for practical applications

4.3. Raman Spectroscopy of Graphene (GN)

4.3.1. Basic Raman Theory

Raman microscopy has been proven to be a very powerful tool in the analysis of carbon based materials, including carbon nanotubes, bulk graphite, and graphene (GN) [160]. Within the Raman spectroscopy technique, the geometric structure and bonding properties of the materials can be visualised. Even small differences in geometric structure can lead to significant variations in the observed Raman spectrum of a carbonic molecule. This sensitivity to geometric structure is important for analysis of the different carbon based materials (i.e. diamond, CNTs, carbon nanoribbons and graphite, etc.), where the different forms vary only in terms of the relative position of their carbon atoms and their type of bonding to one another [161]. Consequently, the shapes, intensities and positions of the peaks in the Raman spectrum give considerable information for distinguishing between different types of carbon materials. The major features in the Raman spectrum of carbon materials are the so-called G and D peaks, which are positioned at around 1,560 and 1,360 cm⁻¹, respectively, for visible excitation [162]. Figure 4.7 compares the Raman spectrums of different types of carbon materials: graphite, metallic and semiconducting nanotubes as well as high and low sp³ amorphous carbons. As can be seen in the figure, the positions and shapes of peaks are different for all types of carbon materials.

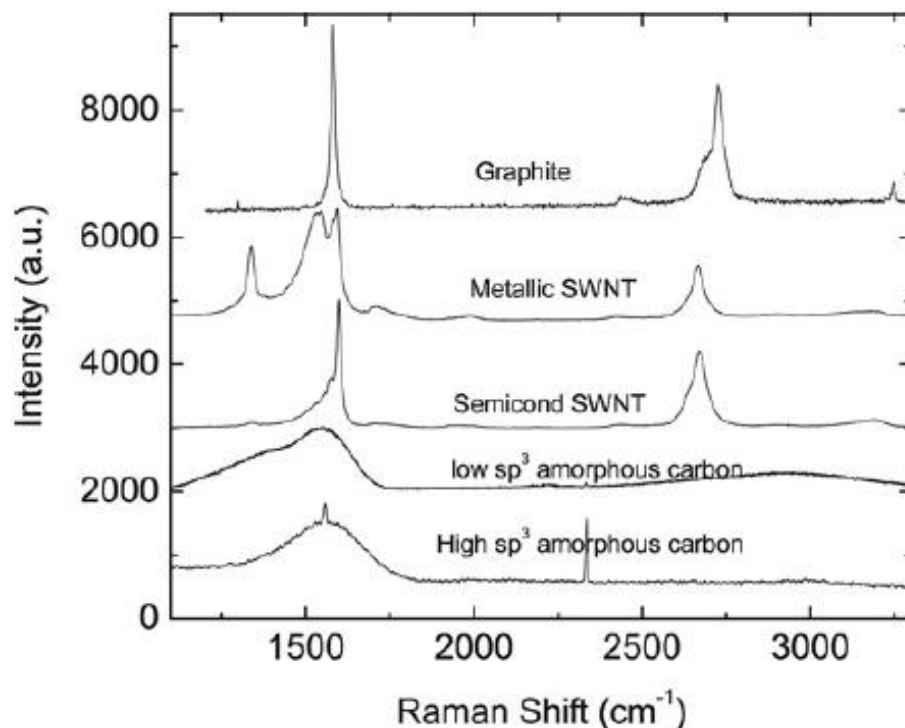


Figure 4.7: Raman spectra of graphite, metallic and semiconducting carbon nanotubes as well as low and high sp^3 amorphous carbons [162]

A simplified schematic of a typical Raman microscopy setup can be observed in Figure 4.8. In principle, a monochromatic light source, a laser light in the range of near IR light to ultra violet (UV) light (typically a 633 nm or 532 nm laser), is sent onto a sample via a series of mirrors and microscopic lenses. This light is then scattered both inelastically and elastically by the sample. This scattered light is then transmitted via a series of mirrors to a two-way mirror, where it is then split away from the incident laser beam. The scattered light is then filtered via the use of a notch filter to remove elastic scattered light. The inelastically scattered light is then split into its constituent wavelengths using a diffraction grating and a charge coupled detector (CCD) is used to measure the wavenumber shifts and intensity of the scattered light, with the Raman spectra of the sample finally being obtained [163].

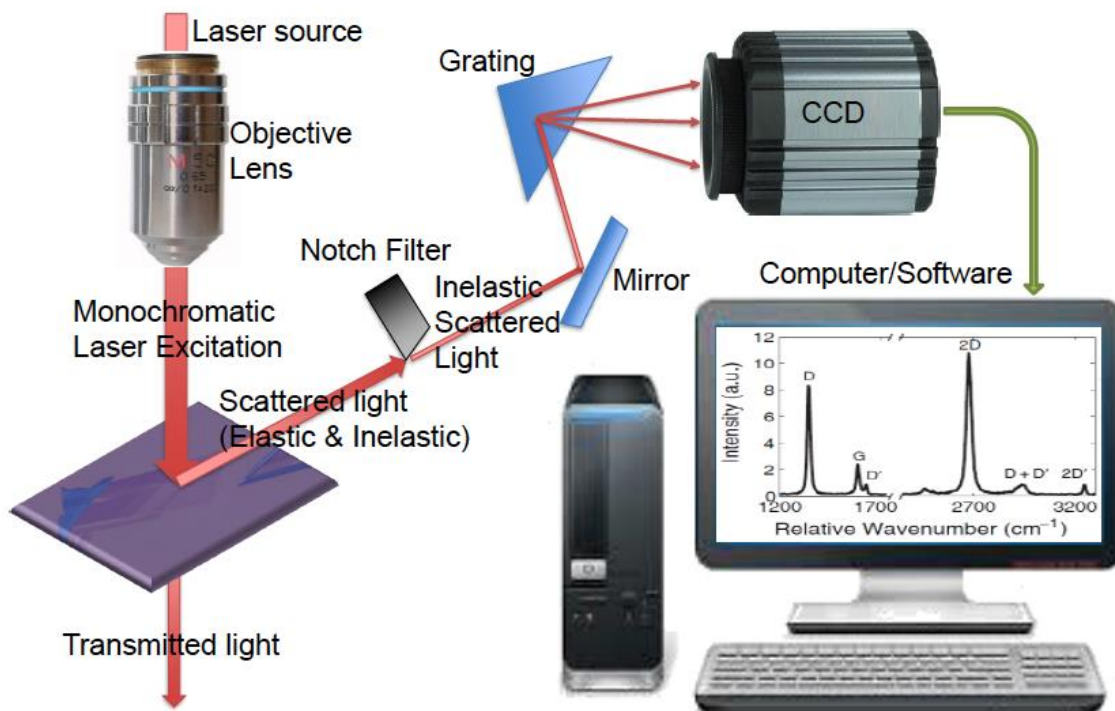


Figure 4.8: Schematic image of Raman instrumentation for obtaining the Raman spectra of a sample

4.3.2. The Raman Spectrum of Graphene (GN)

In Graphene (GN), there are three key Raman bands:

- G Band (around $1,582\text{ cm}^{-1}$) is a sharp band and corresponds to planar sp^2 bonded carbon in GN, graphite and CNTs;
- D band (around $1,350\text{ cm}^{-1}$) is a disorder band and corresponds to sp^2 carbon rings (i.e. defects in sp^2 carbon) and is often regarded as an indicator for defects. It is worth noting that the intensity of D band is proportional to the degree of defects in materials with sp^2 carbon (graphite, CNTs, GN). This band is quite weak in both graphite and GN and if a D band is observed in the Raman spectrum, then there are defects in the carbon materials;
- 2D (G') band (around $2,685\text{ cm}^{-1}$) is the final band and the second order of the D band, being generally used to identify the number of GN layers.

A comparison of the Raman spectra of GN and graphite (composed of millions of layers of GN stacked together) has been made in Figure 4.9a, and measured at 514.5 nm excitation [164]. As can be seen, two major bands (G and 2D bands) are observed in both the GN and graphite samples. While G peak is observed at $1,580\text{ cm}^{-1}$, the 2D (G') band is evident at $\sim 2,700\text{ cm}^{-1}$ for GN, however, these peaks are observed differently for graphite. Regarding which, Figure 4.9b illustrates the differences of 2D bands obtained from GN and graphite, where it can be seen there is a significant variation in the shape and intensity of the 2D peak of GN compared to graphite.

According to the results, the 2D peak in graphite consists of $2D_1$ and $2D_2$, around $\frac{1}{4}$ and $\frac{1}{2}$ the height of the G peak, respectively. GN has a single, sharp 2D peak, about four times more intense than the G peak [164].

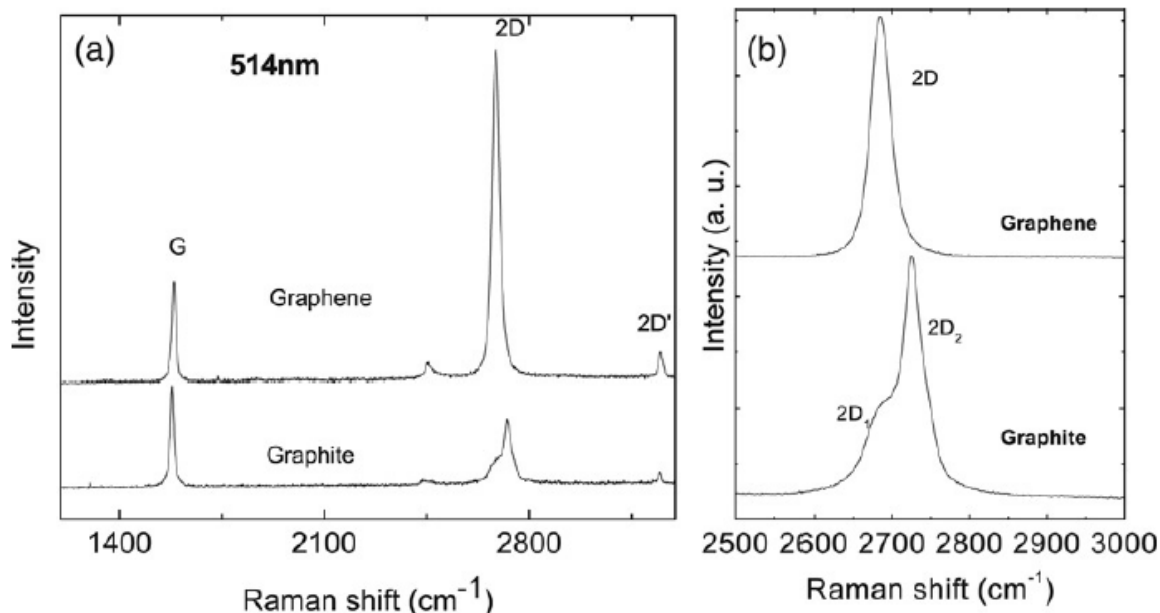


Figure 4.9: (a) Comparison of the Raman spectra of GN and graphite measured at 514.5 nm; (b) comparison of the 2D peaks in GN and graphite [162]

It is observed that these Raman spectra demonstrate the ability to differentiate between single layer GN and graphite. Moreover, the Raman spectrum can differentiate single, double, and triple layers by looking into the positions and shapes of the G and 2D bands, which is explained in the next subsection.

4.3.3. Using Raman Microscopy to Measure the Significant Parameters of Graphene (GN)

It is important to understand Raman spectroscopy in GN and so here, the layers, effects of edges, defects and disorder of GN structure are discussed by considering the key features of Raman bands (D, G, 2D bands). First of all, Raman spectroscopy is capable of determining the number of layers of GN by positioning and shaping of the 2D band. Figure 4.10 shows the differences between single, double, triple and multi-layer GN and also illustrates these bands from GN mapping. According to the graphs, the single layer GN in the 2D band has a single, sharp, symmetric peak. On the other hand, adding successive layers of GN (for bi-layer, triple layer and multiple layers) causes the 2D band to be broken into various individual components. This band splitting and gap behaviour of the 2D band increases, while going from a single layer to multilayer GN. Furthermore, the shape of a 2D band varies when comparing single layer GN with multiple layers of GN samples.

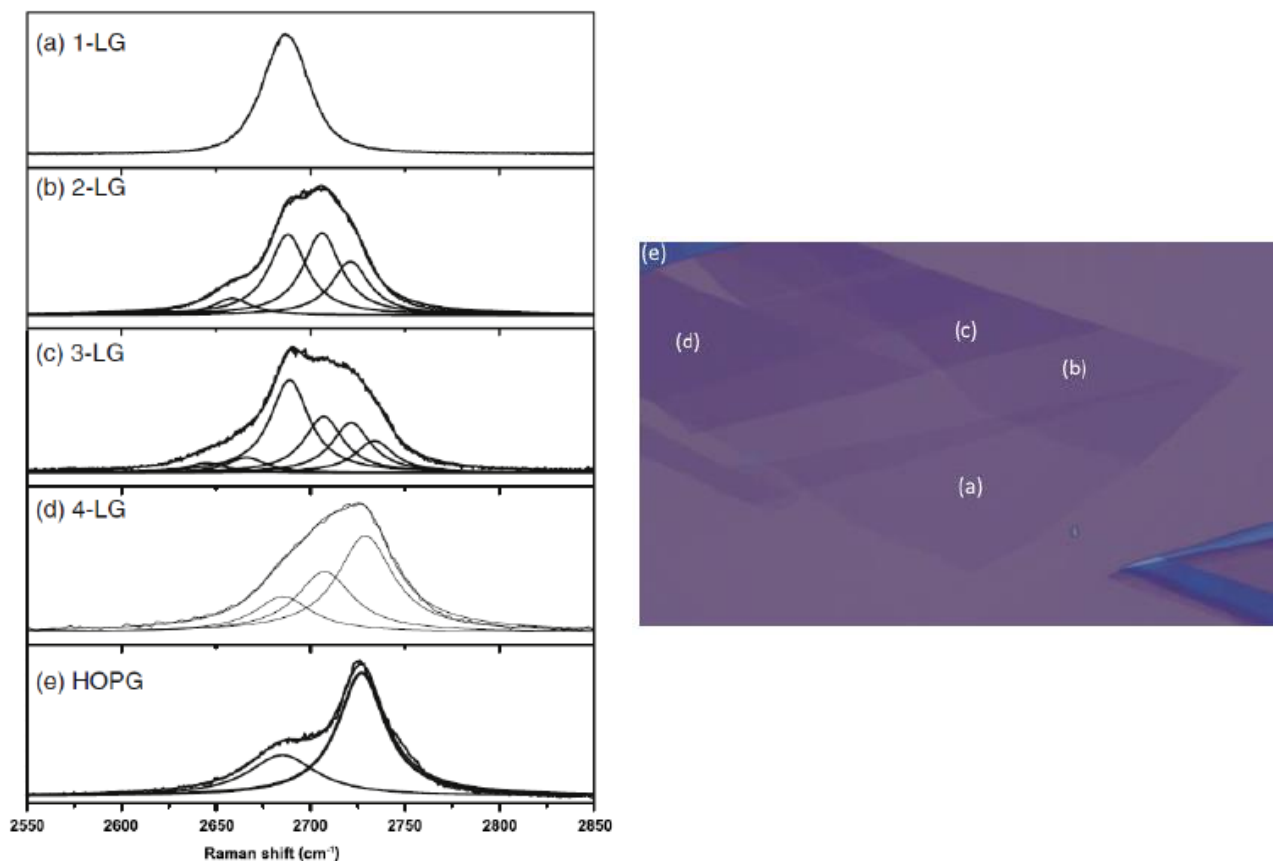


Figure 4.10: (a) The 2D band exhibits a sharp peak of single layer GN; (b) the 2D band of bi-layer GN; (c) The 2D band of three layer GN; (d) 4 layer; (e) the 2D band of multiple layer GN (nearly graphite); GN mapping of these different layers of GN is shown on the right side of the figure [165]

Another interesting aspect of 2D band characteristics is that single layer GN can be identified from the peak intensity ratio of the 2D and G bands. That is, the intensity ratio of the 2D peak decreases when moving from single layer GN to bilayer or multilayer GN. In Figure 4.11, it can be seen that while single layer GN has a high peak ratio of 2D, graphite (composed of millions of layers of GN stacked together) has a low one. In the literature the ratio is denoted as I_{2D}/I_G , as illustrated in Figure 4.11, and this is equal to at least two or higher for single layer GN, depending on the quality of that produced. The Raman spectra in the figure is obtained from a CVD-grown GN sample transferred onto SiO_2 [166], and it is observed that a single layer GN was coated onto a SiO_2 layer via the CVD process. Moreover, the D band is not observed in the high quality of GN.

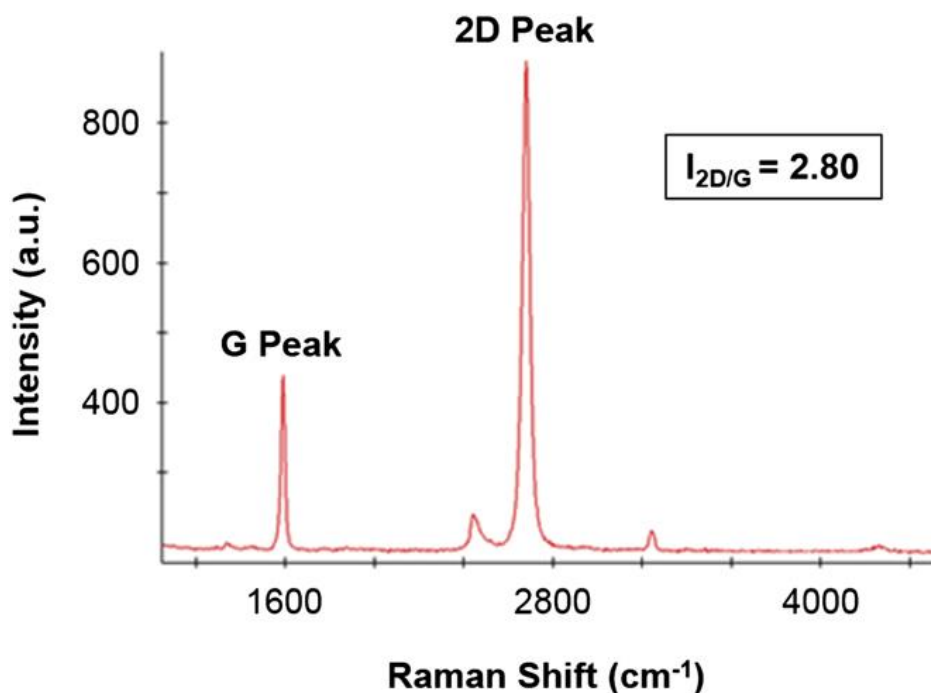


Figure 4.11: Raman spectrum of a single layer CVD-grown graphene sample transferred onto SiO₂ [166]

Another interesting feature can be derived from the Raman spectrum is the edges of different layers of GN samples. Figure 4.12a shows zigzag and armchair edges schematically that are considered ideal edges in single layer GN. Notably, a perfect zigzag edge (it is supposed in pristine single layer GN) cannot produce a D peak [167]. However, for a disordered edge, the sample edges can be seen as defects and the D peak will appear in a Raman spectra. Figure 4.12b compares the D peaks in the Raman spectra of GN and graphite at 514.5 nm excitation. As can be seen in the figure, a single D peak is observed at the sample edge for single layer GN, however, the D peak at the edge of graphite is composed of two peaks (D₁ and D₂), as the behaviour of 2D band. In addition, the ratio $I(D)_{\min}/I(D)_{\max}$ can be used to measure edge imperfection [168].

It is important to notice that the G band intensity is roughly uniform along the graphene surface. On the other hand, the D band can be detected only near the graphene edges. It has been considered that the D band intensity ratios in Raman spectra vary differently in armchair and zigzag graphene edges. Obtained Raman spectra measurements revealed that the D band measured at edges with zigzag orientation is less intense than at edges with armchair orientation.

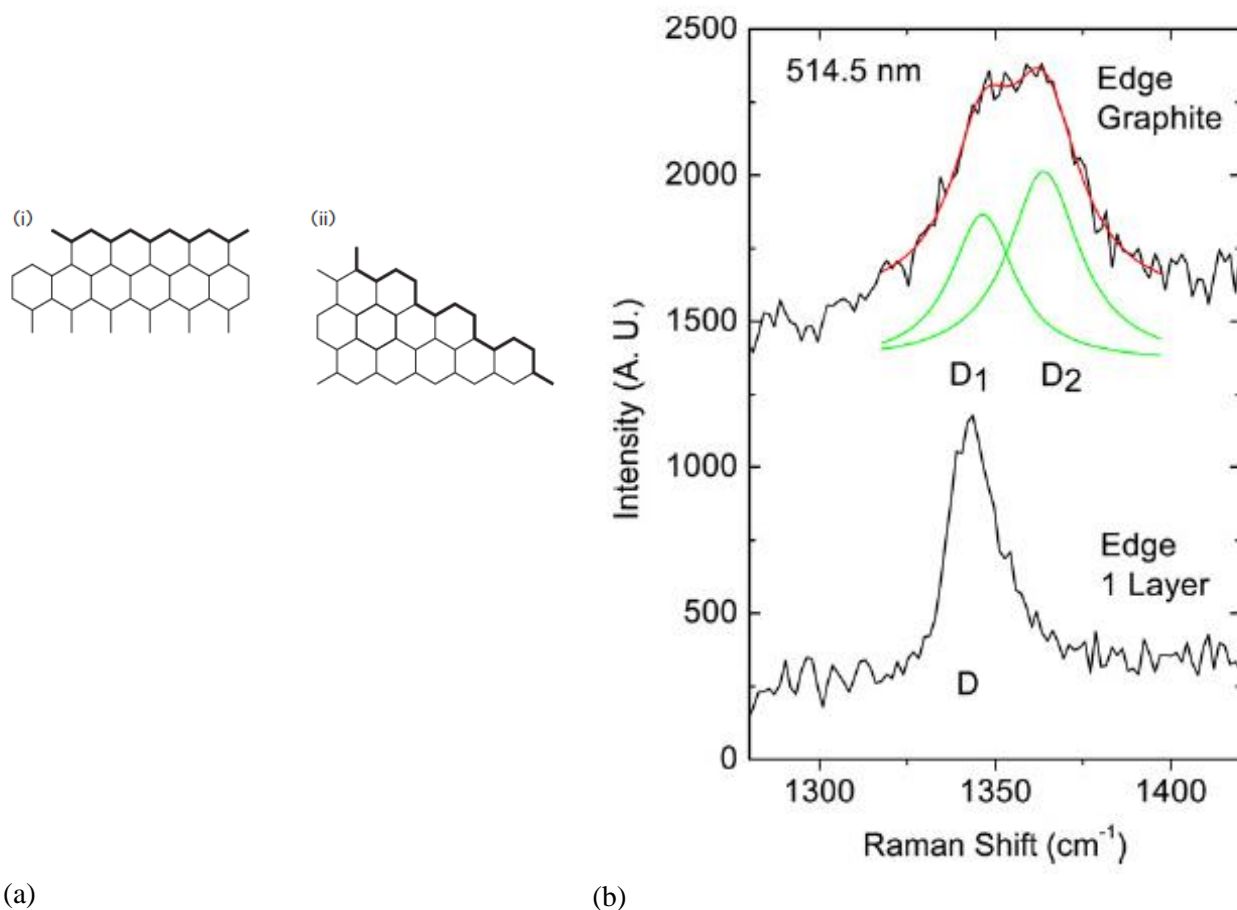


Figure 4.12: (a) (i) Zigzag edge of GN structure and (ii) armchair edge of GN structure; (b) Raman spectra of graphite and graphene edges [169]

Likewise, when analysing edges, the D band is also investigated to display disorders or defects in the sample material. The intensity ratio of the D band is the proportion of the level of defects in the structure of the sample [161]. The main effects in the evolution of the Raman spectrum are D band appearance and the increase in the intensity ratio of the D band with respect to the G band, namely $I(D)/I(G)$, to determine whether there is a disorder or defect in the material.

Furthermore, the Raman spectrum of GN is quite sensitive to changes in the interaction between graphene and a substrate that is important for the development of potential applications of GN and device fabrication. A systematic Raman study of single layer graphene (SLG) produced by mechanical cleavage on different substrates is presented in Figure 4.13. The kind of substrate can be identified unambiguously by Raman spectroscopy from its characteristic 2D band feature [169].

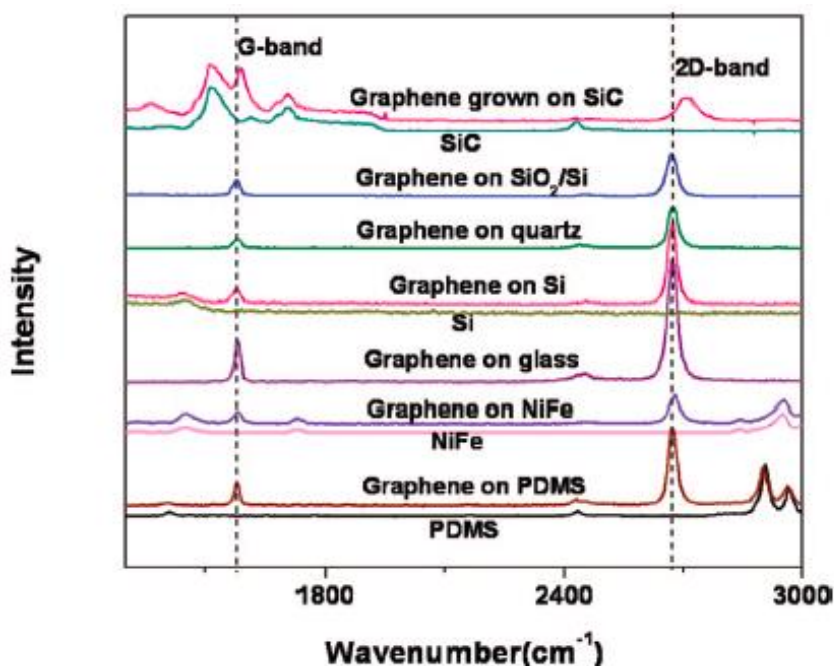


Figure 4.13: The Raman spectra of single layer GN on different substrates via the mechanical cleavage method [169]

4.4. Scanning Electron Microscopy (SEM)

Another characterisation tool for displaying the geometric structure of GN is the scanning electron microscopy (SEM) technique which scans a focused electron beam onto a sample to exhibit its topography and composition information [170]. The incident electron beam interacts with the atom structure in the test sample, which then releases a range of signals that can be detected, analysed and pictured. Figure 4.14 illustrates the typical principle of SEM on a test sample.

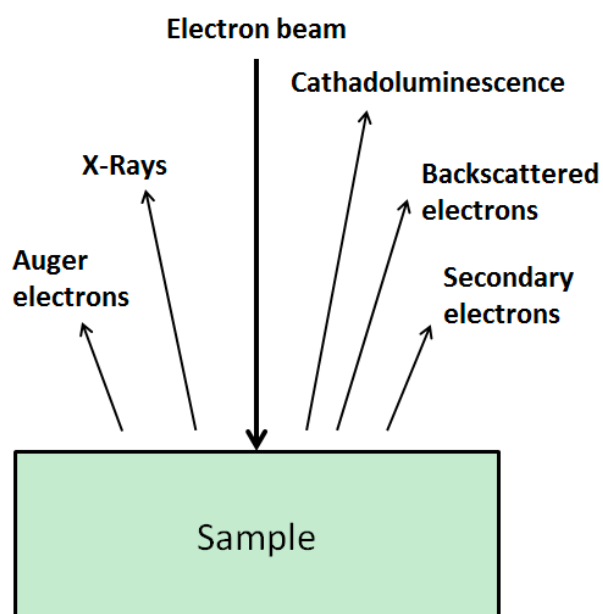


Figure 4.14: Output signals in SEM [170]

SEM plays a significant role in characterising GN, particularly direct imaging of CVD grown GN on copper without transfer. As can be seen in Figure 4.15, GN is observed in darker contrast in the SEM images due to the blockage effect of secondary electrons (SE) [171].

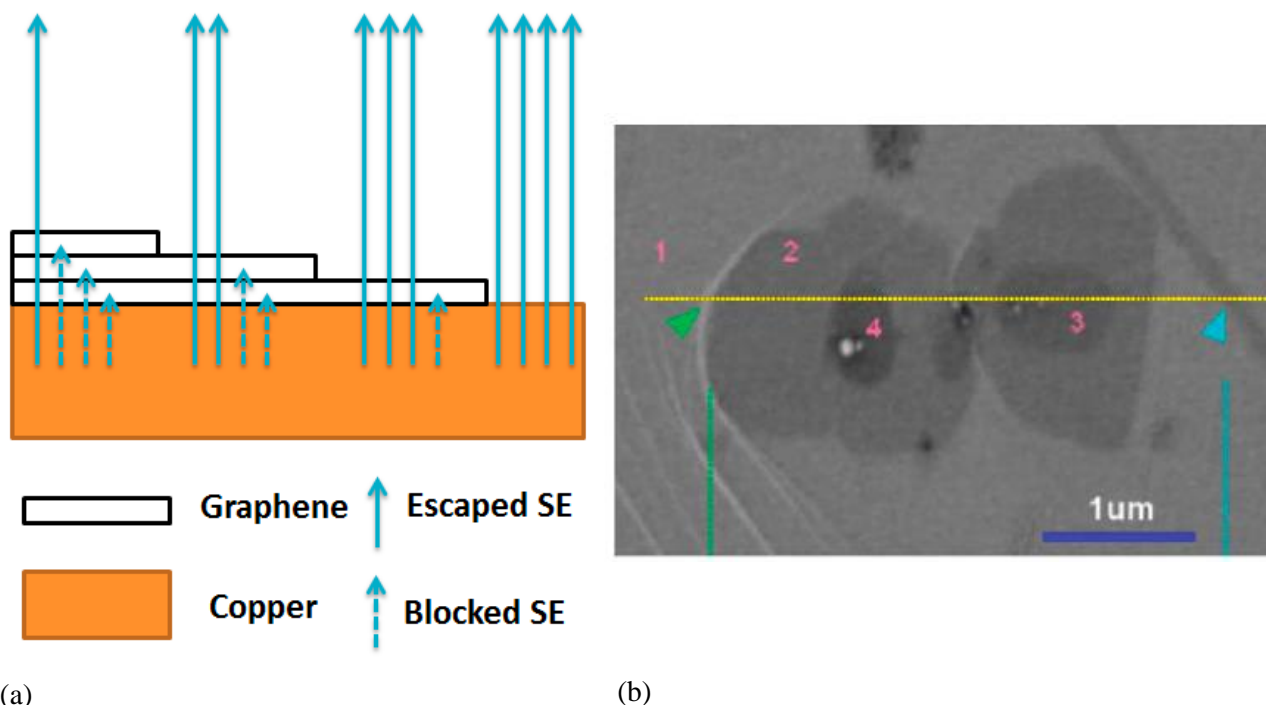


Figure 4.15: (a) Schematic of emitted secondary electrons (SE) blocked by graphene (GN); (b) typical SEM image of CVD grown GN on copper foil. The areas 1,2,3, and 4 with increasing darkness can be attributed to single layer, bilayer, three layer and four layer GN samples, respectively [171]

4.5. Development of Graphene (GN) – An Enabled ECG Electrode Using the CVD Method

The unique structures and superior electronic and electrical characteristics of GN and the amenability of nanomaterial functioning in ECG sensing, hence, to this end, the two are merged here via a simple and feasible fabrication process, whereby an Ag substrate in a typical ECG electrode is patterned by Graphene (GN) as a cladding layer. Based on this technique, it has been presented for the first time here that GN was coated on Ag layer of conventional Ag/AgCl type ECG electrode. It has been demonstrated here also that GN-coated electrodes provided better performances than conventional Ag/AgCl electrodes in ECG measurements, which will be discussed in the next chapter.

Here, the development of GN grown on Ag/AgCl typical ECG electrode is explored using the CVD technique. The GN synthesis, transfer of GN onto the Ag substrate via copper and also the quality of a GN-coated electrode are investigated in this section. Moreover, the obtained images via Raman spectroscopy and SEM are also exhibited here. At the end of this section, the electrical

characteristics of the GN-coated ECG electrode are revealed with regard to the electrical conductivity measurements using a two-probe technique.

4.5.1. Details of the CVD Process Implemented in this Work

In order to fabricate a GN-coated Ag/AgCl ECG electrode, the CVD technique is chosen to grow GN on Ag substrates of the electrode from a copper layer. This has advantages over transition into different metals, such as Ni, Cu, and Si substrates, such as being easier to transfer GN onto different substrates and also CVD-grown GN is an inexpensive and feasible method for single layer GN synthesis when compared to other production methods.

In this project, GN growth is on Ag substrates by transferring from a Cu substrate via the CVD process, which was carried out by a specialist graphene company [172] based in Manchester. The GN was produced utilising hydrogen (H_2) to remove oxygen from the pump system and methane (CH_4) gas to grow single layer GN on copper substrates based on the CVD procedure at a very high temperature (around $1000^\circ C$), similar to those used in the literature [173]. Figure 4.16 shows the whole procedure of CVD for synthesising a GN-coated Ag ECG electrode. As can be seen from the figure, first of all, GN is grown on Cu foil via the CVD process and then a graphene-copper (GN-Cu) substrate is placed on a spin coater to cover the top side of the substrate with a PMMA layer. After fitting the PMMA/GN/Cu substrate together, this triple layer is then placed into a bath of ammonium persulfate ($(NH_4)_2S_2O_8$) to etch away the copper (Cu) from the bottom side of triple layer (PMMA/GN/Cu) until it has been completely removed. After this has happened, the PMMA/GN layer is cleaned and the $(NH_4)_2S_2O_8$ residues are removed by placing it into a deionised (DI) water bath several times. After the PMMA/GN layer is dried, this double layer is placed onto the target substrate (Ag based electrode). Finally, the PMMA/GN/Ag electrode substrate is placed into an acetone solution to remove the PMMA from the sample. Afterwards, the GN/Ag electrode substrate is removed from the solution and dried. However, even with the acetone treatment, the PMMA residues can be still on the substrate. At the end of the CVD process, a very thin layer GN (around $3.7 \text{ \AA} \cong 0.37 \text{ nm}$) is coated on top of the Ag layer of the ECG electrode.

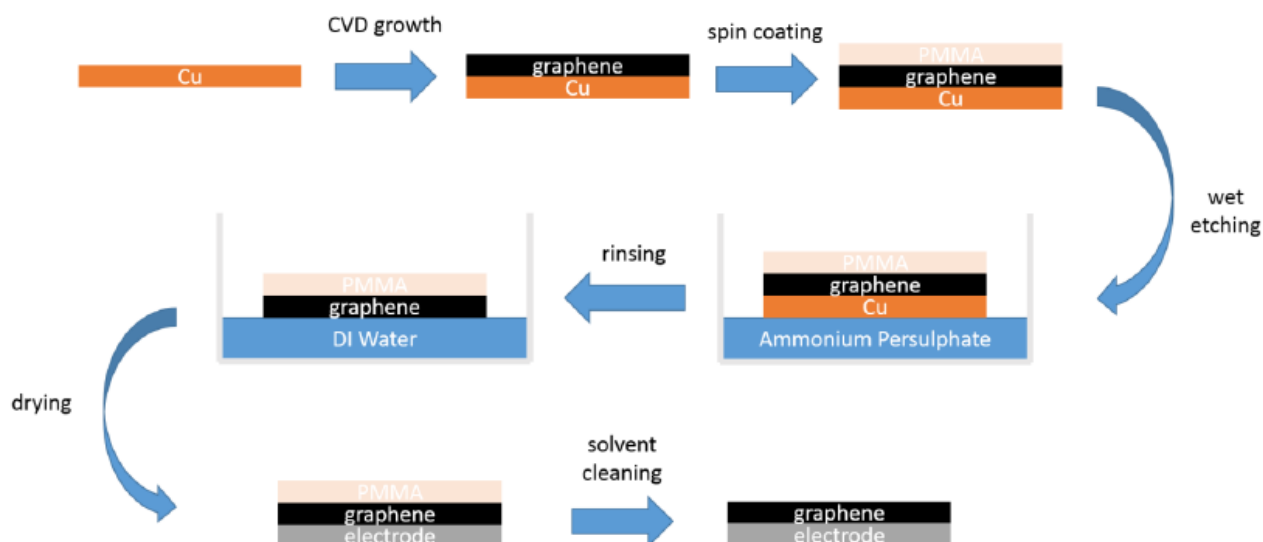


Figure 4.16: Schematic diagram showing the CVD coating process for synthesising a GN-coated Ag electrode

4.5.2. Characterisation of Graphene (GN) - Coated Silver (Ag) Electrode Using Raman Microscopy

Synthesised GN coated ECG electrodes are characterised by Raman spectroscopy, SEM, and two-probe electrical measurement. All the GN sample transfers to the Ag substrate via the CVD process and the Raman spectroscopy (via a confocal Raman microscope) measurements presented in this thesis were carried out in collaboration with 2-DTech, a GN specialising company [172]. Scanning electron microscopy (SEM) images in the thesis were taken with the Zeiss Supra field emission electron gun (FEG)-SEM at Brunel University London.

Regarding the experiments on Raman spectroscopy, the Raman spectra of GN-grown Cu, a bare Ag electrode and a GN-grown Ag electrode were analysed by taking a 10 point measurement across the whole sample surface at 488 nm excitation. Additionally, these 10-point measurements were subsequently obtained using a 514 nm laser in order to get clearer Raman data and rule out any fluorescence signals from the underlying substrate. First of all, the Raman spectrum of the GN-grown Cu was measured (Figure 4.17a) to differentiate the GN on Cu and then the Raman spectra of the GN-grown Ag electrode was analysed to compare it to that of the bare Ag electrode, using 488 nm laser excitation, as can be seen in Figure 4.17b. The results revealed that all three important bands (G, D, and 2D) were observed in the Raman spectrum and thus, the GN-grown processes can be characterised.

According to Figure 4.17a, only G and 2D peaks were observed from the Raman spectra of the GN-coated on Cu sample. Furthermore, it can be seen that a single layer GN was identified for the sample of GN-grown Cu after the CVD process, which was due to the high intensity ratio of I_{2D}/I_G

(around 5-7). In addition, a shift in the 2D-peak position of single layer GN has been observed in the range of $2711 - 2723 \text{ cm}^{-1}$. The value of the full width at half maximum varies in the range of $25 - 31 \text{ cm}^{-1}$, which represents the single layer GN [162]. Figure 4.17b shows the comparison of the Raman spectrum for the GN-coated Ag electrode and the conventional bare Ag/AgCl electrode. It is apparent that the presence of the 2D-peak in the GN-coated electrode differentiates the presence of GN from the bare electrode; the comparison of 2D peak presence was focused in red and black squares.

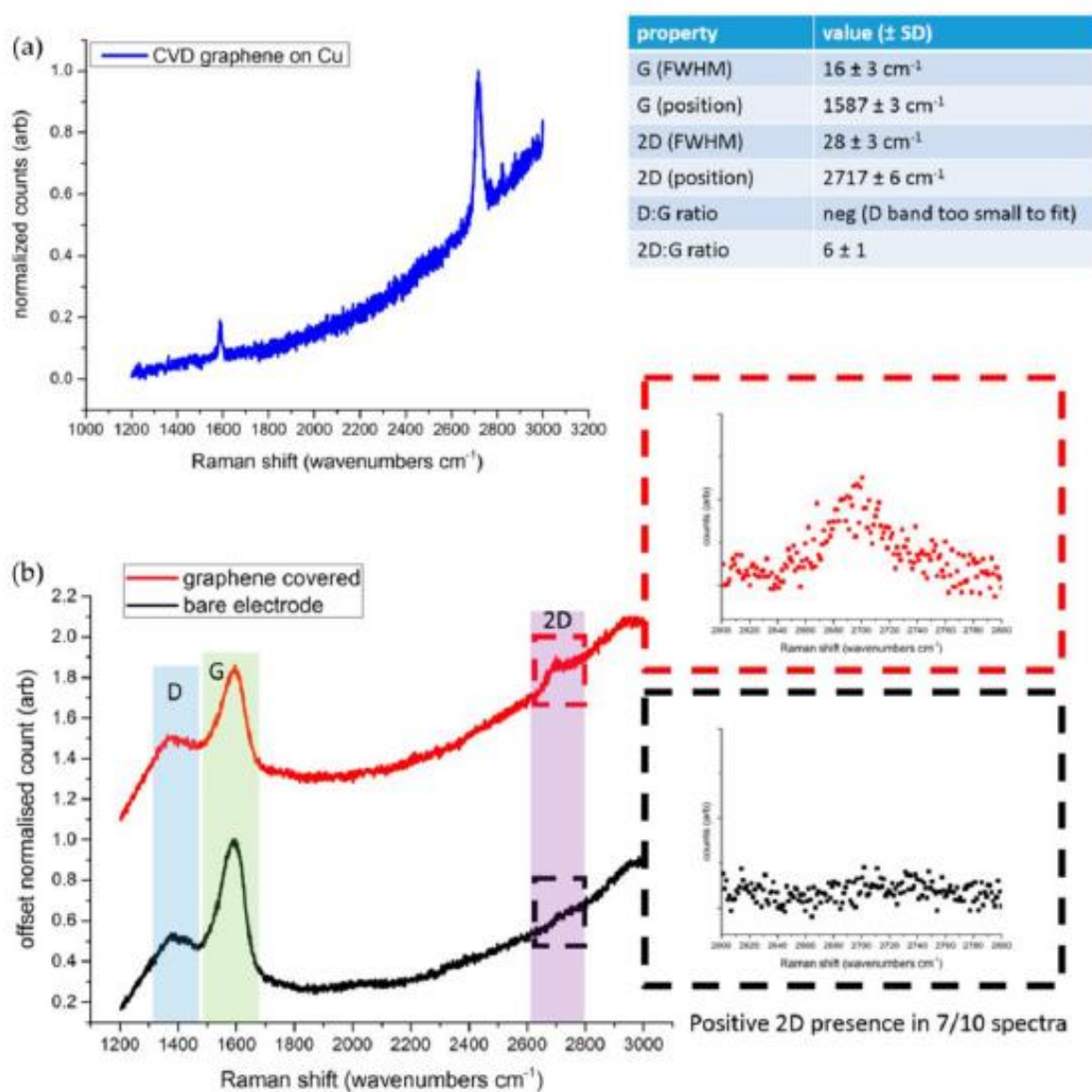


Figure 4.17: Raman analysis of graphene (GN) and a bare Ag/AgCl electrode. **(a)** Raman spectrum of GN-grown on Cu is shown after chemical vapour deposition (CVD); and **(b)** Raman spectrum of a GN-coated Ag electrode and a conventional dry Ag/AgCl electrode, which is shown for comparison

4.5.3. Scanning Electron Microscopy (SEM) Characterisation

Figure 4.18 shows four typical different SEM images of bare conventional Ag/AgCl and GN-coated electrodes with different magnification scales (10 μm and 1 μm). As can be seen from the images, GN has expanded through almost the entire cross-section of the electrode and that it was designed to increase the contact area between the electrode and the skin. These porous structure layers were observed under the scanning electron microscopy (SEM), just after the GN coating process via CVD. SEM images of the GN-coated electrode were taken after several experimental studies. Accordingly, several patterns of residual points were detected just above GN layer on the surface of the electrode (these can be seen in the figure as white areas). In addition, these residual points may occur during the wet transfer process of GN on the Ag substrate and PMMA residues could vary on the surface of the electrode. This can lead the appearance of a defect on the GN-coated sample, as a D band is seen in the Raman analysis in Figure 4.17b. However, because of the high proportional GN effect on the Ag substrate, these images further show that the GN coating has smoothed the surface and hence, can improve the skin-to-electrode contact, with better ECG signals being detected.

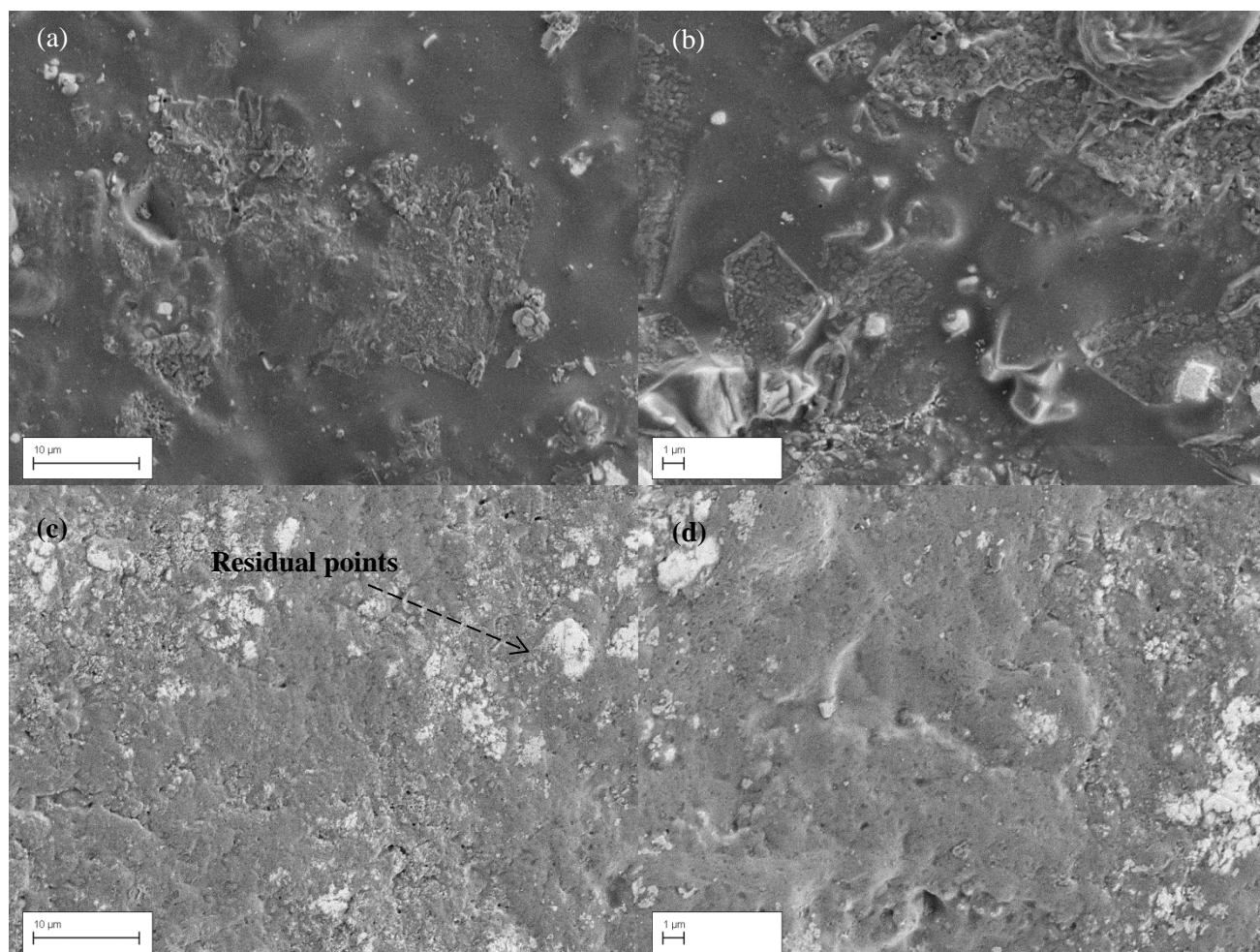


Figure 4.18: Scanning electron micrographs (SEMs) showing: (a) and (b) typical SEM images of a dry electrode before coating; (c) and (d) a graphene-coated dry ECG electrode

4.5.4. Electrical Characteristics of a GN-coated Electrode

To determine the electrical property (resistance through the samples) of synthesised graphene, a two-probe measurement is conducted on the samples before and after GN coating to compare the electrical conductivity values. Figure 4.19 indicates a typical two-probe measurement using a Keithley 2000 multi-meter to read resistances of the bare Ag/AgCl and GN-coated electrodes. Electrical conductivities are calculated from the resistances and dimensions of the electrodes by the following the equation:

$$R = \frac{1}{\sigma} \times \frac{H}{A} = \sigma = \frac{H}{R \times A} \quad (4.1)$$

where, electrical conductivity (σ) is proportional to the length (H) of the electrode, and it is inversely proportional to the resistances (R) and area-thickness (A) of the electrodes. In the experiments, both electrodes are of the same length and area, which are 12mm and 1mm, respectively (the thickness of GN is negligible ~ 0.37 nm). The electrical properties of the bare and GN-coated Ag electrodes were measured at room temperature using a digital multi-meter and the resistance values were obtained as 212 Ω and 28 Ω for the bare and GN-coated Ag electrodes, respectively. After the calculation, the electrical conductivity (σ) of the Ag electrodes before and after GN coating was measured from the derivation of the above equation as 393 S/m and 2,976 S/m, respectively.

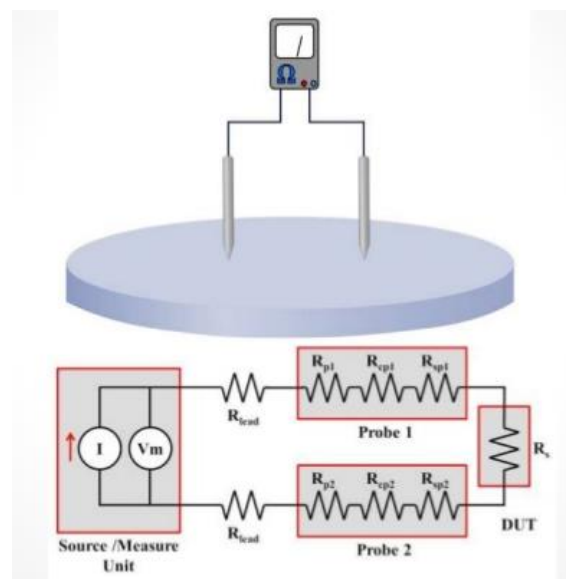


Figure 4.19: Schematic of two-point probe configuration for the resistance measurement of samples [170]

4.5.5. Theoretical Comparison of Skin-Electrode Interface and Its Equivalent Circuit Model Using Ag/AgCl and GN-based ECG Electrodes

Electrical model of the skin-electrode interface was described in previous chapter, Section 3.1.5. According to the information, which is mentioned in that chapter, impedance of the skin-electrode interface (Z) affects the proportion of electrical composition which will be conducted by the electrode. In order to acquire high quality ECG data, the impedance of the skin-electrode interface should be minimized, and the capacitance of the skin-electrode interface should be increased. In this section, the effect of GN will be analyzed in the regard of skin-electrode interface, and the impedance effect of GN will be compared with the conventional Ag/AgCl electrodes. This is because it is important to realize that low impedance is essential for efficient electrode performance, thus effecting ECG signals proportionally. In order to better understand the electrical behavior of the skin-electrode interface and bioimpedance measurements, a simplified equivalent circuit model is shown in Figure 4.20. This equivalent circuit was modelled by analyzing Figure 3.10a, which is exist in the previous chapter, and only interested with components between the skin and electrode.

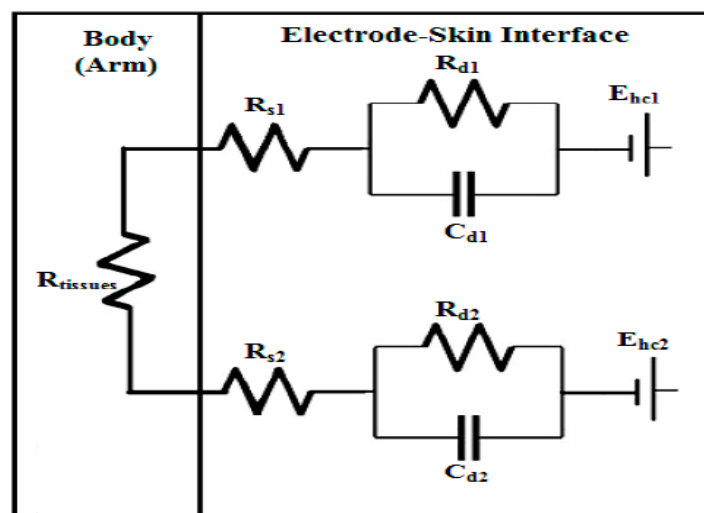


Figure 4.20: The simplified equivalent circuit for the electrodes system in bio-impedance measurements

The impedance analysis of skin-electrode interface was performed by applying two electrodes, as can be seen in Figure 4.20, thus total impedance value is divided by two [183]. In this approach, the applied two electrodes of each electrode type (GN-coated and conventional Ag/AgCl) are assumed to be the same (e.g., identical size, identical material, produced from the same manufacture). The electrode circuit components values for the first electrode are also assumed to be identical with the second electrode ($C_d = C_{d1} = C_{d2}$, $R_d = R_{d1} = R_{d2}$, and $R_s = R_{s1} = R_{s2}$). Here, the capacitance C_d represents the electrical charge between the electrode and skin. R_d corresponds to the resistance that occurs between the skin and electrode during charge transfer, and R_s represents the resistance of the

electrolyte gel and skin tissue [184]. R_{tissues} is the resistance which is sourced by tissues. R_{tissues} value is small relative to the impedance of the electrode-skin interface. For a health human arm's tissue is known be almost 150Ω [184], while the impedance of the skin electrode interface is larger than $1 \text{ M}\Omega$. Hence, R_{tissues} can be negligible for the calculation of skin-electrode impedance and its contribution is considered in R_s .

Equation (4.2) describes the total impedance of the skin-electrode interface for a single electrode as a function of frequency.

$$Z(\omega) = R_s + \frac{R_d/jC_d\omega}{R_d+1/jC_d\omega} = R_s + \frac{R_d}{1+j\omega C_d R_d}, \omega = 2\pi f \quad (4.2)$$

Where f is the frequency (Hz). This formula can be used to compare the impedance of skin-electrode interface using GN-coated electrode to that of conventional Ag/AgCl electrode. Z_g represents the impedance of skin-electrode interface using GN-coated electrode, while Z_s represents the impedance of skin-electrode interface for conventional Ag/AgCl electrode. Due to high electrical conductivity of GN, R_d for GN-based electrode was taken less than that of obtained from Ag/AgCl electrode. Liu et al [185] demonstrated higher capacitance values when GN was coated on an electrode in supercapacitor study. Hence, it is assumed here that C_d can be assigned higher capacitance values for GN-based electrode compared to that of Ag/AgCl electrode. R_s values are assumed here nearly same, however lower resistance is estimated in GN-based electrodes. The estimated values for the electrode circuit model components (R_d , C_d , and R_s) for GN-coated and Ag/AgCl electrodes are given in Table 4.3. The electrode-skin interface model components were estimated by applying near values of which were published in the study of [186].

Table 4.3: Estimated values for electrode circuit model components (R_d , C_d , and R_s)

Electrode type	R_d (k Ω)	C_d (nF)	R_s (Ω)
GN-coated	150	19	247
Ag/AgCl	214	15	280

Because of the high electrical conductivity characteristics of graphene (GN), GN-coated electrode would produce lower R_d and R_s values than pre-gelled Ag/AgCl electrodes. Furthermore, the effect of high electron mobility properties in GN sheets would increase electrical charge potential. Recording biological signals at high C_d values is translated to better biological signal quality [187].

Using the formula (4.2), the impedance measurement is performed for each type of electrode using the values in Table 4.3. According to these values, the impedance for electrode-skin interface for GN-coated electrode is determined as:

$$Z_g = R_s + \frac{R_d}{1+j2\pi f C_d R_d} \quad (4.3)$$

When the circuit model components values of GN-coated were applied as in Table 4.3, Z_g is founded as 438 k Ω . Similarly, when the values of pre-gelled Ag/AgCl electrodes were assigned as in Table 4.3, the impedance for electrode-skin interface for Ag/AgCl electrodes (Z_s) is founded as 555 k Ω using the formula of 4.3. It is worth to mention here that less skin-electrode impedance results better ECG signal quality with high amplitude of QRS complex. In this theoretical study, it is clearly seen that GN-coated electrodes demonstrated less impedance values than that of Ag/AgCl electrodes which means GN-coated electrodes would demonstrate to obtain better ECG signal in experimental study. These values can be varied in the practical work which will be demonstrated in the next chapter.

4.6. Summary

In this chapter, the general background information of graphene (GN) has been provided, including its electromechanical and thermal characteristics as well as the production methods. Moreover, the characterisation tools of GN have been investigated using Raman spectroscopy and SEM. Regarding the GN-coating procedure, the CVD process has been explained step-by-step in relation to the fabrication of the proposed GN-based ECG electrode. Subsequently, this electrode was characterised by Raman spectroscopy, SEM, and electrical conductivity measurements. Lastly, the skin-electrode contact impedance was theoretically analyzed using GN-based and conventional Ag/AgCl electrodes. In this theoretical study, lower skin-electrode contact impedance values were considered with GN-based electrodes than that of Ag/AgCl electrodes.

CHAPTER 5: EXPERIMENTAL SETUP, RESULTS AND DISCUSSION ON GRAPHENE-BASED ECG ELECTRODES

In this chapter, first of all, a series of simulations of a 2D structure of human skin model are presented using COMSOL software to compare the electrical field evaluation using a GN and Ag layer on top of the electrode. Furthermore, an experimental setup of a 3-lead electrode system is explored using different sizes of Ag/AgCl and GN based electrodes for ECG monitoring. Moreover, experimental analysis of ECG signals is carried out using these four types of ECG electrodes. Subsequently, the effect of electrode placement is selected by attaching the electrodes on the ear and chest. After this, a comparison of skin-electrode contact impedance and signal-to-noise ratio (SNR) values is made for conventional Ag/AgCl and the proposed GN-based ECG electrodes.

5.1. COMSOL Simulation of a Graphene-Enabled ECG Electrode

As the effect of different materials (Graphene versus Ag/AgCl) on skin-electrode contact impedance was explained theoretically in the previous chapter (Subsection 4.5.5), it is important to validate this theoretical analysis of a skin-electrode interface by a simulation of a simplified human-skin model and to investigate the electrical characteristics of the proposed simulation. Finite element software, “COMSOL”, was used to analyse the electrical field variations on the surface of a simplified human skin model by applying two types of electrodes, and to examine the variations in the electrical field on the surface of skin model according to size and inner distances of the electrodes.

A simplified human skin model was considered reflecting the depth of a simulated artery. Two electrodes were used to stimulate the artery and hence, the electrical potential, which is generated by the heart, comes to the surface of the skin and electrical conduction could be carried out by the proposed electrodes in this simulation. Two types of electrodes (conventional Ag/AgCl and GN-coated) were used in the simulation to observe the differentiations in the electrical field and surface charge density perspectives. Furthermore, the electrical field was evaluated by changing the inter-distance between the electrodes and also by increasing their size.

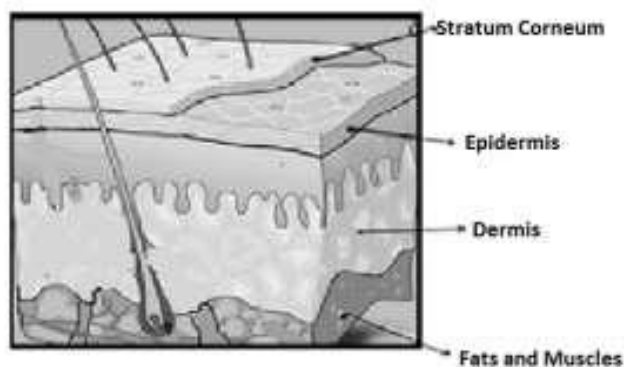
COMSOL Multiphysics software allows the steps in the design modelling, defining the geometry, specifying the physics, meshing the prototype and observing the results on the electrical field surface. Figure 5.1a shows the layers of typical human skin, as drawn by Van de Water [174], consisting of four main layers, referred to as the stratum corneum, epidermis, dermis and layers of sub cutaneous fat and muscles. By utilising this information, a simplified human skin model was

designed with each layer in the COMSOL software, as can be seen in Figure 5.1b. The skin-electrode contact impedance is dependent on the electrical conductivity or resistivity of each layer. In order to activate the skin model in COMSOL electrically, two main characteristics, namely, electrical conductivity and relative permittivity, must be assigned in the regard to the electrical characteristics of each layer. Since the relative permittivity of each layer is constant (~ 1), the electrical conductivity of each of these differs. Here, electrical conductivity values of the stratum corneum, epidermis, dermis, and artery were assigned as 0.0005 S/m, 0.95 S/m, 0.2 S/m, and 0.8 S/m (see in Table 5.1), respectively, in the simulation mode, these values being obtained from [175].

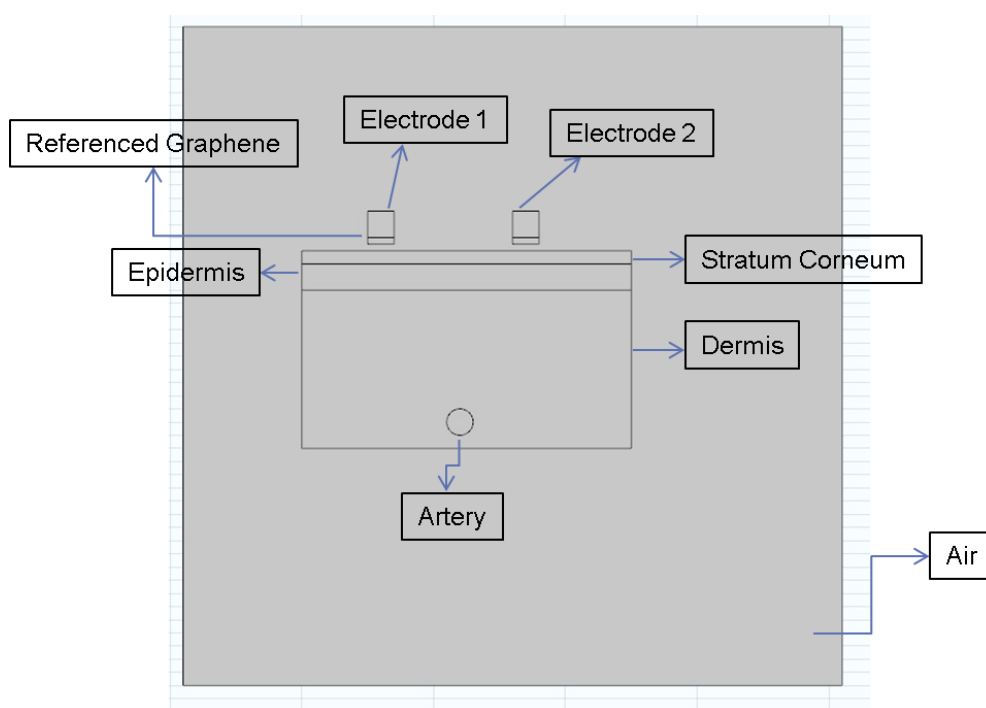
Table 5.1: Electrical conductivity and relative permittivity values of each layer in COMSOL modelling

Layers of Modelling	Electrical Conductivity (S/m)	Relative Permittivity
Graphene (GN)	1.18×10^9	11.5
Silver (Ag)	61.6×10^6	3.4
Stratum corneum	0.0005	1
Epidermis	0.95	1
Dermis	0.2	1
Artery	0.8	1

As can be seen from the figure, there is a bottom layer of the electrode, termed referenced graphene. This bottom layer was filled by Ag first and then GN, in order to compare the electrical characteristics of the two-types of electrode. Accordingly, the simulations were performed for these two types of electrode: conventional Ag/AgCl and GN-coated. The values of electrical conductivity were applied as 6×10^7 S/m and 1×10^9 S/m for Ag and GN, respectively.



(a)



(b)

Figure 5.1: (a) The layers of the human skin [174]; (b) simplified skin model with two electrodes constructed in COMSOL software. Upper layer of both electrodes is filled by Cu, and bottom layer of the electrodes is applied by Ag and GN, respectively

After GN depositing in the bottom layer of the electrode, the concentration distribution of the electrical potential was depicted in Figure 5.2. The electrical field effect shows the electrical composition of an artery, which can be seen in the figure and the capture effect of the electrode on top of the skin layer within the current density lines. This was also analysed in COMSOL and it is apparent in the scale bars (highlighted) that the surface charge density of the GN-coated bottom layer was higher than (two times) the Ag filled electrode, thus capturing more electrical potential from the surface (see Figures 5.2a and 5.2b). It is clear that the GN deposition at the bottom of the

electrodes is capturing more electrical potential due to higher current density. The measurement of electrical field also doubled when using the GN-filled electrode as compared the Ag-filled one.

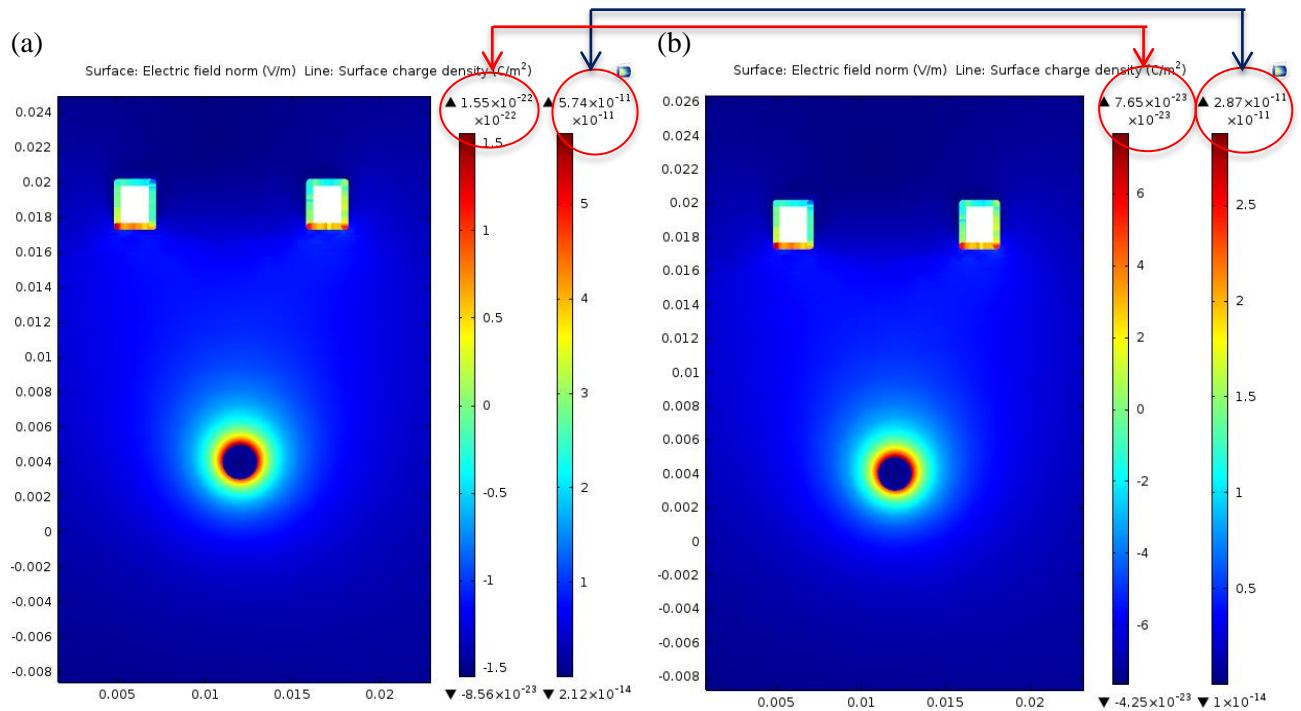


Figure 5.2: Comparison of the electric field effect and surface charge density of the electrodes using (a) GN-based; and (b) conventional Ag/AgCl based electrodes

After all the electrical fields and surface charge density characteristics were simulated, the type of mesh to be used in the construction of the skin-electrode model was provided by COMSOL. Figure 5.3 illustrates the type of mesh selected, where the distribution of the electrical potential through the mesh topography can be observed.

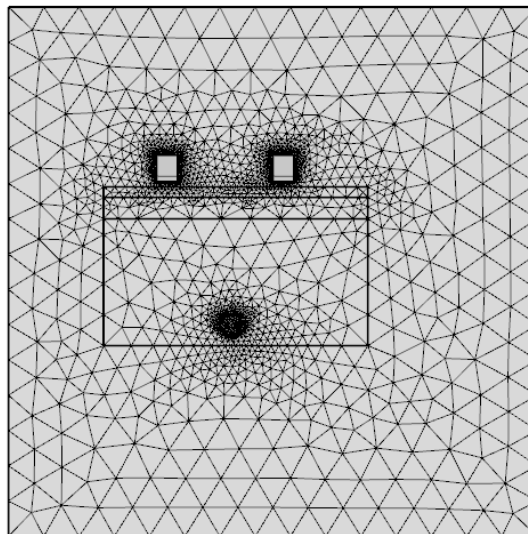


Figure 5.3: Mesh construction of the skin model in COMSOL

In addition, the effect of the inter-electrode distance was examined and the electrical field distribution evaluated through COMSOL software. The inter-distance between the electrodes was adjusted initially as 4mm, and then increased to 6, 8, 10, 12, and 17 mm, successively. It is observed that the electrical field distribution is inversely proportional to the inter-electrode distance and the optimum electrical field was measured as 1.16 V/m at 4 mm. Figure 5.4 shows the electrical field response to the inter-distance between the electrodes.

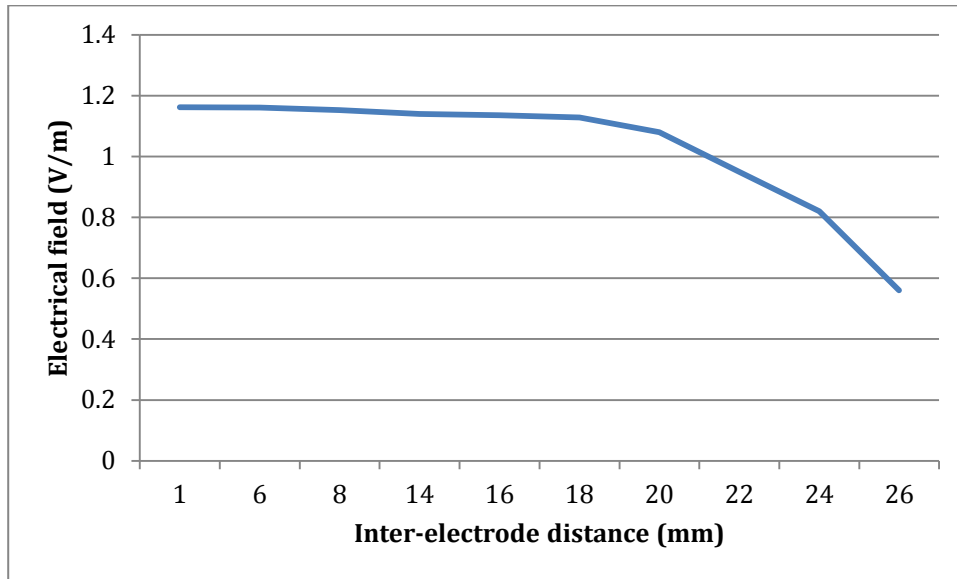


Figure 5.4: The relationship between the inter-distance of the electrodes and the electrical field

The last investigation here, the performance of electrical field, was also evaluated against the change in electrode sizes. In COMSOL modelling, the area of the electrodes was increased from 4mm^2 to 10, 12, and 14mm^2 , consecutively. It is observed that the electrical field magnitude is directly proportional to the size of the electrode and the best performance is evaluated at an area of 14mm^2 with 1.14 V/m. Figure 5.5 illustrates the electrical field ratio against to the change in the size of the electrodes.

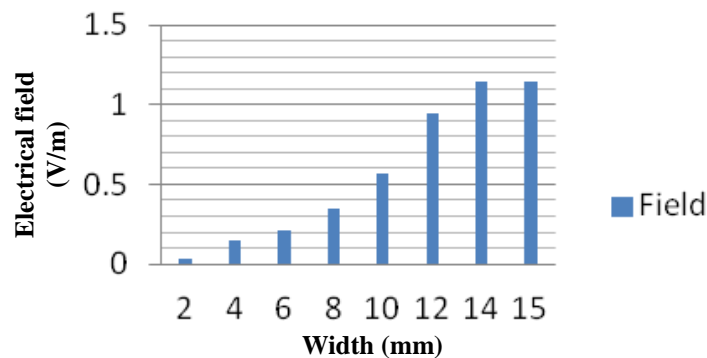


Figure 5.5: The relationship between the width of the electrodes and the electrical field magnitude

5.2. Experimental Setup and Results with Discussion on the ECG Monitoring Using Adhesive Ag/AgCl and Graphene-Coated Electrodes

ECG signals were initially investigated using a patient monitoring system manufactured by Braun International [176]. This instrument was used to compare ECG signals acquired from the conventional Ag/AgCl and proposed GN-coated electrodes. This patient monitoring system has several capabilities of real-time monitoring of ECG, PPG, SpO₂, and respiration rate. The aim of this performance evaluation using Braun patient monitoring was to simplify the measurements and conduct robust performance of GN-coated electrodes over conventional Ag/AgCl electrodes. In the next section, the effect of the electrode placement for optimal ECG monitoring using the proposed GN-based electrodes is examined, with comparison of the results where the electrodes are placed in different positions on the body using both Ag/AgCl and GN-based electrodes in relation to their performances. Figure 5.6a illustrates the Braun patient monitoring system, which was used for performance evaluation here and Figure 5.6b indicates how the electrodes are placed on the chest with lead-1 configuration, which has been explained earlier in Chapter 3, Subsection 3.1.3.

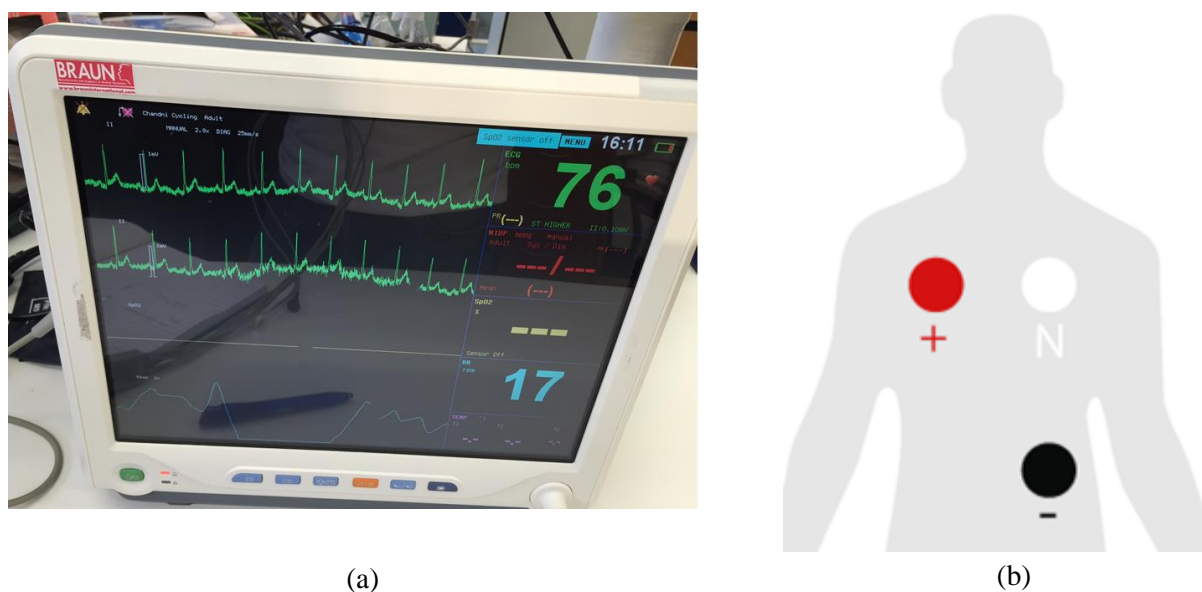


Figure 5.6: (a) Braun patient monitoring system [176]; and (b) the schematic of electrode placement with a 3-lead configuration ECG system

Graphene (GN) was coated on two types of electrodes, which are slightly bigger, known as the Ambu type electrode and a smaller one known as the Covidien type, with a thickness of 0.37 nm. Figures 5.7a and 5.7b show the former just before and after the GN coating process, respectively. This type of electrode has a diameter of 38 mm and a thickness of 1mm. Likewise, Covidien type of electrode is shown in Figures 5.7c and 5.7d, just before and after the GN coating respectively and this type of electrode has a diameter of 24 mm and a thickness of 1 mm. Table 5.2 lists the

properties of the five different tested electrodes, each being identified with a specific name to refer to them later in the figures, as can be seen in Table 5.2.

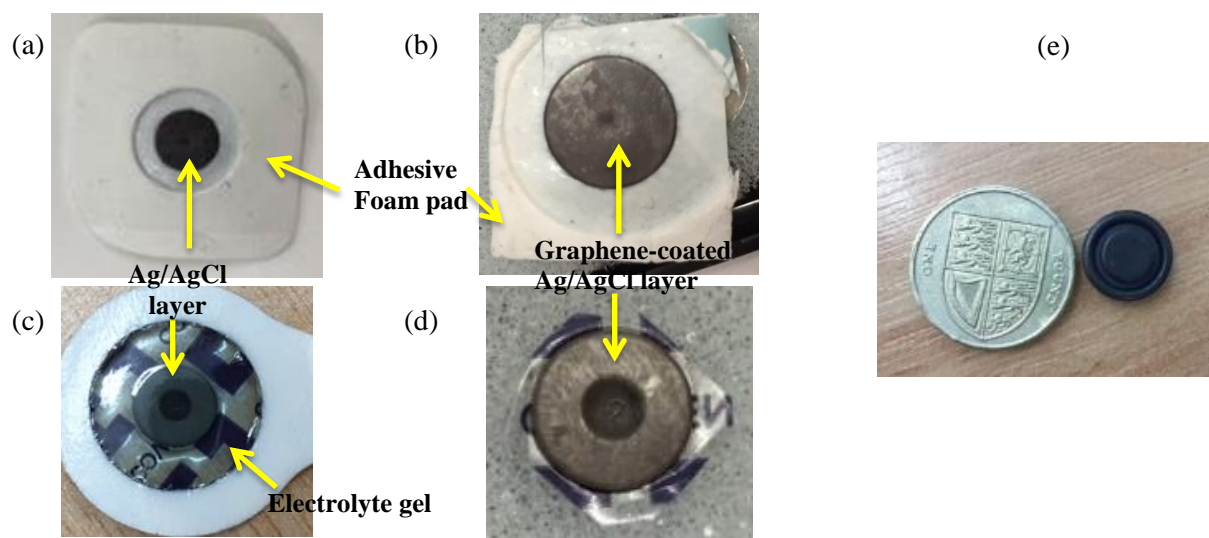
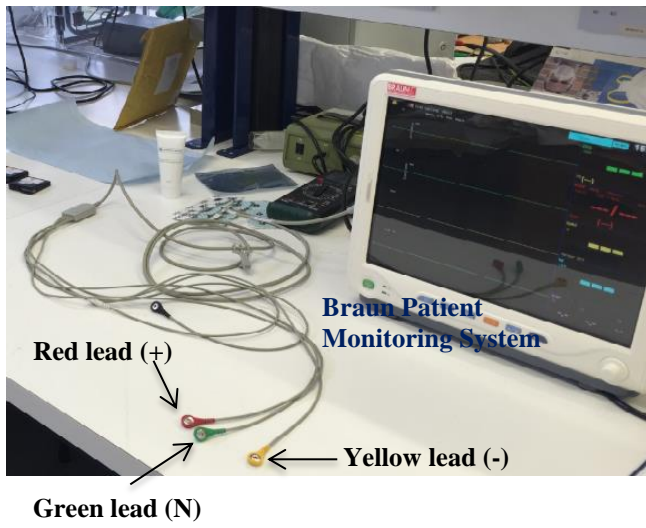


Figure 5.7: Ambu-type bigger size of electrode: (a) Before coating; and (b) after GN coating; (c) Covidien-type smaller size of electrode before coating; (d) after GN is coated on top of the Ag layer of the electrode; and (e) dry Ag/AgCl electrode (even smaller in size than 1 British pound coin)

Table 5.2: The properties of electrodes used for the experiments in ECG monitoring

Name of the electrode	Electrode type	Size – diameter x thickness (mm)
E1	Gel Ag/AgCl Ambu	38x1
E2	Gel Ag/AgCl Covidien	24x1
E3	Graphene-coated Ambu	38x1
E4	Graphene-coated Covidien	24x1
E5	Dry Ag/AgCl	10x2

Furthermore, these electrodes were tested on 10 volunteers to evaluate the performances of the electrodes and to demonstrate the ECG signals obtained from conventional Ag/AgCl and GN-coated electrodes. Figure 5.8 illustrates the test environment in the laboratory and electrode placement on a subject during ECG recording.



(a)


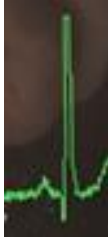
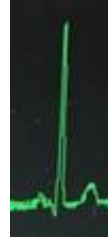


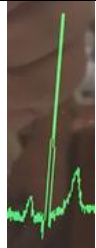

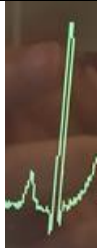
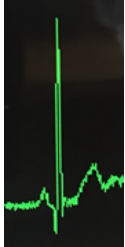
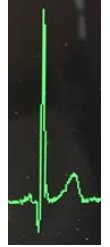





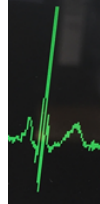
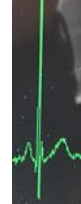
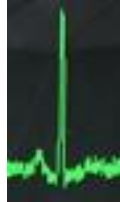
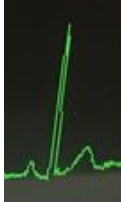


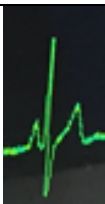
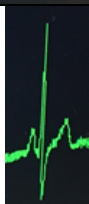
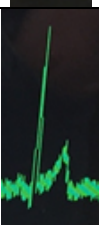

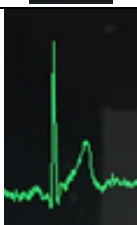



(b)




Figure 5.8: (a) ECG Measurement setup including 3-lead wire-connections; (b) a typical image of ECG measurement using chest-lead (3-lead) configuration

The obtained ECG signals from 10 people (the age of the participants ranged between 24 and 32 years old) are given in Table 5.3, where one ECG waveform is shown per person, including the P wave, QRS complex and T waves. The related personal information is also included in the Table 5.3, such as age, heart rate (HR) and chest type (hairy, slightly-hairy or non-hairy). As can be seen, there is a significant improvement in terms of signal quality for obtained ECG signals using GN-coated electrodes when compared to conventional Ag/AgCl ones. It is also worth mentioning that acquired ECG signals vary depending on the chest-type. For instance, when subject 1 and subject 3 are compared, more noise can be seen in the ECG wave of the former compared to the latter due to the hairy chest.

Table 5.3: Obtained ECG signals from 10 volunteers using conventional Ag/AgCl, GN-coated Ambu and GN-coated Covidien types of electrodes

Subject	Age	ECG Wave (Ag/AgCl)	ECG Wave (GN-Ambu)	ECG Wave (GN-Covidien)	HR	Chest type
1	24				72	Slightly-Hairy

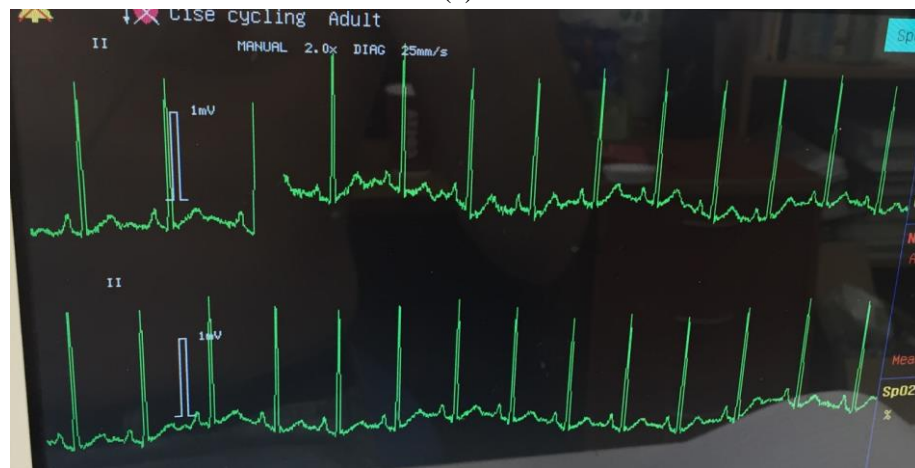
2	29				74	Non-hairy
3	28				76	Non-Hairy
4	29				89	Slightly-Hairy
5	27				74	Non-hairy
6(*)	29				78	Slightly-hairy
7	28				72	Hairy
8	27				74	Slightly-hairy
9	27				76	Hairy

10	32				78	Non-hairy
----	----	---	---	--	----	-----------

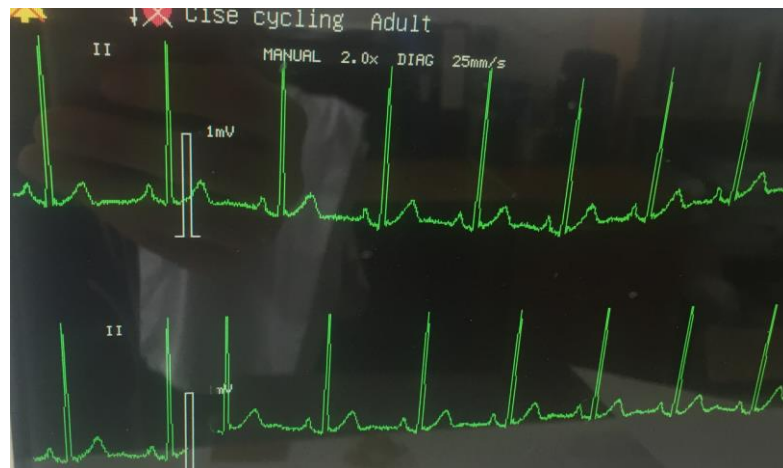
It can be seen clearly in Table 5.3 that GN-coated electrodes improve the ECG signal quality by minimising noise and each P wave, QRS complex and T wave are clearly identified in the obtained ECG. On the other hand, there is signal degradation in the ECG signals when using conventional Ag/AgCl electrodes in some case, due to imperfections in the skin-to-electrode contact. That is, as can be seen in Table 5.3, in hairy-chest type subjects, the obtained ECG signals include noisy data and the main points (P and T waves and QRS complex) in an ECG waveform cannot be identified during the measurements. For example, the signal behaviours of subject 7 and subject 9 are significantly comparable to the other obtained signals, because of the higher contact impedance and lower signal quality. However, the ECG signals were perfectly acquired from the same subjects using the proposed GN-coated electrodes including the critical waves in ECG data, such as the P and T waves, and QRS complex. Figure 5.9 briefly compares the three obtained ECG signals that were acquired using the conventional Ag/AgCl, GN-coated Covidien (smaller size), and GN-coated Ambu (bigger) types of electrodes, respectively. It can be seen clearly that the ECG signal quality was improved using GN, which has the high electrical conductivity and this provides better skin-electrode contact. The electrode size is also another factor that contributes to the signal quality and this has been shown in Figure 5.9. That is, the GN-coated Ambu type of electrode provides better signal-to-noise ratio (SNR) than the GN-coated Covidien type. It is also easy to identify the critical points (P-wave, QRS complex, and T-wave) in the signal obtained using the GN-based bigger size of electrode.



(a)



(b)



(c)

Figure 5.9: ECG recording with (a) a conventional Ag/AgCl electrode; (b) a GN-coated Covidien (smaller size); and (c) a GN-coated Ambu type (bigger size) of electrode

5.3. Performance Evaluation of ECG Signals for Various Electrode Placement Models

5.3.1. Measurements and Comparisons of ECG Signals Obtained by Different Types of Electrodes and Different Placements

Here, ECG signals acquired from five different types of electrodes (adhesive Ag/AgCl Covidien, Ag/AgCl Ambu, GN-coated Covidien, GN-coated Ambu, and dry electrodes) were compared in

terms of signal quality and SNR by placing them at different locations on the body using a wearable e-health module [177]. In this case, the chest- and ear-leads were examined as positions of the 3-electrode system. In addition, the effect of the reference (DRL) electrode position during the ECG measurement was measured.

ECG signals were separately measured from the proposed GN-based electrodes and conventional pre-gelled Ag/AgCl electrodes (Ambu and Covidien types) as well as from the dry electrode via an ECG acquisition system (e-Health and Arduino) using a 3-lead electrode system. Figure 5.10a indicates the integrated e-Health and Arduino ECG measurement system with 3-lead wires, whilst Figure 5.10b shows a block diagram of the ECG measurement system proposed in this work, including the Bluetooth module for transmitting signals to the smartphone for further processing. Initially, a USB protocol is used for UART communication to observe and analyse ECG signals on a PC. Subsequently, the obtained ECG signals were transmitted to the smartphone to display the signals on a developed app, which will be explained in more detail and shown in the next chapter.

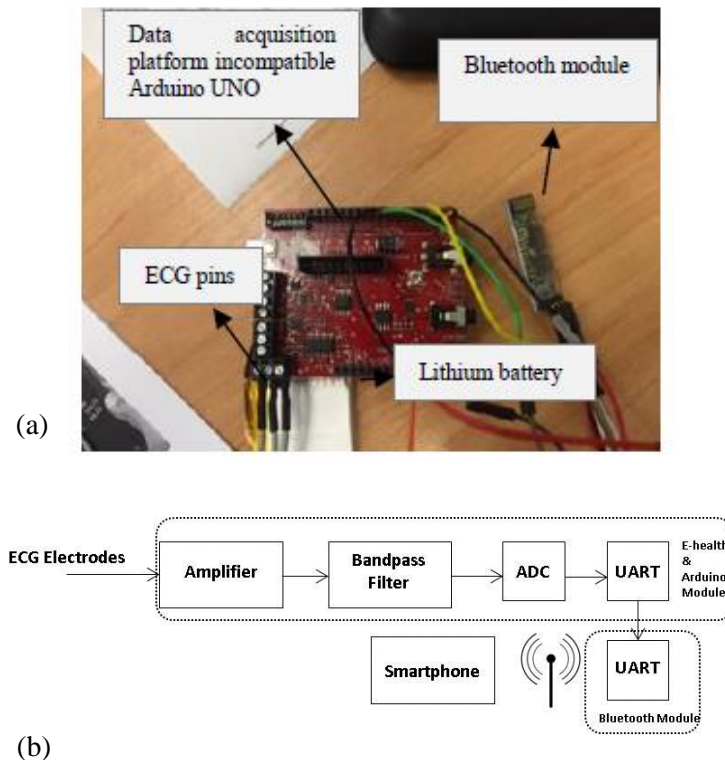


Figure 5.10: (a) ECG data acquisition system with Arduino; (b) block diagram of the ECG measurement system including a wireless communication module

In order to obtain the ECG signal, lead I configuration (Chapter 3, Section 3.1.3) was conducted throughout the experimental testing of ECG electrodes on a 29-year-old male subject; where two active electrodes were attached onto either his chest or near his ear. The other driven-right-leg (DRL) electrode was attached either onto his left side waist or left arm as a reference electrode in

order to reduce the common-mode power line interference. Nevertheless, ECG signals throughout the experiments were mainly obtained by attaching the reference electrode to the waist. The details of the electrode placement and related ECG signals are examined in depth with figures later in this section. ECG signals were filtered by a bandpass filter between 0.5 and 100 Hz to avoid aliasing due to signals above 100 Hz, as shown in Figure 5.10b. An additional notch filter was applied at 50 Hz to eliminate powerline frequency during the sampling and amplifying ECG signals at the signal acquisition system. All of the ECG signals were measured in lead I according to Einthoven's triangle, as described earlier [94 using an ECG sampling module (integrated e-Health and Arduino) and observed initially within a software tool called KST [178] which monitors obtained ECG signals in real-time in a PC environment. Furthermore, ECG signals were rebuilt and analysed in Matlab in order to compare the acquired ECG signals of the proposed work with other studies. Power consumption is critical for such an application as this. The system runs from a lithium battery (see Figure 5.10a), which has a 500mAh capacity and lasts approximately 30 hours, which depends on the use of the Bluetooth module as it consumes a significant proportion of the available power.

In the proposed system, as pointed out earlier, there are five different types of electrodes (see in Table 5.2) used for ECG measurements, and each type was tested for two different scenarios: chest-based and ear-based ECG monitoring systems. Hence, there are 10 different scenarios in total, which were displayed on KST software. Regarding the chest-based ECG monitoring system, two active electrodes were placed at the right and left chest, and one was deployed as a reference electrode. In the ear-based ECG monitoring system, the first active electrode was placed just behind the ear and the second was attached to the upper neck. Similarly, the last electrode in the ear-based system was used as a reference.

Electrocardiogram (ECG) signals were recorded using these electrodes in different placements and monitored on a PC using the KST software. The electrode placement was carried out in different scenarios, totaling ten, each being based either on a chest- or ear-based ECG monitoring system. Figure 5.11 shows the electrode placement of the first scenario (S1), which was carried out with the conventional Ambu type Ag/AgCl electrode (E1) on a chest-based system and it obtained ECG signals.

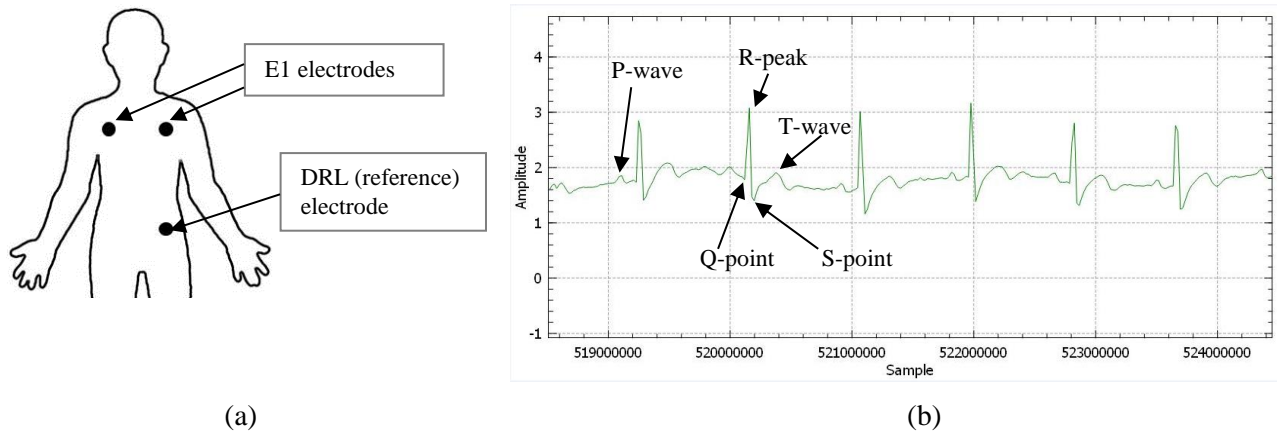


Figure 5.11: Scenario 1 (S1): **(a)** Electrode placement with E1 type electrodes on the chest; **(b)** obtained ECG signals while the subject was in a sitting position

As can be seen from the Figure 5.11, a clear ECG signal was obtained through the E1 type (defined in Table 5.2) of electrode, which provides high SNR (21.21 dB) due to a pre-gelled approach that improves skin-to-electrode conductivity. Another important observation from the figure is that all critical signs (P wave, QRS complex, and T wave) were clearly identified on the obtained ECG signal. The next experiment evaluated the effect of electrode placement by attaching the electrodes near-the-ear region using the same type E1 electrodes. Here, one active electrode was placed just behind-the-ear, and another was attached on the upper neck area, as can be seen in Figure 5.12. It is should be noted that the distance between these active electrodes has to be such that a high QRS amplitude can be detected [179]. Nedios et al. [179] investigated the correlation between the distance of applied electrodes and QRS-amplitude. It was observed in their experiments that there was a strong positive correlation between inter-electrode distance and ECG signal amplitude. The best shortest distance was around 8 cm in order to obtain the highest signal amplitude (max value was 1.82 mV). Hence, it was determined that the distance between the two active electrodes would be around 8 cm in the current experiments. Nedios et al. [179] also observed that a comparable ECG signal can be obtained in the shortest distance of 3.5 cm. However, the QRS signal amplitude (max value was 0.7 mV) was significantly less than that for 8 cm. Figure 5.12 illustrates the electrode placement on the ear-based system using the same E1 type of electrode.

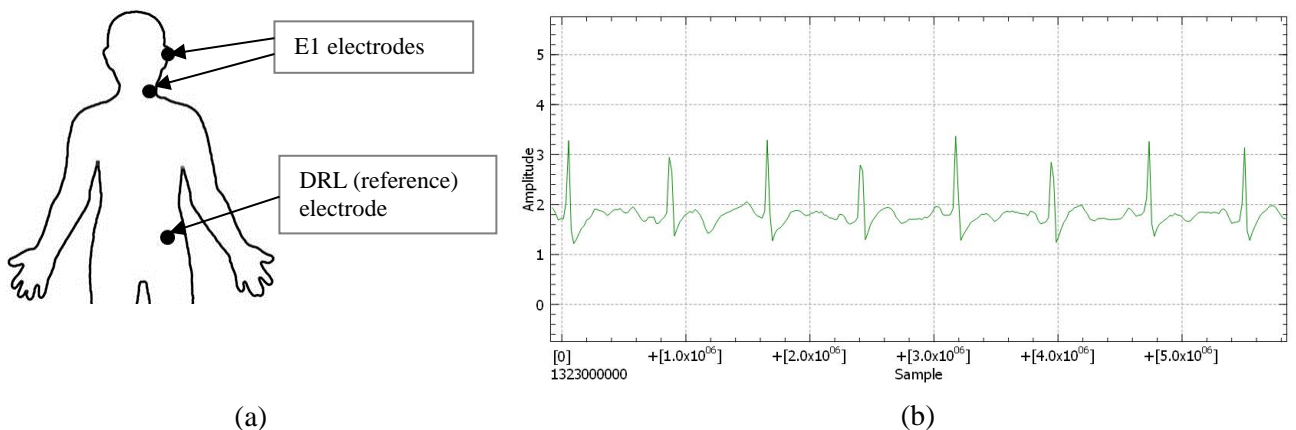


Figure 5.12: Scenario 2 (S2): (a) Electrode placement with E1 type electrodes near-the-ear; (b) obtained ECG signals while the subject was in a sitting position

Figure 5.12 clarifies that ECG signals still can be obtained from the ear-based system using the same E1 type of electrode. This difference from the previous figure (Figure 5.11) is that the P-wave and T-wave could not have been identified at some point during the experiments due to the distance to the heart. However, the proposed system still provides high signal amplitude and clearly visible R-peaks. In the scenario 3 (S3), another electrode type (E2) was used to evaluate the performance of the system. Figure 5.13 illustrates the electrode placement of the E2 type of electrode, and obtained ECG signals through the chest-based system.

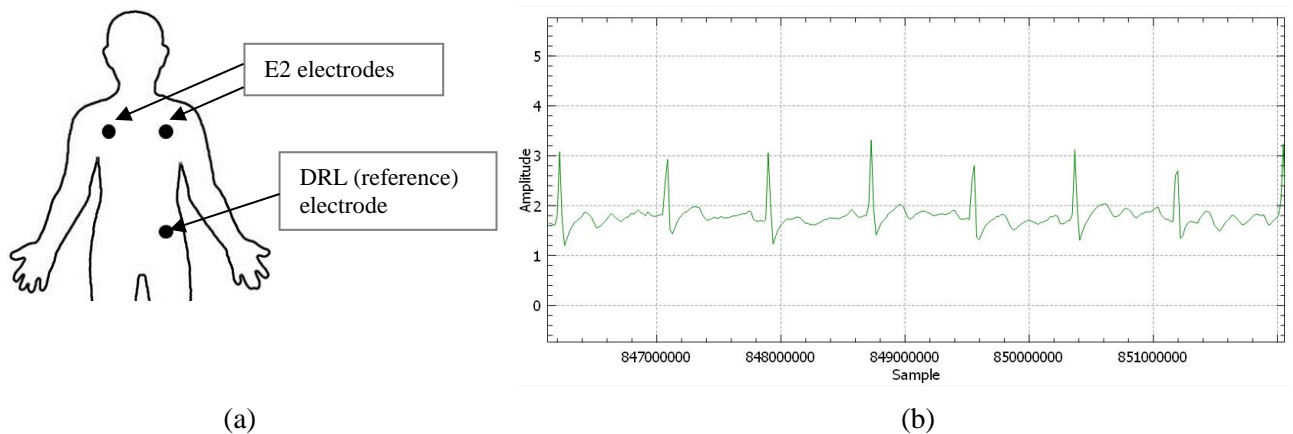


Figure 5.13: Scenario 3 (S3): (a) Electrode placement with E2 type electrodes on the chest; (b) obtained ECG signals while the subject was in a sitting position

It can be seen that the amplitude of the QRS complex in the obtained ECG signal (in Figure 5.13) is lowered due to the use of the E2 type of electrode, which has a smaller size and thus, the recorded signal can be degraded, for as described earlier, there is a correlation between the size of the electrode and the obtained ECG signal (see Figure 5.5). Nevertheless, the ECG recording process was successfully carried out and, similarly, all critical waves were observed including the P-wave, QRS complex, and T waves. In the next step, which is scenario 4, these E2 types of electrodes were attached behind-the-ear to record ECG signals. Figure 5.14 shows the placement of the tested electrodes and also, the recorded ECG signals.

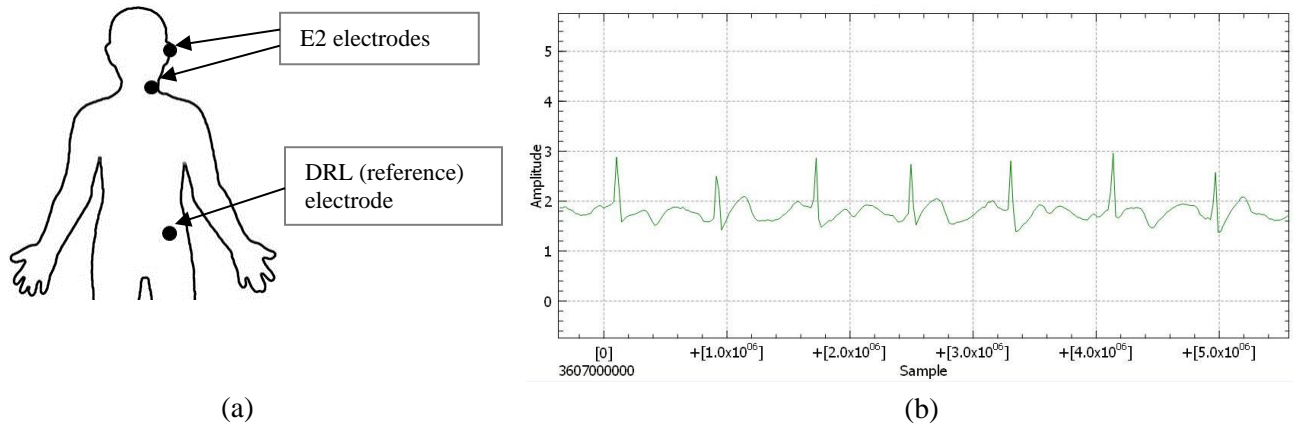


Figure 5.14: Scenario 4 (S4): (a) Electrode placement with E2 type electrodes on the ear; (b) obtained ECG signals while the subject was in a sitting position

It is observed that E2 types of electrodes provide less signal amplitude (amplitude $< 3\text{mV}$) and (SNR) (15.34 dB) than that of the E1 types (amplitude $> 3\text{ mV}$ in some cases), when Figure 5.14 is compared with Figure 5.12. Another evaluation from this figure (Figure 5.14) is that the signal amplitude was also degraded based on the near-the-ear proposed system compared to that of chest-based system (Figure 5.13). In addition, some critical signs cannot be identified in the obtained ECG signal, such as P and T waves at certain points, as can be seen in Figure 5.14. In order to increase the signal amplitude of the QRS complex and to eliminate the noise of the obtained signals, the impedance between the skin and electrode should be lowered. In scenario 5, graphene (GN) based Ambu types of electrodes (E3) were applied to obtain ECG signals with improved SNR (27.03 dB). Figure 5.15 demonstrates the placement of GN-coated electrodes on the chest and the acquired ECG signals.

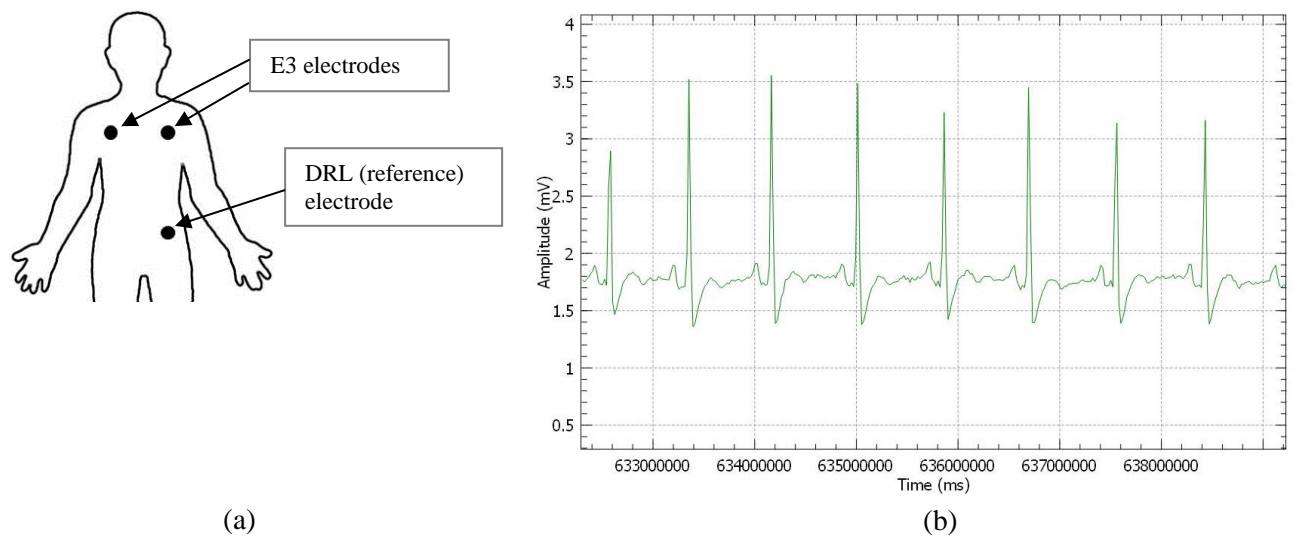


Figure 5.15: Scenario 5 (S5): (a) Electrode placement with E3 type electrodes on the chest; (b) obtained ECG signals while the subject was in a sitting position

Due to the high electrical conductivity values of GN, the highest signal amplitude (≥ 3.5 mV) was achieved during the scenario 5 (S5) experiments using the E3 type of electrodes. Figure 5.15 illustrates that almost all the amplitude of the QRS complex was higher than 3 mV and all the critical signs in an ECG waveform were observed with better accuracy, including the P-wave, QRS complex and T waves. With the promising electrical characteristics of GN, lowering the impedance between the electrode and skin and hence, the signal amplitude leads to further on obtaining high quality ECG signals from the ear. In scenario 6 (S6), the performance of the ear-based system was examined using the E3 type of electrodes. Figure 5.16 shows the electrode placement and the acquired ECG signals through just behind the ear.

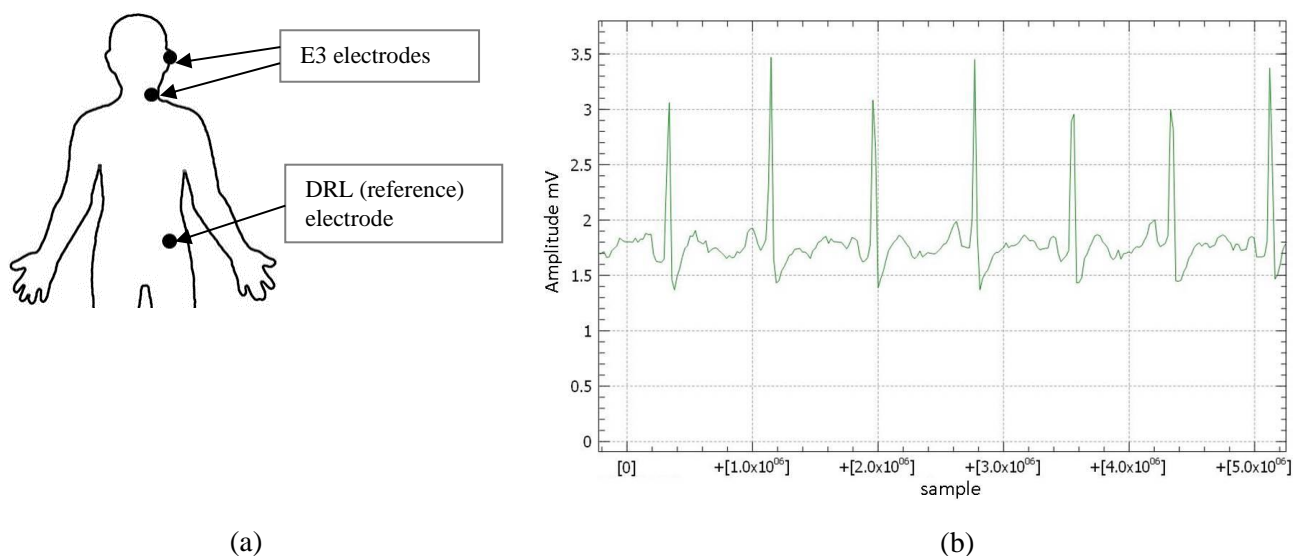


Figure 5.16: Scenario 6 (S6): (a) Electrode placement with E3 type electrodes on the ear; (b) obtained ECG signals while the subject was in a sitting position

As can be seen from Figure 5.16, whilst there were several signal fluctuations on the obtained signal, the signal amplitude of the QRS complex was still of a high value (nearly 3.5 mV) and the P-wave was visible throughout this experiment. It can clearly be seen that the obtained ECG signal using GN-coated electrodes (E3) has higher SNR than that of the conventional Ag/AgCl electrodes (E2), when Figure 5.16 is compared to Figure 5.14 under the same condition, which was based on the ear-lead ECG recording system. Furthermore, GN was applied to the smaller sized Covidien type of electrode (E4) and tested on the subject to evaluate the performance in scenario 7 (S7). Figure 5.17 illustrates the placement of this type of electrode (E4), and the obtained ECG signals via the chest-based system.

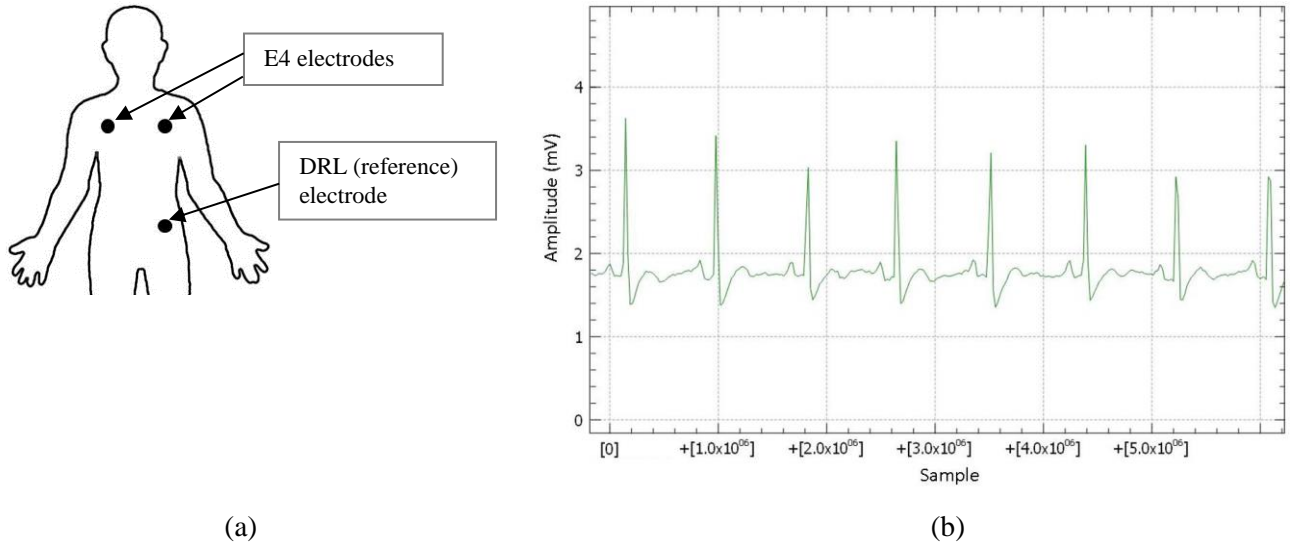


Figure 5.17: Scenario 7 (S7): **(a)** Electrode placement with E4 type electrodes on the chest; **(b)** obtained ECG signals while the subject was in a sitting position

The GN-based Covidien type of electrode (E4) was tested in this scenario and the recorded ECG signal clearly shows all the critical waves were observed. However, the signal amplitude of the QRS complex was lower than that of the recorded ECG signals with the E3 type of electrode due to the small size compared to the E4 type. On the other hand, a comparable and high value ECG signal was acquired using the E4 type of electrode, which brings to attention in the development of ear-based device due to being small in size. Consequently, in scenario 8, these GN-coated Covidien based electrodes (E4) were tested near-the-ear region to observe the performance of the proposed system. Figure 5.18 shows the placement of E4 electrodes based on the ear-lead system and recorded ECG signals.

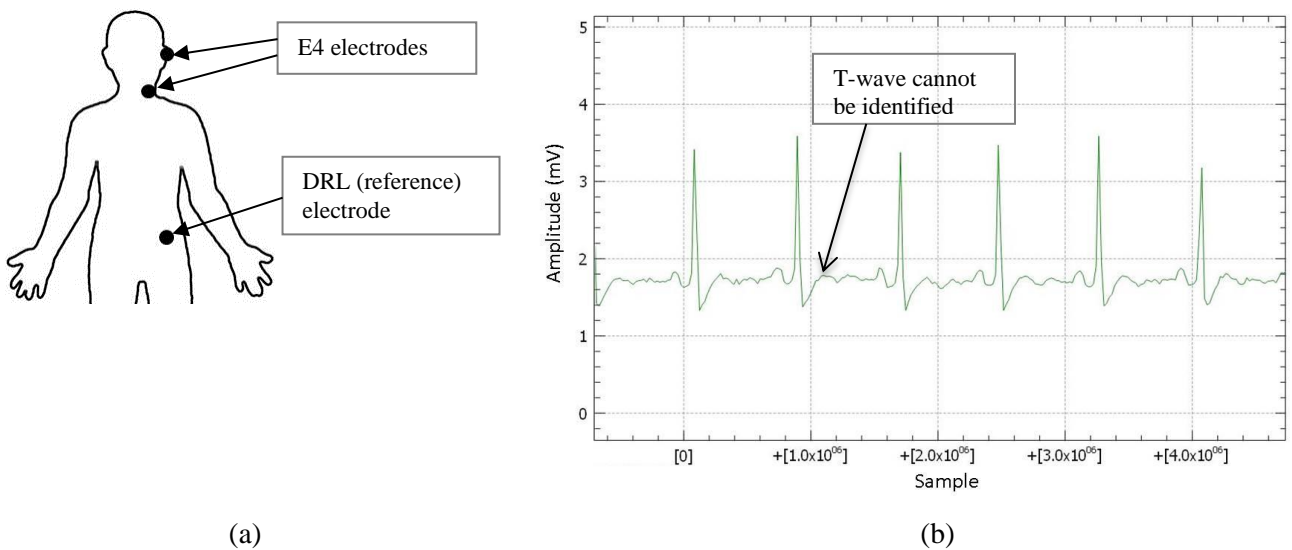


Figure 5.18: Scenario 8 (S8): **(a)** Electrode placement with E4 type electrodes on the ear; **(b)** obtained ECG signals while the subject was in a sitting position

As can be seen from Figure 5.18, the obtained ECG signal from near-the-ear using the E4 type of electrode was comparable to the obtained chest-based ECG signal. Whilst it is difficult to identify the T-wave in the obtained signal, the P wave and QRS complex were both identified with high signal amplitude ($\geq 3\text{mV}$). This demonstrates that GN plays a significant role in reducing skin-contact impedance and thus, improves the signal amplitude of the acquired ECG signal. This can be seen in Figure 5.18 and Figure 5.16 (GN-coated electrodes) when comparing the outcomes to those of Figure 5.14 and Figure 5.12 (electrodes without GN coating). Another experiment was carried out to analyse the effect of dry type electrodes (E5) rather than pre-gelled ones in regards to ECG recording systems in scenario 9. First of all, this type of electrode (E5) was applied on the chest and Figure 5.19 illustrates both the placement of the electrodes and the acquired ECG signals via this chest-based system.

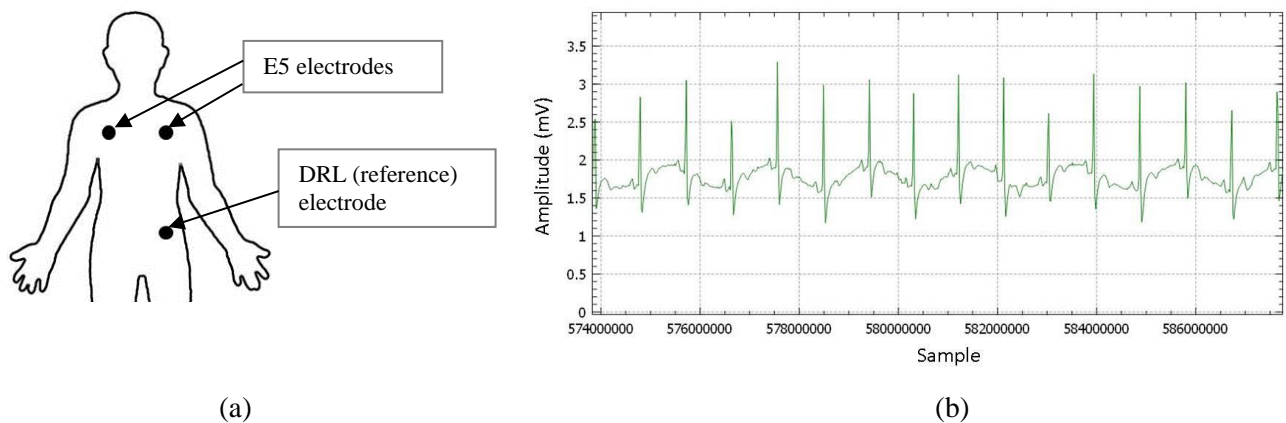


Figure 5.19: Scenario 9 (S9): **(a)** Electrode placement with E5 type electrodes on the chest; **(b)** obtained ECG signals while the subject was in a sitting position

In this scenario, it is observed that fluctuations can be seen throughout the experiments regarding the ECG recording using the E5 type of electrode. Despite the signal amplitude being comparable and the QRS complex visible, the T-wave is not clear at some points in the obtained ECG waveform and a skin contact noise has occurred that is interfering with the signals. The reason for this, is due to the high impedance between the skin and electrode owing to lack of gel. These types of electrodes (E5) were also tested on the ear-based recording system in scenario 10 in order to evaluate the performance. Figure 5.20 shows the placement of the dry type of electrodes and the obtained ECG signals.

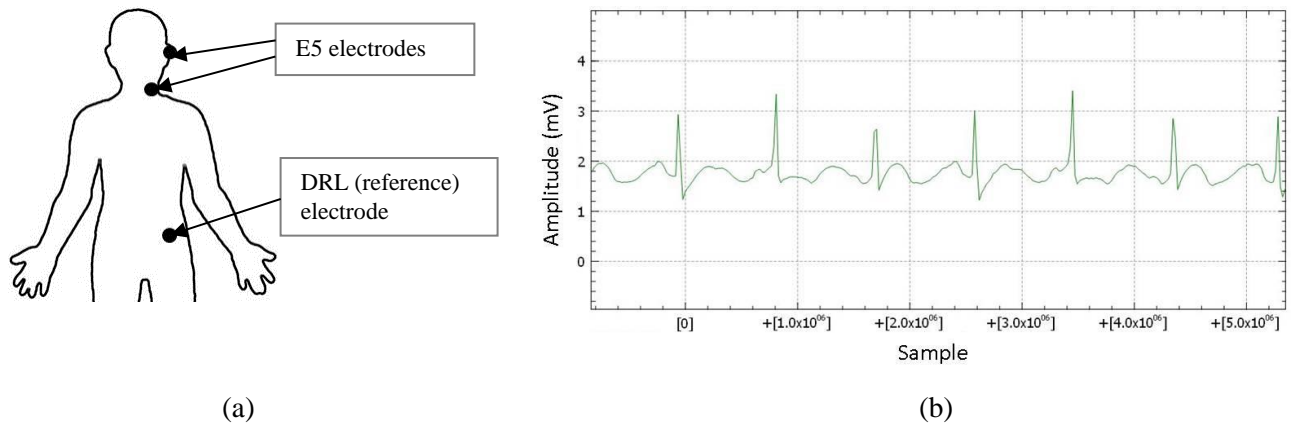


Figure 5.20: Scenario 10 (S10): (a) Electrode placement with E5 type electrodes on the ear; (b) obtained ECG signals while the subject was in a sitting position

As can be seen from figure 5.20, the obtained ECG signal involves fluctuations as well as a lack of a high standard of an ECG waveform. Only R peaks are observed successfully after a high response time (16 seconds) of applying electrodes to the ear. Moreover, the P waves and T-waves are not identified perfectly and weak signal amplitude is detected throughout the experiment of this scenario. Finally, an investigation focused on the effect of the position of the reference electrode on the obtained ECG signals was performed (S11). This was to elicit the acquired ECG signal when two active GN-coated electrodes (E3 type electrodes) were mounted on the ear area and the DRL (reference) electrode was placed on the left arm, as can be seen in Figure 5.21.

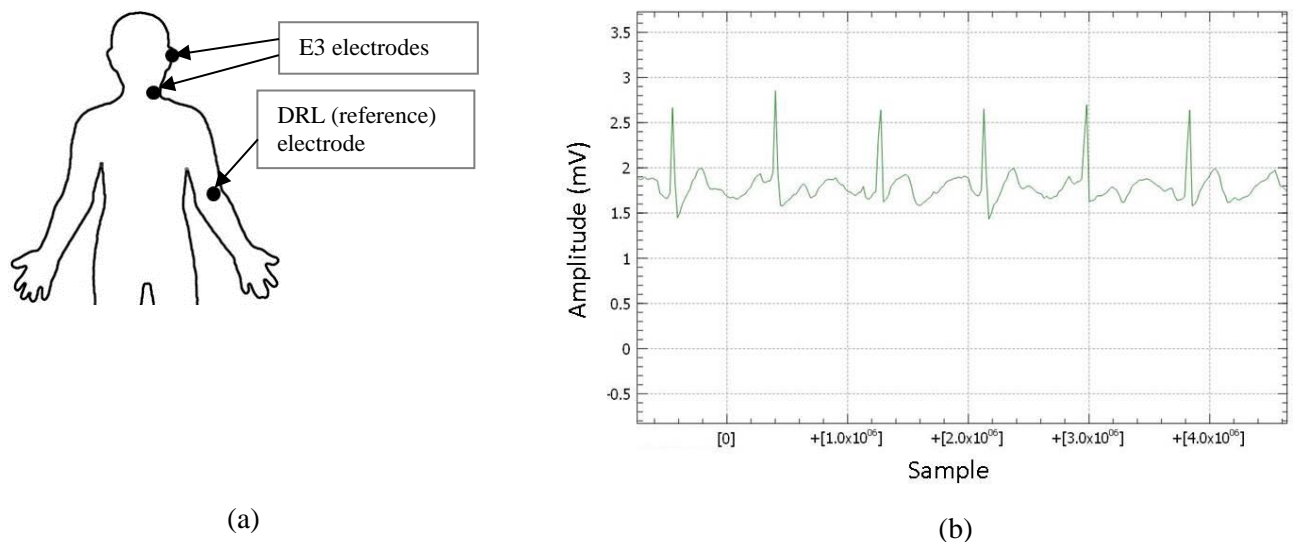


Figure 5.21: Scenario 11 (S11): (a) Electrode placement with E3 type electrodes on the ear and the reference electrode being placed on the left arm; (b) obtained ECG signals while the subject was in a sitting position

It can be clearly seen that the obtained ECG signal by attaching the reference electrode on the arm has lower signal amplitude (≥ 2.5 mV) than that when attaching it to the waist, when Figure 5.21 is compared to Figure 5.16. Only the R-peaks are visible in this scenario, for the other critical signs are not clarified accurately, including the P-wave, and T-wave. The outcomes of this scenario also

support work by Nedioš et al. [179], who elicited that inter-electrode distance affects the signal amplitude proportionally. Here, it is clearly observed that when the reference electrode is mounted on the arm, which is closer than the waist electrode, the inter-electrode distance is shortened and thus, the signal amplitude of the QRS complex in the obtained ECG signal is degraded with high fluctuations, as can be seen in Figure 5.21.

To further evaluate the performance of the electrodes, ECG signals were analysed to calculate the signal-to-noise ratio (SNR) using the following equation [180]:

$$\text{SNR} = 20\log(S/(S'-S)) \quad (5.1)$$

where, S is the filtered ECG signal with a frequency ranging from 0.5 Hz to 100 Hz, and S' is defined as the ECG signal without filtering. Before calculation, the power line interference (50 Hz) was removed from both signals. Furthermore, the mean standard deviation is considered in the calculations and it is varied in each scenario. For instance, the standard deviation of Scenario 1 is defined as 0.28 ($\sigma_1 = 0.28$). The overall system performance is analysed in Table 5.4, which summarises the SNR of the 10 different scenarios represented in Figure 5.11 – Figure 5.21, respectively and the table also presents the response times for these scenarios.

Table 5.4: Calculated SNRs and the response times of the ECG signals obtained with different electrodes and placements

Experimental Scenarios (see the Figures from 5.11 to Figure 5.21)	Standard Deviation (σ)	SNR (dB)	Response Time (s)
Scenario 1	0.28	21.21	0.85
Scenario 2	0.37	17.27	1.17
Scenario 3	0.31	21.23	0.90
Scenario 4	0.39	15.34	1.25
Scenario 5	0.23	27.03	0.55
Scenario 6	0.27	22.96	0.78
Scenario 7	0.24	25.32	0.6
Scenario 8	0.29	21.74	0.8
Scenario 9	0.43	12.58	~8
Scenario 10	0.48	10.92	~15
Scenario 11	0.45	14.08	1.8

To conclude from the results from Figure 5.11 to Figure 5.21 along with Table 5.4, there is a strong correlation between the figures and the table such that it is clear that the ECG signals obtained from the chest using GN-coated Ambu type electrodes (Scenario 5) are the best, in terms of the detections of various signs of the ECG waveform, including the P-wave, QRS complex and the T-wave, whilst these signals were also less noisy. Moreover, the results clearly reveal that the proposed GN-based electrode for the both Ambu and Covidien type provide better signal quality and performance than the traditional Ag/AgCl one. Another salient result is that a GN-based electrode presents comparable SNR and ECG signals even from behind-the-ear, which is quite a useful location for patients and would be a suitable one for future developments in wearable technology.

Furthermore, the recorded ECG signals were further interrogated using Matlab software such that the experimental results using proposed electrodes could be compared to other proposed ECG recording systems. The typical obtained ECG signals from each electrode are shown in Figure 5.22 in the Matlab environment. Similar to the KST software, the acquired ECG signals with the GN-based electrode were compared to those ECG signals obtained by the conventional Ag/AgCl electrodes. It is observed that there is no significant difference in the obtained ECG signals using the two proposed techniques. However, the waveforms of the ECG signal from GN-coated electrode were much more stable than with the conventional electrodes and the obtained ECG signals with the adhesive Ag/AgCl electrodes exhibited fluctuations during the experiments. The P-wave, QRS complex, and T-wave were clearly visible in both waveforms as well as both the Ambu and Covidien types of electrodes. It has also been elicited that electrodes of a larger size provide less noise due to a larger skin-electrode contact area. The experimental results have demonstrated the potential effective use of both types of GN-coated electrodes in clinical settings.

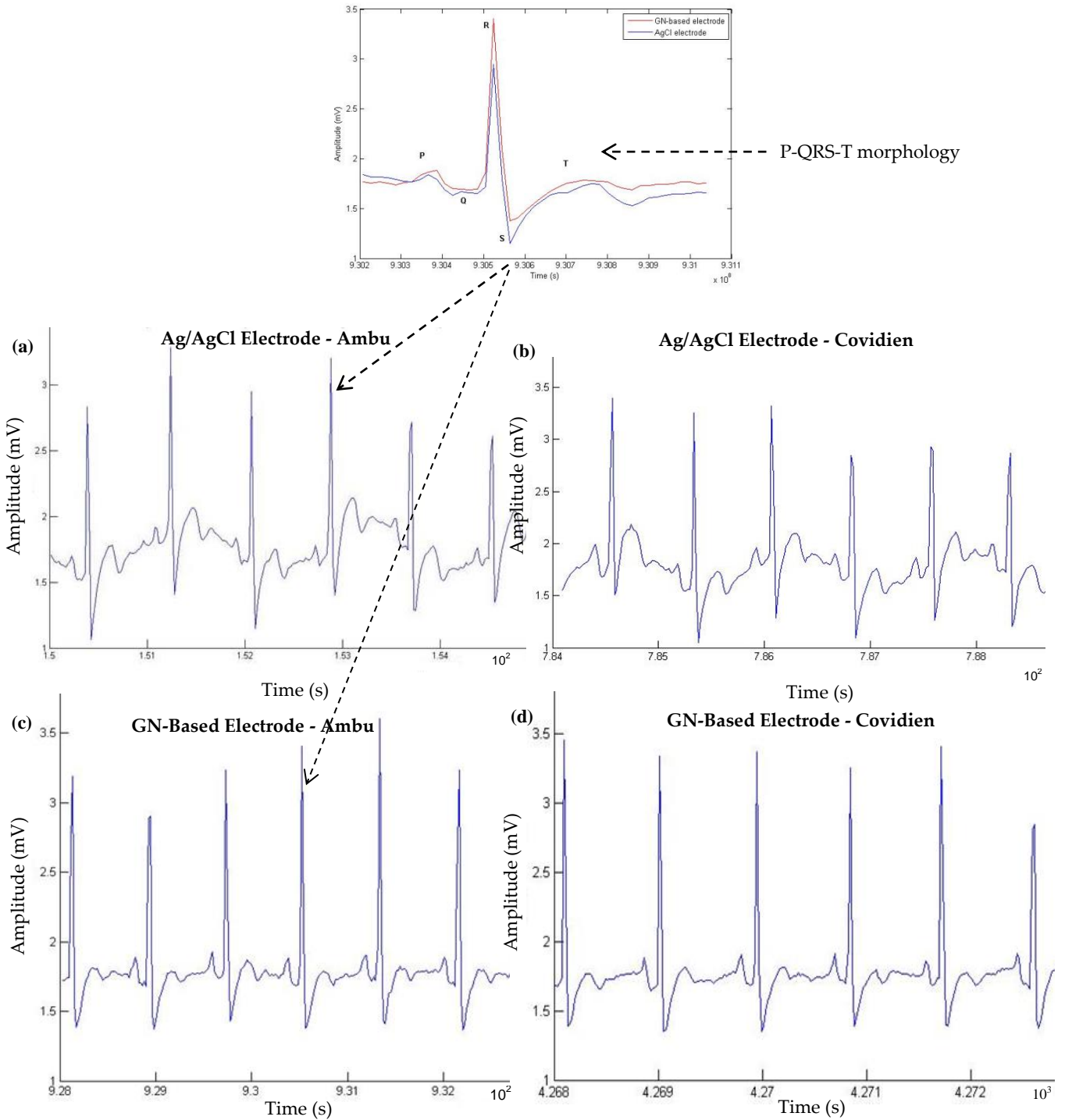


Figure 5.22: Chest-based ECG Signals from an Ag/AgCl electrode and from a GN-based electrode using the Ambu (larger size) and Covidien (smaller size) types of electrodes (a) – (d)

Similarly to the work carried out with the KST software, to evaluate further and compare the performance of the GN-coated and conventional Ag/AgCl electrodes, as ear-lead electrode position was suggested again here to observe whether the signals were still stable. Figure 5.23 shows the recorded ECG signals from the ear-lead system with both traditional Ag/AgCl and GN-coated electrodes using Matlab software.

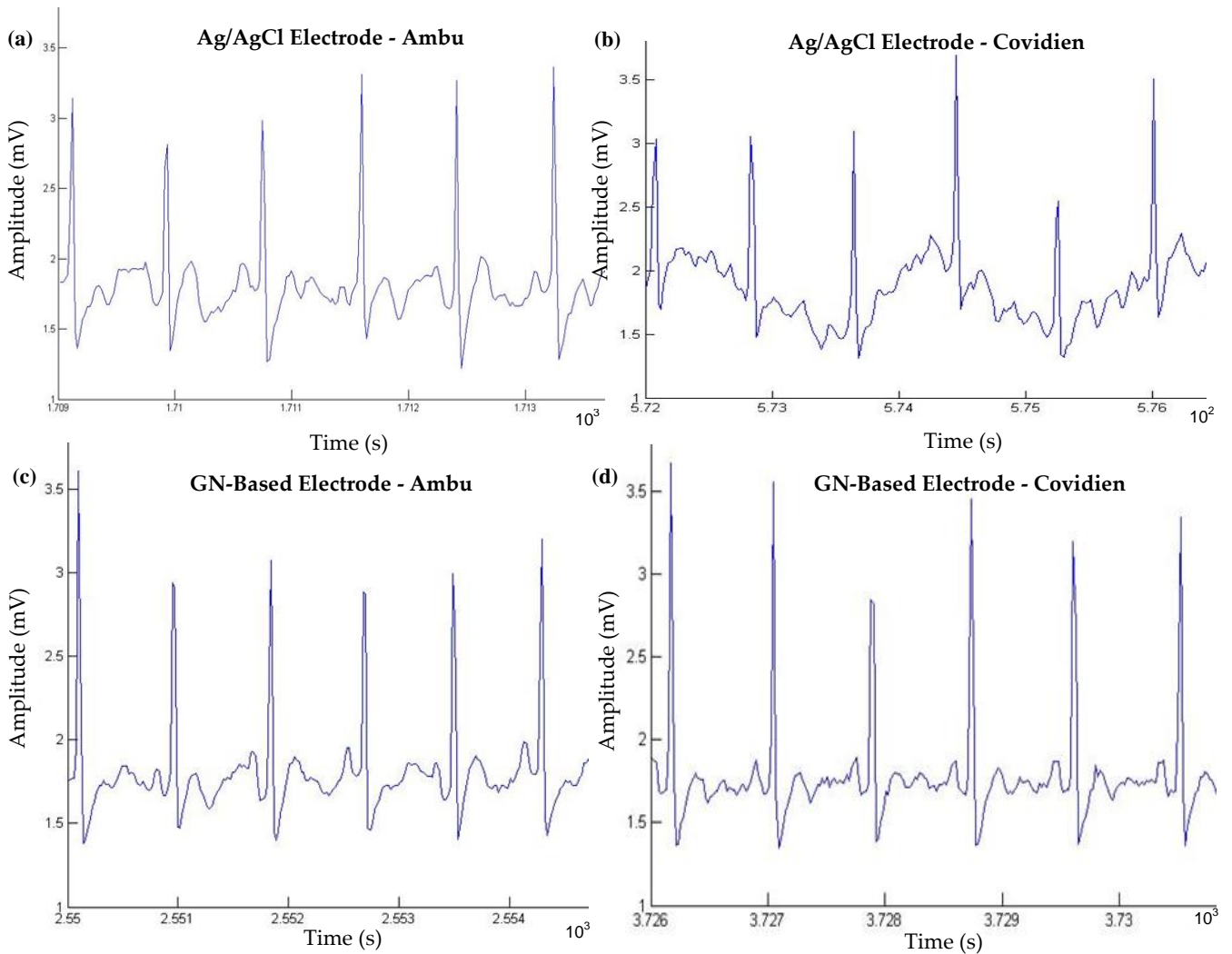


Figure 5.23: Ear-lead based ECG Signals from an Ag/AgCl electrode and from a GN-based electrode using the Ambu (larger size) and Covidien (smaller size) types of electrodes (a) – (d)

As can be seen from Figure 5.23, there are no significant changes to the ECG signals using the Ambu type of electrodes, but on the other hand, the acquired ECG signals are distorted in the case of the Covidien type, for which it is difficult to identify the P and T waves (see Figure 5.23c). However, it is possible to observe the P-wave, QRS complex and the T wave within the Covidien type GN-based electrode, as shown in Figure 5.23d. Moreover, due to the increasing contact area by using the larger size of electrode (Ambu type of electrode), the quality of the ECG waveforms is better than with that of the Covidien type of electrode, as can be seen when comparing Figure 5.23 a-c compared to Figure 5.23 b-d.

In addition to performance evaluation, the acquired ear-lead ECG signals with the proposed GN-based electrode was compared with the recently published work by Da He et al. [74], who reported ECG signals obtained by conventional Ag/AgCl gel electrodes using a behind-the-ear device. In the

results reported, only the R-peaks appeared clearly and various noisy data were also included. By contrast, the results obtained in this study have clearly identified the P-waves, QRS complex and T-waves with less noise, a comparison that can be seen in Figure 5.24. The critical point here is that Da He et al. [74] used two active electrodes owing to the limited skin area near the ear and thus, the DRL (reference) electrode was omitted in their experiments.

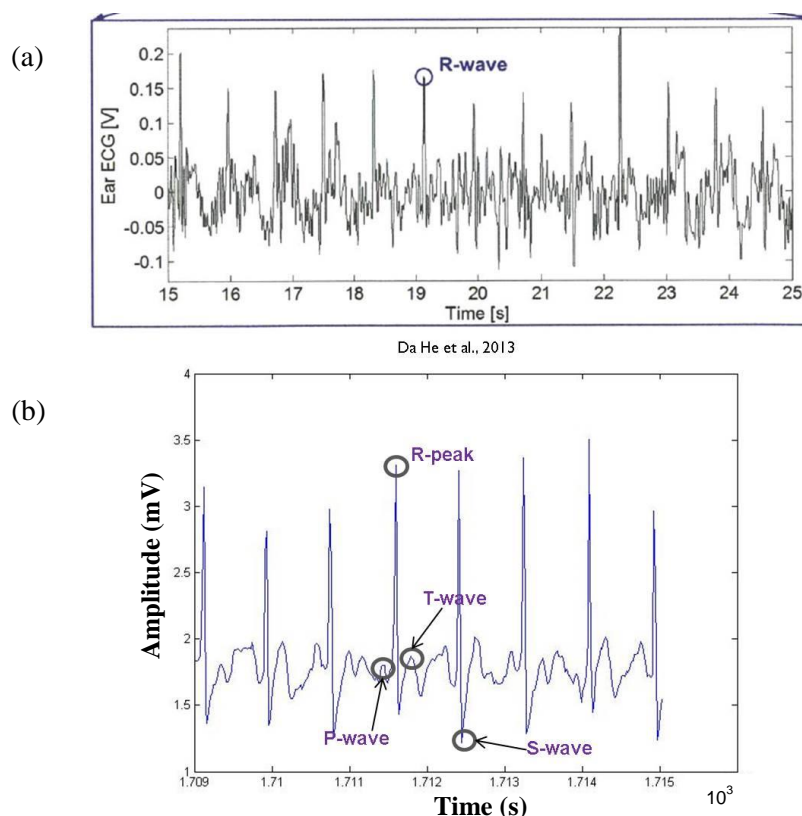


Figure 5.24: Comparison of ECG signals recorded using different electrodes. **(a)** ECG signals recorded by the Ag/AgCl electrode in Da He et al.'s report using an ear-lead position (only R peaks are visible); **(b)** ECG signals recorded by a GN-based electrode using an ear-lead position (all P-QRS-T morphology is identified)

In addition, the performance of the GN-based and Ag/AgCl electrodes was evaluated and compared by giving the power spectrum of the recorded ECG signals using the KST software tool [178] with a Hamming window. Figure 5.25a and b show the power spectral density (PSD) of the ECG signals from both the Ag/AgCl and GN-based electrodes, respectively. It is clearly seen that the frequency response curves for the latter deliver a better power spectrum than Ag/AgCl electrodes, where the critical P-QRS-T morphology of the ECG in the 0-40 Hz frequency range is accurately captured [188]. Analysis of the PSD also confirms that low frequency fluctuations occur for the Ag/AgCl electrodes in the 2-5 Hz range. However, a noisy signal is observed after 40 Hz frequency range for the GN-based electrode. Nevertheless, this is acceptable being caused by very low fluctuations during the ECG recording. The trend of PSD with varying frequencies is similar to that of Yapici et

al.'s PSD results [59]. According to which, the PSD of ECG signals showed that the noise signal was minimised using the Welch periodogram filtering method, which was built-in Matlab. Yapici [59] et al. investigated the effect of GN for fabricating a textile electrode for ECG recording system and they analysed the characterisation of electrode frequency response for further evaluation. When a comparison is made with Yapici et al.'s results in regard to frequency response of the ECG signals, it is observed that the PSD of the ECG signal was around $10 \times 10^{-3} \text{ V}^2/\text{Hz}$ at 10 Hz in the current work (see Figure 5.25b), while for the former's work it was around $3 \times 10^{-3} \text{ V}^2/\text{Hz}$ at the same frequency (10 Hz). This demonstrates that the proposed work obtained higher amplitude of P-QRS-T morphology of the ECG signal than Yapici et al.'s study on a GN-based textile electrode for an ECG recording system.

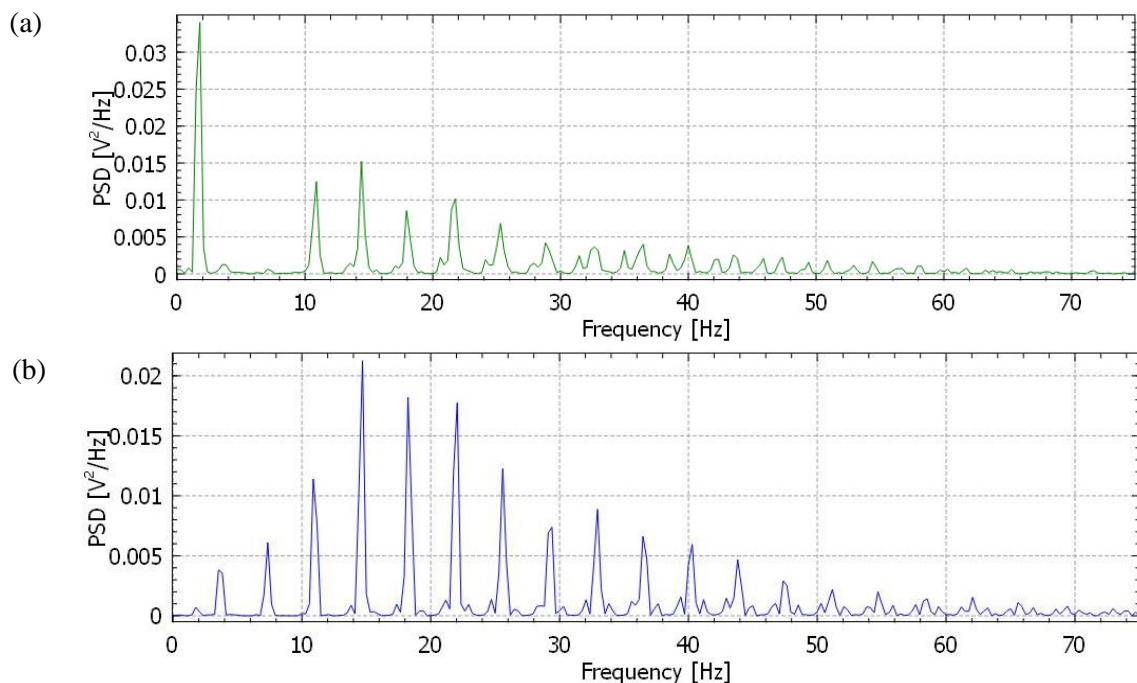


Figure 5.25: Comparison of the frequency response of filtered ECG signals from Ag/AgCl and GN-based electrodes up to 75 Hz: **(a)** Power spectral density (PSD) of ECG recordings (from Figure 8a) for an Ag/AgCl electrode; **(b)** PSD of ECG recordings (from Figure 8c) for a GN-based electrode

5.3.2. Measurements and Comparisons of Skin-Electrode Contact Impedances

Skin-electrode contact impedance measurement has always been of interest due to it providing the reliability of the collected physiological signal. Skin conductivity varies according to different the conditions of either the stratum corneum (whether hairy skin or not) or sweat proportions. In order to get a high quality signal acquisition with minimal noise, the impedance measurement of the skin-electrode should be small and stable. To characterise the impedance of a graphene-coated electrode, a measurement setup was constructed based on earlier techniques reported in the literature [12, 31]. Here, measurements were taken with the electrode-skin contact impedance of three GN-coated

electrodes with different sizes, and compared with that of the conventional Ag/AgCl electrodes using a Wayne Kerr 6500B impedance analyser. Both the conventional Ag/AgCl electrodes and the proposed GN-coated ones were placed adjacent to each other on a person's forearm (between the wrist and the elbow) and both electrodes were attached so as to maintain the same distance (3 cm between them). Each measurement was carried out just after attaching the electrodes (for a period of 45 s) and after removal of skin moisture. The impedance measurements were recorded in the frequency range of 20 Hz to 1 kHz. According to these measurements, the change in impedances with varying frequencies was improved by graphene coating when compared to that of Baek [12] and Meng's [31] results. Figure 5.26 shows the impedance values of conventional Ag/AgCl electrode ranges from 445.05 k Ω (at 20 Hz) to 13.82 k Ω (at 1 kHz), which are similar to those reported in the literature [12, 31] and the impedance of the graphene-coated electrode varies from 65.82 k Ω (at 20 Hz) to 5.10 k Ω (at 1 kHz). The results show that a graphene-coated electrode has lower skin-electrode contact impedance when compared to a conventional Ag/AgCl electrode, resulting in less noise and a higher quality ECG signal, an example of which can be seen in Figure 5.22. Another interesting point from Figure 5.26 is that the contact impedance decreases as the size of the electrode increases (as mentioned earlier, the Ambu type electrode is somewhat bigger than the Covidien type (by 37%), which results in increasing of the contact area between the electrode and the skin.

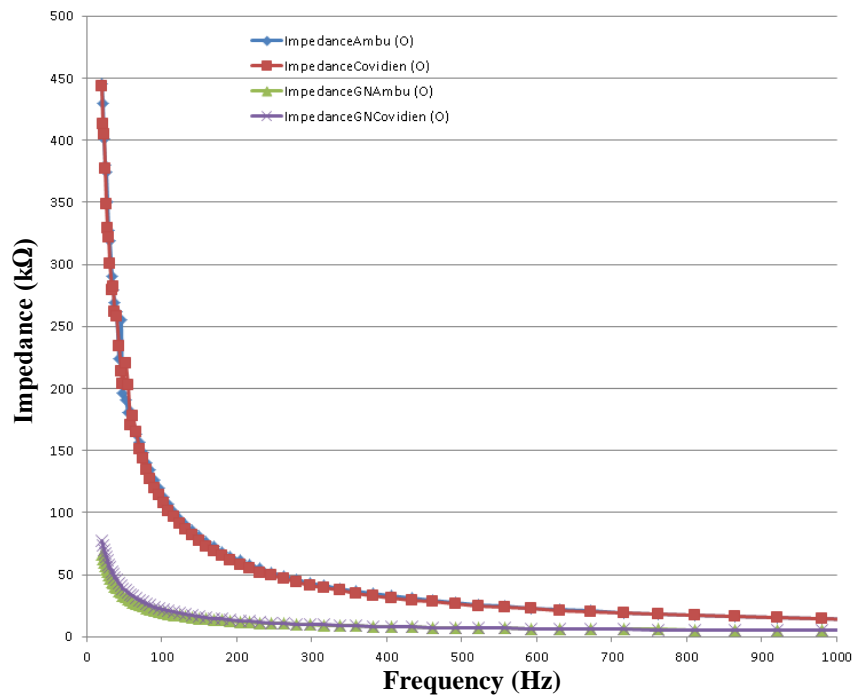


Figure 5.26: The skin-electrode contact impedance of the Ambu (bigger) and Covidien (smaller) types of a conventional Ag/AgCl electrode (shown as ImpedanceAmbu and ImpedanceCovidien) and Graphene-coated electrodes (shown as ImpedanceGNAmbu and ImpedanceGNCovidien)

5.4. Summary

Firstly in this chapter, a simplified human skin model was designed in COMSOL simulation to analyse the electrical field distribution from the artery to the surface of the body and to investigate the surface charge density of Ag/AgCl and GN-coated electrodes. It emerged that GN-based electrodes doubled the electric field distribution and surface charge density compared to the values obtained by the Ag/AgCl electrodes. Subsequently, an experimental setup of a 3-lead electrode system was explored using different sizes of conventional Ag/AgCl and the proposed GN-based electrodes. It was clearly demonstrated that the latter improved the ECG recording when compared to the former regarding signal quality in terms of amplitude of the QRS complex, SNR, response time, frequency response and the skin-electrode impedance values. Finally, experiments on skin-electrode contact impedance have validated the theoretical effect of GN in this context, as put forward in the previous chapter (Chapter 4, Section 4.5.5).

CHAPTER 6: CONCEPT OF INTEGRATED MULTI-FUNCTIONAL WIRELESS BODY MONITORING SYSTEM

Throughout this chapter, a wireless multiple smart sensor system (WMSSS) is presented in conjunction with a smartphone to enable unobtrusive monitoring of an ear-lead ECG integrated with a multiple sensor system, which includes core body temperature (CBT) and PPG sensors. First of all, the design and setup of the ear-based multi-functional monitoring system is proposed. Following this, the experimental results of ECG, CBT and PPG systems are presented respectively, using the proposed ear-based multifunctional device. Subsequently, a developed Android based application on a smartphone is introduced for continuously monitoring of ECG, CBT and PPG using the proposed ear-based device. Lastly, an analysis of the proposed integrated multifunctional wireless body monitoring system is provided and also, the wireless technologies for a telemedicine system are described.

6.1. Design and Experimental Setup of an Integrated Ear-based Device for a Multiple Smart Sensor System

As discussed earlier in Chapter 5, a high amplitude of the QRS complex for an ECG signal can be obtained from behind-the-ear using graphene coated (GN-coated) electrodes. Furthermore, CBT monitoring can be carried out from the tympanic membrane, which is the inner area of an ear, as discussed in Chapter 3. Accordingly, an ear-based device was designed to combine the ECG and CBT sensors together. Here, a continuous, wearable and wireless vital signs patient monitoring system focused on integrating ECG sensors placed behind-the-ear is examined regarding a CBT sensor placed in the ear and a PPG sensor clipped onto the finger. The reason for choosing the ear as a location in this project is that it makes it possible to measure ECG and CBT together, without any inconvenience or discomfort to the subject. Clearly, behind the ear region there is less hair than on the chest, hence it is more suitable and robust for long term ECG monitoring due to the high skin-electrode conductivity of non-hair regions. Additionally, preparation of the skin will not be a necessity for the ear-based scenario and it will not be difficult to remove sensors when compared to the chest area, which thus brings forth a user-friendly perspective to both patients and clinicians.

The smart sensor platform was developed to combine experimentally three different body sensors to monitor physiological signals wirelessly on the smartphone. The three sensors of the proposed system are an ECG with behind-the-ear electrodes, a tympanic sensor in the ear canal for CBT monitoring and a clipped pulse oximeter sensor on the finger for PPG monitoring (heart rate and SpO₂), with the obtained multiple signals being transmitted to a mobile phone via Bluetooth

technology. While the PPG sensor is attached to the finger, the ECG and CBT sensors are integrated in the form of an earbud in order to communicate with a smartphone via a microcontroller unit (MCU) placed on the arm with a small portable case. Figure 6.1 shows a block diagram of the smart sensor system combining the three different physiological signals.

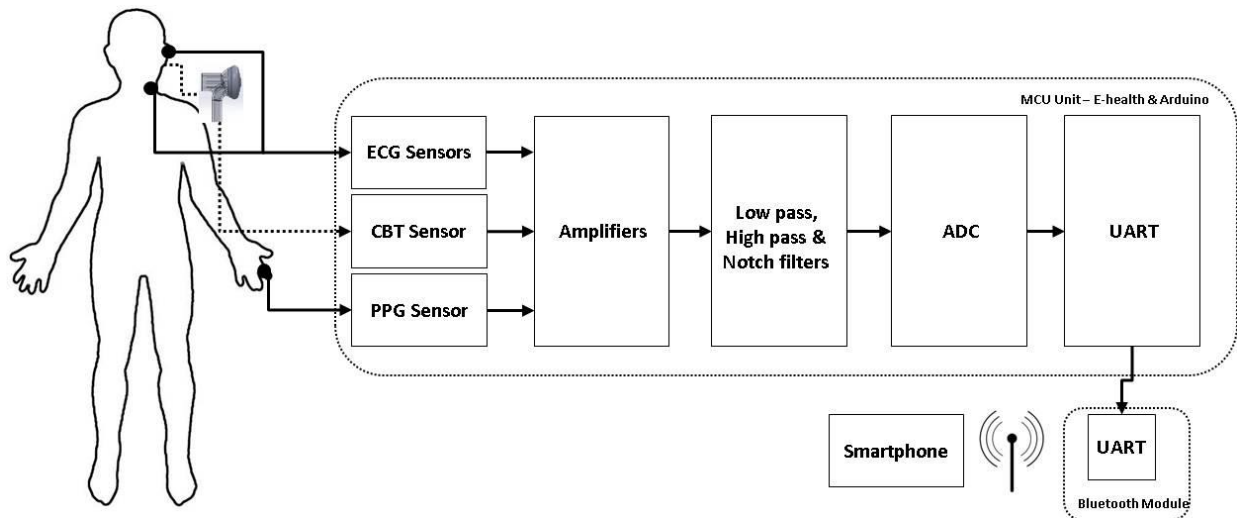


Figure 6.1: System block diagram which including ECG and CBT sensors in an earbud form as well as and PPG sensor attached to the finger

The design and proposed sensors were explored separately for each physiological signal (ECG, CBT, and PPG). Herein the multiple physiological data is transmitted and monitored on a smartphone. An interesting tool to connect smartphones to biosensors is the open-source platform Arduino which is dedicated in this study. Bluetooth communication is the best wireless communication channel in order to establish a link between the Arduino and the smartphone within a highly enough data rate to transmit multiple (ECG, CBT, HR and SpO₂) signals, and to be integrated into a wearable hardware device.

6.1.1. ECG Sensing Unit

As can be seen from the block diagram (see Figure 6.1), ECG and CBT sensors were deployed together, as they were both deployed in a near to the ear location, whilst the PPG sensor was clipped onto the finger. Regarding the ECG measurements, five different electrodes were tested in order to decide the best for ear-lead ECG monitoring with an optimum signal, as discussed earlier in Chapter 5. The experimental results demonstrated that the GN-based Ambu type electrode exhibited the best signal amplitude of the QRS complex and SNR. However, the GN-based Covidien type electrode was chosen here for the ear-lead ECG monitoring due to its effective size when compared to the GN-based Ambu type electrode and also owing to its comparable SNR to conventional wet

Ag/AgCl type electrode. Consequently, the GN-based Covidien type electrode was deemed the optimum sensor for obtaining ECG signals from behind-the-ear. One active ECG electrode was attached just behind-the-ear, while the other was placed on the upper neck and the last driven-right-leg (DRL) electrode was also placed on the arm to eliminate the unwanted distortions and noise. Then, these sensors were integrated into the developed earbud to communicate with the MCU for further analysis, such as the amplifying, filtering and sampling processes. Two stage amplification units were used with gains of 10 and 100 to avoid the noise overriding the ECG signals, which was achieved by an instrumentation amplifier and a micro-power operational amplifier, respectively. The ECG signals were restricted in bandwidth of 0.5-100 Hz using high pass and low pass filters after the first and second steps of amplification, respectively. The power line interference in the ECG signal was filtered using a 50 Hz notch filter to avoid loss of the 50 Hz component of the ECG signals. Figure 6.2a illustrates the electronic circuits, which include an e-Health ECG acquisition system and Arduino UNO in order to adjust the obtained raw ECG signals to suitable ECG data for a wireless link to a smartphone and a Bluetooth module, which is connected to the Arduino's receiver and transmitter pins to transfer physiological data from the Arduino to a smartphone. The placement of the electrodes with the combination of proposed earbud is shown in Figure 6.2b.

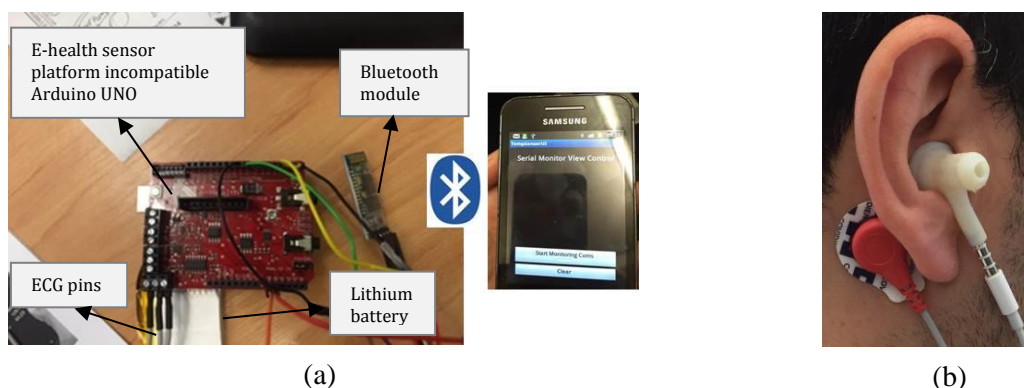


Figure 6.2: (a) ECG acquisition system using an e-Health and Arduino microcontroller platform along with a Bluetooth module for communicating with a smartphone. The ECG monitoring process was carried out by a Lithium Battery which has a capacity of 500mAh; (b) the behind-the-ear proposal with the combination of earbud application.

6.1.2. CBT Sensing Unit

In the proposed smart sensor system, a thermopile sensor, which is non-contact sensor, was used for measuring CBT. Owing to the tympanic membrane directly reflecting the core temperature from the carotid artery, an earbud device was designed for an infrared tympanic sensor that can fix into the device and so that continuous CBT monitoring can be carried out from the ear. The prototype earbud device was designed in SolidWorks and produced using 3D printing technology. This earbud device with an infrared temperature sensor was connected to the MCU, which is the core

controller of the whole smart sensor system, in order to perform signal processing and data transmission wirelessly. The thermopile sensor (MLX90614) [115] was employed for continuous CBT measurement, which provides very sensitive information regarding the core temperature, with 17 bit ADC resolution, leading to an output resolution of 0.02 °C. Figure 6.3 shows the proposed earbud device within the thermopile infrared sensor.

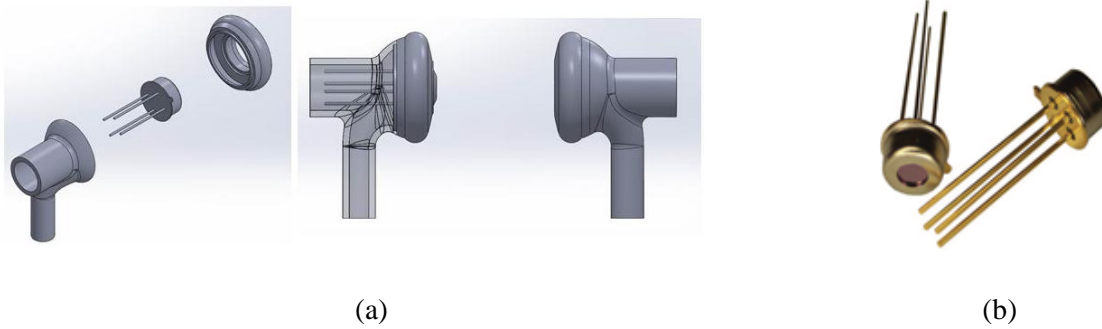
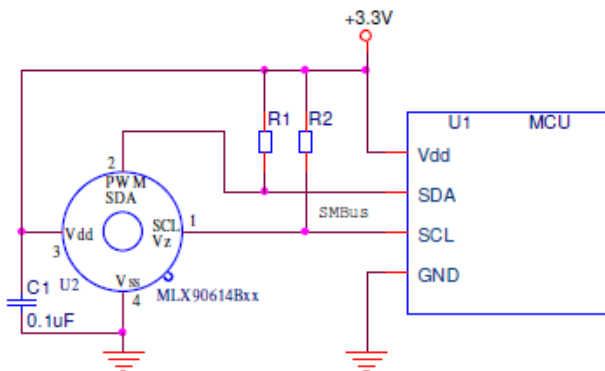


Figure 6.3: (a) The proposed earbud device, which consists of a thermopile infrared sensor, for CBT measurements; (b) MLX 90614 infrared thermometer was used for CBT monitoring experiments

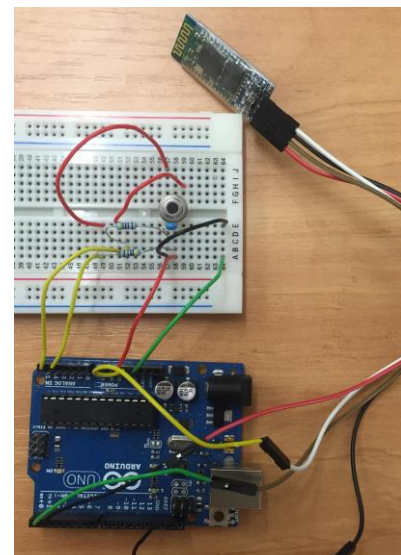
As can be seen from Figure 6.3, the proposed infrared sensor has four pins for connection to Arduino's specific pins so that it can read analogue temperature data. These pins are:

- Vdd, connected to a 3.3V power supply in Arduino, to run the infrared sensor;
- SCL, going to Arduino's analogue pin number 4 (A4);
- SDA, going to Arduino's analogue pin number 5 (A5);
- Vss, connected to the ground pin, where it is placed on Arduino (GND).

Figure 6.4 illustrates the experimental setup for CBT measurements and also the pin connection to the MCU.



(a)



(b)

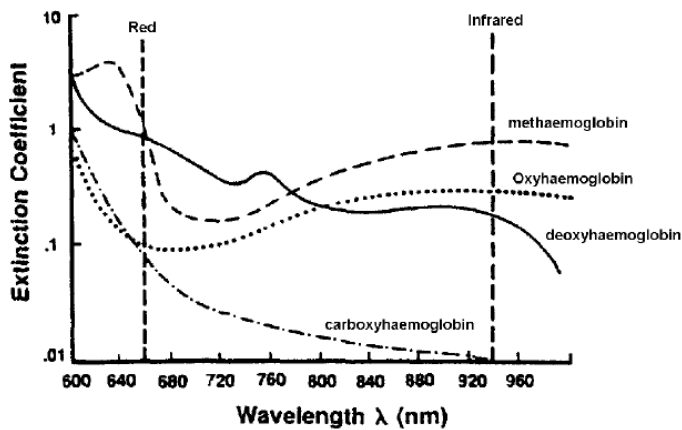
Figure 6.4: (a) The connection of MLX90614 to an MCU with 3.3V power supply; (b) initial experimental setup of CBT measurement using Arduino UNO on a bread board

The thermopile sensor was initially tested on a bread board to observe continuous monitoring of the ambient temperature using a Bluetooth module. The proposed earbud device, which was integrated with a thermopile sensor, was tested for different scenarios to observe the subject's core temperature for the continuous monitoring of CBT, the obtained results are provided in Subsection 6.2.2.

6.1.3. PPG Sensing Unit

The finger-worn PPG sensor consists of a transducer, which initiates two LEDs and a photodiode detector. One of the LEDs emits red light (with a wavelength of $\lambda = 660$ nm) and other delivers an infrared on (with a wavelength of $\lambda = 880$ nm). This technique is known as PPG and the PPG sensor is based on the theory that the colour of blood range depends on the oxygen it contains. Oxygen is transported in the blood by haemoglobin (Hb), and depending on whether hemoglobin is constrained with oxygen, oxyhaemoglobin (HbO_2) or deoxyhaemoglobin (Hb) absorbs light at different wavelengths. However, Hb absorbs more red light at a wavelength of 660 nm than HbO_2 , whilst infrared light is absorbed nearly equally between the two at a wavelength of 880 nm [189], as can be seen in Figure 6.5a. This effect is taken advantage of for pulse oximetry determination by using two LEDs with different wavelengths (660 nm and 880 nm). That is, the ratio of absorption at two wavelengths is utilised to determine blood oxygen saturation by the differentiating absorbance of light. This calculation was examined in the theory chapter, Chapter 3, Subsection 3.3.4, by the equations of 3.9 and 3.10.

In the proposed testbed application regarding the PPG sensor unit, both oxygen saturation in the blood (SpO_2) and heart rate (HR) were measured using an Amperor Bluetooth Finger PPG sensor [181], which is shown in Figure 6.5b. The proposed integrated smart sensor system incorporates a Bluetooth connection to transmit the obtained SpO_2 and HR data from the PPG sensor.



(a)



(b)

Figure 6.5: (a) Haemoglobin absorption spectra [189]; and (b) the tested Amperor PPG monitoring sensor, which shows SpO₂ and the heart rate (HR)

The PPG sensor probe has an infrared source at 880 nm and a photodetector giving current output, which is converted to voltage by an instrumentation amplifier with gain 10, using high and low pass filters between 0.5 and 20 Hz. After digitising and sampling the obtained PPG data, the integrated physiological signals were transmitted to a smartphone for displaying SpO₂ and HR information in an Android based application.

6.2. Experimental Results of an Integrated Ear-based Device for a Multiple Smart Sensor System

In this section, the experimental tests and results are reported for the individual parameter: ECG, CBT, and PPG sensors. Moreover, the integration of the ECG, CBT, and PPG sensors into wearable hardware is exhibited with transmission of the physiological data on a smartphone using Bluetooth technology. After digitising and conditioning the analogue signals from each sensor, the suitable digital physiological data were collected at the data acquisition hardware unit in an appropriate way. The complete data, after being acquired by Arduino, was converted into the form of packets and wirelessly transmitted to an Android based mobile phone. Figure 6.6a illustrates the prototype of the ear-based multisensory system and Figure 6.6b shows the electronic boards responsible for the data acquisition included with all connections for acquiring ECG, CBT data and Bluetooth communication.

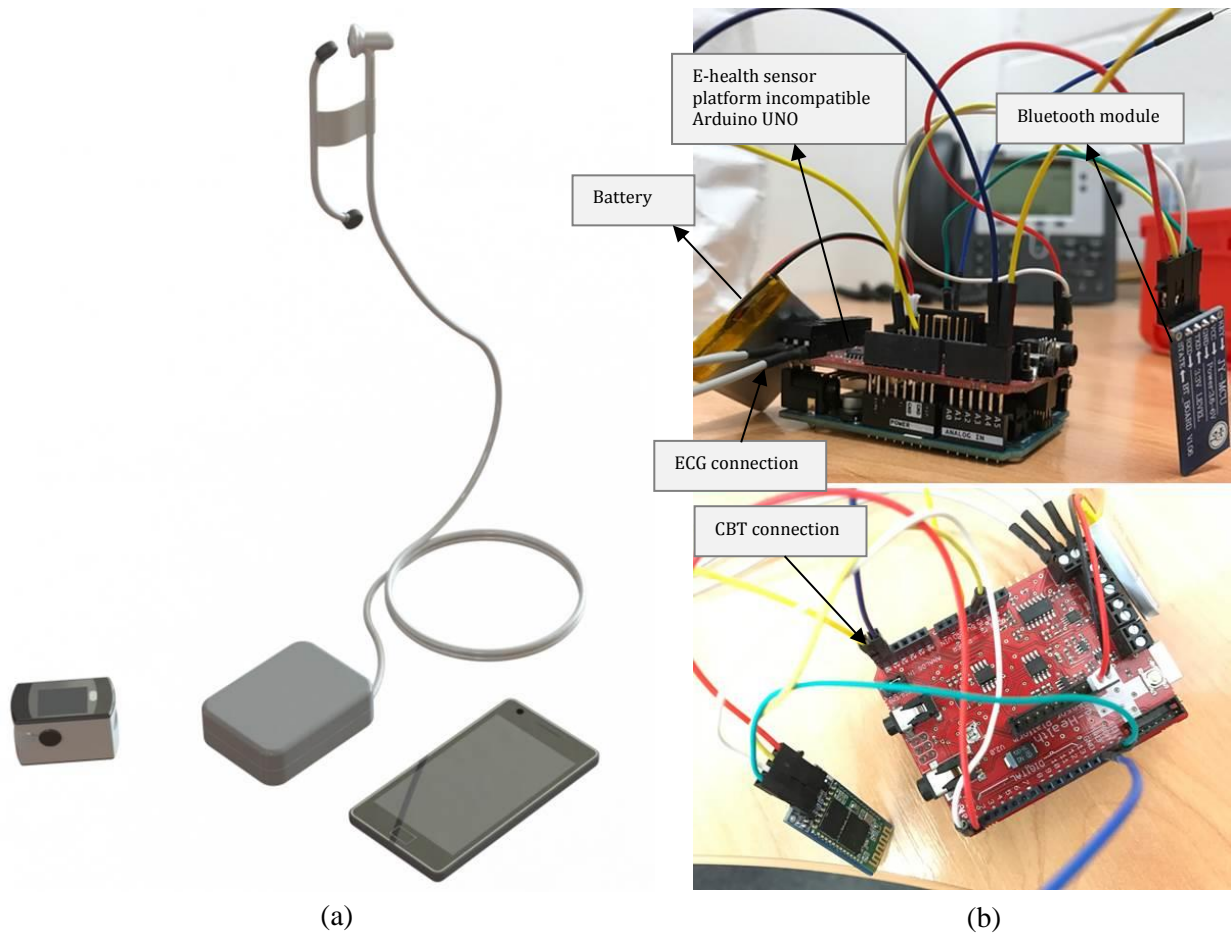


Figure 6.6: (a) The prototype of an ear-based multifunctional wireless monitoring system; (b) a data acquisition hardware unit that consists of ECG, CBT sensor connections, Bluetooth module (HC-05 type [182]) for wireless communication and a lithium-ion battery for powering the sensory system

The data acquisition hardware unit combines the ECG and CBT sensors together, whilst the PPG sensor data are transmitted to the smartphone directly. A developed Android based smartphone application then collects all ECG, CBT, and PPG data to monitor continuously. The prototype earbud device contains a CBT sensor, which is subsequently conjugated with ECG sensors from the upper neck area through the hardware unit. Figure 6.7 shows ECG electrodes placement and the appearance of the general prototype of proposed body sensors, including a subject wearing a smart sensor on the ear.

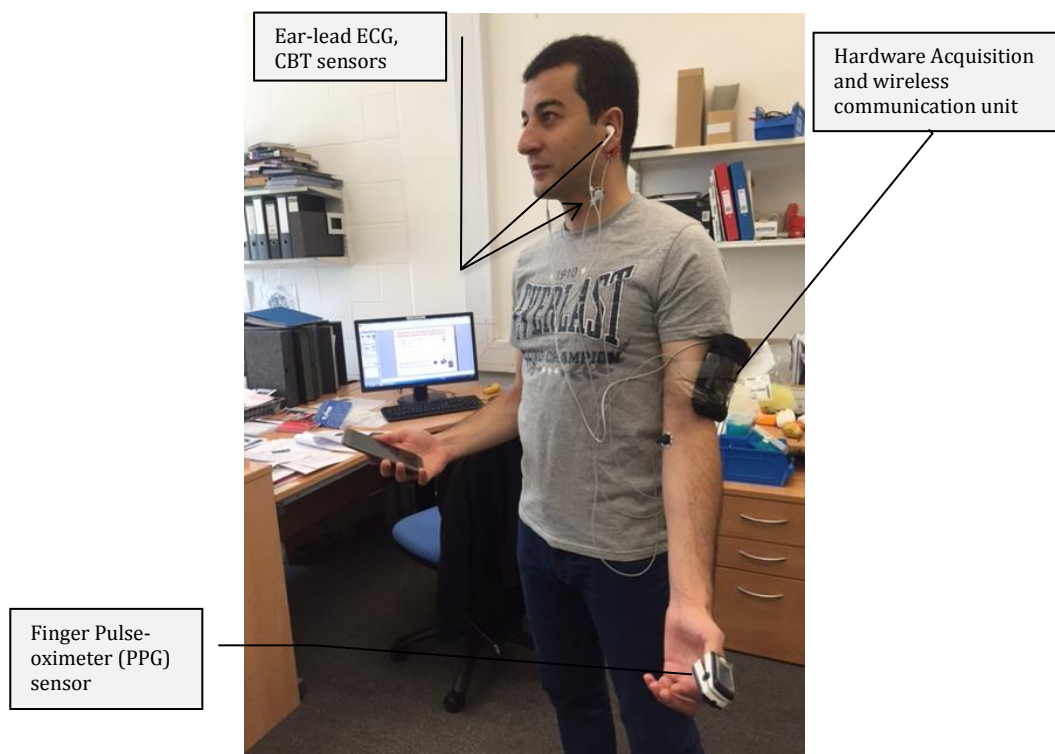


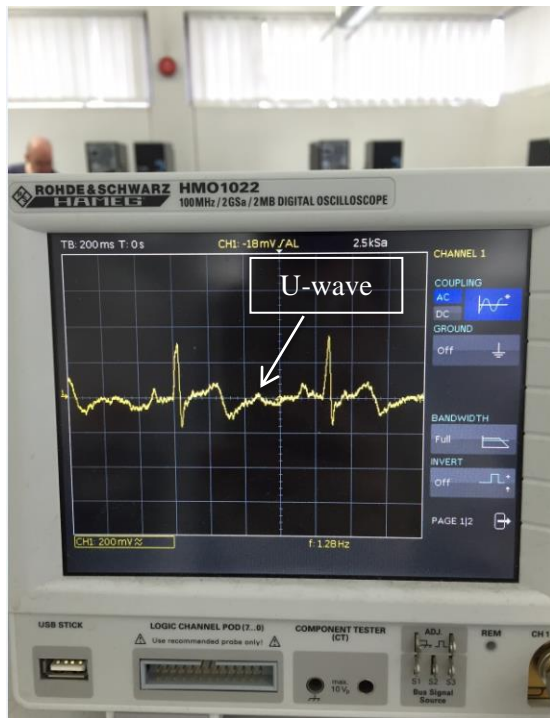
Figure 6.7: Typical setup of the use of the proposed integrated wireless multiple sensors; a CBT sensor was inserted into the proposed earbud device; and GN-coated ECG electrodes were placed on the behind-the-ear and upper neck areas; and a PPG sensor was clipped onto the finger

As can be seen in Figure 6.7, the CBT sensor was placed in the proposed earbud device and ECG sensors were attached the behind the ear and on the upper neck. The connections of these sensors were then combined together in a wire to transmit the collected physiological data to the hardware acquisition unit worn on the left arm. A PPG sensor was also clipped onto the finger and SpO_2 and HR were transmitted to the smartphone in order to be visualised.

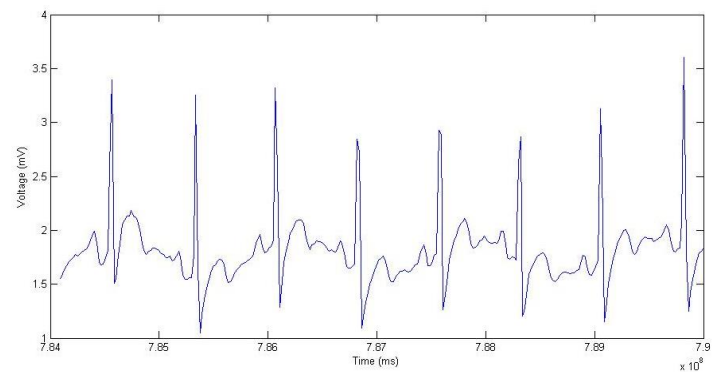
6.2.1. ECG based Experimental Results

The ECG based results were examined using the proposed ear-based integrated multifunctional physiological monitoring system. These were demonstrated in depth in Chapter 5, where different types of electrodes were analysed to obtained ECG signals through chest and ear based devices. GN-based electrodes provided the best ECG signals and the highest amplitude of QRS complex when compared to any other type of electrode. Hence, GN-based electrodes were selected for integration with the proposed smart sensor system.

Figure 6.8a shows the obtained ECG signals on the oscilloscope for the proposed ear-based multifunctional monitoring system and then, the acquired ECG signals were observed in Matlab platform, as can be seen in Figure 6.8b.



(a)



(b)

Figure 6.8: (a) Visualisation of the obtained ECG signals on an oscilloscope; and (b) ECG visualisation using Matlab software via the proposed ear-based multisensory system

Both figures here demonstrate that the proposed ear-based device provides high quality ECG signals, including the critical cardiac signs such as the P-wave, QRS complex, and the T-wave. Furthermore, U-wave, which is a small wave immediately following the T-wave, representing repolarisation of the Purkinje fibres [190], was also observed in some cases on the oscilloscope when using the proposed ear-based GN-coated electrodes. It is worth noting that the ECG signals can be acquired by attaching the electrodes behind-the-ear with a third reference electrode and that the proposed ear-based device has demonstrated the purpose of ECG acquisition successfully within the integrated system.

6.2.2. CBT Based Experimental Results

The experimental setup of CBT measurement and the proposed earbud device for CBT monitoring are illustrated in Figure 6.4b and Figure 6.3a, respectively. Here, the CBT sensor was inserted into the earbud was tested while a subject was wearing it and CBT monitoring was carried out wirelessly through a PC. Several analyses were conducted on CBT whilst the subject was exercising to observe the changes in different environments. Figure 6.9 shows obtained CBT variations for 100 seconds from the earbud device with the integrated smart sensory system, while subject was wearing it in different conditions: a) normal sitting; b) after exercising indoors; (c) after walking outside in cold weather; and d) sitting down wearing a thick jacket.

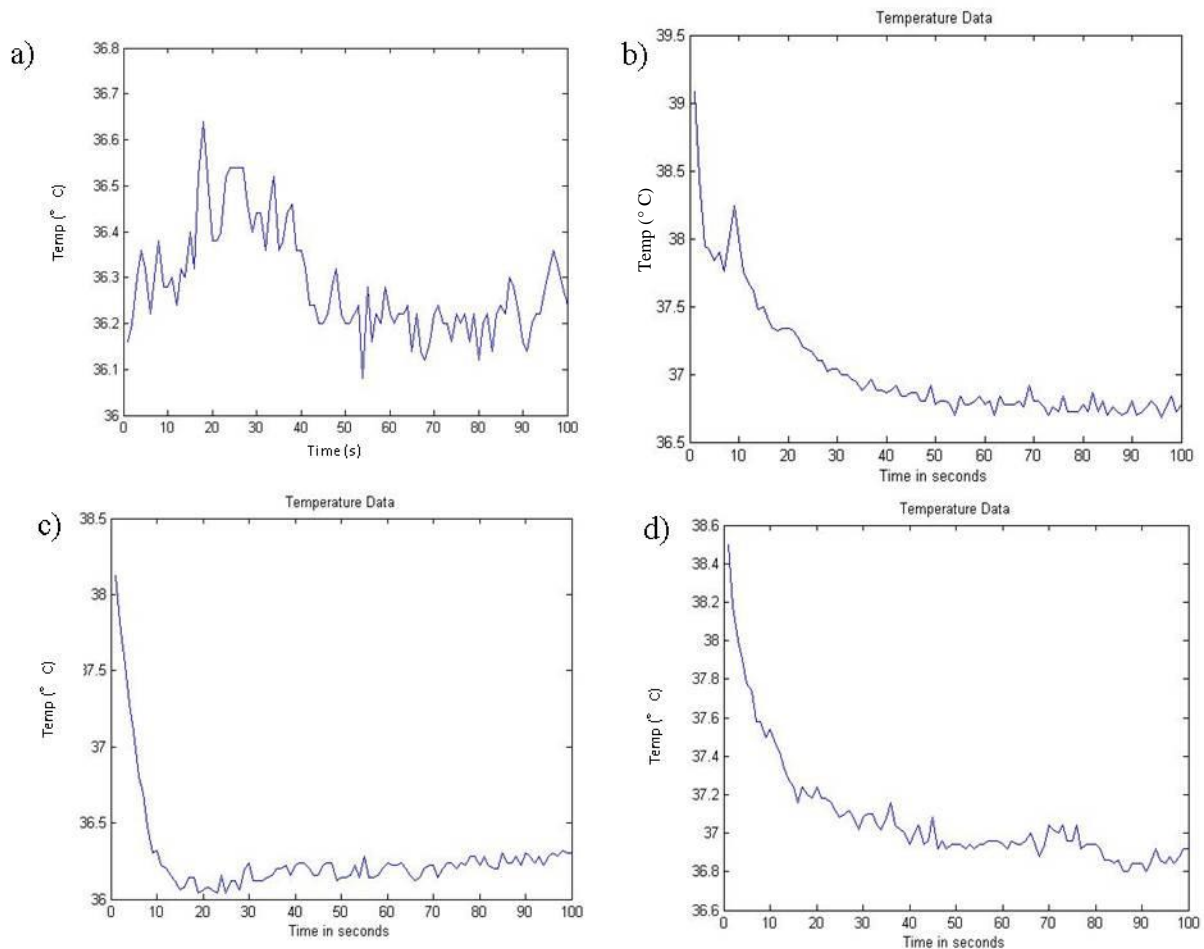


Figure 6.9: Continuous CBT measurements for 100 seconds: (a) Raw CBT data taken from the ear; (b) CBT data just after exercise – five mins running; (c) CBT data after walking outside in cold weather; and (d) final temperature data after sitting for five mins wearing a thick jacket

Figure 6.9 shows four different observations that were captured under different conditions and with different ambient temperature values. It is noticed that due to adjustment of the thermopile sensor in the ear, the temperature was seen at very high degrees at the beginning ($t = 0$). Hence, the temperature measurements were ignored at the beginning, i.e. between $t = 0$ and $t = 5$ seconds, but continuous CBT measurements were analysed after the first 5 seconds ($t > 5$ seconds). Figure 6.9a illustrates typical raw data of CBT taken from the ear without any exercise, which varies between 36°C and 36.7°C , being normal for a healthy person. It is evidenced that CBT increases as the level of exercise gets harder, which can be seen in Figure 6.9b. This temperature was raised to just over 37°C after a five minute running exercise. Figure 6.9c illustrates the changes of core body temperature against the change of ambient temperature. The subject was walking outside in cold and windy weather, with approximately 14°C ambient temperature. Owing to decreasing ambient temperature, the CBT decreased to nearly 36°C during this experiment. In Figure 6.9d, it can be seen how the CBT was captured when the subject was wearing a thick jacket in the office and the ambient temperature was around 23°C . In this case, the CBT was elevated to almost 37.3°C

(Figure 6.9d).

6.2.3. PPG Based Experimental Results

Separate from the proposed ear-based integrated multifunctional system, a pulse oximeter was clipped onto the finger to visualise PPG data as well as SpO₂ and HR. The obtained data through the pulse oximeter were transmitted to a smartphone wirelessly to be observed in an Android based application. Subsequently, the obtained PPG data were analysed under different conditions (normal state and exercise), whilst the subject was wearing the pulse oximeter and the results were displayed on a desktop PC. Figure 6.10 shows the subject's PPG waveform, HR and blood oxygenation together using the PPG sensor clipped onto the finger (Amperor pulse oximeter [181]) connected to a desktop via Bluetooth to transmit the acquired PPG data.

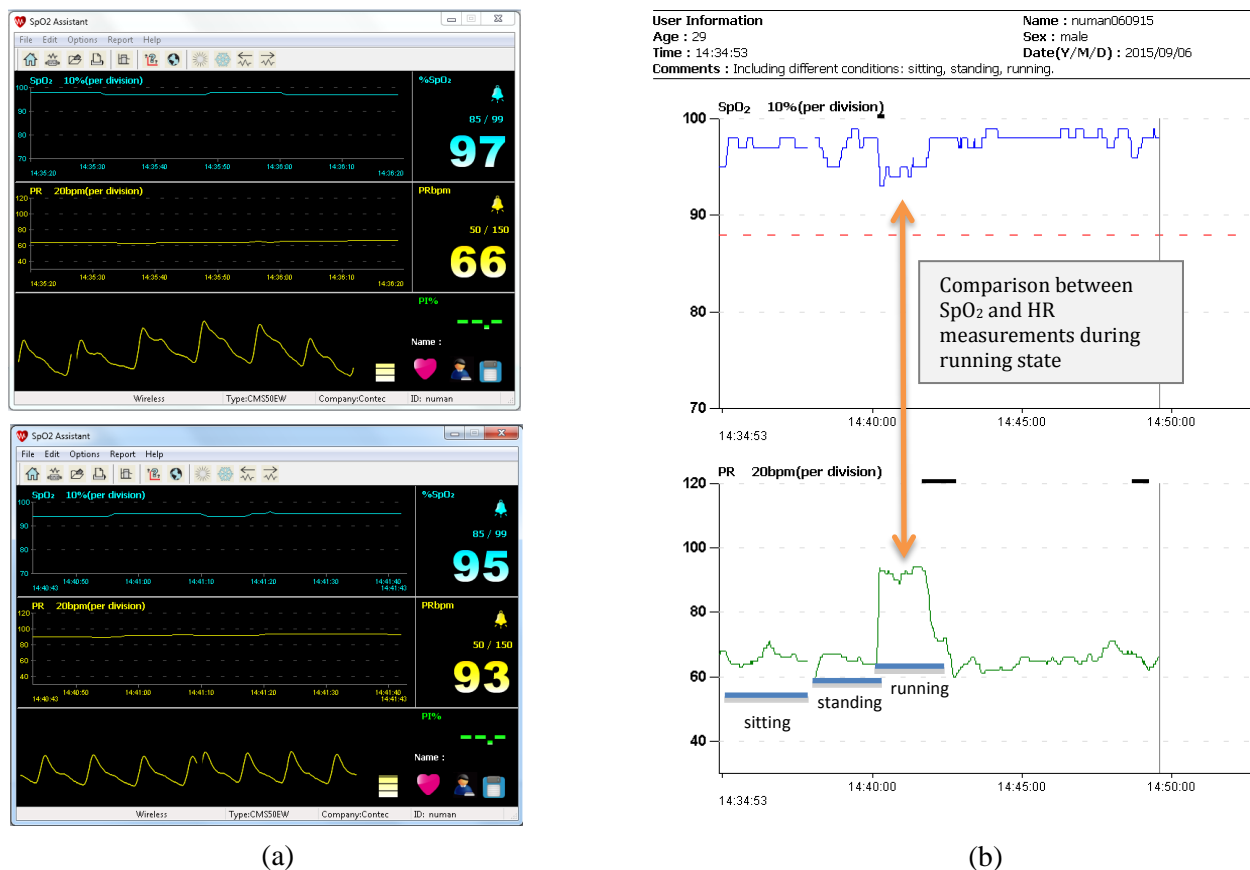


Figure 6.10: (a) Measuring HR and SpO₂ using an Amperor Bluetooth PPG sensor; (b) a PPG measurement on a subject during exercise using the same device

It can be seen in Figure 6.10a, that the values of oxygen saturation in the blood (SpO₂) were around 97% and 95%, and the HR measurements were 66 and 93 beats per minute (bpm) under the sitting and running states, respectively. Figure 6.10b also demonstrates PPG measurement on a 29 year-old subject with respect to SpO₂ and HR during the exercise. As can be seen from the figure, there were variations regarding the PPG data during a 15-minute exercise that included sitting, standing and

running. In particular, during the period of running, there was a sharp increase HR values, whilst the blood oxygenation values were decreasing. These data were captured and displayed on a desktop PC. The PPG data were then transmitted to a smartphone via a Bluetooth connection to display the physiological signals, including SpO₂ and HR.

6.3. Android Based Smartphone Application for Visualising Continuous Health Monitoring

A smartphone application was developed initially to monitor ECG signals obtained from the proposed ear-based multifunctional device using both GN-based and traditional adhesive Ag/AgCl electrodes. The acquired ECG signals were observed in real-time wirelessly using Bluetooth communication. The software, called as AndroECG, which has been developed by the researchers of University of Applied Sciences Graz [194], has extra benefits over displaying ECG data continuously such as when calculating HR and saving received data. The software was designed in the Android Studio program using Java programming language, which is implemented on an Android based Samsung smartphone. The flow diagram of the proposed continuous wireless ECG monitoring system is shown in Figure 6.11.

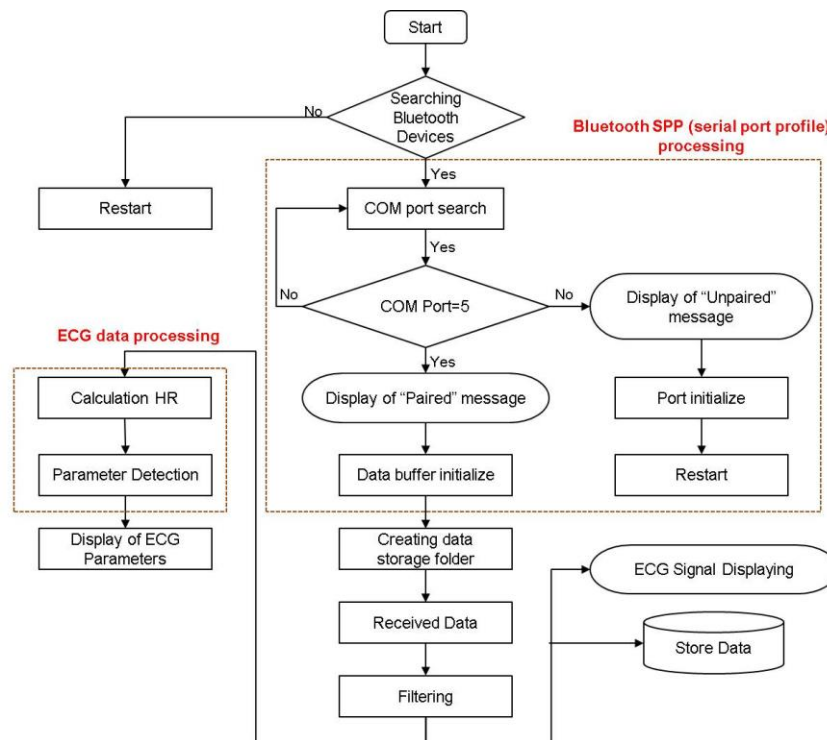


Figure 6.11: Software flow diagram of the proposed ECG continuous monitoring system for smartphone application

AndroECG [194] is able to receive, display, save and transmit ECG data from a subject continuously and wirelessly. The application flow starts with a Bluetooth pairing object to conduct Bluetooth connection between the proposed ear-based ECG device and a smartphone. After pairing

the devices, the user has the opportunity to display the received ECG data in real-time and a background task takes care of calculating the current heart rate in beats-per-minute (BPM). Two additional services are provided to store the received data simultaneously after transferring ECG data from Arduino electronic circuit. Moreover, the subject has the opportunity to save the symptoms occurring according to the currently stored data, the database structure of which can be seen in Figure 6.12d. Furthermore, the stored ECG data can be transmitted to a server or remote clinic by AndroECG, so that transmitted the ECG data can be analysed by a clinician at a distance. Figure 6.12a shows the displayed ECG signals on the smartphone using a traditional Ag/AgCl electrode, whilst Figure 6.12b indicates mobile ECG signals obtained by GN-coated electrodes. Figure 6.12c and Figure 6.12d illustrate extra parameters for the developed ECG mobile application.

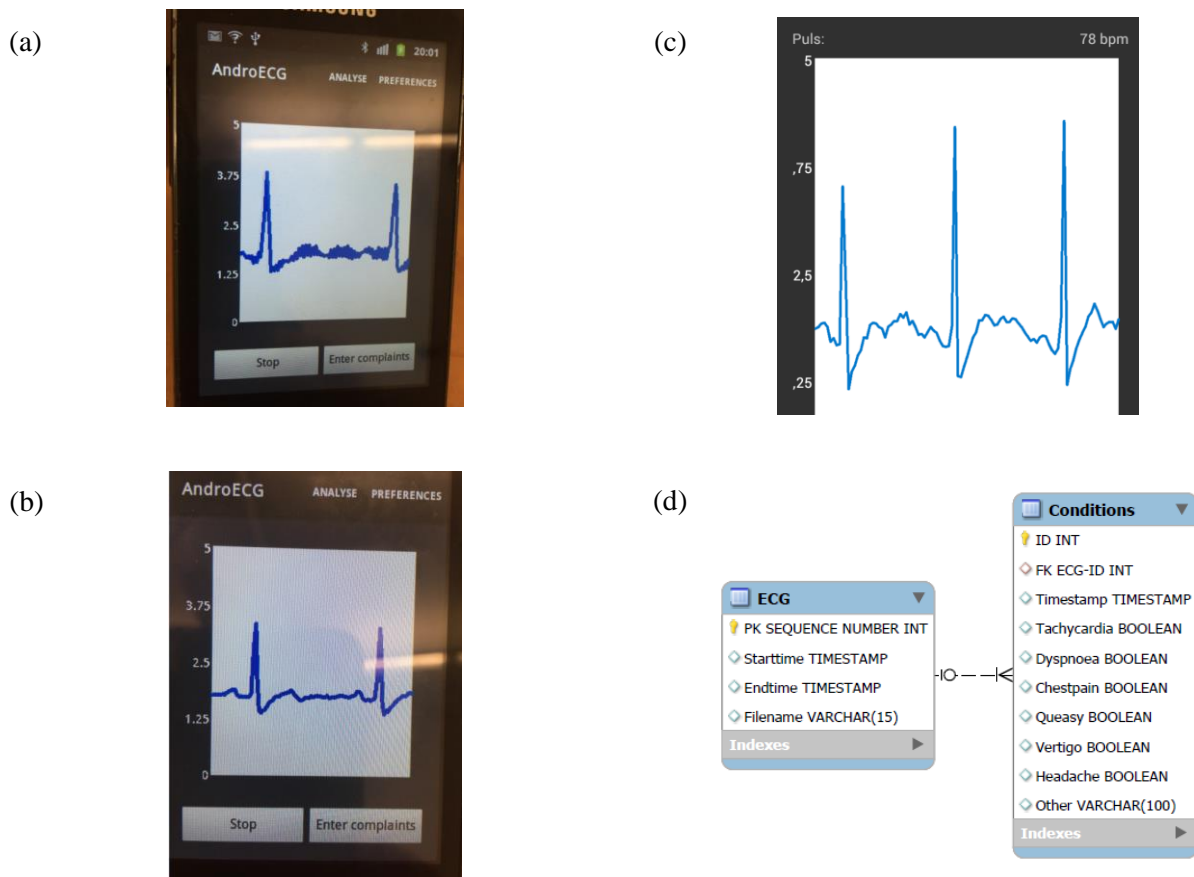


Figure 6.12: Monitoring of ECG signals on a smartphone by (a) Ag/AgCl electrodes; and (b) GN-coated electrodes; (c) HR calculation is shown; (d) a health condition match process: an obtained ECG sequence is compared to the stored values of health issues such as Tachycardia

As can be seen in Figure 6.12, it is evident that the ECG signals were improved by GN-based electrodes when compared to traditional Ag/AgCl. The proposed smartphone application also calculates HR by deriving two consecutive R-peaks. Moreover, a stored ECG sequence can be

analysed to identify specific health issues, which are defined in the software algorithm, such as Tachycardia or Vertigo, as can be seen in figure 6.12d. When the mobile ECG data acquired by Ag/AgCl electrodes are compared with those from GN-based electrodes, it is obvious that the ECG signals using the latter have better signal quality and are able to display all critical cardiac signs, such as the P-wave, QRS complex and the T-wave. In fact, only the QRS complex was identified in mobile ECG signals obtained by the traditional Ag/AgCl electrodes. Hence, it has been demonstrated that graphene (GN) based electrodes provide better experimental results than Ag/AgCl electrodes even in a mobile application.

Subsequently, a smartphone application was developed for the continuous monitoring of CBT measurements. In order to do so, a Bluetooth connection was established between the smartphone and microcontroller unit, then measured CBT values were transmitted to the smartphone for display. Regarding the smartphone application for PPG monitoring, due to Bluetooth connectivity being an attribute of the pulse oximetry device, a smartphone application of the commercial device available in the Android applications store could be used to obtain and display the PPG signal for SpO₂ and the HR. Figure 6.13a shows the smartphone application obtained CBT continuously and wirelessly, whilst Figure 6.13b illustrates the PPG application for both the SpO₂ and HR measurements.

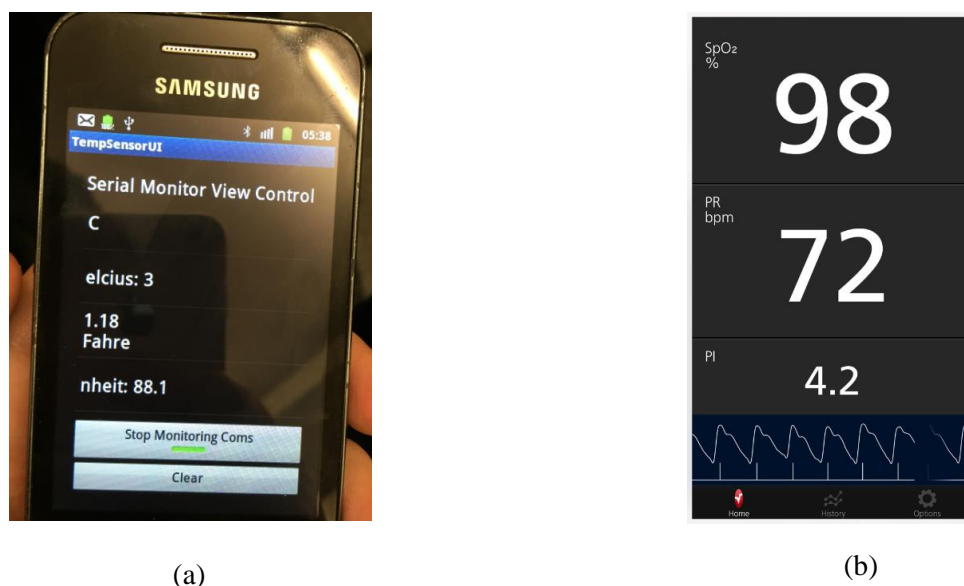


Figure 6.13: Smartphone applications for CBT and PPG signals: **(a)** CBT measurement shows the body temperature in this case as Celcius (31.18 °C) and Fahrenheit (88.1 °F); **(b)** PPG application on a smartphone using a commercially available Amperor Bluetooth PPG sensor produced by Contec [181]

6.4. Analysis of the Wireless Transmission of an ECG Mobile Application

Wireless transmission plays a critical role in enabling successful transfer of health data from an integrated monitoring device to a smartphone. There have been several attempts using different types of wireless infrastructures for communicating the collected health status. Table 6.1 summarises the most important parameters of these wireless infrastructures for wearable health monitoring systems (WHMS).

The specifics of wireless infrastructures of WHMS have to be optimised according to the aim of wearable device. The common desired features regarding WHMS have been low-power, miniaturized, short-range and small antennas due to the operation of wearable devices being on the human body. Consequently, the most popular wireless technologies for WHMS are ZigBee, which operates with low-cost, low data-rate communication with a long battery life and Bluetooth, which has low-cost fabrication and small antennae for communication. As can be seen in Table 6.1, Bluetooth has several advantages over ZigBee, not least, larger bandwidth, whereby it can transfer health information to a server simultaneously and hence, is quite efficient for healthcare applications. Moreover, Bluetooth is used commonly in short-range applications, which are quite feasible for WHMS, given the need for wearable devices for exchanging data from a short distance using mobile devices.

Table 6.1: A summary of the wireless technologies for wearable wireless health monitoring systems

Potential Wireless Technologies	Range (Typical)	Data Rate	Number of Nodes	Frequency Bands (MHz)	Remarks
MedRadio	2 m	200-800 kb/s	N/A	402-405	Large antenna and limited bandwidth
RFID	0-100 m	Tens of Mb/s	Up to 1,000	433	Large antenna, limited bandwidth, and crowded spectrum
WLAN	35-120 m	54-150 Mb/s	255	2,400-2,500	Small antennas, large bandwidth
ZigBee	10-100 m	250 kb/s	Unlimited	2,400-2,500	Small antennas, limited bandwidth

Bluetooth	1-10 m	1-3 Mb/s	7+1	2,400-2,500	Small antenna, large bandwidth
-----------	--------	----------	-----	-------------	-----------------------------------

Given the advantages and useful features of Bluetooth technology, wireless body area networks are implemented with it. Hence, the proposed ear-based wearable wireless monitoring system was conducted with Bluetooth, using the HC-05 Bluetooth module consisting of different modes in its processing system. Figure 6.14 shows the Bluetooth serial module deployed for the current research, which is paired with a smartphone.



Figure 6.14: A view of the Bluetooth module while pairing it with a smartphone

In order to carry out the transmission of integrated health data to a smartphone via a Bluetooth module, calculation of the bandwidth is needed. As mentioned earlier, there are three different channels (ECG, CBT and PPG) that need to be transmitted through Bluetooth communication. The communication module has the capability to transmit data over Bluetooth with a maximum baud rate 115,200 bps. For the proposed system, CBT measurement operates at 20 Hz sampling frequency (16-bit samples), whilst the ECG sensor works at 250 Hz frequency (16-bit samples) with three electrodes and PPG operating at a 30 Hz (16-bit samples), with two photodiodes. Hence, the total data rate will comprise the aggregation of each measured signal's bit rates. The total minimum bandwidth of the system will then be:

$$\text{Baud Rate (BR)} = \text{bit rate of (CBT (kbps) + ECG (kbps) + PPG (kbps))}$$

$$\text{BR} = (\text{sampling frequency of CBT}) * (\text{Nyquist-criteria}) * (\text{sampling bit number}) + (\text{sampling frequency of ECG}) * (\text{Nyquist-criteria}) * (\text{sampling bit number}) * (\text{number of electrodes}) + (\text{sampling frequency of PPG}) * (\text{Nyquist-criteria}) * (\text{sampling bit number}) * (\text{number of electrodes})$$

$$\text{BR} = 20 * 2 (\text{Nyquist-criteria}) * 16 + 250 * 2 * 16 * 3 + 30 * 2 * 16 * 2 = 0.64 + 24 + 1.92$$

$$\text{BR} = 26.56 \text{ kbps.}$$

The above baud rate is much less than that for overall Bluetooth transmission, for which the transmission capacity is 115.2 kbps. Hence, the residual bandwidth will be enough to perform two-way handshaking and allow for sending the bio potentials successfully.

6.5. Summary

The process of designing the proposed wireless multiple smart sensor system (WMSSS) has been described in this chapter. First, the design and setup of an ear-based multifunctional monitoring system was explained. Subsequently, the experimental results and analysis of ECG, CBT, and PPG systems were demonstrated, respectively. Then, an Android based smartphone application was developed for continuous ECG signal monitoring. This ECG-based application has many advantages, such as calculation of heart rate as well as saving the obtained ECG signals and sending them to the server for the purpose of remote patient monitoring. Furthermore, a simple smartphone application was implemented for continuous CBT monitoring and a commercial smartphone application was utilised for PPG monitoring to display SpO₂ and HR. Lastly, wireless technologies were presented for wireless body area networks (WBAN) and the advantages of Bluetooth and ZigBee technologies over other wireless networks were evidenced. Also, in the last transmission baud rate (bandwidth) of the proposed Bluetooth communication was determined.

CHAPTER 7: CONCLUSION and FUTURE WORK

7.1. Conclusion

The key aims of this project were to investigate the effect of graphene (GN) on ECG acquisition systems and to obtain GN-based ECG electrodes for providing higher quality ECG signals when compared to those obtained by traditional Ag/AgCl methods. As a result of the unique structures and superior characteristics of GN and its derivatives, GN-based nanomaterials are amenable to be used in a wide range of applications, including biomedical and biosensor applications. Due to high electrical conductivity, free electron movement on the surface and the availability of fabrication of many GN-functionalised nanocomposites, it is favourable for the synthesising of high performance electrode materials. These superior properties of GN make it possible to achieve the desired sensitivity and measurability for several targets in bio-sensing applications. Several studies concerning ECG sensing applications applied using different types of materials were critically reviewed and the outcomes analysed. It was observed that there is a high demand for robust, reliable, sensitive and accurate ECG monitoring devices in which different types of materials can be used to fabricate new sensors for ECG applications.

In this work, a novel graphene (GN)-coated ECG electrode was developed and its performance was tested in terms of quality-of-signal and durability. The electrodes were obtained by CVD grown on Cu and the structures were transferred to Ag substrates. The experimental results clearly showed improved performance with graphene-coated electrodes. The signal-to-noise ratio has been improved significantly by 12% to 23%, due to GN coating, whilst the quality of the ECG signal in terms of the shape of its morphology is much better when compared to electrodes without GN coating. It was also found that the quality of GN-coated electrodes was not significantly degraded even after multiple uses (10 times). In sum, the experimental results revealed that the obtained ECG signals from 10 different subjects were improved using GN-coated electrodes compared to those when conventional adhesive Ag/AgCl electrodes were deployed.

The characteristics of graphene coating on the conventional electrode were also investigated experimentally using SEM images, Raman spectroscopy, and impedance measurements. The measurements/observations from these experiments have clearly an improvement due to graphene coating. The SEM images show a smoother surface of GN coating, which would increase skin-to-electrode contact. The Raman spectroscopy measurement confirms that there is no presence of the 2D-band before the GN coating process, however, however, Raman spectrum consists of a pronounced 2D-peak of comparable intensity to the G-peak and a pronounced reduction in the full

width at half maximum (FWHM) of the D- and G-bands (see Figure 4.17a and b). As mentioned earlier, these Raman spectroscopy measurements fit with single-layer GN deposition onto a substrate, thereby evidencing separation of itself from the case of graphite or multiple-layer GN deposition. Impedance measurements of the proposed ECG electrodes have shown a lower level being exhibited in GN-coated electrodes when compared those without coating, which increases the sensitivity of the electrode (65 k Ω versus 445 k Ω at 20 Hz).

Finite element modelling (FEM) of a skin–electrode was also developed to understand the electrical activities of such an interface model. The simulation results suggest that the GN coating improves the current density and electric field in the region of interest by a factor two when compared those obtained by Ag-coated electrodes. These results hold promise for further development of the new nanomaterial-enabled dry electrodes for electrophysiological sensing in wearable technologies.

Furthermore, electrode placement investigations were carried out with different scenarios to find out a measurable ECG signal from near the ear to develop an ear-based multi-functional wireless wearable monitoring system. Subsequently, an ear-lead multiple smart sensor system was presented in this project with a 3D printed earbud design, which integrates the ECG and CBT sensors together. First of all, an ECG electrode set-up was demonstrated as obtaining ECG signals from behind-the-ear in contrast to traditional chest-based measurements. The results acquired are very promising, whereby detection of the components of an ECG signal (P-wave, QRS complex, and T-wave) is highly achievable using graphene-based electrodes. The proposed ear-based multifunctional device has a number of advantages: fixed electrode positions; user comfort; robustness; user-friendliness; and it is a reduced motion artifact as well as being discreet. Due to these advantages, an ear-based physiological monitoring system was modeled with continuous monitoring on an Android based smartphone, providing real-time data control for the patients and also clinicians. This device includes non-intrusive sensors for ECG, CBT, and PPG with high accuracy. Moreover, an Android based app was developed and tested, in order to display ECG, CBT, HR, and SpO₂ physiological data on a person's smartphone. Moreover, observations were made of the influence of sensor positioning on signal quality and skin-electrode contact impedance using various types of ECG electrodes. Even though a chest-based sensor positioning provided the best SNR (27.03 dB) and lowest contact impedance values (65 k Ω at 20 Hz), an ear-based proposed sensor system also demonstrated promising results (22.96 dB SNR with GN-coated electrode) compared to other prototypes. Additionally, the proposed system ameliorates the difficulties of wearable devices, giving patients significantly less restriction by eliminating the need for adapting intrusive equipment or using a laptop to monitor the obtained physiological data. The design of the proposed ear-based multiple smart sensor system also provides wireless transfer of data using

Bluetooth technology to connect to a smartphone for further analysis. Experimental results and analysis clearly exhibited the feasibility of the concept and interoperability of the biosensors as well as providing solutions to key technological and scientific problems.

7.2. Future Works

First of all, the proposed GN based ECG sensor still has PMMA residues left from transferring graphene grown by chemical vapour deposition (CVD), which remains a challenge for maximising the effect of GN in regard to ECG monitoring. New approaches can be developed for a simple cleaning method for removing PMMA residues that can reduce impairments to the electronic properties of GN-coated electrodes. If a high-quality graphene coating process on Ag substrates can be carried out, then skin-electrode impedance can be much reduced and the proposed ECG sensor's performance can be improved further.

Furthermore, the developed mobile healthcare platform could be extended by applying the following suggestions in order to minimise the data acquisition module and to achieve even more promising performance regarding physiological signals monitoring.

- In this study, adhesive gel was applied to GN-coated electrodes for acquiring ECG signals from the body. Implementation of GN based dry type ECG sensors could help in conforming to the skin without the need for adhesive gels, thereby improving the impedance of the skin-electrode interface. To this end, another dry type ECG electrode could be fabricated with GN coating using the CVD process in the future. Likewise, other GN-production techniques can be utilised to synthesise dry type ECG electrodes, such as liquid-based exfoliation and further comparisons could then be made.
- In this research, GN has demonstrated valuable electrical characteristics when coated with Ag substrate in ECG monitoring, as exhibited in experimental results. Apart from ECG acquisition, GN also can be grown on sensors for temperature and SpO₂ measurements. Fabricating GN-based temperature sensors and photodetectors can result in better performance for CBT and PPG monitoring due to sensitive temperature coefficient resistivity and rapid responsivity characteristics.
- Implementing a PPG sensor on the ear lobe can minimise the multifunctional experimental development and the proposed system will be capable of integrating with other ECG and CBT sensors in an ear-based device.
- The designed system may be developed further within printed wearable electronics to enhance the level of comfort, flexibility and wearability of multiple physiological sensors, which can be combined into a single, unobtrusive and ease-of-use miniaturised package.

Fabrication of a flexible and wearable hybrid electronics patch means that it can be worn near the ear area, whereby the motion of the artefact can be minimised with a discreet solution. The signals detected from these sensors can then be wirelessly transmitted to a smartphone, in which a dedicated app will be installed for continuous monitoring and obtaining further physiological measurements, such as blood pressure and heart rate variability (HRV).

REFERENCES

- [1] P. Bifulco, M. Cesarelli, A. Fratini, M. Ruffo, G. Pasquariello, and G. Gargiulo, "A Wearable Device for Recording of Biopotentials and Body Movements," in *MeMeA 2011 - 2011 IEEE International Symposium on Medical Measurements and Applications, Proceedings*, 2011, pp. 469–472.
- [2] A. Milenković, C. Otto, and E. Jovanov, "Wireless sensor networks for personal health monitoring: Issues and an implementation," *Comput. Commun.*, vol. 29, no. 13–14, pp. 2521–2533, Aug. 2006.
- [3] N. Manivannan, N. Celik, and W. Balachandran, "Evaluation of a Behind-the-Ear ECG Device for Smartphone based Integrated Multiple Smart Sensor System in Health Applications," *Int. J. Adv. Comput. Sci. Appl.*, vol. 7, no. 7, pp. 409–418, 2016.
- [4] J. Yoo, L. Yan, S. Lee, H. Kim, and H. J. Yoo, "A wearable ECG acquisition system with compact planar-fashionable circuit board-based shirt," *IEEE Trans. Inf. Technol. Biomed.*, vol. 13, no. 6, pp. 897–902, 2009.
- [5] C. A. Boano, M. Lasagni, and K. Romer, "Non-invasive measurement of core body temperature in Marathon runners," in *2013 IEEE International Conference on Body Sensor Networks*, 2013, pp. 1–6.
- [6] S. Laxminarayan, M. J. Buller, W. J. Tharion, and J. Reifman, "Human core temperature prediction for heat-injury prevention," *IEEE J. Biomed. Heal. Informatics*, vol. 19, no. 3, pp. 883–891, 2015.
- [7] M. O. Wiens, E. Kumbakumba, N. Kissoon, J. M. Ansermino, A. Ndamira, and C. P. Larson, "Pediatric sepsis in the developing world: Challenges in defining sepsis and issues in post-discharge mortality," *Clinical Epidemiology*, vol. 4, no. 1, pp. 319–325, 2012.
- [8] C. L. Petersen, T. P. Chen, J. M. Ansermino, and G. A. Dumont, "Design and evaluation of a low-cost smartphone pulse oximeter," *Sensors (Basel)*, vol. 13, no. 12, pp. 16882–16893, 2013.
- [9] J. Allen, "Photoplethysmography and its application in clinical physiological measurement," *Physiol. Meas.*, vol. 28, no. 3, pp. R1–R39, 2007.
- [10] M. M. Puurtinen, S. M. Komulainen, P. K. Kauppinen, J. A. V Malmivuo, and J. A. K. Hyttinen, "Measurement of noise and impedance of dry and wet textile electrodes, and textile electrodes with hydrogel," in *Annual International Conference of the IEEE Engineering in Medicine and Biology - Proceedings*, 2006, pp. 6012–6015.
- [11] A. Gruetzmann, S. Hansen, and J. Uller, "Novel dry electrodes for ECG monitoring," *Physiol. Meas.*, vol. 28, pp. 1375–1390, 2007.
- [12] J. Y. Baek, J. H. An, J. M. Choi, K. S. Park, and S. H. Lee, "Flexible polymeric dry electrodes for the long-term monitoring of ECG," *Sensors Actuators, A Phys.*, vol. 143, no. 2, pp. 423–429, 2008.

- [13] S. Leonhardt and A. Aleksandrowicz, “Non-contact ECG monitoring for automotive application,” in *Proc. 5th Int. Workshop on Wearable and Implantable Body Sensor Networks, BSN2008, in conjunction with the 5th Int. Summer School and Symp. on Medical Devices and Biosensors, ISSS-MDBS 2008*, 2008, pp. 183–185.
- [14] S. Fuhrhop, S. Lamparth, and S. Heuer, “A textile integrated long-term ECG monitor with capacitively coupled electrodes,” in *2009 IEEE Biomedical Circuits and Systems Conference, BioCAS 2009*, 2009, pp. 21–24.
- [15] I. J. Wang, L. De Liao, Y. Te Wang, C. Y. Chen, B. S. Lin, S. W. Lu, and C. T. Lin, “A wearable mobile electrocardiogram measurement device with novel dry polymer-based electrodes,” in *IEEE Region 10 Annual International Conference, Proceedings/TENCON*, 2010, pp. 379–384.
- [16] N. Gandhi, C. Khe, D. Chung, Y. M. Chi, and G. Cauwenberghs, “Properties of dry and non-contact electrodes for wearable physiological sensors,” in *Proceedings - 2011 International Conference on Body Sensor Networks, BSN 2011*, 2011, pp. 107–112.
- [17] a. Rashkovska, I. Tomasic, and R. Trobec, “A Telemedicine application: ECG data from wireless body sensors on a Smartphone,” *2011 Proc. 34th Int. Conv. MIPRO*, pp. 262–265, 2011.
- [18] E. M. Fong and W. Y. Chung, “Mobile cloud-computing-based healthcare service by noncontact ECG monitoring,” *Sensors (Basel)*, vol. 13, no. 12, pp. 16451–16473, 2013.
- [19] G. Yang, L. Xie, and L. R. Zheng, “Evaluation of non-contact flexible electrodes connected with a customized IC-steps towards a fully integrated ECG sensor,” in *NORCHIP 2013*, 2013.
- [20] T. I. Oh, S. Yoon, T. E. Kim, H. Wi, K. J. Kim, E. J. Woo, and R. J. Sadleir, “Nanofiber web textile dry electrodes for long-term biopotential recording,” *IEEE Trans. Biomed. Circuits Syst.*, vol. 7, no. 2, pp. 204–211, 2013.
- [21] L. Bor-Shyh, W. Chou, W. Hsing-Yu, H. Yan-Jun, and P. Jeng-Shyang, “Development of Novel Non-Contact Electrodes for Mobile Electrocardiogram Monitoring System,” *IEEE J. Transl. Eng. Heal. Med.*, vol. 1, no. 2013, pp. 1–8, 2013.
- [22] K. Ito, Y. Fukuoka, G. Cauwenberghs, and A. Ueno, “Noncontact Sensing of Electrocardiographic Potential and Body Proximity by In-bed Conductive Fabrics University of California San Diego , CA , USA,” *Comput. Cardiol. (2010)*, vol. 40, pp. 523–526, 2013.
- [23] V. K. Varadan, P. S. Kumar, S. Oh, H. Kwon, P. Rai, N. Banerjee, and R. E. Harbaugh, “e-Nanoflex Sensor System: Smartphone-Based Roaming Health Monitor,” *J. Nanotechnol. Eng. Med.*, vol. 2, no. 1, p. 011016, 2011.
- [24] V. K. Varadan, P. S. Kumar, S. Oh, L. Kegley, and P. Rai, “e-bra With Nanosensors for Real Time Cardiac Health Monitoring and Smartphone Communication,” *J. Nanotechnol. Eng. Med.*, vol. 2, no. 2, pp. 1–7, 2011.
- [25] P. Rai, P. S. Kumar, S. Oh, H. Kwon, G. N. Mathur, V. K. Varadan, and M. P. Agarwal, “Smart healthcare textile sensor system for unhindered-pervasive health monitoring,” in

SPIE Smart Structures and Materials + Nondestructive Evaluation and Health Monitoring, 2012, p. 83440E–83440E–10.

- [26] L. S. Hsu, S. W. Tung, C. H. Kuo, and Y. J. Yang, “Developing barbed microtip-based electrode arrays for biopotential measurement,” *Sensors (Basel)*, vol. 14, no. 7, pp. 12370–12386, 2014.
- [27] S. Kwon, J. Kim, S. Kang, Y. Lee, H. Baek, and K. Park, “CardioGuard: a brassiere-based reliable ECG monitoring sensor system for supporting daily smartphone healthcare applications,” *Telemed. J. E. Health.*, vol. 20, no. 12, pp. 1093–1102, 2014.
- [28] J. C. Batchelor and A. J. Casson, “Inkjet printed ECG electrodes for long term biosignal monitoring in personalized and ubiquitous healthcare,” *Proc. Annu. Int. Conf. IEEE Eng. Med. Biol. Soc. EMBS*, vol. 2015-Novem, pp. 4013–4016, 2015.
- [29] A. A. Chlaihawi, B. B. Narakathu, S. Emamian, A. Eshkeiti, S. Guruva, A. Reddy, B. J. Bazuin, and M. Z. Atashbar, “Development of Flexible Dry ECG Electrodes Based on MWCNT / PDMS Composite,” *Proc. Sensors 2015, IEEE*, pp. 1–4, 2015.
- [30] Y. Meng, Z. B. Li, X. Chen, and J. P. Chen, “A flexible dry micro-dome electrode for ECG monitoring,” *Microsyst. Technol.*, vol. 21, no. 6, pp. 1241–1248, 2014.
- [31] Y. Meng, Z. Li, and J. Chen, “A flexible dry electrode based on APTES-anchored PDMS substrate for portable ECG acquisition system,” *Microsyst. Technol.*, vol. 22, no. 8, pp. 2027–2034, 2016.
- [32] B. Liu, Z. Luo, W. Zhang, Q. Tu, and X. Jin, “Silver nanowire-composite electrodes for long-term electrocardiogram measurements,” *Sensors Actuators, A Phys.*, vol. 247, pp. 459–464, 2016.
- [33] S. M. Lee, H. J. Byeon, J. H. Lee, D. H. Baek, K. H. Lee, J. S. Hong, and S.-H. Lee, “Self-adhesive epidermal carbon nanotube electronics for tether-free long-term continuous recording of biosignals,” *Sci. Rep.*, vol. 4, p. 6074, 2014.
- [34] W. Pei, H. Zhang, Y. Wang, X. Guo, X. Xing, Y. Huang, Y. Xie, X. Yang, and H. Chen, “Skin-potential variation insensitive dry electrodes for ECG recording,” *IEEE Trans. Biomed. Eng.*, vol. 9294, no. 99, pp. 1–8, 2016.
- [35] K.-I. Jang, H. N. Jung, J. W. Lee, S. Xu, Y. H. Liu, Y. Ma, J.-W. Jeong, Y. M. Song, J. Kim, B. H. Kim, A. Banks, J. W. Kwak, Y. Yang, D. Shi, Z. Wei, X. Feng, U. Paik, Y. Huang, R. Ghaffari, and J. a. Rogers, “Ferromagnetic, Folded Electrode Composite as a Soft Interface to the Skin for Long-Term Electrophysiological Recording,” *Adv. Funct. Mater.*, vol. 26, no. 40, pp. 7281–7290, 2016.
- [36] M. Poliks, J. Turner, K. Ghose, Z. Jin, M. Garg, Q. Gui, M. Schadt, and F. Egitto, “A Wearable Flexible Hybrid Electronics ECG Monitor,” *IEEE 66th Electron. Components Technol. Conf.*, pp. 1623–1631, 2016.
- [37] M. Dai, X. Xiao, X. Chen, H. Lin, W. Wu, and S. Chen, “A low-power and miniaturized electrocardiograph data collection system with smart textile electrodes for monitoring of cardiac function,” *Australas. Phys. Eng. Sci. Med.*, pp. 1–12, 2016.

- [38] D. Pani, A. Dessi, J. F. Saenz-Cogollo, G. Barabino, B. Fraboni, and A. Bonfiglio, "Fully Textile, PEDOT:PSS Based Electrodes for Wearable ECG Monitoring Systems," *IEEE Trans. Biomed. Eng.*, vol. 63, no. 3, pp. 540–549, 2016.
- [39] Y. Noh, J. R. Bales, B. a. Reyes, J. Molognani, A. L. Clement, G. D. Pins, J. P. Florian, and K. H. Chon, "Novel Conductive Carbon Black and Polydimethylsiloxane ECG Electrode: A Comparison with Commercial Electrodes in Fresh, Chlorinated, and Salt Water," *Ann. Biomed. Eng.*, vol. 44, no. 8, pp. 1–16, 2016.
- [40] M. A. Yokus and J. S. Jur, "Fabric-based wearable dry electrodes for body surface biopotential recording," *IEEE Trans. Biomed. Eng.*, vol. 63, no. 2, pp. 423–430, 2016.
- [41] C. O'Mahony, K. Grygoryev, A. Ciarlone, G. Giannoni, A. Kenthao, and P. Galvin, "Design, fabrication and skin-electrode contact analysis of polymer microneedle-based ECG electrodes," *J. Micromechanics Microengineering*, vol. 26, no. 8, p. 84005, 2016.
- [42] A. I. Aulia, R. Kolla, S. Klaus, and W. Voelker, "A Wearable 1-Lead Necklace ECG for Continuous Heart Rate Monitoring," *IEEE 18th Int. Conf. e-Health Networking, Appl. Serv.*, pp. 16–19, 2016.
- [43] S. Imani, A. J. Bhandodkar, A. M. V. Mohan, R. Kumar, S. Yu, J. Wang, and P. P. Mercier, "A wearable chemical-electrophysiological hybrid biosensing system for real-time health and fitness monitoring," *Nat. Commun.*, vol. 7, p. 11650, 2016.
- [44] Y. Khan, M. Garg, Q. Gui, M. Schadt, A. Gaikwad, D. Han, N. a. D. Yamamoto, P. Hart, R. Welte, W. Wilson, S. Czarnecki, M. Poliks, Z. Jin, K. Ghose, F. Egitto, J. Turner, and A. C. Arias, "Flexible Hybrid Electronics: Direct Interfacing of Soft and Hard Electronics for Wearable Health Monitoring," *Adv. Funct. Mater.*, pp. 1–12, 2016.
- [45] K. Takahashi, M. Soichiro, and S. Kenji, "A Smart Clothe for ECG Monitoring of Children with Autism Spectrum Disorders," *Int. Conf. Comput. Help. People with Spec. Needs, ICCHP 2016*, pp. 552–562, 2016.
- [46] J. Pan and W. J. Tompkins, "A Real-Time QRS Detection Algorithm," *IEEE Trans. Biomed. Eng.*, vol. BME-32, no. 3, pp. 230–236, 1985.
- [47] B. Liu, Z. Luo, W. Zhang, Q. Tu, and X. Jin, "Carbon nanotube-based self-adhesive polymer electrodes for wireless long-term recording of electrocardiogram signals," *J. Biomater. Sci. Polym. Ed.*, vol. 27, no. 18, pp. 1899–1908, 2016.
- [48] D. N. Mathias, J. Park, E. Kim, and Y. H. Joung, "Development of a novel noncontact ECG electrode by MEMS fabrication process," *Trans. Electr. Electron. Mater.*, vol. 17, no. 3, pp. 150–154, 2016.
- [49] T. Le, H. Han, and T. Hoang, "A Low Cost Mobile ECG Monitoring Device Using Two Active Dry Electrodes," *IEEE Sixth Int. Conf. Commun. Electron.*, pp. 271–276, 2016.
- [50] T. Kim, J. Park, J. Sohn, D. Cho, and S. Jeon, "Bioinspired, Highly Stretchable, and Conductive Dry Adhesives Based on 1D-2D Hybrid Carbon Nanocomposites for All-in-One ECG Electrodes," *ACS Nano*, vol. 10, no. 4, pp. 4770–4778, 2016.

- [51] H. C. Jung, J. H. Moon, D. H. Baek, J. H. Lee, Y. Y. Choi, J. S. Hong, and S. H. Lee, "CNT/PDMS composite flexible dry electrodes for long-term ECG monitoring," *IEEE Trans. Biomed. Eng.*, vol. 59, no. 5, pp. 1472–1479, 2012.
- [52] T. Thap, K. H. Yoon, and J. Lee, "Graphite based electrode for ECG monitoring: Evaluation under freshwater and saltwater conditions," *Sensors (Switzerland)*, vol. 16, no. 4, 2016.
- [53] J. Kariuki, E. Ervin, and C. Olafson, "Development of a novel, low-cost, disposable wooden pencil graphite electrode for use in the determination of antioxidants and other biological compounds," *Sensors (Switzerland)*, vol. 15, no. 8, pp. 18887–18900, 2015.
- [54] A. K. Geim and A. H. MacDonald, "Graphene: Exploring carbon flatland," *Phys. Today*, vol. 60, no. 8, pp. 35–41, 2007.
- [55] C. H. Chen, C. Te Lin, W. L. Hsu, Y. C. Chang, S. R. Yeh, L. J. Li, and D. J. Yao, "A flexible hydrophilic-modified graphene microprobe for neural and cardiac recording," *Nanomedicine Nanotechnology, Biol. Med.*, vol. 9, no. 5, pp. 600–604, 2013.
- [56] Y. Wang, Z. Li, J. Wang, J. Li, and Y. Lin, "Graphene and graphene oxide: Biofunctionalization and applications in biotechnology," *Trends in Biotechnology*, vol. 29, no. 5, pp. 205–212, 2011.
- [57] Z. Yin, J. Zhu, Q. He, X. Cao, C. Tan, H. Chen, Q. Yan, and H. Zhang, "Graphene-Based materials for solar cell applications," *Advanced Energy Materials*, vol. 4, no. 1, 2014.
- [58] Y. Xuan, Y. Q. Wu, T. Shen, M. Qi, M. A. Capano, J. A. Cooper, and P. D. Ye, "Atomic-layer-deposited nanostructures for graphene-based nanoelectronics," *Appl. Phys. Lett.*, vol. 92, no. 1, 2008.
- [59] M. K. Yapici, T. Alkhidir, Y. A. Samad, and K. Liao, "Graphene-clad textile electrodes for electrocardiogram monitoring," *Sensors Actuators B Chem.*, vol. 221, pp. 1469–1474, 2015.
- [60] C. W. Mundt, K. N. Montgomery, U. E. Udoh, V. N. Barker, G. C. Thonier, A. M. Tellier, R. D. Ricks, R. B. Darling, Y. D. Cagle, N. A. Cabrol, S. J. Ruoss, J. L. Swain, J. W. Hines, and G. T. A. Kovacs, "A multiparameter wearable physiologic monitoring system for space and terrestrial applications," *IEEE Trans. Inf. Technol. Biomed.*, vol. 9, no. 3, pp. 382–391, 2005.
- [61] R. Paradiso, G. Loriga, and N. Taccini, "Wealthy, a wearable healthcare system: new frontier on e-textile," *J. Telecommunications Inf. Technol.*, vol. 4, pp. 105–113, 2005.
- [62] V. Shnayder, B. Chen, K. Lorincz, T. R. F. F. Jones, and M. Welsh, "Sensor networks for medical care," *Tech. Rep. TR-08-05, Div. Eng. Appl. Sci. Harvard Univ.*, no. June, pp. 1–16, 2005.
- [63] Memsic, "MICAz datasheet: 6020-0065-05 rev," *San Jose, CA, California*, vol. Revision 6, pp. 1–2, 2003.
- [64] Moteiv, "Telos Manual," 2004.
- [65] P. S. Pandian, K. Mohanavelu, K. P. Safeer, T. M. Kotresh, D. T. Shakunthala, P. Gopal, and V. C. Padaki, "Smart Vest: Wearable multi-parameter remote physiological monitoring system," *Med. Eng. Phys.*, vol. 30, no. 4, pp. 466–477, 2008.

- [66] S. Kwon, D. Lee, J. Kim, Y. Lee, S. Kang, S. Seo, and K. Park, "Sinabro: A smartphone-integrated opportunistic electrocardiogram monitoring system," *Sensors (Switzerland)*, vol. 16, no. 3, 2016.
- [67] J. H. Yap, Y.-H. Noh, and D.-U. Jeong, "Implementation of mobile healthcare monitoring system with portable base station," *5th International Conference on Convergence and Hybrid Information Technology, ICHIT 2011*, vol. 206 CCIS. pp. 475–480, 2011.
- [68] Y. H. Lin, C. F. Lin, and H. Z. You, "A driver's physiological monitoring system based on a wearable PPG sensor and a smartphone," in *Communications in Computer and Information Science*, 2011, vol. 223 CCIS, pp. 326–335.
- [69] J. M. Sanches, B. Pereira, and T. Paiva, "Headset Bluetooth and cell phone based continuous central body temperature measurement system.," *Conf. Proc. IEEE Eng. Med. Biol. Soc.*, vol. 2010, pp. 2975–2978, 2010.
- [70] W. Song, H. Yu, C. Liang, Q. Wang, and Y. Shi, "Body monitoring system design based on android smartphone," in *Proceedings of the 2012 World Congress on Information and Communication Technologies, WICT 2012*, 2012, pp. 1147–1151.
- [71] "ZTP-135SR Thermometrics Thermopile IR Sensor," 2012. [Online]. Available: <http://www.alliedelec.com/m/d/9fa458adb9114ab6a505eed592be56aa.pdf>. [Accessed: 29-Dec-2016].
- [72] D. Da He, E. S. Winokur, T. Heldt, and C. G. Sodini, "The ear as a location for wearable vital signs monitoring," in *2010 Annual International Conference of the IEEE Engineering in Medicine and Biology Society, EMBC'10*, 2010, pp. 6389–6392.
- [73] M. Z. Poh, K. Kim, A. Goessling, N. Swenson, and R. Picard, "Cardiovascular monitoring using earphones and a mobile device," *IEEE Pervasive Comput.*, vol. 11, no. 4, pp. 18–26, 2012.
- [74] D. Da He, E. S. Winokur, and C. G. Sodini, "An ear-worn vital signs monitor," *IEEE Trans. Biomed. Eng.*, vol. 62, no. 11, pp. 2547–2552, 2015.
- [75] O. T. Inan, M. Etemadi, R. M. Wiard, L. Giovangrandi, and G. T. a Kovacs, "Robust ballistocardiogram acquisition for home monitoring.," *Physiol. Meas.*, vol. 30, no. 2, pp. 169–85, 2009.
- [76] C. M. Lochner, Y. Khan, A. Pierre, and A. C. (UC B. Arias, "All-organic optoelectronic sensor for pulse oximetry.," *Nat. Commun.*, vol. 5, p. 5745, 2014.
- [77] S. Xu, Y. Zhang, L. Jia, K. E. Mathewson, K.-I. Jang, J. Kim, H. Fu, X. Huang, P. Chava, R. Wang, S. Bhole, L. Wang, Y. J. Na, Y. Guan, M. Flavin, Z. Han, Y. Huang, and J. a Rogers, "Soft Microfluidic Assemblies of Sensors, Circuits, and Radios for the Skin," *Science (80-.)*, vol. 344, no. 70, pp. 70–74, 2014.
- [78] P. Kakria, N. K. Tripathi, and P. Kitipawang, "A real-time health monitoring system for remote cardiac patients using smartphone and wearable sensors," *Int. J. Telemed. Appl.*, vol. 2015, 2015.

- [79] J. Kim and H. Ko, "Reconfigurable Multiparameter Biosignal Acquisition SoC for Low Power Wearable Platform," *Sensors*, vol. 16, no. 12, pp. 1–13, 2016.
- [80] M. Konijnenburg, S. Stanzione, L. Yan, D. Jee, J. Pettine, R. Van Wegberg, H. Kim, C. Van Liempd, R. Fish, J. Schuessler, H. De Groot, C. Van Hoof, R. F. Yazicioglu, and N. Van Helleputte, "A Multi(bio)sensor Acquisition System With Integrated Processor, Power Management, 8 × 8 LED Drivers, and Simultaneously Synchronized ECG, BIO-Z, GSR, and Two PPG Readouts," *IEEE J. Solid-State Circuits*, vol. 51, no. 11, pp. 2584–2595, 2016.
- [81] R. Mukkamala, J.-O. Hahn, O. T. Inan, L. K. Mestha, C.-S. Kim, H. Toreyin, and S. Kyal, "Toward Ubiquitous Blood Pressure Monitoring via Pulse Transit Time: Theory and Practice," *IEEE Trans. Biomed. Eng.*, vol. 62, no. 8, pp. 1879–1901, 2015.
- [82] E. A. P. J. Prawiro, C. I. Yeh, N. K. Chou, M. W. Lee, and Y. H. Lin, "Integrated Wearable System for Monitoring Heart Rate and Step during Physical Activity," *Mob. Inf. Syst.*, vol. 2016, 2016.
- [83] "MIT-BIH ST Change Database." .
- [84] P. J. Soh, G. A. E. VVandenbosch, M. Mercuri, and D. M. M.-P. Schreurs, "Wearable Wireless Health Monitoring," *IEEE Microw. Mag.*, vol. 16, no. 4, pp. 55–70, 2015.
- [85] M. Jain, N. Kumar, and S. Deb, "A multi-signal acquisition system for preventive cardiology with cuff-less BP measurement capability," *2016 8th Int. Conf. Commun. Syst. Networks, COMSNETS 2016*, pp. 1–6, 2016.
- [86] C. Watson, "Cardiovascular Physiology," in *Human Physiology*, Jones & Barlett Learning, 2015, pp. 143–172.
- [87] L. Sherwood, "Cardiac Physiology," in *Human Physiology*, Brooks/Cole-Thomson Learning, 2007, pp. 232–289.
- [88] "Cardiac Conduction System." [Online]. Available: <http://www.nottingham.ac.uk/nursing/practice/resources/cardiology/function/conduction.php>. [Accessed: 07-Jan-2017].
- [89] A. Khaja and G. Flaker, "Bachmann's bundle: Does it play a role in atrial fibrillation?," *PACE - Pacing and Clinical Electrophysiology*, vol. 28, no. 8, pp. 855–863, 2005.
- [90] J. Sundnes, G. T. Lines, X. Cai, B. F. Nielsen, K.-A. Mardal, and A. Tveito, *Computing the Electrical Activity in the Heart*. Springer Science & Business Media, 2007.
- [91] J. E. Hall and A. C. Guyton, *Guyton and Hall Textbook of Medical Physiology*, vol. 53. 2011.
- [92] R. E. Klabunde, "Cardiovascular Physiology Concepts (2nd Ed.)," *Lippincott Williams & Wilkins*, p. 256, 2012.
- [93] S. Wagner and D. Strauss, *Marriott's practical electrocardiography*. Philadelphia : Wolters Kluwer Health/Lippincott Williams & Wilkins, 2014.

- [94] J. Malmivuo and R. Plonsey, *Bioelectromagnetism: Principles and Applications of Bioelectric and Biomagnetic Fields*. Oxford University Press, 2012.
- [95] K. K. Kim and K. S. Park, “Effective coupling impedance for power line interference in capacitive-coupled ECG measurement system,” in *5th Int. Conference on Information Technology and Applications in Biomedicine, ITAB 2008 in conjunction with 2nd Int. Symposium and Summer School on Biomedical and Health Engineering, IS3BHE 2008*, 2008, pp. 256–258.
- [96] A. Aleksandrowicz and S. Leonhardt, “Wireless and Non-contact ECG Measurement System – the “Aachen SmartChair,” *Integr. Vlsi J.*, vol. 47, no. 4, pp. 5–8, 2007.
- [97] Y. M. Chi, T. P. Jung, and G. Cauwenberghs, “Dry-contact and noncontact biopotential electrodes: Methodological review,” *IEEE Rev. Biomed. Eng.*, vol. 3, pp. 106–119, 2010.
- [98] L. Sörnmo and P. Laguna, *Bioelectrical Signal Processing in Cardiac and Neurological Applications*, vol. 16. 2014.
- [99] G. M. Friesen, T. C. Jannett, M. A. Jadallah, S. L. Yates, S. R. Quint, and H. T. Nagle, “A Comparison of the Noise Sensitivity of Nine QRS Detection Algorithms,” *IEEE Trans. Biomed. Eng.*, vol. 37, no. 1, pp. 85–98, 1990.
- [100] D. H. Lee, “Development of a Mobile Phone Based e-Health Monitoring Application,” *Int. J. Adv. Comput. Sci. Appl.*, vol. 3, no. 3, pp. 38–43, 2012.
- [101] M. Sund-Levander and E. Grodzinsky, “Time for a change to assess and evaluate body temperature in clinical practice,” *Int. J. Nurs. Pract.*, vol. 15, no. 4, pp. 241–249, 2009.
- [102] T. H. Y. Ling, L. J. Wong, J. E. H. Tan, and K. Y. Kiu, “Non-intrusive Human Body Temperature Acquisition and Monitoring System,” in *Proceedings - International Conference on Intelligent Systems, Modelling and Simulation, ISMS*, 2015, vol. 2015-October, pp. 16–20.
- [103] R. Rhoades and R. Pflanzner, *Human Physiology*. Brooks/Cole; 4th Revised edition edition, 2003.
- [104] D. S. Moran and L. Mendal, “Core Temperature Measurement,” *Sport. Med.*, vol. 32, no. 14, pp. 879–885, 2002.
- [105] M. N. Sawka, K. B. Pandolf, and B. C. Wenger, “Thermoregulatory Responses to Acute Exercise-Heat Stress and Heat Acclimation,” *Handb. Physiol. Environ. Physiol.*, no. February, pp. 157–185, 1996.
- [106] K. Shiraki and M. Yousef, *Man in Stressful Environments: Thermal and Work Physiology*. The University of Michigan, 1987.
- [107] C. G. Cattaneo, S. M. Frank, T. W. Hesel, H. K. El-Rahmany, L. J. Kim, and K. M. Tran, “The accuracy and precision of body temperature monitoring methods during regional and general anesthesia,” *Anesth Analg*, vol. 90, no. 4, pp. 938–945, 2000.

- [108] A. L. Chue, R. L. Moore, A. Cavey, E. a Ashley, K. Stepniewska, F. Nosten, and R. McGready, “Comparability of tympanic and oral mercury thermometers at high ambient temperatures,” *BMC Res. Notes*, vol. 5, no. 1, p. 356, 2012.
- [109] T. E. Terndrup, J. R. Allegra, and J. A. Kealy, “A comparison of oral, rectal, and tympanic membrane-derived temperature changes after ingestion of liquids and smoking,” *Am. J. Emerg. Med.*, vol. 7, no. 2, pp. 150–154, 1989.
- [110] M. M. Green, D. F. Danzl, and H. Praszkiar, “Infrared tympanic thermography in the emergency department,” *J. Emerg. Med.*, vol. 7, no. 5, pp. 437–440, 1989.
- [111] C. Zhen, Z. Xia, L. Long, and Y. Pu, “Accuracy of Infrared Ear Thermometry in Children: A Meta-Analysis and Systematic Review,” *Clin. Pediatr. (Phila.)*, vol. 53, no. 12, pp. 1158–1165, 2014.
- [112] B. K. Timby, *Fundamental Nursing Skills and Concepts, 8th Edition*. Lippincott Williams & Wilkins, 2005.
- [113] M. Liess, H. Karagözoglu, and H. Ernst, “Reducing thermal transient induced errors in thermopile sensors in ear thermometer applications,” *Sensors Actuators, A Phys.*, vol. 154, no. 1, pp. 1–6, 2009.
- [114] G. Peng, Z. Liu, and L. Liu, “Application of ZTP135S-R sensor in thermometer,” *Int. Electron. Elem.*, no. 4, pp. 38–40, 2006.
- [115] “Melexis MLX90614 Infrared Thermometer,” 2014. [Online]. Available: <https://www.melexis.com/en/product/MLX90614/Digital-Plug-Play-Infrared-Thermometer-TO-Can>. [Accessed: 17-Sep-2016].
- [116] Y. Mendelson, “Pulse oximetry: Theory and applications for noninvasive monitoring,” in *Clinical Chemistry*, 1992, vol. 38, no. 9, pp. 1601–1607.
- [117] M. Z. Poh, N. C. Swenson, and R. W. Picard, “Motion-tolerant magnetic earring sensor and wireless earpiece for wearable photoplethysmography,” *IEEE Trans. Inf. Technol. Biomed.*, vol. 14, no. 3, pp. 786–794, 2010.
- [118] T. Tamura, Y. Maeda, M. Sekine, and M. Yoshida, “Wearable Photoplethysmographic Sensors—Past and Present,” *Electronics*, vol. 3, no. 2, pp. 282–302, 2014.
- [119] R. R. Anderson and J. A. Parrish, “The optics of human skin,” *J. Invest. Dermatol.*, vol. 77, no. 1, pp. 13–19, 1981.
- [120] S. Rhee, B. H. Yang, and H. H. Asada, “Artifact-resistant power-efficient design of finger-ring plethysmographic sensors,” *IEEE Trans. Biomed. Eng.*, vol. 48, no. 7, pp. 795–805, 2001.
- [121] Y. Lee, H. Shin, J. Jo, and Y. K. Lee, “Development of a wristwatch-type PPG array sensor module,” in *Digest of Technical Papers - IEEE International Conference on Consumer Electronics*, 2011, pp. 168–171.

- [122] S. Vogel, M. Hülsbusch, T. Hennig, V. Blazek, and S. Leonhardt, "In-ear vital signs monitoring using a novel microoptic reflective sensor," *IEEE Trans. Inf. Technol. Biomed.*, vol. 13, no. 6, pp. 882–889, 2009.
- [123] D. W. Kim, "A new diagnostic method for detecting neuropathic diabetic foot by photoplethysmography," in *Proceedings of the 25th Annual International Conference of the IEEE*, 2003.
- [124] Y. Mendelson and C. Pujary, "Measurement site and photodetector size considerations in optimizing power consumption of a wearable reflectance pulse oximeter," *Proc. 25th Annu. Int. Conf. IEEE Eng. Med. Biol. Soc. (IEEE Cat. No.03CH37439)*, vol. 4, pp. 3016–3019, 2003.
- [125] E. Tur, M. Tur, H. I. Maibach, and R. H. Guy, "Basal perfusion of the cutaneous microcirculation: measurements as a function of anatomic position.," *J. Invest. Dermatol.*, vol. 81, no. 5, pp. 442–446, 1983.
- [126] X. F. Teng and Y. T. Zhang, "The effect of applied sensor contact force on pulse transit time," *Physiol. Meas.*, vol. 27, no. 8, p. 675, 2006.
- [127] J. Allen, K. Overbeck, G. Stansby, and A. Murray, "Photoplethysmography assessments in cardiovascular disease," *Meas. Control*, vol. 39, no. 3, pp. 80–83, 2006.
- [128] W. B. Murray and P. A. Foster, "The peripheral pulse wave: Information overlooked," *J. Clin. Monit.*, vol. 12, no. 5, pp. 365–377, 1996.
- [129] J. Allen, J. R. Frame, and A. Murray, "Microvascular blood flow and skin temperature changes in the fingers following a deep inspiratory gasp," *Physiol. Meas.*, vol. 23, no. 2, pp. 365–373, 2002.
- [130] V. F. Blanc, M. Haig, M. Troli, and B. Sauvé, "Computerized photo-plethysmography of the finger.," *Can. J. Anaesth.*, vol. 40, no. 3, pp. 271–8, 1993.
- [131] R. Stojanovic and D. Karadaglic, "A LED-LED-based photoplethysmography sensor.," *Physiol. Meas.*, vol. 28, no. 6, pp. N19–N27, 2007.
- [132] T. Rusch, R. Sankar, and J. Scharf, "Signal Processing Methods for Pulse Oximetry," *Compt. Biol. Med.*, vol. 26, no. 2, pp. 143–159, 1995.
- [133] O. Preining, "The physical nature of very, very small particles and its impact on their behaviour," *J. Aerosol Sci.*, vol. 29, no. 5–6, pp. 481–495, 1998.
- [134] A. A. Balandin, S. Ghosh, W. Bao, I. Calizo, D. Teweldebrhan, F. Miao, and C. N. Lau, "Superior thermal conductivity of single-layer graphene," *Nano Lett.*, vol. 8, no. 3, pp. 902–907, 2008.
- [135] K. S. Novoselov, A. K. Geim, S. V. Morozov, D. Jiang, Y. Zhang, S. V. Dubonos, I. V. Grigorieva, and A. A. Firsov, "Electric Field Effect in Atomically Thin Carbon Films," *Science (80-.)*, vol. 306, no. 5696, pp. 666–669, 2004.

- [136] C. N. R. Rao, A. K. Sood, K. S. Subrahmanyam, and A. Govindaraj, "Graphene: The new two-dimensional nanomaterial," *Angewandte Chemie - International Edition*, vol. 48, no. 42, pp. 7752–7777, 2009.
- [137] A. K. Geim and K. S. Novoselov, "The rise of graphene," *Nat. Mater.*, vol. 6, no. 3, pp. 183–191, 2007.
- [138] F. Schwierz, "Graphene transistors," *Nat. Nanotechnol.*, vol. 5, no. 7, pp. 487–496, 2010.
- [139] M. D. Stoller, S. Park, Z. Yanwu, J. An, and R. S. Ruoff, "Graphene-Based ultracapacitors," *Nano Lett.*, vol. 8, no. 10, pp. 3498–3502, 2008.
- [140] S. Casaluci, M. Gemmi, V. Pellegrini, A. Di Carlo, and F. Bonaccorso, "Graphene-based large area dye-sensitized solar cell modules," *Nanoscale*, vol. 8, no. 9, pp. 5368–78, 2016.
- [141] N. Celik, W. Balachandran, and N. Manivannan, "Graphene-based biosensors: methods, analysis and future perspectives," *IET Circuits, Devices Syst.*, vol. 9, no. 6, pp. 434–445, 2015.
- [142] F. Schedin, A. Geim, S. Morozov, E. Hill, P. Blake, M. Katsnelson, and K. Novoselov, "Detection of individual gas molecules adsorbed on graphene," *Nat. Mater.*, vol. 6, no. 9, pp. 652–655, 2007.
- [143] S. Bae, H. Kim, Y. Lee, X. Xu, J.-S. Park, Y. Zheng, J. Balakrishnan, T. Lei, H. Ri Kim, Y. Il Song, Y.-J. Kim, K. S. Kim, B. Özyilmaz, J.-H. Ahn, B. H. Hong, and S. Iijima, "Roll-to-roll production of 30-inch graphene films for transparent electrodes," *Nat. Nanotechnol.*, vol. 5, no. 8, pp. 574–578, 2010.
- [144] K. I. Bolotin, K. J. Sikes, Z. Jiang, M. Klima, G. Fudenberg, J. Hone, P. Kim, and H. L. Stormer, "Ultrahigh electron mobility in suspended graphene," *Solid State Commun.*, vol. 146, no. 9–10, pp. 351–355, 2008.
- [145] C. Berger, Z. Song, T. Li, X. Li, A. Y. Ogbazghi, R. Feng, Z. Dai, N. Alexei, M. E. H. Conrad, P. N. First, and W. A. De Heer, "Ultrathin epitaxial graphite: 2D electron gas properties and a route toward graphene-based nanoelectronics," *J. Phys. Chem. B*, vol. 108, no. 52, pp. 19912–19916, 2004.
- [146] W. A. de Heer, C. Berger, X. Wu, P. N. First, E. H. Conrad, X. Li, T. Li, M. Sprinkle, J. Hass, M. L. Sadowski, M. Potemski, and G. Martinez, "Epitaxial graphene," *Solid State Commun.*, vol. 143, no. 1–2, pp. 92–100, 2007.
- [147] W. Norimatsu and M. Kusunoki, "Epitaxial graphene on SiC{0001}: advances and perspectives," *Phys. Chem. Chem. Phys.*, vol. 16, pp. 3501–3511, 2014.
- [148] J. Kedzierski, P.-L. Hsu, P. Healey, P. W. Wyatt, C. L. Keast, M. Sprinkle, C. Berger, and W. a. de Heer, "Epitaxial Graphene Transistors on SiC Substrates," *IEEE Trans. Electron Devices*, vol. 55, no. 8, pp. 2078–2085, 2008.
- [149] Y. Zhang, L. Zhang, and C. Zhou, "Review of chemical vapor deposition of graphene and related applications," *Acc. Chem. Res.*, vol. 46, no. 10, pp. 2329–2339, 2013.

- [150] X. Li, W. Cai, J. An, S. Kim, J. Nah, D. Yang, R. D. Piner, A. Velamakanni, I. Jung, E. Tutuc, S. K. Banerjee, L. Colombo, and R. S. Ruoff, "Large-area synthesis of high quality and uniform graphene films on copper foils," *Science* (80-.), vol. 324, no. 5932, pp. 1312–1314, 2009.
- [151] Q. Yu, J. Lian, S. Siriponglert, H. Li, Y. P. Chen, and S. S. Pei, "Graphene segregated on Ni surfaces and transferred to insulators," *Appl. Phys. Lett.*, vol. 93, no. 11, 2008.
- [152] P. Sutter, J. T. Sadowski, and E. Sutter, "Graphene on Pt(111): Growth and substrate interaction," *Phys. Rev. B - Condens. Matter Mater. Phys.*, vol. 80, no. 24, 2009.
- [153] A. Kumar and C. Lee, "Synthesis and Biomedical Applications of Graphene: Present and Future Trends," in *Advances in Graphene Science*, InTech Open, 2013, pp. 55–75.
- [154] Y. Hernandez, V. Nicolosi, M. Lotya, F. Blighe, Z. Sun, S. De, I. T. McGovern, B. Holland, M. Byrne, Y. Gunko, J. Boland, P. Niraj, G. Duesberg, S. Krishnamurti, R. Goodhue, J. Hutchison, V. Scardaci, A. C. Ferrari, and J. N. Coleman, "High yield production of graphene by liquid phase exfoliation of graphite," *Nat. Nanotechnol.*, vol. 3, no. 9, pp. 563–8, 2008.
- [155] S. Stankovich, D. A. Dikin, G. H. Dommett, K. M. Kohlhaas, E. J. Zimney, E. A. Stach, R. D. Piner, S. T. Nguyen, and R. S. Ruoff, "Graphene-based composite materials," *Nature*, vol. 442, no. 7100, pp. 282–286, 2006.
- [156] A. Ciesielski and P. Samorì, "Graphene via sonication assisted liquid-phase exfoliation.," *Chem. Soc. Rev.*, vol. 43, no. 1, pp. 381–98, 2014.
- [157] Y. Si and E. T. Samulski, "Synthesis of water soluble graphene," *Nano Lett.*, vol. 8, no. 6, pp. 1679–1682, 2008.
- [158] D. V Kosynkin, A. L. Higginbotham, A. Sinitskii, J. R. Lomeda, A. Dimiev, B. K. Price, and J. M. Tour, "Longitudinal unzipping of carbon nanotubes to form graphene nanoribbons.," *Nature*, vol. 458, no. 7240, pp. 872–876, 2009.
- [159] K. Novoselov, V. Fal, and L. Colombo, "A roadmap for graphene," *Nature*, vol. 490, no. 7419, pp. 192–200, 2012.
- [160] J. C. Charlier, P. C. Eklund, J. Zhu, and A. C. Ferrari, "Electron and phonon properties of graphene: Their relationship with carbon nanotubes," *Carbon Nanotub.*, vol. 111, no. 2008, pp. 673–709, 2008.
- [161] M. Wall, "The Raman Spectroscopy of Graphene and the Determination of Layer Thickness," *Thermo Sci.*, p. 5, 2011.
- [162] A. C. Ferrari, "Raman spectroscopy of graphene and graphite: Disorder, electron-phonon coupling, doping and nonadiabatic effects," *Solid State Commun.*, vol. 143, no. 1–2, pp. 47–57, 2007.
- [163] E. Smith and G. Dent, *Modern Raman Spectroscopy: A Practical Approach*. 2005.

- [164] A. Ferrari, J. Meyer, V. Scardaci, C. Casiraghi, M. Lazzeri, F. Mauri, S. Piscanec, D. Jiang, K. Novoselov, S. Roth, and A. K. Geim, "Raman Spectrum of Graphene and Graphene Layers," *Phys. Rev. Lett.*, vol. 97, no. 18, pp. 1–4, 2006.
- [165] L. M. Malard, M. A. Pimenta, G. Dresselhaus, and M. S. Dresselhaus, "Raman spectroscopy in graphene," *Physics Reports*, vol. 473, no. 5–6, pp. 51–87, 2009.
- [166] T. Demirbas and M. Baykara, "Nanoscale tribology of graphene grown by chemical vapor deposition and transferred onto silicon oxide substrates," *J. Mater. Res.*, vol. 31, no. 13, pp. 1914–1923, 2016.
- [167] Y. You, Z. Ni, T. Yu, and Z. Shen, "Edge chirality determination of graphene by Raman spectroscopy," *Appl. Phys. Lett.*, vol. 93, no. 16, 2008.
- [168] C. Casiraghi, A. Hartschuh, H. Qian, S. Pliscanec, C. Georgia, A. Fasoli, K. S. Novoselov, D. M. Basko, and A. C. Ferrari, "Raman spectroscopy of graphene edges," *Nano Lett.*, vol. 9, no. 4, pp. 1433–1441, 2009.
- [169] Y. Y. Wang, Z. H. Ni, T. Yu, Z. X. Shen, H. M. Wang, Y. H. Wu, W. Chen, and A. T. S. Wee, "Raman studies of monolayer graphene: The substrate effect," *J. Phys. Chem. C*, vol. 112, no. 29, pp. 10637–10640, 2008.
- [170] J. Goldstein, D. E. Newbury, D. C. Joy, C. E. Lyman, P. Echlin, E. Lifshin, L. Sawyer, and J. R. Michael, *Scanning Electron Microscopy and X-ray Microanalysis*, vol. 44, no. 0. 2003.
- [171] J. Xie and J. Spallas, "Different Contrast Mechanisms in SEM Imaging of Graphene," *Agil. Technol.*, 2012.
- [172] "2-DTech Graphene Company." [Online]. Available: <http://www.2-dtech.com>. [Accessed: 19-Feb-2017].
- [173] C. Mattevi, H. Kim, and M. Chhowalla, "A review of chemical vapour deposition of graphene on copper," *J. Mater. Chem.*, vol. 21, no. 10, pp. 3324–3334, 2011.
- [174] J. Van de Water, P. Philips, and L. Thouin, "Bioelectric Impedance New Developments and Clinical Application," *Arch. Surg.*, vol. 102, no. 6, pp. 541–547, 1971.
- [175] D. Umer, G. Ellahi, W. Ellahi, S. Ayub, and Z. Din, "Bio-electrical Impedance Plethysmography-Designing an Efficient Non-invasive Electrode for Cardiac Rate Analysis," 2013.
- [176] "Braun International Patient Monitoring System." [Online]. Available: <http://www.brauninternational.com/shop-home/medical/patient-monitoring/central-monitoring-systems-detail#.WM8Ljkue-c8>. [Accessed: 10-Mar-2017].
- [177] "Cooking Hacks E-Health Module." [Online]. Available: <https://www.cooking-hacks.com/ehealth-sensor-shield-biometric-medical-arduino-raspberry-pi>. [Accessed: 07-Mar-2017].
- [178] "KST Visualizing Data." [Online]. Available: <https://kst-plot.kde.org/kst1/handbook/plugins-vector-processing.html>. [Accessed: 01-Mar-2017].

- [179] S. Nedios, I. Romero, J. H. Gerds-Li, E. Fleck, and C. Kriatselis, "Precordial electrode placement for optimal ECG monitoring: Implications for ambulatory monitor devices and event recorders," *J. Electrocardiol.*, vol. 47, no. 5, pp. 669–676, 2014.
- [180] J. V. Tranquillo, "Biomedical Signals and Systems," *Synth. Lect. Biomed. Eng.*, vol. 8, no. 3, pp. 1–233, 2013.
- [181] "Pulse Oximeter Module." [Online]. Available: <http://www.contecmed.com/>. [Accessed: 19-Oct-2016].
- [182] "HC Bluetooth Transceiver Module." [Online]. Available: <http://www.gearbest.com/>. [Accessed: 29-Nov-2016].
- [183] E. T. McAdams, P. Henry, J. M. Anderson, and J. Jossinet, "Optimal electrolytic chloriding of silver ink electrodes for use in electrical impedance tomography.," *Clin. Phys. Physiol. Meas.*, vol. 13 Suppl A, pp. 19–23, 1992.
- [184] B. R. Eggins, "Skin contact electrodes for medical applications," *Analyst*, vol. 118, no. 4, pp. 439–42, 1993.
- [185] J. Liu, M. Notarianni, G. Will, V. T. Tiong, H. Wang, and N. Motta, "Electrochemically exfoliated graphene for electrode films: Effect of graphene flake thickness on the sheet resistance and capacitive properties," *Langmuir*, vol. 29, no. 43, pp. 13307–13314, 2013.
- [186] A. Albulbul, "Evaluating Major Electrode Types for Idle Biological Signal Measurements for Modern Medical Technology," *Bioengineering*, vol. 3, no. 3, p. 20, 2016.
- [187] S. Grimnes and O.G. Martinsen, *Bioimpedance and Bioelectricity Basics*. 2008.
- [188] G. D. Clifford, "ECG statistics, noise, artifacts, and missing data," *Adv. Methods Tools ECG Data Anal.*, pp. 55–99, 2006.
- [189] S. Bagha and L. Shaw, "A Real Time Analysis of PPG Signal for Measurement of SpO₂ and Pulse Rate," *Int. J. Comput. Appl.*, vol. 36, no. 11, pp. 45–50, 2011.
- [190] A. R. Pérez Riera, C. Ferreira, C. Ferreira Filho, M. Ferreira, A. Meneghini, A. H. Uchida, E. Schapachnik, S. Dubner, and L. Zhang, "The enigmatic sixth wave of the electrocardiogram: The U wave," *Cardiology Journal*, vol. 15, no. 5, pp. 408–421, 2008.
- [191] M. K. Yapici, T. E. Alkhidir, "Intelligent Medical Garments with Graphene-Functionalized Smart-Cloth ECG Sensors," *Sensors*, vol. 17, no. 4, pp. 1-12, 2017.
- [192] S. K. Ameri, R. Ho, H. Jang, Y. Wang, D. M. Schnyer, D. Akinwande, N. Lu, "Thinnest transparent epidermal sensor system based on graphene," *In Electron Devices Meeting (IEDM)*, IEEE, Dec 3 (pp. 18-4), 2016.
- [193] C. Lou, R. Li, Z. Li, T. Liang, Z. Wei, M. Run, X. Yan, X. Liu, "Flexible graphene electrodes for prolonged dynamic ECG monitoring," *Sensors*, vol. 16, no. 11, 2016.
- [194] B. Schnalzer, E. M. Winter, H. Burgsteiner, "Mobile ECG Software Application - AndroECG", *FH Joanneum, The University of Applied Sciences Graz*, 2015.